Volume 67A
Number 4
July–August 1963

Physics and Chemistry

6

U.S. DEPARTMENT OF COMMERCE

SECTION A

JOURNAL OF RESEARCH

NATIONAL BUREAU OF STANDARDS

Journal of Research

of the

National Bureau of Standards

A. Physics and Chemistry

JULY-AUG. • 1963

VOLUME • 67A

NUMBER • 4

Editor: C. W. Beckett

Associate Editors: D. D. Wagman
J. M. Richardson

Publication dates:
Feb. 1, Apr. 1, June 1, Aug. 1, Oct. 1, Dec. 1, 1963

JOURNAL OF RESEARCH

The National Bureau of Standards Journal of Research reports research and development in the fields of activity shown at right. Also included from time to time are survey articles on topics closely related to the Bureau's scientific and technical program.

The Journal is published in four separate sections as follows:

A. Physics and Chemistry

Contains papers of interest primarily to scientists working in these fields. Issued six times a year. Annual subscription: domestic, $4.00; foreign, $4.75.

B. Mathematics and Mathematical Physics

Presents studies and compilations designed mainly for the mathematician and the theoretical physicist. Issued quarterly. Annual subscription: domestic, $2.25; foreign, $2.75.

C. Engineering and Instrumentation

Reports research and development results of interest chiefly to the engineer and the applied scientist. Issued quarterly. Annual subscription: domestic, $2.25; foreign, $2.75.

D. Radio Propagation

Reports work in radio propagation, upper atmospheric physics, and communications. Issued six times a year. Annual subscription: domestic, $4.00; foreign, $4.75.

U.S. DEPARTMENT OF COMMERCE
Luther H. Hodges, Secretary

NATIONAL BUREAU OF STANDARDS
A. V. Astin, Director

Functions and Activities

The functions of the National Bureau of Standards are set forth in the Act of Congress, March 3, 1901, as amended. These include the development and maintenance of the national standards of measurement and the provision of means and methods for making measurements consistent with these standards; the determination of physical constants and properties of materials; the development of methods and instruments for testing materials, devices, and structures; advisory services to government agencies on scientific and technical problems; invention and development of devices to serve special needs of the Government; and the development of standard practices, codes, and specifications. The work includes basic and applied research, development, engineering, instrumentation, testing, evaluation, calibration services, and various consultation and information services. The Bureau also serves as the Federal technical research center in a number of specialized fields. The scope of activities of the National Bureau of Standards is suggested in the following listing of the divisions and sections engaged in technical work.

Washington, D.C.

Electricity. Resistance and Reactance. Electrochemistry. Electrical Instruments. Magnetic Measurements. Dielectrics. High Voltage.

Metrology. Photometry and Colorimetry. Refractometry. Photographic Research. Length. Engineering Metrology. Mass and Scale. Volumetry and Densimetry.

Heat. Temperature Physics. Heat Measurements. Cryogenic Physics. Equation of State. Statistical Physics.

Radiation Physics. X-ray. Radioactivity. Radiation Theory. High Energy Radiation. Radiological Equipment. Nucleonic Instrumentation. Neutron Physics.

Analytical and Inorganic Chemistry. Pure Substances. Spectrochemistry. Solution Chemistry. Standard Reference Materials. Applied Analytical Research. Crystal Chemistry.

Mechanics. Sound. Pressure and Vacuum. Fluid Mechanics. Engineering Mechanics. Rheology. Combustion Controls.

Polymers. Macromolecules: Synthesis and Structure. Polymer Chemistry. Polymer Physics. Polymer Characterization. Polymer Evaluation and Testing. Applied Polymer Standards and Research. Dental Research.

Metallurgy. Engineering Metallurgy. Microscopy and Diffraction. Metal Reactions. Metal Physics. Electrolysis and Metal Deposition.

Inorganic Solids. Engineering Ceramics. Glass. Solid State Chemistry. Crystal Growth. Physical Properties. Crystallography.

Building Research. Structural Engineering. Fire Research. Mechanical Systems. Organic Building Materials. Heat Transfer. Inorganic Building Materials. Metallic Building Materials.

Applied Mathematics. Numerical Analysis. Computation. Statistical Engineering. Mathematical Physics. Operations Research.

Data Processing Systems. Components and Techniques. Computer Technology. Measurements Automation. Engineering Applications. Systems Analysis.

Atomic Physics. Spectroscopy. Infrared Spectroscopy. Solid State Physics. Electron Physics. Atomic Physics.

Instrumentation. Engineering Electronics. Electron Devices. Electronic Instrumentation. Mechanical Instruments. Basic Instrumentation.

Physical Chemistry. Thermochemistry. Surface Chemistry. Organic Chemistry. Molecular Spectroscopy. Molecular Kinetics. Mass Spectrometry.

Office of Weights and Measures

Boulder, Colo.

Cryogenic Engineering. Laboratory. Cryogenic Equipment. Cryogenic Processes. Properties of Materials. Cryogenic Technical Services.

Central Radio Propagation Laboratory

Ionosphere Research and Propagation. Low Frequency and Very Low Frequency Research. Ionosphere Research. Prediction Services. Sun-Earth Relationships. Field Engineering. Radio Warning Services. Vertical Soundings Research.

Radio Propagation Engineering. Data Reduction Instrumentation. Radio Noise. Tropospheric Measurements. Tropospheric Analysis. Propagation-Terrain Effects. Radio-Meteorology. Lower Atmosphere Physics.

Radio Systems. Applied Electromagnetic Theory. High Frequency and Very High Frequency Research. Modulation Research. Antenna Research. Navigation Systems.

Upper Atmosphere and Space Physics. Upper Atmosphere and Plasma Physics. Ionosphere and Exosphere Scatter. Airglow and Aurora. Ionospheric Radio Astronomy.

Radio Standards Laboratory

Radio Physics. Radio Broadcast Service. Radio and Microwave Materials. Atomic Frequency and Time-Interval Standards. Millimeter-Wave Research.

Circuit Standards. High Frequency Electrical Standards. Microwave Circuit Standards. Electronic Calibration Center.

Order all publications from the Superintendent of Documents
U.S. Government Printing Office, Washington D.C. 20402

Use of funds for printing this publication approved by the Director of the Bureau of the Budget (June 19, 1961).

JOURNAL OF RESEARCH of the National Bureau of Standards—A. Physics and Chemistry
Vol. 67A, No. 4, July–August 1963

Symmetry Splitting of Equivalent Sites in Oxide Crystals and Related Mechanical Effects

J. B. Wachtman, Jr., H. S. Peiser, and E. P. Levine

(January 18, 1963)

Changes in the symmetry of a crystal caused by an applied strain have been used to show in what circumstances an internal friction peak can result from the motion of isolated point defects. General rules are given to make the prediction, and these are applied to several structures of common oxides. The prediction for rutile is compared with experimental results which are interpreted by the movement of titanium ions between interstitial positions in the structure.

1. Introduction

Point defects, such as vacancies and interstitial atoms, are important in the deformation of crystalline solids. They cause Nabarro-Herring creep and interact with dislocations. Knowledge on jump frequencies between neighboring defect sites is therefore interesting and may be obtainable from internal-friction studies. From the disappearance of the internal-friction peak in α-iron when deprived of carbon and nitrogen, Snoek [1] [1] proposed his theory on the stress-induced jumping of interstitial atoms in body-centered cubic structures. As summarized by Berry [2], this model has been diversely applied to the study of other *bcc* metals such as tantalum containing carbon, oxygen, or nitrogen, and vanadium containing oxygen or nitrogen. Many new problems arise. It is natural, for example, to ask if such studies can be useful in ceramic oxides and other nonmetallic crystals.

The purpose of this paper is to present rules to show in what circumstances isolated point defects can contribute to internal friction, and to predict for specific oxides the types of defect which can be expected to give an internal-friction peak. There exist similar phenomena which by this stated purpose are excluded from discussion. For example, a point defect, such as an oxygen vacancy, may be constrained to remain in the neighborhood of a relatively immobile dislocation or defect such as a substitutional impurity atom. The motion of this oxygen vacancy can be studied by internal friction. The activation energy determined in such an experiment may differ from that for a free vacancy. Some discussion of pairs of point defects including pairs of atoms making up a split-interstitial site can be found elsewhere [2,3].

The approach in this paper might be termed the crystallographic method and should be compared with the "elastic dipole" being used by Nowick and co-workers [4] by analogy with the electric dipole because of the insight obtained by comparing dielectric and mechanical relaxation. The local distortion which interacts with a homogeneous strain does not have the symmetry of a true dipole, and "elastic dipole" should be understood as denoting a centrosymmetric local distortion and not as a type of dipole.

The "elastic dipole" method has developed out of work on mechanical and related electrical effects by A. S. Nowick and collaborators including B. S. Berry, R. W. Dreyfus, W. R. Heller, and R. B. Laibowitz [3,4,5,6,7,8]. A general paper is being prepared by Nowick and Heller [9].

The essential ideas of the crystallographic method have been previously introduced [10]. The present paper gives a fuller discussion and presents a series of applications.

2. Theory

2.1. Equivalence of Sites Under Arbitrary Strain

The box in the upper left-hand corner of figure 1 represents a perfect, strain-free crystal. We are concerned with the state of affairs in a crystal containing defects which is placed under an externally imposed homogeneous strain. The approach used in the elastic-dipole method, as given, for example, by B. S. Berry [2], although he does not use the term "elastic dipole", is to begin with the perfect, unstrained crystal, next to consider a defect introduced, setting up a local distortion, and finally to consider how the distorted portion of the crystal interacts with an externally applied strain. In the crystallographic method, the perfect crystal is considered to be homogeneously strained and a point defect is then inserted in either of two positions which were equivalent in the unstrained, perfect crystal. If the positions in the strained, perfect crystal were still

[1] Figures in brackets indicate the literature references at the end of this paper.

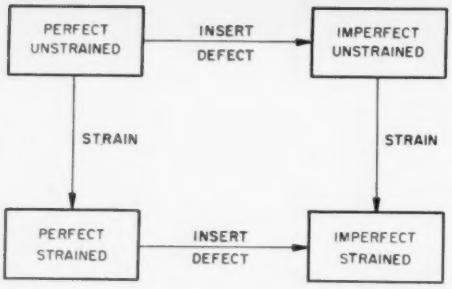

FIGURE 1. *Scheme showing two hypothetical ways of producing an imperfect, strained crystal from a perfect, unstrained crystal.*

equivalent, no internal friction would result, because a point defect would have the same energy if placed on either position and should therefore have no preference for either position. If, however, these positions in the strained, perfect crystal are inequivalent, the point defect should have different energies when placed on the two positions and a preferred distribution should result, leading to internal friction if the jump rate of the point defect is approximately equal to the frequency of the alternating strain. Therefore, only the behavior of the perfect crystal under strain need be considered in predicting the possible existence or absence of an internal friction peak which is caused by a point defect which can occupy a given set of equivalent positions in the crystal. When a peak is permitted on symmetry grounds, its magnitude may or may not be adequate for detection by a given experiment.

Now consider the effect of a homogeneous strain on a single crystal. We can think of a crystal as made up of a set of identical unit cells. Strain distorts these cells but, if the strain is homogeneous, all the cells will distort in the same way and so remain equivalent. Therefore, we need only consider what happens in one unit cell. It is convenient to choose the smallest possible cell—the primitive cell—which can be repeated in space to generate the crystal. In so doing, we have exploited the translation symmetry of homogeneous strain. There remains one other general symmetry property of homogeneous strain; it is always centrosymmetric. Thus a center of symmetry in a crystal cannot be removed by homogeneous strain and two positions in a crystal which are equivalent due to a center of symmetry cannot be made inequivalent by homogeneous strain.

These facts form the basis of *Rule 1:* Internal friction cannot occur if there is only one position per primitive cell (i.e., per lattice point in the strict crystallographic sense) or if there are only two, which are related by a center of symmetry. Internal friction should occur for some state of strain if there are two positions unrelated by a center of symmetry or if there are three or more positions.

To illustrate the application of this rule, consider the hypothetical two-dimensional oxide, MO, shown in figure 2. The positions are labeled according to the conventions used in the International Tables for

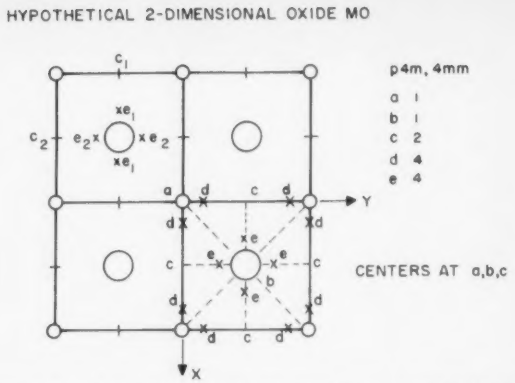

FIGURE 2. *A two-dimensional illustration of a crystal showing four unit cells.*

Each type of position is given the letter symbol as in ref. 11 and the number per unit cell is given.

X-ray Crystallography [11]. The metal ions are at positions *a* at the corners of the cells. There is only one *a*-type position per cell. Thus, all metal ion sites must remain equivalent under homogeneous strain. The oxygen sites also remain equivalent under homogeneous strain because there is only one *b*-type site per lattice point. Thus, we could not expect internal friction for either type of vacancy or for a substitutional impurity. The situation is different for interstitial ions, however. The largest interstitial position is labeled *c* and there are two per cell, c_1 and c_2. There is no center of symmetry to relate them, so some state of strain must exist which will split the set of *c*-type sites into two inequivalent subsets of equal size. In this case, we speak of a splitting factor of two; in the case of no splitting, we speak of a splitting factor of one. Now consider the four *e*-type positions. Interstitial hydrogen might take up such a position, close to the oxygen and equidistant from the two metal ions. The center of symmetry at the oxygen position keeps e_1 equivalent to e_1, and e_2 equivalent to e_2 after strain. Here we have a set of four sites per primitive cell splitting into two sets of two each and again we have a splitting factor of two.

The type of position actually occupied by a point defect must, of course, be used in these considerations and this is not always obvious. An impurity atom at a site (say *a* of fig. 2) may shift and form covalent bonds with some but not all of its initially equivalent neighbors, in which case it would have the symmetry of one of the neighboring special positions of lower symmetry (say *d* of fig. 2). Even when covalent bonds are not formed, the same result may be caused by the Jahn-Teller effect. In either case, alternating strain could then cause jumps from one of the *d*-type positions neighboring an *a*-type position to another. A more complicated situation would arise if the *a*-type position also split into subsets under a suitable strain (this is not true for our hypothetical oxide, MO, but a more complicated example could be given for which it is true.) One would then have to consider jumps, characterized by activation energy E_a, between *d*-type positions

neighboring an a-type positions and jumps, characterized by an activation energy E_a, between a-type positions. If d-type positions are occupied because of the formation of covalent bonds, E_d and E_a will both probably be large and there is no general reason to assume one is much larger than the other. For Jahn-Teller symmetry lowering, however, it appears that E_d would usually be appreciably less than E_a. Jahn-Teller effects are known to exist [12] and sites of lower symmetry for "substitutional" atoms may be preferred by as much as about 0.1 ev. This is a rather low value compared to the activation energy for motion of point defects of the type important in material transport processes, which is found [13] to range upward from about 0.4 ev for the alkali halides and is probably higher in the refractory oxides. If E_d is only a small fraction of E_a, one might expect to see two internal friction peaks in a curve of internal friction as a function of temperature at constant frequency, f. One peak should occur at a temperature for which the jump frequency, ν_d, of the impurity atom between d-type positions neighboring a single a-type position approximately matches the experimental frequency. At this temperature, the jump frequency, ν_a, between a-type positions would be negligibly small if E_a is several times larger than E_d. If the temperature is raised enough to make ν_a approximately equal f, the value of ν_d will become much larger. In effect, the motion over d-type sites averages out, so far as the internal friction peak caused by jumps between a-type sites is concerned, and for the discussion of symmetry restrictions on the high temperature peak, it is possible to treat the impurity atom as if it occupied the a-type sites rather than the d-type. This argument underlies our subsequent discussion of the symmetry conditions for internal friction associated with various point defects in the refractory oxides. For example, we discuss oxygen vacancies as if they occupied sites with the full symmetry of the oxygen position whereas it seems quite possible that Jahn-Teller symmetry lowering occurs. Throughout the discussion we assume that jumps between the sites of full symmetry have an appreciably higher activation energy than jumps between neighboring sites of lower symmetry and we limit our consideration to the high temperature range for which the jumps between sites of full symmetry could give internal friction peaks if permitted by symmetry.

2.2. Equivalence of Sites Under Specific States of Strain

The splitting factor is simply the number of inequivalent subsets into which the original set of initially equivalent positions splits. Usually the splitting will be into equal subsets (i.e., into subsets of equal size.) Thus, a set of six positions would be expected to split into two subsets of three positions or into three subsets of two positions or into six subsets of a single position. Under very special conditions, the set might split into a subset of two and a subset of four positions. Such splittings into unequal subsets do occasionally occur. We proceed to formulate a rule for the case of splitting into equal subsets. If this rule is blindly applied to a case of splitting into unequal subsets, it will sometimes signal trouble by giving nonintegral values of the splitting factor. These situations can also be treated by the present methods, but we omit detailed discussions to save space.

For the case of the splitting into equal subsets, we have *Rule 2:* The splitting factor of equivalent positions is equal to a fraction whose numerator is equal to the ratio of the order of the point group of the unstrained crystal to the order of the position point symmetry in the unstrained crystal; the denominator is the same ratio evaluated for the strained crystal. The quantity in Rule 2 is just the fraction whose numerator is the number of equivalent positions in a set in the unstrained crystal and whose denominator is the number of positions in a subset in the strained crystal. The expression in the numerator requires a little explanation. If an atom is put down in the unit cell of a crystal at a point having no position symmetry (i.e., a general position) and then acted upon by the symmetry elements of the crystal, a set of n atoms will be generated, which is equal to the order of the point group of the crystal, written n(PG). If the atom were put down at a position having some symmetry (special position), called the position point symmetry, then some of the positions generated by the action of the symmetry operations would coincide. To take this into account, we must divide out the number of coincident positions to obtain the number of distinct positions. Thus, the numerator is the number of equivalent positions in the general case divided by the number which coincide when the position has position point symmetry denoted by PPS. The denominator is the same quantity evaluated in the strained crystal. Subscript zero will be used to refer to the unstrained crystal and subscript one to refer to the strained crystal. We shall give an application of Rule 2, but first let us consider how to evaluate the action of a specific strain on PG_0 to obtain PG_1, and on PPS_0 to obtain PPS_1. Consider the symmetry of the components of homogeneous tensile strain or shear strain; i.e., what is the highest point symmetry (not necessarily crystallographic symmetry) consistent with the existence of a given strain. Take a point at the center of a sphere. Initially this point will have a symmetry which includes any possible crystallographic point symmetry; we wish to know the maximum symmetry possible after each component of strain has been applied. The two types of strain components are illustrated in two dimensions (for ease of visualization) in the upper part of figure 3, which shows the distortion of a square under tensile strain and under shear strain. The lower part of figure 3 shows the three dimensional point group (convention as in reference 11) which a sphere would possess after each of these strains. The point group for tensile strain, $PG_{xx} = \infty/mmm$, contains an infinite fold axis. That is, a rotational symmetry axis of any order is consistent with the axis of a tensile strain although axes higher than 6-fold cannot exist in crystals. The point group for shear strain,

PG_{xy}=2/mmm (abbreviated mmm), is seen to differ from PG_{xx} in containing no axis higher than 2-fold and in the orientation of the symmetry elements which it does contain. Any state of strain can be made up of combinations of tension and shear strains. The symmetry elements in a strained crystal will be those common to the unstrained crystal and to the strain.

Curie's principle [14] postulates that a homogeneously strained crystal will have the symmetry elements common to the point group of the unstrained crystal and to the strain for the given mutual orientation of the symmetry elements of the initial crystal point group and of the imposed strain. Curie's principle has been discussed especially by Shubnikov [15] and Koptsik [16]. We assume that this principle applies to position point symmetry, i.e., that the point symmetry of a position in the strained crystal consists of the symmetry elements common to the original position point symmetry and to the strain (again in the given mutual orientation).

Let us apply these ideas to the specific case of position *c*, the largest interstitial hole, in our hypothetical oxide, MO. Figure 4 shows the effect of strain ϵ_{xx}. The point group of the unstrained crystal, PG_0, is 4mm, which means a 4-fold axis intersected by two sets of mirror planes. This is shown in a pattern in which the small solid square represents the 4-fold axis and the heavy lines represent the mirror planes. The points show a set of eight equivalent general positions generated from one position so the order of the group is 8. We now take the symmetry elements in common with the point group of the strain ϵ_{xx}, that is, we take the intersection, denoted by the symbol $\cap$, of the two groups of symmetry operations. There is a logical difficulty (but no practical difficulty) in taking the symmetry elements common to a three dimensional point group, PG_{xx}, and a two dimensional point group, 4mm. One simply takes those elements of PG_{xx} which have meaning with respect to the plane of 4mm and finds which of these are also present in 4mm; the result is the intersection desired. The common elements are one 2-fold axis and two mirror planes giving us 2mm (equivalent to mm2) for PG_1 with order 4. The position *c* has two mirror planes which intersect in a 2-fold axis so that PPS_0 is 2mm with order 4. Taking the intersection with PG_{xx}, the point group of ϵ_{xx}, simply gives us $PPS_1 = PPS_0$. The splitting factor is thus 2. Now consider the action of the shear strain ϵ_{xy}, shown in figure 5 (the reference axes for components are Cartesian). The two figures on the left of the diagram are the same as in figure 4, but note the change in the point group of the strain. Taking the intersection of PG_0 with the point group PG_{xy} again gives us 2mm for PG_1. The intersection of PG_{xy} with PPS_0, however, contains only the 2-fold axis so that $n(PPS_1)=2$. The splitting factor thus equals 1. In other words, internal friction would not be allowed for ϵ_{xy}, but it would be permitted for ϵ_{xx}.

This rapid sketch indicates how the real, three-dimensional oxides can be treated.

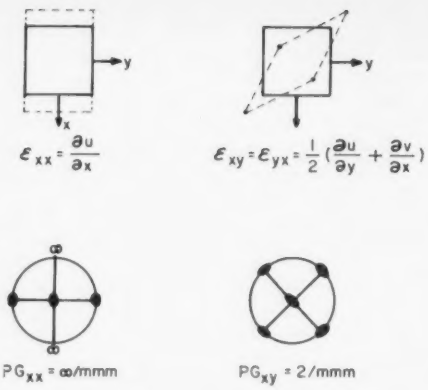

FIGURE 3. *The effect of tensile strain, ϵ_{xx}, and shear strain, ϵ_{xy}, on a square.*

Stereograms show the point group associated with each strain in three dimensions.

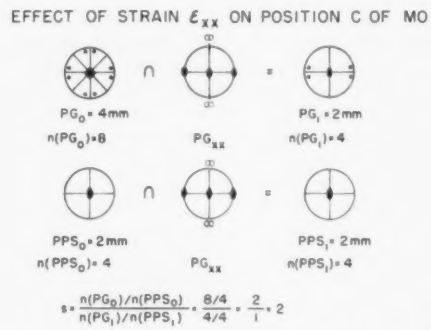

FIGURE 4. *An illustration of the effect of tensile train in lowering the point group symmetry and position point symmetry.*

The point group of the tensile strain, PG_{xx}, is drawn for three dimensions. Its application to two dimensions is simple; only the subgroup of operations appropriate to the plane under discussion need be considered.

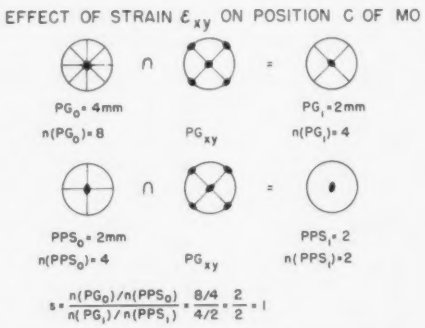

FIGURE 5. *An illustration of the effect of shear strain in lowering the point group symmetry and position point symmetry.*

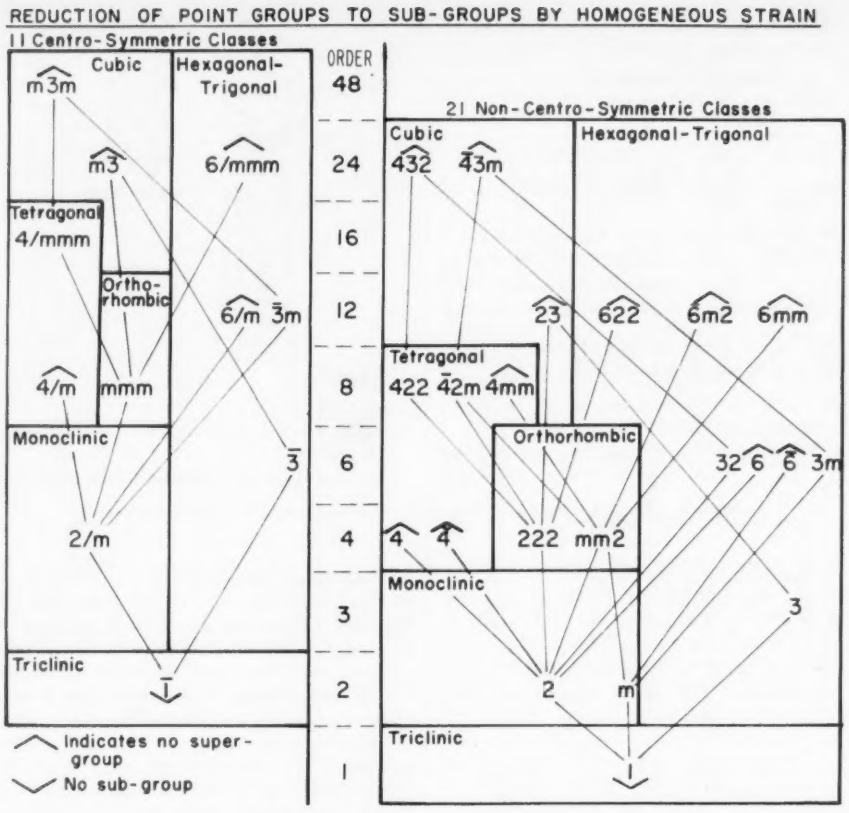

IT IS A NECESSARY CONDITION THAT A SUB-GROUP BELONG TO A DIFFERENT CRYSTAL SYSTEM THAN THE CORRESPONDING SUPER-GROUP

FIGURE 6. *Reduction of point groups to subgroups by homogeneous strain.*

2.3. Calculation of Possible Subgroups

There is a general table [10] which can be used to speed up the calculations somewhat. This table is shown in figure 6. There are only 32 crystallographic point-groups and homogeneous strain can only lower a given point group to one of its subgroups. Also, strain cannot change the crystal property of being centrosymmetric or non-centrosymmetric, so that the table splits into two separate parts. Further conditions arise because no strain can eliminate a two-fold axis perpendicular to or a plane of symmetry parallel to a three-, four-, or six-fold axis without also destroying the higher axial symmetry. Reduction to a subgroup turns out always to be accompanied by a change of crystal system (and a change in Bravais Lattice). This statement follows from the fact that even the most general strain in a crystal can be represented by a triaxial ellipsoid referred to Cartesian axes. A three-fold or higher axis restricts the triaxial ellipsoid to an ellipsoid of revolution which has mirror planes in all planes parallel to the unique axis and two-fold axes in all directions perpendicular to the unique axis. When all these conditions are taken into account, the table shown results. Point group 4/mmm, for example, can go only to mmm in the orthorhombic system or further to 2/m in the monoclinic system or further to 1 in the triclinic system. Point group 23 can either degrade to 3 or 222, but the former can only go to 1, whereas 222 can retain one of its diads independently of the other two.

3. Predictions for Specific Structures

3.1. Corundum-Type Structures (Al_2O_3)

Let us turn to some specific refractory oxides and other structures of interest, beginning with aluminum oxide in the stable, alpha form. This has the corundum structure, space group $R\bar{3}c$, point group $\bar{3}m$, with 3 Al_2O_3 in the rhombohedral unit cell. The calculations for this structure follow the lines of the example just given; the results are shown in figure 7 with a drawing of the aluminum and hole positions. The drawing has been slightly idealized, following Kronberg [17], by showing the aluminum ions in

Al_2O_3 (CORUNDUM)

$R\bar{3}c$ $\bar{3}m$

POSITION	NO.	SPLITTING ε_{xx}	ε_{zz}	ε_{xy}	ε_{xz}
b (HOLES)	2	1	1	2	2
c (ALUMINUM)	4	1	1	2	2
e (OXYGEN)	6	2*	1	3	3

CENTERS AT b AND MIDWAY BETWEEN TWO b POSITIONS IN SAME BASE PLANE

* UNEQUAL SPLITTING

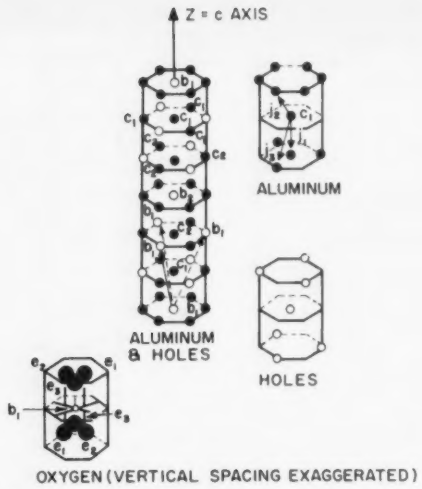

FIGURE 7. *Splitting factors for selected positions in the corundum structure.*

planes instead of being slightly displaced; the results, however, hold for the real structure. Starting at the hole in the base of the cell marked b_1 and moving along the c axis, we come to two aluminum ions, a hole, two more aluminum ions, and then the hole in the base of the next cell. The other aluminum ions and holes are arranged in identical chains which are parallel, but which have been moved up or down one position spacing. The oxygen ions are on hexagonal close-packed sheets at right angles to the aluminum chains. Our table shows that the tensile strains ϵ_{xx} or ϵ_{zz} cause no splitting of the sets of hole positions or aluminum positions. Shear strain causes a splitting into two equal subsets. The holes are labeled b_1 and b_2. A b_1 position is shown with its 6 neighboring b_2 positions. One might expect an inert gas such as helium to occupy the holes and to diffuse by b_1 to b_2 type jumps. Internal friction experiments using shear strain might thus provide information of direct interest concerning the diffusion of noble gases in corundum. The set of aluminum positions splits into the subsets c_1 and c_2. A c_1 position is shown with the neighboring c_2 positions in the two adjacent sheets (all aluminum positions in the same sheet are c_1 positions). There are three distinct types of jumps from a c_1 position to a c_2 position: j_1 is parallel to the c axis and passes between three equidistant oxygen ions; j_2 and j_3 must pass around an oxygen ion. In an internal friction experiment, we would have a relaxation process taking place by three parallel paths and the fastest path would be rate-determining. In diffusion, a series of steps is involved and the slowest step in the particular series would be rate determining. The usefulness of internal friction relative to cation diffusion in corundum is thus problematical and further work is needed on the combination of jumps required in diffusion. An interesting experiment involving aluminum positions would be the attempt to observe the interchange of aluminum and chromium ions in ruby by doing an internal friction experiment in shear. Turning now to the set of oxygen positions, we see that this splits into three subsets, e_1, e_2, and e_3. Here again a detailed theory of the combination of jumps involved in diffusion is needed, but it seems that some information of interest could be gained. In summary, for corundum it appears that internal friction experiments should be of direct interest to noble gas diffusion and very probably of interest in relation to oxygen diffusion (if nonstoichiometric alumina exists as various workers have suggested), but that the relation of internal friction to cation diffusion is problematical.

3.2. Periclase-Type Structures (MgO)

The results for MgO are shown in figure 8. There are just one magnesium ion and one oxygen ion per primitive cell so that no splitting occurs for either position. There are two large interstitial positions per primitive cell, but they are related by a center of symmetry so that no splitting takes place. The set of interstitial positions equidistant from three oxygen atoms does split into two subsets, but it seems unlikely that any impurity would occupy these positions. It thus appears that internal friction experiments are unlikely to give any information about isolated point defects in MgO. Pairs of point defects, however, are subject to different symmetry conditions as previously mentioned and internal friction experiments should be quite useful in the study of such pairs as a trivalent ion associated with a magnesium vacancy. There is also the previously mentioned possibility of the lowering of symmetry by the Jahn-Teller effect and the accompanying possibility of mechanical relaxation.

3.3. Rutile-Type Structures (TiO_2)

The situation for rutile is shown in figure 9. Here splitting exists for the titanium positions, the

MgO (ROCK SALT STRUCTURE)

Fm3m m3m

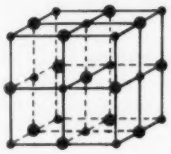

POSITION	NO.	SPLITTING $\mathcal{E}_{xx}$	SPLITTING $\mathcal{E}_{xy}$
a (MAGNESIUM)	1	1	1
b (OXYGEN)	1	1	1
c (LARGE INTERSTITIAL)	2	1	1
f (INTERSTITIAL EQUIDISTANT FROM 3 OXYGEN)	8	1	2

FIGURE 8. *Splitting factors for selected positions in the rocksalt structure.*

TiO_2 (RUTILE)

$P4_2/mnm$ 4/mmm

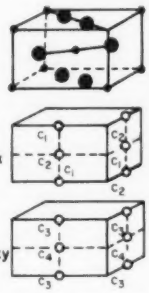

POSITION	NO.	SPLITTING $\mathcal{E}_{xx}$	$\mathcal{E}_{zz}$	$\mathcal{E}_{xy}$	$\mathcal{E}_{zy}$	GENERAL
a (TITANIUM)	2	1	1	2	1	2
c (INTERSTITIAL TITANIUM)	4	2	1	2	2	4
f (OXYGEN)	4	1	1	2	1	2
OBSERVED LARGE PEAK		YES	NO	NO	—	—

FIGURE 9. *Splitting factors for selected positions in the rutile structure.*

oxygen positions and the positions which interstitial titanium would be expected to occupy. The patterns of splitting are different and internal friction experiments seem to offer a good way to get information about the type of defect present in lightly reduced rutile. Data have been reported from two investigations [18, 19] which are in good agreement with each other. A peak was found in vacuum-reduced rutile which was not present when the specimen was stoichiometric. The peak occurs under strain ϵ_{xx} so that isolated oxygen vacancies are not responsible because the splitting factor for oxygen positions under strain ϵ_{xx} is one. The splitting factor for titanium interstitial positions under ϵ_{xx} is two and the existence of the peak suggests that the predominant type of point defect in vacuum-reduced rutile is the titanium interstitial. No peak is observed under strain ϵ_{xy}, although the splitting factor for titanium interstitial sites is two. The interpretation of the defect causing the observed peak is thus uncertain; the interpretation which appears most probable is that the defect responsible is either a titanium interstitial (with a contribution to the internal friction under ϵ_{xy} too small to be observed) or a pair of titanium interstitials. Such a pair, with one interstitial in the edge of a (100) face and the other in the center of an adjacent (010) face would [18] give a peak under ϵ_{xx}, but not under ϵ_{xy} or ϵ_{zz}.

3.4. Fluorite-Type Structures (ThO_2)

Turning now to thoria with the fluorite structure shown in figure 10, we see that the thorium positions, the oxygen positions, and the largest interstitial positions do not split under any strain so that this structure is not a promising one for internal friction studies of isolated point defects unless Jahn-Teller symmetry lowering leads to symmetry permitted internal friction as previously discussed. An internal friction peak attributed to pairs composed of a substitutional calcium ion and an oxygen vacancy has been reported [20].

3.5. Diamond-Type Structures (C)

The next structure to be considered is the diamond structure shown in figure 11. The carbon positions do not split, nor do the larger holes called the tetrahedral interstitial sites. There are, however, smaller interstitial sites which a small ion might occupy. Weiser [21] has calculated the binding energy for several interstitial ions in either the tetrahedral or the "hexagonal" interstitial position in germanium or silicon which have the diamond structure. He concludes that for lithium, the "hexagonal'' site is more probable than the tetrahedral site. This gives the opportunity for an interesting internal friction experiment, as the lithium ions should not contribute to internal friction if they are in tetrahedral sites,

ThO_2 (FLUORITE STRUCTURE)

Fm3m m3m

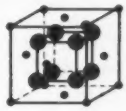

POSITION	NO.	SPLITTING $\mathcal{E}_{xx}$	SPLITTING $\mathcal{E}_{xy}$
a (THORIUM)	1	1	1
b (LARGE INTERSTITIAL)	2	1	1
c (OXYGEN)	2	1	1

FIGURE 10. *Splitting factors for selected positions in the fluorite structure.*

C (DIAMOND STRUCTURE)

Fd3m m3m

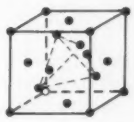

POSITION	NO.	SPLITTING $\mathcal{E}_{xx}$	SPLITTING $\mathcal{E}_{xy}$
a (CARBON)	2	1	1
b (TETRAHEDRAL)	2	1	1
d ("HEXAGONAL" INTERSTITIAL)	4	1	2

FIGURE 11. *Splitting factors for selected positions in the diamond structure.*

but are permitted by symmetry to do so if they are in "hexagonal" sites.

Southgate [22] has found an internal friction peak associated with oxygen in silicon. This could occur if the oxygen occupies "hexagonal" interstitial positions, but another possibility is that the oxygen is present in the tetrahedral holes, but occupies a special position of lower symmetry than the tetrahedral position. This is analogous to the substitutional positions *a* and *d* of our hypothetical two-dimensional oxide, MO, discussed previously. Infrared spectra indicate [23, 24] that the oxygen atom is in the tetrahedral hole, but is more tightly bound by covalent bonds to two of the four tetrahedrally situated silicon atoms; the oxygen atom thus occupies a position of lower symmetry and the occurrence of an internal friction peak is then consistent with the present theory. One can look upon the existence of an internal friction peak caused by isolated oxygen interstitials in silicon as proof that they do not occupy sites with the full symmetry of the tetrahedral interstitial position.

3.6. Perovskite-Type Structures ($BaTiO_3$)

The perovskite structure is shown in figure 12. The oxygen positions split and this might be an interesting structure to study.

3.7. Wurtzite-Type Structures (BeO)

The wurtzite structure, which is the structure of both BeO and ZnO is shown in figure 13. Two of the components of shear strain cause splitting of anion, cation, and interstitial positions. This structure thus appears quite suitable for internal friction studies using the appropriate shear strain.

3.8. Spinel-Type Structures ($MgAl_2O_4$)

Finally, the spinel structure is shown in figure 14. The magnesium positions do not split, but the aluminum and the oxygen positions do. Spinel is known to form a solid solution with Al_2O_3 and internal friction studies might be of interest.

4. Summary

In summary, internal friction appears to offer a unique method of obtaining information on atomic jump rates for isolated point defects, but only under very special symmetry conditions as given by Rules 1 and 2, or by the elastic dipole method, which is believed to give the same results so far as indicating the possible presence or absence of mechanical relaxation.

The writers thank A. S. Nowick and W. R. Heller for discussing the elastic dipole theory prior to the publication of its general form and for helpful discussions concerning the possibility that atoms occupy positions of lower symmetry than might at first be supposed.

CUBIC $BaTiO_3$ (PEROVSKITE STRUCTURE)

Pm3m m3m

POSITION	NO.	SPLITTING $\mathcal{E}_{xx}$	$\mathcal{E}_{xy}$
a (BARIUM	1	1	1
b (TITANIUM)	1	1	1
c (OXYGEN)	3	2*	2*

*UNEQUAL SUBSETS, 3=2+1

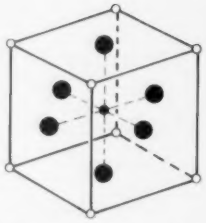

FIGURE 12. *Splitting factors for selected positions in the perovskite structure.*

BeO (WURTZITE STRUCTURE)

$P6_3mc$ 6mm

2 BeO IN PRIMITIVE CELL

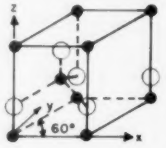

POSITION	$\mathcal{E}_{xx}$	$\mathcal{E}_{yy}$	$\mathcal{E}_{zz}$	$\mathcal{E}_{xy}$	$\mathcal{E}_{xz}$	$\mathcal{E}_{yz}$
a (TRIGONAL INTERSTITIAL)	1	1	1	2	2	1
b BERYLLIUM	1	1	1	2	2	1
b' OXYGEN DISPLACED ALONG c AXIS FROM b	1	1	1	2	2	1
b" (TETRAGONAL INTERSTITIAL) DISPLACED ALONG c-AXIS FROM b'	1	1	1	2	2	1

FIGURE 13. *Splitting factors for selected positions in the wurtzite structure.*

Al_2MgO_4 (SPINEL STRUCTURE)

Fd3m m3m

8 (Al_2MgO_4) IN fcc CELL

2 (Al_2MgO_4) IN PRIMITIVE CELL

POSITION	NO.	SPLITTING $\mathcal{E}_{xx}$	$\mathcal{E}_{xy}$
a (MAGNESIUM)	2	1	1
d (ALUMINUM)	4	1	2
e (OXYGEN)	8	1	2

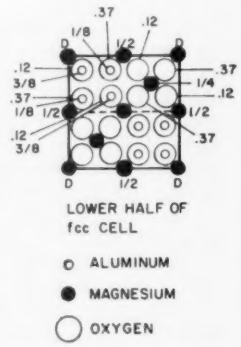

FIGURE 14. *Splitting factors for selected positions in the spinel structure.*

5. References

[1] J. Snoek, Physica **8,** 711 (1941).
[2] B. S. Berry, Acta Met. **10,** 271 (1962).
[3] Y. Haven and J. H. van Santen, J. Chem. Phys. **22,** 1146 (1954); Nuovo Cimento **7** (Suppl.), 605 (1958).
[4] A. S. Nowick and R. W. Heller, Bull. Am. Phys. Soc. **7,** 224 (1962).

[5] R. B. Laibowitz and R. W. Dreyfus, Bull. Am. Phys. Soc. **7,** 224 (1962).
[6] R. W. Dreyfus, Phys. Rev. **121,** 1675 (1961).
[7] R. W. Dreyfus and A. S. Nowick, J. App. Phys. **33,** 473 (1962).
[8] R. W. Dreyfus and A. S. Nowick, Phys. Rev. **126,** 1367 (1962).
[9] A.S. Nowick and W. R. Heller (submitted to Advances in Physics).
[10] J. B. Wachtman, Jr., and H. S. Peiser, App. Phys. Letters **1,** 20 (1962).
[11] International Tables for X-ray Crystallography, Vol. I. Edited by N. F. M. Henry and K. Lonsdale, Kynoch Press (1952).
[12] D. S. McClure, Solid State Phys. **9,** 399. Edited by F. Seitz and D. Turnbull, Academic Press (1959).
[13] J. S. Dryden and J. R. Meakins, Discussions Faraday Soc. **23,** 39 (1957).
[14] P. Curie, J. phys. **3,** 393 (1894).
[15] A. V. Shubnikov, Izvest. ANSSSR, Ser. fiz. **13,** 347 (1949).
[16] V. A. Koptsik, Kristallografiya **2,** 99 (1957). Soviet Phys.-Cryst. **2,** 95 (1957).
[17] M. L. Kronberg, Acta Met. **5,** 507 (1957).
[18] J. B. Wachtman, Jr., and L. R. Doyle, Internal Friction in Rutile Containing Point Defects (in preparation).
[19] R. D. Carnahan, Ph. D. Thesis at Northwestern University (1963). Thesis directed by J. O. Brittain.
[20] J. B. Wachtman, Jr., Mechanical and Electrical Relaxation in ThO^2 Containing CaO, Phys. Rev. **131,** No. 2 (1963).
[21] K. Weiser, Phys. Rev. **126,** 1427 (1962).
[22] P. D. Southgate, Proc. Phys. Soc. (London) **76,** 385 (1960).
[23] W. Kaiser, P. H. Keck, and C. F. Lange, Phys. Rev. **101,** 1264 (1956).
[24] H. J. Hrostowski and R. H. Kaiser, Phys. Rev. **107,** 966 (1957).

(Paper 67A4–216)

685–226—63——2

JOURNAL OF RESEARCH of the National Bureau of Standards—A. Physics and Chemistry
Vol. 67A, No. 4, July–August 1963

Relaxation Modes for Trapped Crystal Point Defects

A. D. Franklin

(April 10, 1963)

Group representation theory is applied to the problem of calculating the relaxation modes of a point defect trapped near an impurity atom or other defect in a crystal, where more than one set of neighboring sites is available to the point defect. For illustration, the case of a cation vacancy trapped near a divalent impurity in the sodium chloride lattice is treated, including nearest- and next-nearest-neighbor sites.

Haven and van Santen [1][1] and Wachtman [2] have used group theory methods to determine the relaxation modes appropriate to a vacancy trapped in the vicinity of an impurity ion in an ionic crystal. Wachtman applied the results to a study of ThO_2 containing Ca^{++} and oxygen ion vacancies. Haven and van Santen treated the case of a sodium-chloride lattice containing divalent impurities and sodium-ion vacancies. They gave complete solutions for all modes for the relaxation involving only nearest-neighbor positions, and also considered several special cases when next-nearest-neighbor positions were allowed as well. Previously, Lidiard [3] had solved, without restrictions, for the electrically active relaxation involving next-nearest-neighbor positions, but had not distinguished the two distinct modes present in his solutions. Dreyfus [4] showed that Lidiard's solution was indeed equivalent to two electrically active modes. Haven and van Satnen had also obtained two electrically active relaxation modes.

The group theory methods can in fact be very readily extended to include any number of additional sets of neighbors. The problem of the undriven relaxation can be expressed mathematically in matrix form [2]:

$$\left(\frac{d}{dt}I+C\right)\vec{p}=0 \tag{1}$$

where I is the identity matrix; C is a matrix in which the element in the ith row and jth column is the negative probability per unit time of a jump from the jth into the ith site, and in which the ith diagonal element is the sum of all jump probabilities out of the ith site; and $\vec{p}$ is the vector whose ith component is the probability of occupation of the ith site by the point-defect. The eigenvectors of C in the space of $\vec{p}$ are then the relaxation modes.

Since by definition the various sets are not carried into each other by the point-group operations of the crystal, they correspond to independent, orthogonal subspaces of the vector space defined by the occupation probability of the allowed sites. Hence the relaxation modes corresponding to the various appropriate irreducible representations of the point group can be found separately for each set, and then combined in a simple fashion. The relaxation modes for the whole system, involving all allowed sites, will be just linear combinations of the modes for the several sets, combining together only modes belonging to the same irreducible representation and arising, as partners, from the same symmetry-basis functions as discussed by Bethe [5].

Use of standard matrix algebra methods [6] allows the problem to be solved. A real, orthogonal transformation matrix may be formed from the uncombined relaxation modes as columns. This matrix transforms C to reduced form, from which the eigenvalues and the coefficients in the linear combinations of uncombined relaxation modes that constitute the eigenvectors may be calculated. The eigenvalues are just the reciprocal relaxation times. One eigenvalue is always zero, corresponding to the equilibrium distribution of the defects. If the corresponding normalized eigenvector is $\vec{u}_1$, and the other normalized eigenvectors are denoted by $\vec{u}_i$, then the solutions to eq (1) can be written

$$\vec{p}=\left[\vec{u}_1+\sum_{i=2}^{N} f_i\vec{u}_i\right]\left(\sum_k u_{1k}\right)^{-1}$$

$$f_i=f_{i0}\exp\left[-\lambda_i t\right]$$

where the f_{i0} are determined by the initial distribution, the u_{1k} are the components of $\vec{u}_1$, and the λ_i are the eigenvalues, and N is the total number of sites available.

Application of this technique to the problem of the motion of a sodium-ion vacancy trapped near a divalent impurity ion in the sodium-chloride lattice, and allowing jumps among nearest and next-nearest neighbors as well as interchange between the impurity ion and the vacancy on a nearest-neighbor site, results in the following (unnormalized) relaxation modes [7]:

[1] Figures in brackets indicate the literature references at the end of this paper.

Mode number	Description	Irreducible representation [8]	Relaxation frequency	Occupation ratio, a
1	Equilibrium	A_{1g}	0	w_2/w_4
2	Hydrostatic	A_{1g}	$2(w_3+2w_4)$	-2
3, 4, 5, 6	Uniaxial compression	E_{2g}	$(3w_1+w_3+2w_4)$ $\pm[(3w_1+w_3-2w_4)^2+2w_3w_4]^{\frac{1}{2}}$	$[(3w_1+w_3-2w_4)$ $\mp[(3w_1+w_3-2w_4)^2+2w_3w_4]^{\frac{1}{2}}]/w_4$
7, 8, 9	Shear	T_{1g}	$2(2w_1+w_3)$	
10, 11, 12	Inactive	T_{1u}	$2(3w_1+w_2+w_3)$	
13, 14, 15, 16, 17, 18	Electrical	T_{2u}	$(w_1+w_2+w_3+2w_4)$ $\pm[(w_1+w_2+w_3-2w_4)^2+4w_3w_4]^{\frac{1}{2}}$	$[(w_1+w_2+w_3-2w_4)$ $\mp[(w_1+w_2+w_3-2w_4)^2+4w_3w_4]^{\frac{1}{2}}]/w_4$

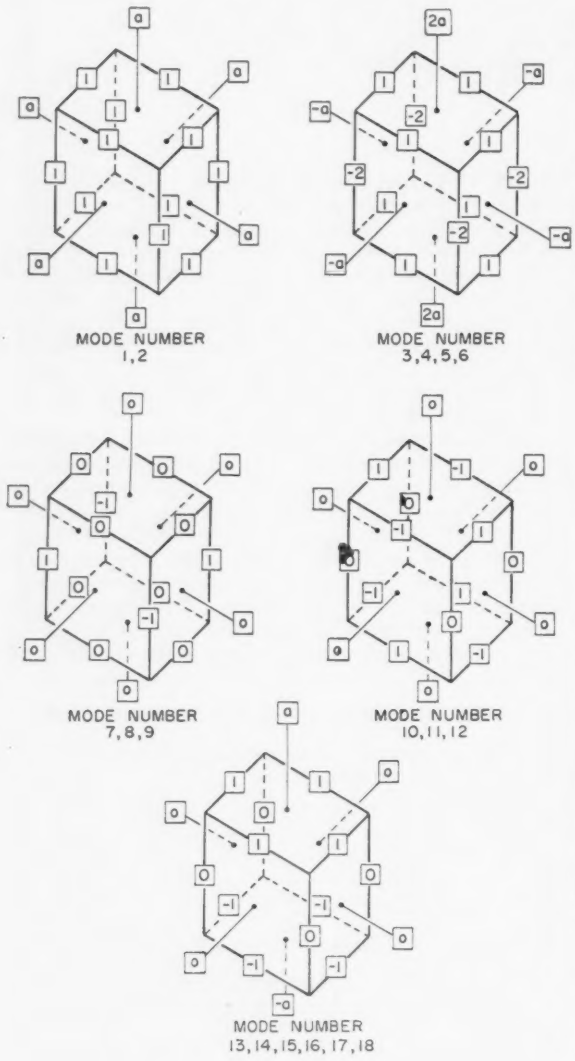

In this table, the w's represent the jump frequencies for the unit motions, as follows: w_1—between nearest-neighbor positions; w_2—interchange of the impurity ion and the vacancy in a nearest-neighbor position; w_3—nearest-neighbor to next-nearest-neighbor position; and w_4—the reverse of w_3. For any group, such as modes 7, 8, and 9, having the same relaxation frequency, any linear combination will also be a relaxation mode. In the group 3, 4, 5, and 6, there are two pairs distinguished by the cube axis along which the uniaxial compression acts. Note that relaxation along the third axis is the negative sum of those along the other two axes. In the electrically active group 13 to 18, there are three pairs, again corresponding to the three independent cube axes. The occupation ratios, a, given in the last column are defined in the sketches shown in the figure for the various modes.

The author is grateful to J. B. Wachtman, Jr., for the original suggestion that led to undertaking this problem, and to both J. B. Wachtman, Jr., and A. H. Kahn for extremely enlightening discussions.

References

[1] Y. Haven and J. H. van Santen, Nuovo Cimento **7,** 605 (1958).
[2] J. B. Wachtman, Jr., Phys. Rev. **131,** No. 2 (1963).
[3] A. B. Lidiard, Bristol Conference Report on Defects in Crystalline Solids, 1954 (The Physical Society, London, 1955), p. 283.
[4] R. W. Dreyfus, Phys. Rev. **121,** 1675 (1961).
[5] H. Bethe, Ann. Phys. **3,** 133 (1929).
[6] J. S. Lomont, Applications of Finite Groups (Academic Press, New York, 1959), p. 73.
[7] R. W. Dreyfus (private communication) has also obtained these same relaxation modes, using a somewhat different technique.
[8] The notation used here is that of H. Eyring, J. Walter, and G. E. Kimball, Quantum Chemistry (Wiley & Sons, New York, N.Y., 1944).

(Paper 67A4–217)

JOURNAL OF RESEARCH of the National Bureau of Standards—A. Physics and Chemistry
Vol. 67A, No. 4, July–August 1963

A Note on the Galvanomagnetic and Thermoelectric Coefficients of Tetragonal Crystalline Materials

W. C. Hernandez, Jr., and A. H. Kahn

(March 2, 1963)

The independent Hall, magnetoresistive, and thermoelectric coefficients for a tetragonal crystal have been tabulated and geometric configurations for their experimental measurement have been determined. These coefficients have been calculated on assumptions of several simple ellipsoidal models, in the range of nondegenerate statistics. Implications of experimentally observed isotropy or anisotropy of transport properties on the structure of the energy surfaces are noted.

1. Introduction

Detailed studies on the transport properties of rutile require tabulations of independent tensor coefficients. In this report we display these transport coefficients and method of measurement for galvanomagnetic and thermoelectric effects in tetragonal crystal structures. In anticipation of future experimental and theoretical results these transport coefficients have been calculated on the basis of various ellipsoidal energy band structures compatible with tetragonal symmetry.

2. Galvanomagnetic Coefficients

The electric current density components J_i and electric field components E_i are related by the conductivity tensor σ_{ij} in the following way:

$$J_i=\sigma_{ij}(\mathbf{H})E_j, \tag{1}$$

where the conductivity is understood to be a function of the magnetic field vector **H** and the Einstein summation convention is used. For weak field galvanomagnetic effects a series expansion of σ in powers of H up to second order is frequently sufficient. To second order the current is given by

$$J_i=\sigma_{ij}^{(0)}E_j+\sigma_{ijk}^{(1)}E_jH_k+\sigma_{ijkl}^{(2)}E_jH_kH_l. \tag{2}$$

The superscripts indicate the corresponding power of H, but these will frequently be omitted without causing ambiguity. The restrictions of crystal symmetry [1][1] and the Onsager reciprocal relations [2, 3] greatly limit the number of independent conductivity coefficients in eq (2). The symmetry conditions of the tetragonal point group of rutile (D_{4h}) require that eq (2) remain invariant under rotations about three perpendicular 2-fold axes, one of which is also a 4-fold axis. The Onsager relations require that $\sigma_{ij}^{(0)}$ and $\sigma_{ijkl}^{(2)}$ be symmetric, while $\sigma_{ijk}^{(1)}$ must be antisymmetric on interchange of i and j. The resulting independent components are produced in tables 1, 2 and 3. Note that for zero order there are two coefficients, for first order two, and for second order there are seven.

TABLE 1. *Zero order magneto-conductive coefficients*

Asterisks denote the coefficients which will be taken as the independent quantities. Indices 1, 2, 3 refer to crystal axes, 3 being the 4-fold axis.

$$\sigma_{11}^{*}=\sigma_{22}$$

$$\sigma_{33}^{*}$$

All others vanish.

TABLE 2. *First order magneto-conductive coefficients*

$$\sigma_{123}^{*}=-\sigma_{213}$$

$$\sigma_{132}^{*}=\sigma_{231}=-\sigma_{312}=-\sigma_{321}$$

All others vanish.

TABLE 3. *Second order magneto-conductive coefficients*

$$\sigma_{1111}^{*}=\sigma_{2222}$$

$$\sigma_{3333}^{*}$$

$$\sigma_{1122}^{*}=\sigma_{2211}$$

$$\sigma_{1212}^{*}=\sigma_{1221}\quad\sigma_{2121}=\sigma_{2112}$$

$$\sigma_{1133}^{*}=\sigma_{2233}$$

$$\sigma_{1213}^{*}=\sigma_{1312}=\sigma_{2313}=\sigma_{3213}=\sigma_{2331}=\sigma_{3123}=\sigma_{3132}=\sigma_{3231}$$

$$\sigma_{2311}^{*}=\sigma_{3322}$$

All others vanish.

More often than not, experimental measurements yield resistivity coefficients, the reciprocal of the conductivity. The resistivity coefficients are given up to the second order by

$$E_i=[\rho_{ij}^{(0)}+\rho_{ijk}^{(1)}H_k+\rho_{ijkl}^{(2)}H_kH_l]J_j. \tag{3}$$

[1] Figures in brackets indicate the literature references at the end of this paper.

The same symmetry conditions apply as before, and the independent resistive coefficients will be identified by the same subscripts. The coefficients are given in table 4.

TABLE 4. *Magnetoresistive coefficients in terms of magnetoconductive coefficients*

Expressions are correct to second order in the magnetic field

$$\rho_{ii}=\frac{1}{\sigma_{ii}} \qquad i=1, 2, 3$$

$$\rho_{ijk}=-\frac{\sigma_{ijk}}{\sigma_{ii}\sigma_{jj}} \qquad i, j, k=1, 2, 3$$

$$\rho_{iiii}=-\frac{\sigma_{iiii}}{\sigma_{ii}^2} \qquad i=1, 2, 3$$

$$\rho_{iijj}=\frac{\sigma_{ikj}\sigma_{kji}}{\sigma_{ii}\sigma_{jj}\sigma_{kk}}-\frac{\sigma_{iijj}}{\sigma_{ii}\sigma_{jj}} \qquad \begin{matrix} i, j=1, 2, 3 \\ i\neq j\neq k\neq i \end{matrix}$$

$$\rho_{iiij}=\frac{\sigma_{ikj}\sigma_{kij}}{\sigma_{ii}^2\sigma_{kk}}-\frac{\sigma_{iiij}}{\sigma_{ii}^2} \qquad \begin{matrix} i, j=1, 2, 3 \\ i\neq j\neq k\neq i \end{matrix}$$

3. Experimental Determination of Magnetoresistive Coefficients

The zero order resistivities are measured in the usual way. The two coefficients ρ_{11} and ρ_{33} refer to the resistivities perpendicular and parallel to the 4-fold axis, respectively. Typical experimental orientations and geometries have been determined for obtaining the magnetoresistive coefficients. The first order, or Hall, coefficients are described in table 5, and the second order in table 6. Numerals 1, 2, 3 in the tables refer to crystal axes; 1 and 2 being 2-fold and 3 being the 4-fold axis.

TABLE 5. *Configurations for measurement of Hall effect in tetragonal crystals*

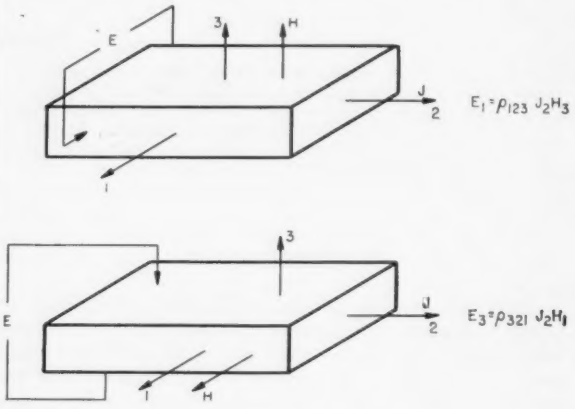

TABLE 6. *Configurations for measurement of magnetoresistive coefficients of tetragonal crystals*

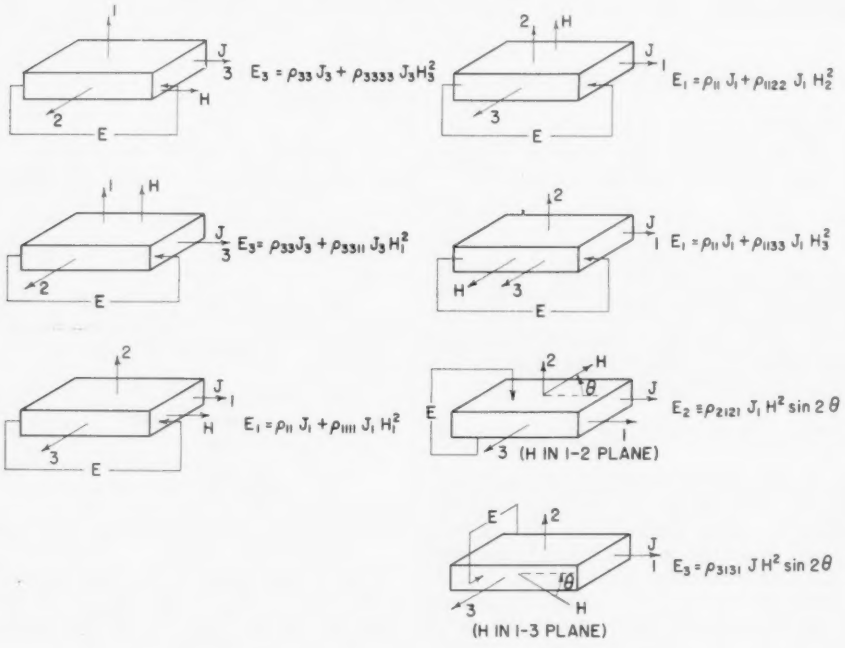

4. Magnetoconductive Coefficients on the Basis of Simple Ellipsoidal Models

Experimental and theoretical studies of band structure and transport coefficients may be aided by calculations of the transport properties of simple many ellipsoid energy surface configurations. This type of analysis of magnetoresistance has been very successful in the determination of the band structures of silicon and germanium [4, 5].

First we discuss the magnetoconductive coefficients of a single ellipsoid. Rather than using a Boltzmann equation, we follow Brooks [5] method of following the motion of a single charge carrier on the energy surface under the influence of applied fields, and then averaging over a Maxwell distribution of carriers. The equations of motion for an electron on an ellipsoidal energy surface, in the effective mass approximation, are the three equations

$$\frac{dv_i}{dt}=\frac{e}{m_i}E_i+\frac{e}{m_ic}(v_jH_k-v_kH_j), \tag{4}$$

where the subscripts indicate components or effective masses along principal directions of the ellipsoid, and i, j, k are cyclic permutations of 1, 2, 3. These equations of motion are solved to second order in **H**, giving the velocity as a function of time. The acquired motion is obtained by averaging over a distribution of free drift times given by $(1/\tau)e^{-t/\tau}$. The resultant acquired current averaged over the Maxwell distribution of electrons is

$$\begin{aligned}\langle ev_i\rangle=&\frac{e^2\langle\tau\rangle}{m_i}E_i+\frac{e^3\langle\tau^2\rangle}{m_im_jc}E_jH_k-\frac{e^3\langle\tau^2\rangle}{m_im_kc}E_kH_j\\&-\frac{e^4\langle\tau^3\rangle}{m_i^2m_kc^2}E_iH_j^2-\frac{e^4\langle\tau^3\rangle}{m_i^2m_jc^2}E_iH_k^2\\&+\frac{e^4\langle\tau^3\rangle}{m_im_jm_kc^2}E_kH_iH_k+\frac{e^4\langle\tau^3\rangle}{m_im_jm_kc^2}E_jH_jH_k.\end{aligned} \tag{5}$$

In eq (5) it is understood that the relaxation time τ is independent of direction, but perhaps dependent on energy. The angular brackets indicate averages of τ over the Maxwellian energy distribution. The total current is just the average current multiplied by the number of electrons in the ellipsoid.

We shall consider now the resistivity coefficients for several configurations of ellipsoids compatible with crystal symmetry. The assumption is made that the total conductivity of the array is the sum of the conductivities of the individual ellipsoids. Thus we assume that a relaxation time exists for each ellipsoid, and that intervalley scattering is negligible.

4.1. Single Ellipsoid

In this case $m_1=m_2\neq m_3$. The configuration is shown in figure 1. The results for the resistive coefficients are as follows:

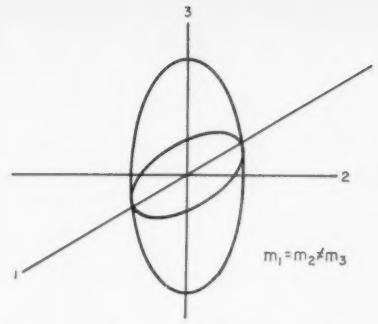

FIGURE 1. *Single ellipsoid for tetragonal symmetry.*

$$\rho_{123}=-\rho_{132}=\frac{-1}{nec}\frac{\langle\tau^2\rangle}{\langle\tau\rangle^2}$$

$$\rho_{1212}=\frac{m_1}{m_3}\rho_{1213}=\frac{1}{2m_3nc^2\langle\tau\rangle}\left[\frac{\langle\tau^3\rangle\langle\tau\rangle-\langle\tau^2\rangle^2}{\langle\tau\rangle^2}\right]$$

$$\rho_{1133}=\rho_{3311}=\frac{m_3}{m_1}\rho_{1122}=\frac{1}{m_1nc^2\langle\tau\rangle}\left[\frac{\langle\tau^3\rangle\langle\tau\rangle-\langle\tau^2\rangle^2}{\langle\tau\rangle^2}\right]$$

$$\rho_{1111}=\rho_{3333}=0.$$

4.2. Four Ellipsoid Model

In this case the ellipsoids can have three different masses, but are placed along the 2-fold axes, as shown in figure 2. The effective masses m_1, m_2, m_3 apply to ellipsoid number 1 of figure 2. The masses for the other ellipsoids are obtained by rotation. The resistive coefficients are:

$$\rho_{123}=\frac{-1}{nec}\frac{\langle\tau^2\rangle}{\langle\tau\rangle^2}\frac{4m_1m_2}{(m_1+m_2)^2}$$

$$\rho_{132}=\frac{1}{nec}\frac{\langle\tau^2\rangle}{\langle\tau\rangle^2}$$

Notice that $\frac{\rho_{123}}{\rho_{132}}=\frac{4m_1m_2}{(m_1+m_2)^2}=$constant.

$$\rho_{1122}=\frac{1}{nm_3c^2\langle\tau\rangle}\left[\frac{2(m_1^2+m_2^2)}{(m_1+m_2)^2}\frac{\langle\tau^3\rangle\langle\tau\rangle}{\langle\tau\rangle^2}-\frac{\langle\tau^2\rangle^2}{\langle\tau\rangle^2}\right]$$

$$\rho_{1212}=\frac{-1}{2nm_3c^2\langle\tau\rangle}\left[\frac{4m_1m_2}{(m_1+m_2)^2}\langle\tau^3\rangle\langle\tau\rangle-\frac{\langle\tau^2\rangle^2}{\langle\tau\rangle^2}\right]$$

$$\rho_{1133}=\frac{2}{(m_1+m_2)nc^2\langle\tau\rangle}\left[\frac{\langle\tau^3\rangle\langle\tau\rangle}{\langle\tau\rangle^2}-\frac{4m_1m_2}{(m_1+m_2)^2}\frac{\langle\tau^2\rangle^2}{\langle\tau\rangle^2}\right]$$

$$\rho_{1313}=\frac{-1}{(m_1+m_2)nc^2\langle\tau\rangle}\left[\frac{\langle\tau\rangle\langle\tau^3\rangle-\langle\tau^2\rangle^2}{\langle\tau\rangle^2}\right]$$

$$\rho_{3311}=\frac{(m_1+m_2)}{2m_1m_2nc^2\langle\tau\rangle}\left[\frac{\langle\tau\rangle\langle\tau^3\rangle-\langle\tau^2\rangle^2}{\langle\tau\rangle^2}\right]$$

$$\rho_{1111}=\rho_{3333}=0.$$

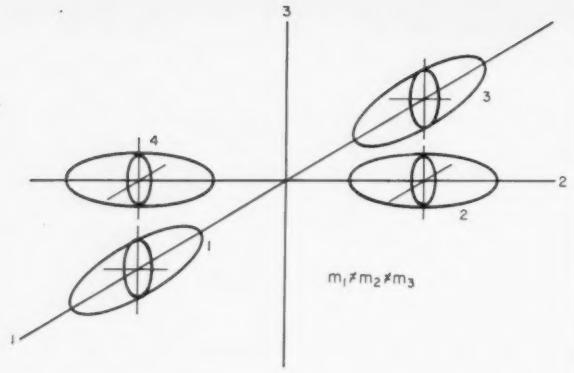

FIGURE 2. *Four ellipsoids for tetragonal symmetry.*

4.3. Five Ellipsoids

There is a possibility that more than one energy surface will be populated. To give an example, we shall consider a combination of cases (a) and (b), as shown in figure 3. The resultant resistivities are:

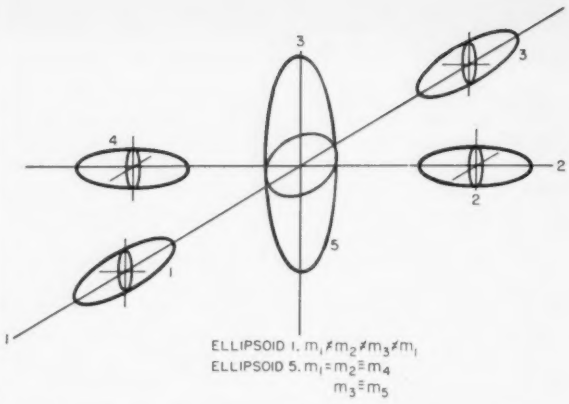

FIGURE 3. *Five ellipsoids for tetragonal symmetry.*

$$\rho_{123}=\frac{-1}{ec}\frac{\langle\tau^2\rangle}{\langle\tau\rangle^2}\frac{m_1m_2m_3^2n_1+m_1^2m_2^2n_2}{\left[(m_1+m_2)m_4\frac{n_1}{2}+m_1m_2n_2\right]^2}$$

$$\rho_{132}=\frac{1}{ec}\frac{\langle\tau^2\rangle}{\langle\tau\rangle}\frac{\left[(m_1+m_2)m_4m_5\frac{n_1}{2}+m_1m_2m_3n_2\right]}{(m_5n_1+m_3n_2)\left[(m_1+m_2)m_4\frac{n_1}{2}+m_1m_2n_2\right]}.$$

$$\rho_{1212}=1\frac{1}{c^2}\frac{\langle\tau^3\rangle}{\langle\tau\rangle^2}\frac{[m_4^2m_5n_1+m_1m_2m_3n_2]m_1m_2}{\left[(m_1+m_2)m_4\frac{n_1}{2}+m_1m_2n_2\right]^2m_3m_5}+\frac{1}{2c^2}\frac{\langle\tau^2\rangle^2}{\langle\tau\rangle^3}\frac{\left[(m_1+m_2)m_4m_5\frac{n_1}{2}+m_1m_2m_3n_2\right]^2}{\left[(m_1+m_2)m_4\frac{n_1}{2}+m_1m_2n_2\right]^2[m_5n_1+m_3n_2]m_3m_5}$$

$$\rho_{1122}=\frac{1}{c^2}\frac{\langle\tau^3\rangle}{\langle\tau\rangle^2}\frac{\left[(m_1^2+m_2^2)m_4^2m_5\frac{n_1}{2}+m_1^2m_2^2m_3n_2\right]}{\left[(m_1+m_2)m_4\frac{n_1}{2}+m_1m_2n_2\right]^2m_3m_5}-\frac{1}{2c^2}\frac{\langle\tau^2\rangle^2}{\langle\tau\rangle^3}\frac{\left[(m_1+m_2)m_4m_5\frac{n_1}{2}+m_1m_2m_3n_2\right]^2}{\left[(m_1+m_2)m_4\frac{n_1}{2}+m_1m_2n_2\right]^2[m_5n_1+m_3n_2]m_3m_5}$$

$$\rho_{1133}=\frac{1}{c^2}\frac{\langle\tau^3\rangle}{\langle\tau\rangle^2}\frac{\left[(m_1+m_2)m_4^3\frac{n_1}{2}+m_1^2m_2^2n_2\right]}{\left[(m_1+m_2)m_4\frac{n_1}{2}+m_1m_2n_2\right]^2m_4}-\frac{1}{c^2}\frac{\langle\tau^2\rangle^2}{\langle\tau\rangle^3}\frac{[m_4^2n_1+m_1m_2n_2]^2m_1m_2}{\left[(m_1+m_2)m_4\frac{n_1}{2}+m_1m_2n_2\right]^3m_4}$$

$$\rho_{1313}=\frac{-1}{c^2}\frac{\langle\tau^3\rangle}{\langle\tau\rangle^2}\frac{[m_4^2m_5n_1+m_1m_2m_3n_2]}{\left[(m_1+m_2)m_4\frac{n_1}{2}+m_1m_2n_2\right][m_5n_1+m_3n_2]m_4}$$

$$+\frac{1}{2c^2}\frac{\langle\tau^2\rangle^2}{\langle\tau\rangle^3}\frac{[m_4^2n_1+m_1m_2n_2]\left[(m_1+m_2)m_4m_5\frac{n_1}{2}+m_1m_2m_3n_2\right]}{\left[(m_1+m_2)m_4\frac{n_1}{2}+m_1m_2n_2\right]^2[m_5n_1+m_3n_2]m_4}$$

$$\rho_{3311}=\frac{1}{c^2}\frac{\langle\tau^3\rangle}{\langle\tau\rangle^2}\frac{\left[(m_1+m_2)m_4^2m_5\frac{n_1}{2}+m_1m_2m_3^2n_2\right]}{[m_5n_1+m_3n_2]^2m_1m_2m_4}-\frac{1}{c^2}\frac{\langle\tau^2\rangle^2}{\langle\tau\rangle^3}\frac{\left[(m_1+m_2)m_4m_5\frac{n_1}{2}+m_1m_2m_3n_2\right]^2}{\left[(m_1+m_2)m_4\frac{n_1}{2}+m_1m_2n_2\right][m_5n_1+m_3n_2]^2m_1m_2m_4}.$$

In all the previous formulas the temperature dependence of the resistivities depends upon averages of several powers of τ. For power law scattering, $\tau=\tau_0\epsilon^{-p}$, where ϵ is the energy and p the power, we have

$$\langle\tau^n\rangle=\tau_0^n\frac{(kT)^{-np}\Gamma\left(\frac{5}{2}-np\right)}{\Gamma\left(\frac{5}{2}\right)}. \tag{6}$$

It might be worth noting that in tetragonal crystals anisotropic effects make themselves known in lower order magnetoresistive coefficients than for cubic cases. Thus, for example, information concerning anisotropy of the energy surfaces can be obtained from the Hall coefficient of TiO_2, while one must go to magnetoresistive to see the lowest order effects of cubic anisotropy in Si or Ge.

5. Thermoelectric Power

The electric current density components J_i and the thermal current components Q_i are related to the electric field components E_i and the temperature gradient components $\frac{\partial T}{\partial X_j}$ in the following way:

$$J_i=A_{ij}^{11}E_j+A_{ij}^{12}\frac{\partial T}{\partial X_j} \tag{7}$$

$$Q_i=A_{ij}^{21}E_j+A_{ij}^{22}\frac{\partial T}{\partial X_j} \tag{8}$$

However, in order to apply Onsager's theorem to the above coefficients we must rewrite the equations in terms of affinities and fluxes [6]. Thus (7) and (8) become

$$-\frac{J_i}{e}=B_{ij}^{11}\frac{1}{T}\frac{\partial M}{\partial X_j}+B_{ij}^{12}\frac{\partial}{\partial X_j}\frac{1}{T} \tag{9}$$

$$Q_i=B_{ij}^{21}\frac{1}{T}\frac{\partial M}{\partial X_j}+B_{ij}^{22}\frac{\partial}{\partial X_j}\frac{1}{T}, \tag{10}$$

where e is the charge of an electron and μ is the electrochemical potential. The Onsager theorem states that $B_{ij}^{kl}=B_{ji}^{lk}$ and thereby reduces the number of independent coefficients. Accordingly, the number of the independent coefficients A_{ij}^{kl} is also reduced. Applying the restrictions of crystal symmetry to the coefficients A_{ij}^{kl} it follows that there are two independent elements $A_{11}^{kl}=A_{22}^{kl}$ and A_{33}^{kl}.

The absolute thermoelectric power is defined as the change in voltage per unit change in temperature difference at zero current. So setting J_i equal to zero and using the above results we get:

$$E_i=-\frac{A_{ii}^{12}}{A_{ii}^{11}}\frac{\partial T}{\partial X_i}. \tag{11}$$

The voltage V is given by

$$V_i=\int_{x_1}^{x_2}E_i dx_i=-\int_{x_1}^{x_2}\frac{A_{ii}^{12}}{A_{ii}^{11}}\frac{\partial T}{\partial X_i}dx_i$$

$$=-\int_{T_1}^{T_2}\frac{A_{ii}^{12}}{A_{ii}^{11}}dT_i. \tag{12}$$

The absolute thermoelectric power is

$$\frac{dV_i}{dT}=-\frac{A_{ii}^{12}}{A_{ii}^{11}}=S_i. \tag{13}$$

It follows that we have two possible values of the thermoelectric power, $-\frac{A_{11}^{12}}{A_{11}^{11}}$ and $-\frac{A_{33}^{12}}{A_{33}^{11}}$, corresponding to the one and three axes respectively. We see also that the Onsager theorem does not give us any limitation on the possible numbers of values of the thermoelectric power but only gives us relations between it and other thermoelectric coefficients.

6. Thermoelectric Power on the Basis of Simple Ellipsoidal Models

We begin with the Boltzmann transport equation [7]:

$$-\frac{2\pi e}{h}E\cdot\nabla_k f+\frac{\partial f}{\partial T}v\cdot\nabla T=\frac{f-f_0}{\tau(\epsilon)}. \tag{14}$$

Since the electric field and temperature gradient are always small and their squares and products can be neglected, we obtain an approximate solution of eq (14) by putting $f=f_0$ on the left side where f_0 is the equilibrium distribution. Using

$$\frac{\partial f_0}{\partial T}=T\frac{\partial}{\partial T}\left(\frac{\epsilon-\zeta}{T}\right)\frac{\partial f_0}{\partial\epsilon}$$

we get

$$f=f_0+\tau v_j\frac{\partial f_0}{\partial E}\left(\frac{\partial T}{\partial X_j}\frac{\epsilon}{T}+T\frac{\partial T}{\partial X_j}\frac{\partial}{\partial T}\left(\frac{\zeta}{T}\right)+eE_j\right), \tag{15}$$

where ζ is the Fermi energy, and ϵ the energy. The electric current density is given by [7]:

$$J=\frac{-e}{4\pi^3}\int vfdk. \tag{16}$$

Using our solution for f and writing in terms of components of J we get:

$$J_i=K_{ij}\left[e^2E_j+eT\frac{\partial}{\partial X_j}\left(\frac{\zeta}{T}\right)\right]+L_{ij}\left[\frac{e}{T}\frac{\partial T}{\partial X_j}\right], \tag{17}$$

where

$$-\frac{1}{4\pi^3}\int_0^\infty \tau v_i v_j \frac{\partial f_0}{\partial \epsilon}\, dk = K_{ij} \tag{18}$$

$$-\frac{1}{4\pi^3}\int_0^\infty \tau v_i v_j \frac{\partial f_0}{\partial \epsilon}\, E dk = L_{ij}. \tag{19}$$

Setting $J_i=0$, we calculate the thermoelectric power in the same manner as section 5. The result is:

$$S_i=-\frac{1}{e}\left[\frac{L_{ii}-\zeta K_{ii}}{K_{ii}}\right]\frac{1}{T}. \tag{20}$$

(Here we anticipated the results $K_{ij}=L_{ij}=0$ if $i\neq j$.) Assuming a single ellipsoidal energy surface and using $dk=\frac{d\epsilon dS}{\text{grad}_k \epsilon}$ as the element of volume where dS is an element of surface of the ellipsoid, we find upon performing the indicated integration:

$$K_{ii}=\frac{\sigma_{ii}(p)}{e^2}$$

$$L_{ii}=\frac{kT}{e^2}\left(\frac{5}{2}-p\right)\sigma_{ii}(p). \tag{21}$$

We have again assumed $\tau=\tau_0\epsilon^{-p}$. (The above results are obvious on comparison with the expression for σ_{ii} by Abeles and Meiboom [3].) The thermoelectric power for a single ellipsoid may be written:

$$S_i=\frac{-1}{eT}\left[\frac{\left(\frac{5}{2}-p\right)kT\sigma_{ii}-\zeta\sigma_{ii}}{\sigma_{ii}}\right]. \tag{22}$$

The case for many ellipsoids is easily gotten from the above result. Since conductivities simply add we have the result:

$$S_i=-\frac{1}{eT}\frac{\left[\left(\frac{5}{2}-p\right)kT\sum_k \sigma_{ii}^{(k)}-\sum_k \zeta^{(k)}\sigma_{ii}^{(k)}\right]}{\sum_k \sigma_{ii}^{(k)}}, \tag{23}$$

where k refers to the kth ellipsoid. We note that if ζ, measured from the bottom of the ellipsoid, is constant for all ellipsoids of the configuration then the thermoelectric power is independent of direction and is given by

$$S=-\frac{1}{eT}\left[\left(\frac{5}{2}-p\right)kT-\zeta\right]. \tag{24}$$

Thus the simplest case which could yield an anisotropic thermoelectric power and also have tetragonal symmetry would be the five ellipsoid case discussed earlier.

Using the relationship

$$e^{\zeta/kT}=\frac{1}{2}nh^3(2\pi mkT)^{-3/2} \tag{25}$$

we can express the thermoelectric power in terms of the density of electrons, temperature, and effective masses.

6.1. Single-Ellipsoid Case

The masses are those indicated in figure 1. Using eqs (24) and (25) we get for the case of a single ellipsoid:

$$S_i=S=-\frac{1}{e}G, \tag{26}$$

where

$$G=2k-k\log n+\frac{3}{2}k\log T-k\log\frac{1}{2}h^3(2\pi mk)^{-3/2} \tag{27}$$

and

$$m=(m_1m_2m_2)^{1/3}. \tag{28}$$

6.2. Four Ellipsoid Case, Figure 2

Carrying out a similar calculation for the four ellipsoid case we get:

$$G=2k-k\log\frac{n}{4}+\frac{3}{4}k\log T-k\log\frac{1}{2}h^3(2\pi mk)^{-3/2},$$

with eqs (26) and (28) still true. Note that the only change is the division of the density of electrons by 4. This is just what we would expect since equal voltage sources in parallel produce a voltage equal to one of the sources. Thus the presence of many ellipsoids is seen as an effective reduction of the number of carriers.

6.3. Five Ellipsoid Models

We shall consider the simplest anisotropic case of five ellipsoids as shown in figure 3. Using eqs (23) and (25), we obtain for the two values of the thermoelectric power:

$$G_a=\frac{\frac{n_1}{2}\left(\frac{1}{m_1}+\frac{1}{m_2}\right)G_1+\frac{n_2}{m_4}G_2}{\frac{n_1}{2}\left(\frac{1}{m_1}+\frac{1}{m_2}\right)+\frac{n_2}{m_4}}$$

$$G_c=\frac{\frac{n_1}{m_3}G_1+\frac{n_2}{m_5}G_2}{\frac{n_1}{m_3}+\frac{n_2}{m_5}},$$

where

$$G^1=2k-k\log\frac{n_1}{4}+\frac{3}{2}k\log T-k\log\frac{1}{2}h^3(2\pi m^1k)^{-3/2}$$

$$G^2=2k-k\log n_2+\frac{3}{2}k\log T-k\log\frac{1}{2}h^3(2\pi m^2k)^{-3/2}$$

$$m^1=(m_1m_2m_3)^{1/3}$$

$$m^2=(m_4^2m_5)^{1/3}.$$

Here $S_a = -\frac{G_a}{e}$ is the thermoelectric power perpendicular to the 4-fold axis and $-\frac{G_c}{e}$ is the thermoelectric power along the 4-fold axis.

7. Phonon-Drag Contribution to the Thermoelectric Power

In all the former work, the phonon-drag contribution [8, 9] to the thermoelectric power was ignored. According to Frederikse [9] the thermoelectric power is given by:

$$S = -\frac{1}{e}\left[\frac{K_2}{K_1 T} - \frac{\zeta}{T} + \frac{K^1}{K_1}\right], \tag{29}$$

where $-\frac{1}{e}\frac{K^1}{K_1}$ is the extra term due to phonon drag. For the case of lattice scattering ($p = \frac{1}{2}$), i.e., $\Lambda_{ei} >> \Lambda_{e\varphi}$,

$$\frac{K^1}{K_1} = \frac{3}{4}\pi^{1/2}\frac{\Lambda_{ph}}{\Lambda_{e\varphi}}\left(\frac{2ms^2}{kT}\right)^{1/2} k, \tag{30}$$

where

s = speed of sound,
Λ_{ph} = phonon-phonon mean free path,
$\Lambda_{e\varphi}$ = electron-phonon mean free path,
Λ_{ei} = electron-impurity ion mean free path,
$m = (m_1 m_2 m_3)^{1/3}$.

We have the result that the thermoelectric power of a single ellipsoid is given by:

$$S = -\frac{1}{e}\left[2k - \frac{\zeta}{T} + \frac{3}{4}\pi^{1/2}\frac{\Lambda_{ph}}{\Lambda_{e\varphi}}\left(\frac{2ms^2}{kT}\right)^{1/2} k\right]. \tag{31}$$

Any easy extension to the case of many ellipsoids is obtained by use of [10]

$$\underset{\text{total } S_i}{S_i} = \frac{\sum_k S_k \sigma_i^k}{\sum_k \sigma_i^k}. \tag{32}$$

Here S_k indicates the thermoelectric power of a single ellipsoid and σ_i^k its conductivity in the ith direction. This is easily seen to be equivalent to our former method of treating the case of many ellipsoids.

NOTE: The formulas of sections 4.3 and 6.3 are derived on the basis of a single relaxation time for the different bands. Generalization to different relaxation times for each band is straightforward.

8. References

[1] W. A. Wooster, A textbook on crystal physics, ch. 1 (Cambridge University Press, 1938).
[2] L. Onsager, Phys. Rev. **37,** 405 (1931); **38,** 2265 (1931).
[3] J. Yahia and J. A. Marcus, Phys. Rev. **113,** 137 (1959).
[4] B. Abelès and S. Meiboom, Phys. Rev. **95,** 31 (1954).
[5] H. Brooks, Advances in electronics and electron physics, vol. 8, p. 127 (Academic Press Inc., 1955).
[6] H. B. Callen, Thermodynamics, p. 295 (John Wiley & Son Inc., 1960).
[7] A. H. Wilson, The theory of metals, 2d edition, p. 200 (Cambridge University Press, 1953).
[8] C. Herring, Phys. Rev. **96,** 1163 (1954).
[9] H. P. R. Frederikse, Phys. Rev. **92,** 248 (1953).
[10] D. K. C. MacDonald, Thermoelectricity: an introduction to the principles, p. 114 (John Wiley & Sons, 1962).

(Paper 67A4–218)

JOURNAL OF RESEARCH of the National Bureau of Standards—A. Physics and Chemistry
Vol. 67A, No. 4, July–August 1963

Photolytic Behavior of Silver Iodide [1]

G. Burley [2]

(February 24, 1963)

Silver iodide exposed to high intensity radiation in the visible light spectrum was found to yield a powder X-ray diffraction pattern showing marked deviations from ideality. It was found possible to correlate these with a decrease in primary extinction, indicating a constant progress from an ideal to a mosaic type crystallinity. Large single crystals showed pronounced asterism in transmission Laue photographs under similar experimental conditions. Small amounts of colloidal silver were detected. A mechanism for this process in silver iodide is proposed, in general agreement with the theory of the photographic process. The primary difference from the other silver halides appears to be a considerably slower rate, permitting the observation of a two step process in detail.

1. Introduction

No detailed investigation of the mechanism of the changes induced in silver iodide by exposure to light in the visible region appears to have been made previously. In the course of this work, the photolytic behavior of silver iodide has been found to differ considerably from that of the other silver halides. In general, polycrystalline specimens of both silver chloride and silver bromide darken rapidly under these conditions, due to the formation of free silver. Powder X-ray diffraction patterns clearly show a decrease of the pattern for the halide, accompanied by a corresponding increase of that for silver, with increasing length of exposure to a constant intensity light source. The behavior of silver iodide under similar conditions and an analysis of the results obtained constitute the results reported in this paper.

2. Experimental Procedure

Single crystals of silver iodide were exposed to the light of an arc lamp for 1 week. Initially transparent, they slowly became opaque. Microscopic examination showed that the initially smooth surfaces gradually roughened and resembled a polycrystalline aggregate. This alteration gradually progressed into the interior of the crystals. Certain sensitizers and halogen acceptors, such as sulfur dioxide and *n*-butyl alcohol, were found to accelerate this process.

Because the action of light on silver iodide appeared to be primarily a surface phenomenon most subsequent work was done with powder specimens.

The powder was packed into a rectangular cavity and the surface smoothed. The mount was placed in a closed container and irradiated with a bar filament microscope lamp through a 5 mil polyester sheet. An atmosphere of *n*-butyl alcohol was maintained at its vapor pressure. This was chosen because it accelerated the reaction only to such an extent as not to hide its essential details. The sample was irradiated for a fixed length of time and an X-ray diffractometer pattern obtained immediately. An angular range sufficient to cover the first nine lines of the diffraction pattern for the hexagonal phase was traversed each time. For the copper X-radiation used this included the range from 20 to 50° in 2θ, where θ is the Bragg angle. A scanning rate of 0.5° per minute of the angle 2θ was used for maximum resolution. Approximately monochromatic radiation was obtained by use of a nickel foil filter. Cumulative exposure times to light of 200 hr were reached in this manner.

In a related experiment a large hexagonal single crystal, of approximately 5 mm diam and 1 mm thickness, prepared by slow evaporation of a 50 percent aqueous solution of hydriodic acid saturated with silver iodide, was exposed to light in the same manner. Laue transmission X-ray diffraction diagrams were taken at timed intervals. Molybdenum X-radiation was used to minimize absorption effects.

3. Results

The powder X-ray diffraction patterns for silver iodide showed large changes in the intensities of certain lines, related to the length of exposure to light. The relative intensities of certain lines as a function of cumulative exposure time are shown in figure 1. The most striking feature of this graph is the fact that there was a rapid and immediate increase for the (100), (101), (102), and (103) reflections, while other reflection intensities remained constant. After a period of time, varying with the light intensity and spectral characteristics of the source, these reflections reached a plateau. After this induction period the (002) reflection intensity then began to increase while the others leveled off. There was no decrease in intensity for any reflection.

[1] This research was supported by the National Science Foundation under Grant No. 19648.

[2] This work constituted a portion of a thesis submitted by the author to Georgetown University, Washington, D.C., in partial fulfillment of the requirements for the Ph. D. degree (1962).

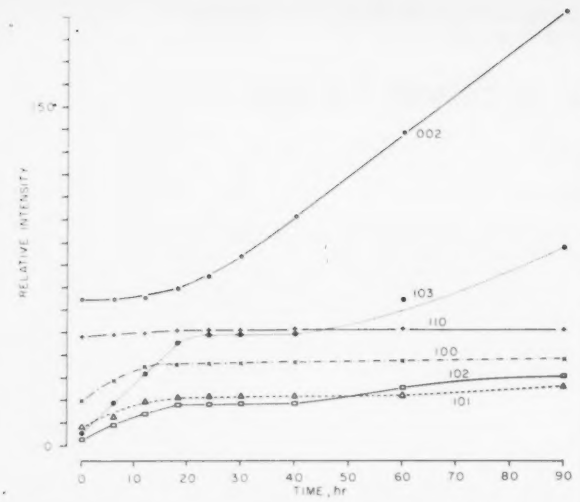

FIGURE 1. *Relative intensities of several low angle powder X-ray diffraction lines for silver iodide, as a function of irradiation time by light in the visible region* (CuKα *radiation*).

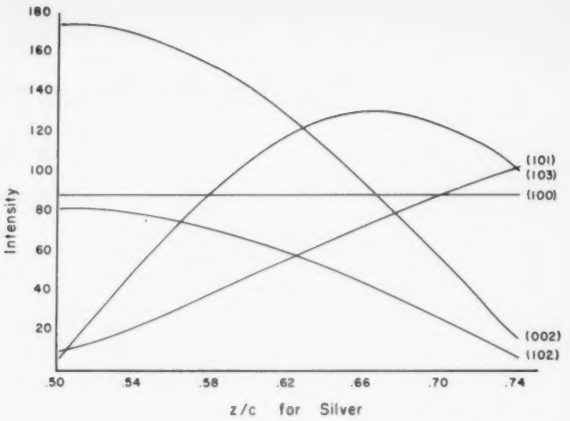

FIGURE 2. *Calculated intensities for several reflections of hexagonal silver iodide, as a function of the variable z/c positional parameter for the silver atom.*

Secondly, the number and angular positions of the X-ray powder diffraction lines were found to remain essentially invariant during the entire procedure. No systematic shift was detectable.

Thirdly, the powder diffraction patterns of light-irradiated silver iodide were re-examined for the presence of metallic silver. The (110) reflection of silver has the largest intensity and appears at a 2θ angle of 38.11°. On the diffraction patterns of silver iodide samples irradiated for 50 hr a very small and broad peak was located at this position. The peak increased slightly in height with successive exposures to light. This clearly established the presence of finely divided silver in amounts large enough to be detected by the X-ray method after exposure times longer than 50 hr.

4. Intensity Changes

The problems to be solved included finding an explanation for the anomalous intensity changes observed and correlating this with the theory of the photographic process.

The effect of varying the positional parameters of the atoms on the magnitude of the intensities was investigated first. Silver iodide can exist in both a cubic zincblende and a hexagonal wurtzite form at room temperature. No distortion of the structure for the cubic zincblende-type phase is possible without destroying the symmetry. In the hexagonal wurtzite-type structure the x and y parameters of both atoms are fixed and only the z parameters can vary. In addition, the origin may be chosen arbitrarily and can be placed at the iodine position for convenience. The only variable possible for an atomic shift is then the z parameter of the silver atom. The variation of the amplitude of the structure factors for the observed diffraction lines was calculated over a fairly large range of values for the silver z parameter. The result is shown in graphical form in figure 2. It is obvious that no atomic shift is possible which will increase all intensities simultaneously.

Another possibility which had to be considered was the existence of stacking faults. This refers to random deviations of layers from the required progression for either the hexagonal or face-centered cubic lattice which are ABAB . . . and ABCABC . . . , respectively. Deviations may be introduced by either growth or deformation faulting.

The experimental details for this behavior have been reported in the closely analogous case of cobalt metal [1].[3] The general theory for mistakes in layer structures was published at the same time by Wilson [2, 3]. The diffraction pattern for a layer type structure with stacking faults has sharp diffraction lines when $(h-k)/3$ has integer values (where h and k are Miller indices); in all other cases the lines are broadened. This behavior was not observed for silver iodide.

The lines with integer values of $(h-k)/3$, indexed in the hexagonal system, are, however, the only ones which occur also for the zincblende-type cubic polymorph. These were the only diffraction lines whose intensity did not change during the initial phase of the illumination. The implications of this behavior will be considered later.

An explanation in terms of a defect structure appears equally unlikely since the line widths and incoherent background scattering did not change markedly. Annealing of a defect structure does increase the peak heights of the diffraction diagram, but the area under the peak profiles remains constant.

[3] Figures in brackets indicate the literature references at the end of this paper.

Since the line width variations observed in this experiment were within the experimental error, none of the peak height changes can be attributed to this cause.

Radical intensity differences for lines in an X-ray powder diffraction diagram may also be due to preferred orientation of the crystallites. For layer structure especially one, or several, sets of planes may have more than a proportional share of these crystallites in reflecting position. In this case certain diffraction peaks, originating from sets of planes having a larger than statistical number in reflecting position are enhanced, and the intensity from most other sets of planes is decreased. This was not observed for silver iodide.

A closely related effect concerns a change of relative intensities caused by crystal growth or aggregation on a submicroscopic scale in certain preferred directions. Since two distinct stages in the change were observed, during each of which certain diffraction lines increased in height while none diminished it seems unreasonable to suppose that under these circumstances a change in preferred orientation or crystal habit occurred.

The only major remaining cause for large intensity changes was the possibility of extinction in the initial samples. This refers to the attenuation of the diffracted beam by regions of perfection within the crystallite. Since there appeared to be a surface fragmentation of the larger single crystals by light it was easy to extend this idea to the small crystallites in the powder. This fragmentation could be expected to reduce the coherently scattering block size and consequently to decrease the extinction. The details of this mechanism will be discussed in the following section.

A generally used method of reducing the perfection of a crystal depends on the use of thermal shock to introduce mosaic-type disorder. The powder sample of silver iodide was immersed in liquid nitrogen repeatedly and X-ray diffraction patterns were obtained. The intensities of the diffraction lines changed in proportionately the same amounts to the first plateau stage as for the samples irradiated by light, as shown in figure 3. This constituted another indication that the observed intensity changes were due to a decrease in extinction and led to the more detailed study described below.

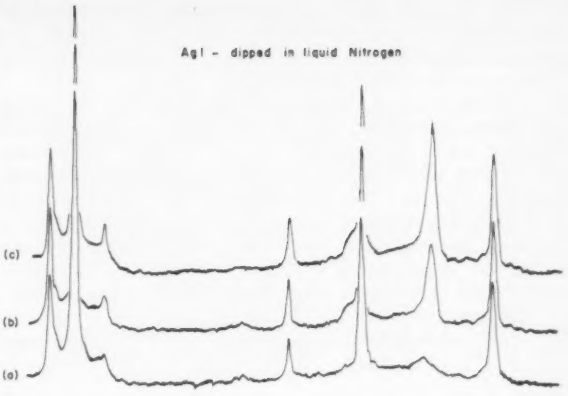

FIGURE 3. *Powder X-ray diffraction profiles for silver iodide.*
(a) Initial.
(b) 3 min immersion in liquid nitrogen.
(c) 10 min immersion in liquid nitrogen.

5. Extinction

Darwin [4] in 1922 derived an approximation by which allowance can be made for the primary extinction in reflections from crystals whose units are larger than ideally mosaic. The ratio of the diffracted intensity with extinction to that without extinction is given by

$$\frac{I_{ext}}{I_0}=\frac{\tanh\,(sq)}{sq}$$
$$=1-\left\{\frac{4k}{3}\quad {}^{2}\left(\frac{e^2}{mc^2}\right)^2 pF^2t_0^2/\gamma_0\gamma_r\right\}$$

where

s = number of reflecting planes in perfect sequence,
q = amplitude reflected from a single plane of atoms,
N = Avogadro's number,
d = interplanar spacing,

$\frac{e^2}{mc^2}$ = classical radius of electron = 2.818×10^{-13} cm,

p = polarization factor,
F = structure factor,
t_0 = thickness penetrated,
γ_0, γ_r = direction cosines with the normal to the plate for the incident and diffracted rays.

The factor $4k/3$ has an approximate numerical value of 1/2. The term enclosed by the braces is the extinction coefficient and will hereafter be designated ϵ. This expression is essentially wavelength independent for any one reflection. Darwin based his original expression on the assumptions of a plate of infinite lateral extent with the reflecting planes parallel to the surface.

Neither of Darwin's assumptions actually holds for a polycrystalline sample. For this the scattering regions are of approximately equal dimensions and the planes are at arbitrary angles to the surface.

In 1951 Ekstein derived an independent extinction formula on the basis of small spherical perfect crystallites [5]. It was originally derived for neutron diffraction and involves peak rather than integrated intensities. For electromagnetic radiation it has the form

$$\frac{I_{ext}}{I_0}=1-\left\{\frac{7}{16}\left(\frac{e^2}{mc^2}\right)^2 N^2F^2D^2\lambda^2\right\}.$$

This formula has a second order wave length dependence as shown here. Thus it should be possible experimentally to confirm the applicability of one or the other formula.

Since at least a substantial part of the observed intensity anomaly for unirradiated silver iodide powder could be ascribed to the primary extinction effect, the wavelength dependence could be investigated. For this purpose manganese filtered iron, nickel filtered copper, and zirconium filtered molybdenum X-radiations were used in three separate series of experiments. The wavelengths of these are 1.9360 A, 1.5405 A, and 0.7093 A, respectively.

The results obtained for the (100), (101), (102), and (103) reflections are shown in table 1. The peak

TABLE 1. *Observed values of extinction coefficient for silver iodide*

hkl	λ	I_{final}	I_{init}	I_i/I_f	p	I_i/pI_f	ϵ
100	Mo	56	35	0.62	0.99	0.62	0.38
	Cu	72	40	.56	.93	.60	.40
	Fe	87	46	.54	.88	.61	.39
101	Mo	41	11	.27	.97	.28	.72
	Cu	48	12	.25	.90	.28	.72
	Fe	68	16	.23	.86	.28	.72
102	Mo	36	6	.17	.96	.18	.82
	Cu	42	6	.14	.85	.17	.83
	Fe	61	8	.13	.77	.17	.83
103	Mo	120	12	.10	.94	.11	.89
	Cu	108	10	.09	.76	.12	.88
	Fe	150	12	.08	.67	.12	.88

intensities were used here. Because of the uniformity of the line width this is directly proportional to the integrated area under each curve. A polarization correction, designated as p, was applied. I_{init} represents the intensity with an extinction effect and I_{final} the intensity without this effect; the ratio of I_{init}/pI_{final} remains approximately constant for all three wavelengths used. Thus the experimental data indicate approximately a zero order wavelength dependence, in agreement with the Darwin formula.

Most of the crystallites grow in the form of either plates or truncated hexagonal pyramids. The dominant face is thus the basal plane. The reference vector for the direction cosines was taken as the normal to this plane. Using the Darwin formula the relative extinction coefficients were calculated for the $\{10l\}$ reflections for each of the three wave lengths used. Values for the structure factor, F, were obtained from single crystal precession photographs. The results are shown in table 2. Since only relative values of the F^2 terms were used, these were not directly comparable to the observed values. In the absence of any other criteria the (103) reflection was used as a comparison standard in each case. The significance of the agreement is thus primarily in the value of ϵ obtained for the other reflections. The agreement between the observed and calculated values is quite good and can be taken as final confirmation that the initial increases in intensity are due to a decrease in primary extinction.

TABLE 2. *Calculated values of extinction coefficients for silver iodide*

λ	*hkl*	θ	F^2_{rel}	$d^3\times10^{16}$	$A/\gamma_0\gamma_r$	ϵ_{rel}
Fe	100	14.07	21	15.86	1.26	0.36
	101	16.00	38	12.33	1.80	.73
	102	20.76	35	7.46	3.70	.83
	103	27.18	100	4.49	2.30	.89
Cu	100	11.15	21	15.86	1.04	.35
	101	12.67	38	12.33	1.50	.70
	102	16.38	35	7.46	3.13	.82
	103	21.32	100	4.49	2.00	.89
Mo	100	5.11	21	15.86	1.00	.39
	101	5.80	38	12.33	1.31	.73
	102	7.46	35	7.46	2.63	.81
	103	9.63	100	4.49	1.65	.88

Using the Darwin formula for the extinction correction, an approximate value of D, the extent of the originally coherent scattering blocks has been calculated. For the silver iodide samples this was in the vicinity of 10^{-5} cm. This is larger than for most crystals by about a factor of ten. It can be compared to an estimated average penetration of about 2×10^{-5} by X-rays into the powder slab, calculated from the published linear absorption coefficients for the silver and iodine atoms. Silver iodide thus presents a very unusual case, where linear absorption limits the penetration to the order of the perfect region.

The major deviation from the extinction behavior is shown by those reflections which can be indexed on the basis of both the hexagonal wurtzite-type and the face-centered cubic zincblende-type structures. For hexagonal indexing these are the (002) and (110) reflections. Neither of these two reflections changes appreciably during the early stages of this process indicating that the coherence of blocks contributing to these remains unchanged. Both structures consist of expanded close-packed layers of iodine atoms, with silver atoms between them. Only the stacking sequence of the layers differs for these two structures. Thus changes in the stacking sequence or displacement of silver atoms to interstitial sites would leave the intensity from these reflections invariant, although the interplanar spacing might not remain constant.

The second stage, indicated by an increase in the intensity of the (002) reflection, did not begin until the initial stage was substantially completed. No marked change was observed for the (110) reflection, probably because extinction effects are limited to reflections with large intensity and low Bragg angles.

The explanation for this behavior on the basis of the powder diffraction data was difficult. For this reason the effect of irradiation by light on large single crystals was further investigated. Laue photographs of a silver iodide crystal showed unambiguously that the second anomalous intensity change was due to fragmentation. This work will be described in the following section.

6. Single Crystal Laue Photographs

Since the conclusions reached from the extinction theory were largely inferential, an effort was made

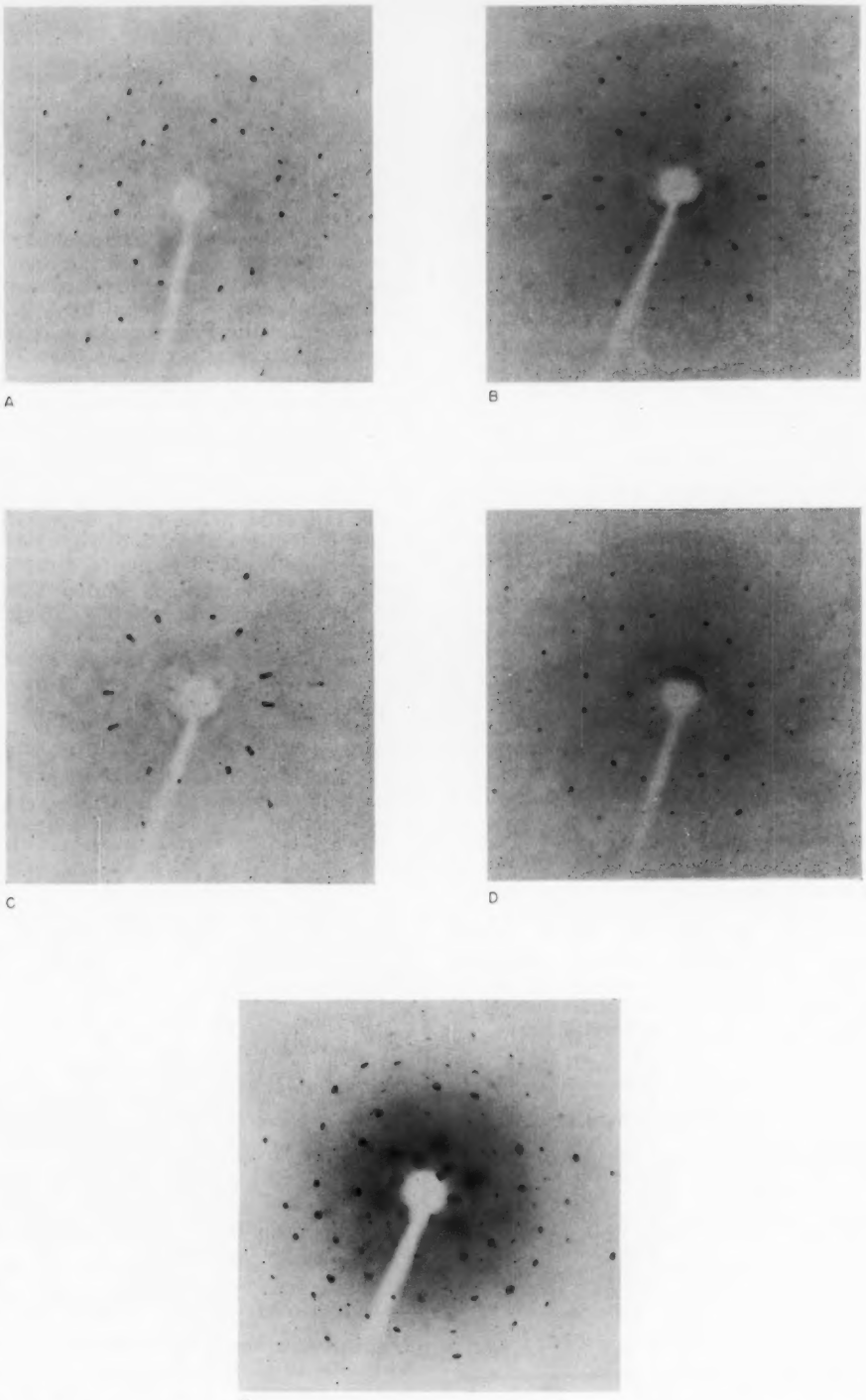

FIGURE 4. *Transmission Laue X-ray diffraction patterns for a thin, single crystal of hexagonal silver iodide after various exposure times to light in the visible region.*

(a) Initial (0) hr.
(b) 20 hr.
(c) 30 hr.
(d) 70 hr.
(e) 100 hr.
The scale is reduced 2:1.

to obtain further evidence by other techniques. Transmission Laue X-ray diffraction photographs were obtained from a large single crystal after varying cumulative periods of exposure to the microscope lamp. The various stages of the observed changes in the single crystal patterns are shown in figure 4a–e. These were recorded at cumulative exposure times to light of 0, 20, 30, 70, and 100 hr, respectively.

The first picture of this series shows the pattern obtained before any irradiation with light. The diffraction maxima are irregular. This is characteristic of the type pattern obtained from a single perfect crystal. The next two pictures were made after 20 and 30 hr exposure time, respectively. These show a pronounced asterism, or radial streaking of diffraction spots, increasing with time. This can be readily explained only on the basis of a variability in the c/a axial ratio, such as would be expected to occur in internally strained crystals [6], or by a one-dimensional distortion of the lattice.

The next picture was made after a 70 hr exposure. The radial asterism has completely disappeared at this point and the diffraction spots are all approximately circular. This type of pattern is characteristic of an ideally mosaic crystal. The last picture shows the pattern after a 100 hr cumulative exposure time. This shows an elongation of the spots in a tangential direction, as well as a number of weak spots not previously observed. This is indicative of a fragmentation of the crystal into small crystallites, but with approximate retention of spatial orientation. As a limit, the tangential elongation into a complete circle would be obtained for a collection of crystallites with random orientation.

The c/a ratio for the ideal wurtzite lattice is 1.633. The (121) Laue reflection was indexed and the spread of c/a ratios calculated. The details are given in figure 5. The maximum c/a ratio was 1.69 and the minimum was 1.59 just before an ideally mosaic crystal formed. This is almost certainly associated with the progressive decrease in the size of the coherently scattering blocks that occurred during the first stage of the change in the powder patterns.

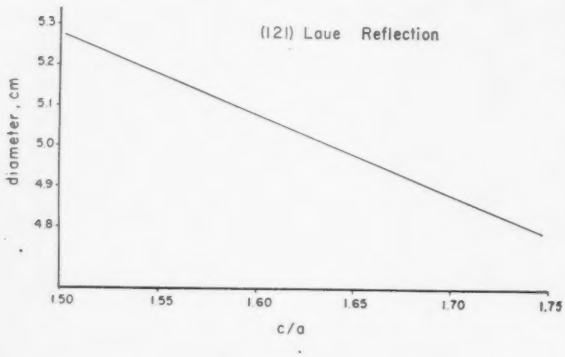

FIGURE 5. *Calculated c/a axial ratios for the (121) Laue reflection as a function of the measured diameter.*

7. Radiation Damage

The introduction of increased disorder in the structure by light is to some extent comparable to the general field of radiation damage. In the latter case very energetic particles or radiation give rise to localized defects. The atoms are displaced by collision, with a certain amount of the energy of the impinging particle transferred to an atom in the crystal. This can lead to secondary displacement of adjacent atoms. In general, fast neutrons are required to effect atomic displacements. Considerably more energy is required for this than is necessary to cause the migration of a silver atom to an interstitial site in silver iodide.

Two samples of silver iodide powder were exposed separately to different high energy radiation in order to determine the effect on the lattice. One was given a total dose of 1 roentgen by 250 kv X-rays, and the other 10 roentgens by Co^{60} γ-radiation. In neither case was there any change in the powder X-ray diffration pattern. This indicates that silver iodide is either not subject to visible damage by considerable doses of radiation from sources of this kind, or that the effect is random to such an extent that it does not appreciably affect the coherent scattering.

Even after extended periods of exposure to X-rays in the 50 kv range no visible darkening was observed. A preliminary quench in liquid nitrogen to reduce the perfection of the crystallites and subsequent exposure to X-rays of the same type produced slight darkening after times of less than 4 hr. This suggests that the silver iodide lattice is sensitized to ionizing radiation by the introduction of some disorder.

8. Mechanism

A qualitative explanation can now be given for the observed behavior of silver iodide in terms of the theory of the photographic latent image.

The latent image is believed to consist of submicroscopic specks of silver in some of the grains. Experimentally, it has been determined that the development of the latent image always begins at grain boundaries, slip planes, or impurity centers [7]. The introduction of strain into the lattice produces many more nucleation centers than exist in the equilibrium structure.

The first satisfactory theory of the latent image was proposed by Gurney and Mott in 1938 [8]. There is evidence that the primary absorption in the AgX crystal occurs as

$$X^- + h\nu \rightarrow X^0 + e^-.$$

Light absorption in the ultraviolet region is required to excite an electron from an X^- ion in an ordinary lattice position. The absorption at longer wavelengths is probably due to X^- ions at dislocations or other disturbed positions in the structure.

Since AgI is a semiconductor the quantum mechanical concepts of the band theory can be used. The

electron is raised from a valence to a conduction band where it can move freely. Hence the AgI becomes photoconducting. The mobile electron moves through the crystal until it becomes trapped by a pre-existing silver nucleus or in a low-lying level of a sensitizer. Thus a center of negative charge is produced, attracting Ag^+ atoms which can move through the crystal via interstitial positions. When a Ag^+ ion reaches the negative center it is neutralized

$$Ag^+ + e^- \rightarrow Ag^0.$$

The silver nucleus is thus enlarged and continues to grow by the same mechanism.

The neutral X atom eventually reaches the surface by a process of electron transfer

$$X^- + X^0 \rightarrow X^0 + X^-.$$

The X atom is a center of missing negative charge and is called a positive hole. The theory required that these positive holes not recombine with the electrons.

In 1953 Hedges and Mitchell modified this theory slightly on the basis of extensive experiments [9]. They proposed that the function of the sensitizer is to trap positive holes, preventing their recombination with electrons. The electrons would then be trapped at crystal imperfections, and the silver particles grow there to form the latent image.

Silver iodide undergoes a photolytic reaction similar to the other silver halides, but at a considerably slower rate. This is in agreement with some very recent work by James and Vanselow [10, 11] on the kinetics of the development of silver iodide emulsions. Neutral silver atoms are formed by combination of electrons and silver ions. The rate of diffusion of these silver ions through the lattice is relatively much more rapid than that of iodine atoms. The migration path is by way of interstitial positions. The change in size and bonding of the silver atoms is sufficient to lead to a lattice distortion. The neutral silver atoms tend to move toward existing defect sites. There they may be effectively trapped and immobilized. The existence of aggregates of these silver atoms at grain boundaries has been shown by Mitchell [12–14] for silver chloride. A similar movement of silver atoms in the silver iodide structure is very probable. The high mobility of the silver with respect to the iodine atoms in silver iodide is well substantiated. The collection of a number of the silver atoms at one dislocation site may be sufficient to cause local plastic deformation. A large number of these small lattice misorientations would be sufficient to explain all the reported observations.

The elastic deformation limits of an ideal crystal are generally exceeded when the lattice change is greater than about 5 percent. At this point the small number of misoriented blocks can exert a strain sufficient to fragment the crystal into an essentially ideal mosaic structure. This stage is represented by the first plateau stage of the X-ray powder diffraction patterns.

Further exposure to light continues the process of misorientation of adjacent blocks due to the strains produced by further silver precipitation. This can continue until a collection of crystallites with substantial orientation differences is formed. The layer type structure appears to be generally preserved at this stage, leading to an enhancement of those reflections for which $h-k=3N$. Simultaneously, there may occur an annealing of growth faults in the face-centered cubic lattice. The total effect is to maintain the remaining reflections essentially constant while the (002) and (103) reflections increase in intensity. This stage is represented by the latter portion of the powder diffraction pattern and the final Laue photograph.

The observed behavior of silver iodide thus appears to be analogous to that of the other silver halides insofar as the photolytic mechanism is concerned. The fundamental difference lies in the rate at which the reactions occur. The considerably slower rate for silver iodide has permitted a more detailed mechanism to be observed for this compound which is in good agreement with the previously proposed theories of the photographic process.

9. References

[1] O. S. Edwards and H. Lipson, Proc. Roy. Soc. London **A180,** 268 (1942).
[2] A. J. C. Wilson, Proc. Roy. Soc. London **A180,** 277 (1942).
[3] A. J. C. Wilson, X-Ray Optics, Methuen & Co., Ltd., London (1949).
[4] C. G. Darwin, Phil. Mag. **43,** 800 (1922).
[5] H. Ekstein, Phys. Rev. **83,** 721 (1951).
[6] C. S. Barrett, Structure of Metals, McGraw-Hill Book Co., Inc., New York (1943).
[7] H. G. van Bueren, Imperfections in Crystals, North Holland Publishing Co., Amsterdam (1960).
[8] R. W. Gurney and N. F. Mott, Proc. Roy. Soc. London **A164,** 151 (1938).
[9] J. M. Hedges and J. W. Mitchell, Phil. Mag. [7] **44,** 357 (1953).
[10] T. H. James and W. Vanselow, Phot. Sci. Eng. **5,** 21 (1961).
[11] T. H. James, W. Vanselow, and R. F. Quirk, Phot. Sci. Eng. **5,** 216 (1961).
[12] T. Evans and J. W. Mitchell, Defects in Crystalline Solids, Physical Society, London (1955).
[13] T. Evans, J. M. Hodges, and J. W. Mitchell, J. Phot. Sci. **3,** 73 (1955).
[14] D. A. Jones and J. W. Mitchell, Phil. Mag. [8] **2,** 1047 (1957).

(Paper 67A4–219)

JOURNAL OF RESEARCH of the National Bureau of Standards—A. Physics and Chemistry
Vol. 67A, No. 4, July–August 1963

Correlation of Muscovite Sheet Mica on the Basis of Color, Apparent Optic Angle, and Absorption Spectrum*

Stanley Ruthberg, Mary W. Barnes,[1] and Ralph H. Noyce[2]

(April 6, 1963)

A detailed experimental study of color, apparent optic angle, and absorption spectrum (0.3 to 16μ of λ) indicates that there are basic chemical and structural differences in muscovite micas. Color identification is based upon spectrophotometer measurements. A method for quantitative evaluation of absorption band activity is defined so that single and multiple band intensities within the spectrum of an individual specimen and within spectra of different specimens can be compared. Three basic spectral types exist for the 0.3 to 1μ λ region which are comprised of various weak lines and absorption regions lying along the base of a deep absorption edge near 0.32μ. Of the three spectral types, one is associated with ruby micas, while the other two are associated with dark green and light green micas. The activities of numerous lines and bands are reported. It is shown that apparent optic axial angle is related to the position of the deep band edge except for a certain class of ruby specimens which show anomalous values. A definitive characterization of muscovite sheet is formulated in terms of the absorption coefficients at 0.44, 0.49, and 0.58μ. Direct associations are shown between certain lines in the visible λ range and certain bands in the near infrared, while the activities of a number of bands in the middle infrared are correlated to color.

1. Introduction

Muscovite mica, a complex crystalline mineral, is readily cleaved into thin elastic laminae which have excellent mechanical and electrical insulating properties. It occurs with large variations in physical appearance. Considerable effort has been expended to determine the range in values of its physical properties and to seek correlations between properties, particularly for those of technical significance to those properties by which the material is classified. At present, classification is by origin and color. The mineral, which occurs throughout the world, varies in color from green to pink. Further selection is based upon such properties as clarity, hardness, ease of splitting, and structural perfection [1, 2, 11].[3] Numerous studies on dielectric constant and power factor [3–11], d-c resistivity [12, 13], electric strength [14, 15], gas evolution [16], thermal conductivity [17], thermal expansion [18], magnetic susceptibility [19, 20], and hardness [21], in addition to many others of chemical, mineralogical [22, 25] and infrared nature [27, 34–39] have failed to reveal any real correlation, and the material is still selected for technical use by arbitrary and empirical procedures which have incomplete or even doubtful quantitative significance.

A basic difficulty is that analytical chemical procedures have not been sensitive enough to differentiate muscovite sheet mica or provide a simple means of correlation with other properties, particularly in view of the complex of minor constituents which appear as isomorphous replacements in the mica structure. The position of a replacement cation in the mica structure is determined more by its size than its valence, although the valence state determines charge balance and hence relative abundance in the layers [25]. Normally, in addition to the major cationic components of K^{+}, Al^{+3}, and Si^{+4}, a number of cations such as Na^{+}, Ca^{+2}, Fe^{+2}, Fe^{+3}, Mg^{+2}, Ti^{+4}, Mn^{+2}, Mn^{+3}, Li^{+}, Cr^{+3}, and V^{+3} occur in the same specimen. Total accuracy of component analysis is of the order of 0.1 percent, while the small amounts of material in isomorphous substitution can be in large relative error. Because of these errors and because calculation to unit formula requires a number of assumptions about the structure, analysis of this material is a special problem [23, 25]. Furthermore, calculation fails if an extraneous mineral is present in unknown proportions, defects are not considered, and the valence states of some cations are not always readily obtained; yet, the distinction of even exceptional specimens such as the rose micas depends upon subtle ratio and valency of small amounts of cations in isomorphous substitution [24]. Although success has been obtained in the classification and correlation of the many different dioctahedral potassium micas as based upon the tetrahedral-octahedral charge relationship [25], muscovite in this scheme is given as an end member of the trisilicic series where hardly any difference is indicated between pink muscovite and muscovite. Yet, the whole group of muscovites in this very narrow band of the trisilicic-tetrasilicic series must be differentiated.

The problem of characterization of muscovite sheet is thus subtle, and the required sensitivity for any differentiation must be found outside presently available chemical and structural analytical techniques. A study was therefore made of certain physical properties chosen because they might be indicative of chemical composition and structure and measurable with sufficient accuracy to allow

*Partially supported by Air Force Cambridge Research Center, ARDC and Defense Materials Service, General Services Administration, U.S. Government.
[1] Now at the Pennsylvania State University, State College, Pa.
[2] Now at Airtronics, Inc., Washington, D.C.
[3] Figures in brackets indicate the literature references at the end of this paper.

quantitative differentiation. Moreover, the properties and procedures chosen permitted inspection of a large number of specimens. Careful interpretations of these properties within groups of muscovite mica may eventually help in understanding the crystal-chemical layer structure. More immediately they may correlate with technologically useful properties.

This paper, then, is not concerned with direct chemical methods but presents a detailed experimental study of the several selected properties. These are (1) color, (2) apparent optic axial angle, and (3) absorption spectrum from the near ultraviolet (300 mμ) to the middle infrared (16μ).

Although color is a major property by which muscovite sheet is sorted, it remains one of the least understood [11, 22, 24]. It should certainly be indicative of compositional variation. One study was made of the role of iron, titanium, and magnesium in the color of biotites [26], but no similar study of the muscovite group is known.

Winchell and Winchell [22] indicate that the apparent optic angle may be dependent upon the cations substituted into the charge layers, but values are available for only a few muscovites, phengites, and some mixings of these types. Little else is known.

Finally, it is reasonable for the absorption spectrum to be sensitive to electronic and molecular differences. Stubican and Roy [27] showed variation of infrared bands with gross isomorphous substitution, such as the change of muscovite to phengite, primarily for wavelengths longer than the first Si–O bands at 9 to 10μ. But, almost no spectral information is available from the near ultraviolet to the near infrared, nor has the large effort in the middle infrared been oriented toward characterization of natural mica sheet.

With the establishment of quantitative procedures and correlation of the properties studied, it is shown that muscovite sheet micas can be systematically differentiated in a manner related to morphological (crystal-chemical layer structure) differences. For example, the infused pink tinge that characterizes the ruby color class of muscovite is related to measurable anomalies, whereas, the other color varieties are fairly consistent within this descriptive behavioral scheme.

2. Specimens

Muscovite mica is normally distinguished by color, primarily as ruby (pinkish buff to cinnamon drab) or nonruby (brown to green), and by origin. Muscovite mica sheet is further classified visually according to an ASTM code which employs eleven categories, labeled V–1 to V–11, of decreasing quality as based upon clarity, uniformity of color, structural perfection, and hardness [28]. Whereas classification under this system is subjective, expert inspectors obtain reasonably consistent and mutually agreeable results by constant intercomparison of samples and by the selection of suitable standard samples. Grading is also based upon the size of the usable area of the given quality. Specimens become rarer as quality and size of usable area increase.

The materials used in this study are described in table 1 according to color, origin, quality, grade, and amount obtained. Six representative origins are included. The items listed represent the colors of commercial sheet muscovite. Dimensions are shown in table 2. These had been classified by expert inspectors before being received by us from Defense Materials Service of the General Services Administration and from Committee F–1 of ASTM. Specimens were cleavage plates ranging in thickness from 0.15 mm to 0.5 mm.

TABLE 1. *Description of muscovite mica used for the study*

Color	Origin	Quality	Grade	Amount
1. Ruby	India	V–1	5	12 pc.
2. Ruby	India	V–2	6	[a] 5 lb.
3. Ruby	India	V–4	6	5 lb.
4. Ruby	India	V–7	6	5 lb.
5. Ruby	United States	V–4	6	5 lb.
6. Ruby	Brazil	V–4	6	5 lb.
7. Ruby, normal good colored.	Brazil	V–1	5	11 pc.
8. Ruby, slightly dark	Brazil	V–1	4 & 5	4 pc.
9. Ruby, medium dark	Brazil	V–1	4 & 5	8 pc.
10. Ruby, very dark (rum ruby).	Brazil	V–1	4,5,5½	4 pc.
11. Ruby [b]	Madras (India)	V–4	6	1 lb.
12. Nonruby	United States	V–4	6	5 lb.
13. Amber, rum bordering on ruby.	Brazil	V–1	5	15 pc.
14. Brown or "dark green"	Tanganyika	V–1	4 & 5	15 pc.
15. Clear Purdy [c]	Canada	V–3	4	1 lb.
16. Light green	Madras	V–1	5 & 5½	20 pc.
17. Dark green	Madras	V–1	5	15 pc.

[a] One pound of No. 6 material (here obtained as cleavage plates of 0.15 to 0.5 mm thickness) yielded 500 or more pieces.
[b] This material was labeled Madras Clear Green but contained many specimens borderline between ruby and nonruby.
[c] Canadian Clear Purdy. This batch appeared borderline between rum and green.

TABLE 2. *Dimensions of grades of mica used in this study*

ASTM size	Area of maximum rectangle	Minimum dimension of one side
Grade	*in.*^{2}	*in.*
4	6 up to 10	1½
5	3 up to 6	1
5½	2¼ up to 3	⅞
6	1 up to 2¼	¾

3. Experimental Methods

3.1 Color

Muscovite micas viewed in transmitted light are well known to range widely in hue and absorbance. Designation is normally in the broad category of ruby or nonruby; however, the title of ruby is more a classification than a description. Pinkish buff to cinnamon drab are generally termed ruby; brown to brownish olive are generally called rum; yellowish olive to green are called green; but as variations in color are continuous none of these designations is

sharply defined, and the classification into ruby and nonruby often depends upon color differences so small as to be scarcely perceptible.

Actually, there are no formally accepted standards for color designation. Instead, an acceptable classification in the mica trade is formulated upon the experience and memory of the inspectors and upon constant intercomparison of representative samples of the color families. To decide color the inspector must take into account the thickness of the specimen, disregard inclusions, cloudy and stained areas, and make comparison to remembered samples.

The only definitive study on the color of mica was that of Judd [29] which established a color standard for ruby mica and was particularly applied to definition of borderline samples between ruby and nonruby. His separation into ruby and nonruby was based upon the lightness index (modified optical absorption coefficient) and hue index and "not on the hue index alone. That is, the grading of mica as ruby or nonruby according to trade practice departs considerably from grading purely on the basis of hue alone, and a specimen of light-colored mica can be considerably greener than a dark borderline specimen and still be graded ruby." He further demonstrated that in spite of the problems encountered, the color designations of the inspectors are "surprisingly reliable and consistent." In fact, the correlation between points on his lightness-hue index plane and the color grading into ruby or nonruby by a mica task committee was "nearly perfect."

A number of factors were involved in the selection of an appropriate procedure for the present color study. One was the desire to consider the whole range of colors exhibited by muscovite sheet. Whereas Judd was particularly successful in the objective sorting of muscovite into ruby or nonruby, his results also showed that even the color category of "ruby" is very complex. A second factor was the consistency of trade-designated color categories. Third, was the fact that absorption spectra would be obtained for a range of wavelengths and would include the visible region, in which the spectrum is itself a measure of color. And lastly, to secure absorption spectra for the myriad of samples necessary to represent all variations in color and origin would have been an overwhelming task.

The procedure used combined the quantitative aspects of the spectrophotometer with a visual sorting operation similar to that outlined by Judd. A familiarity with all the materials of table 1 was first established. These lots were then further sorted into a convenient number of subgroups with visual standards as described below. Representative samples of subgroups were subjected to spectrophotometry. Thus, the quantitative effort was diminished without sacrificing clear-cut correlation of color to spectrum, coordination with trade-designated color descriptions was established, duplication of color measurements was avoided, and large numbers of samples were handled.

The items of table 1 represent the range of colors of commerical sheet muscovite, classified according to trade-accepted standards. Some had been classified as simply ruby or nonruby, each including a range of colors. Others had been further assigned to more definite color, e.g., the various categories of ruby in items 7 to 10, amber, brown, light green, and dark green.

a. Spectrophotometer

A double-beam recording spectrophotometer (Cary, Model 14M) was employed with a lead sulfide detector and a tungsten source. The wavelength scan speed was 2.5 mμ/sec and the chart speed was 2 in./min. The wavelength was not limited to the visible region but ranged from 0.3μ to 1μ. A quantitative measure of color can be derived from the visible region when integrated with the spectral response of the eye. Although the spectrophotometer is far too slow for sample sorting, when used as outlined above it provided excellent quantitative data.

b. Photometer

Often, samples differed in color only because of lightness or shade. Where all samples in a group were of one hue, differing only in lightness, a simple but quantitative photometric (Photovolt Corp., Model 520 M) examination with tungsten source and appropriate narrow band filter was preferred.

c. Visual

The procedure used for color grading was as follows:

1. About 25 specimens were drawn from the item considered. These were spread on a large white matte surface illuminated from above by "cool white" fluorescent lamps and arranged according to the ruby-rum-green color classification, with some departure as noted below. Those closest to the red end of the spectrum were placed at one end of a series, those closest to the green of the spectrum were placed at the other end of the series, and the intermediates were placed between. Account was taken of thickness after observation of the change in color accompanying cleavage of thick specimens into thinner plates.

2. Another batch was drawn from the item, examined in the same manner, and specimens fitted into the series. This was repeated until the series stabilized, i.e., until no further extremes or different colors appeared.

3. Standard samples were generated. A number of specimens were chosen at appropriate intervals along the series. These were cleaved to a thickness of 0.015 to 0.020 in. as measured with a direct-reading micrometer. The trade designated colors included in table 1 served as guideposts or fill-ins for this selection.

4. Rapid sorting then proceeded through the matching of each piece with the closest "standard," compensating for thickness. Thus, subgroups were formed. The sorting continued until about a pound of the item was used. In general, dozens of speci-

mens occupied each subgroup although extreme subgroups often had smaller populations.

Items 7 to 10 of table 1, as trade selected, progressed in color from pinkish buff toward brown. However, as has been noted [29], the color situation of ruby mica is much more complex. In fact the so-called ruby micas can exhibit a progression of colors from nearly colorless through yellowish grey to dark brown and even include specimens of a distinctly green cast. The one distinguishing feature is the inclination to red with increased thickness of sample. The large batch ruby items of table 1, i.e., 2 to 6, did indeed exhibit a wider range of colors than found in items 7 to 10. Some specimens were redder, others greener, and hence the subgroup color categories for ruby micas were chosen to extend beyond those of items 7 to 10. The designations chosen were pink, pink-tan, tan-green, and green, i.e., green cast. Pink and pink-tan overlapped item 7, normal good colored ruby, with pink including specimens more extreme in red. Tan corresponded to item 8, slightly dark. Tan-green overlapped items 9 and 10, while green included those specimens of distinctly green cast.

When the large batch nonruby item, 12, was sorted, a branching in color was observed. This item ranged from olive to green. Color did not simply transform from one to the other but shifted from olive to a distinct dark green on one branch and to a distinct light green on the other, i.e., there were specimens intermediate between olive and dark green and between olive and light green. Nonruby subgroups were chosen as amber, brown, olive, dark green, light green, and lime. The lime was a distinctly different green. An intermediate subgroup on one branch was dark green-olive. On the other branch intermediate subgroups were olive-white-green and white-green, where white-green still retained a smoky appearance as compared to light green.

Finally, one item, 15 (Canadian Clear Purdy), was treated individually. It appeared to be borderline between rum and green. This was distinguished by essentially one hue but variable shade. It was sorted by shade.

3.2. Apparent Optic Angle

Mica is optically biaxial with the negative acute bisectrix nearly normal to the basal cleavage or 001 plane. Thus, cleaved sections give a nearly centered interference figure [30]. The apparent optic angle, that is the emergent optic axial angle as viewed in air, is a property of the crystal sensitively dependent upon the magnitude of the three principal refractive indices and is an easily measured quantity. The equipment used by us is described elsewhere [31]. A precision of better than $\pm 5'$ arc is achieved for good specimens. Waviness of the mica surface, common especially among the lower ASTM groups, however, superimposes an additional uncertainty because of the uncertainty in orientation of the geometric normal to the cleavage plane.

3.3. Absorption Spectra

a. Near UV to Near IR (0.3 to 1μ)

There is little previous information for this part of the spectrum [32, 33]. Absorption spectra were obtained with the Cary 14M double-beam recording spectrophotometer as outlined under color.

b. Near IR to Middle IR (1 to 16μ)

Absorption spectra were obtained with a Beckman IR–4 recording spectrophotometer using standard slit schedule, unpolarized radiation, a NaCl prism, and a wavelength scan speed schedule of 1μ/min except in the 2 to 3.5μ region where the scan speed schedule was reduced to 0.2 or 0.08μ/min. The 1 to 16μ region is separated into two parts by the greatly increased absorption which begins with that of Si—O modes in the 8 to 10μ region and which continues in longer wavelengths. The spectra for wavelengths of 1 to 8μ were obtained with crystal plates of the same order of thickness as for the 0.3 to 1μ region, i.e., approximately 0.2 mm. The longer wavelength region was obtained with laminae of 5 to 12μ thickness. These 5 to 12μ thick laminar specimens were prepared under a low-power microscope with a scapel. With care this can be done after some practice and depends upon the excellent basal cleavage of the material. Such specimens are suitable up to a wavelength of 17μ after which detail is lost through the excessive absorption of more Si—O modes.

A typical spectral trace is shown in figure 1. The presence of most of these bands has been observed before [27, 34–39]. A few have been given definite assignment to O—H, Si—O, and Al—OH vibrations, some have been given a general assignment such as to Si—O—(Al) modes, but most are of unknown origin. Examination of the spectra of numerous representative samples indicated that differences appeared as small changes within multiple band regions such as the 3 to 4μ, and 12 to 15μ wavelength regions of the infrared (see fig. 1) and as the 0.5 to 0.6μ wavelength region of the visible (see fig. 2).

The determination of absorption band intensity is not an established procedure; thus, there is the task of finding a scheme appropriate for the situation. The need is to compare the intensities of the many absorption bands of one individual specimen and to compare the band intensities of one specimen to those of other specimens.

The variation in specimen thickness had to be accounted for. It was convenient to use the absorption coefficient, related to the transmission by Lambert's law that $T=\exp[-\alpha_\lambda t]$. T is the ratio of the transmitted to incident radiant intensities, I/I_0, α_λ the absorption coefficient at a given wavelength, and t the thickness of the specimen. This is for internal absorption. The values obtained with the transmission spectrophotometer must be corrected for surface effects. When a beam passes through an absorbing sheet, it suffers reflections at both surfaces. If the beam is sufficiently attenuated

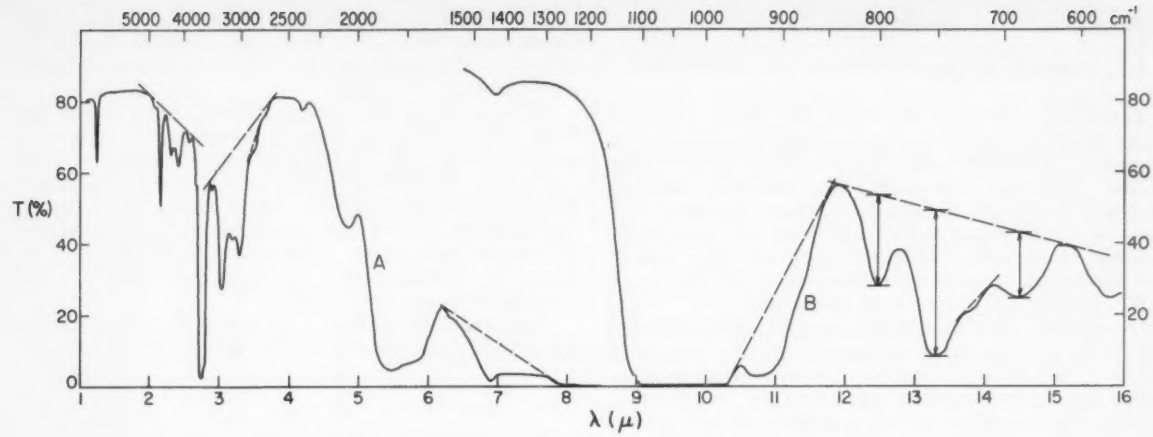

FIGURE 1. *The 1 to 16μ λ absorption spectrum of a ruby muscovite specimen (item 2, table 1).*
A. Thickness of 0.201 mm. B. Thickness of 8μ.

in the crystal plate, multiple internal reflections need not be considered. This is essentially true as long as no interference patterns are observed in the spectrophotometer trace. Then one finds that

$$-\alpha_\lambda t = \ln T' - \ln (1-r)^2$$

where T' is the machine value of the transmission and r is the reflection coefficient. The internal transmission is $T=T'/(1-r)^2$. Evaluation of α_λ and of r may be obtained from two splittings of different thickness from the same specimen, after which the spectral transmissions may be compared for any thicknesses.

When the wavelength corresponds to the peak of an absorption band, the value of α so obtained is the total absorption coefficient at resonance, for it is the sum of the absorptions due to the background and to the resonance condition itself. Thus, it is necessary to separate out the background contribution. This was attempted in these multiple band regions with the aid of base lines placed as indicated by the dashed lines in figure 1. A resonance absorption coefficient (below background), $\alpha_\lambda(R)$, is defined as

$$\alpha_\lambda(R) = -\frac{1}{t} \ln (T_R/T_b)$$

where T_R is the transmission at the resonance band center and T_b is at the hypothetical base line at the same λ (see fig. 1). Note that

$$\frac{T_R}{T_b} = \frac{I_R/I_0}{I/I_0} = \frac{I_R}{I}$$

where I_R is now compared not to the beam intensity before it strikes the crystal but to that which would be transmitted through the crystal if no resonance were present.

The position of the base line for a band had to be established. Whereas, the base line concept has been used before for a well defined, isolated band [27, 40], the present situation is certainly not so simple. To locate the base line, absorption spectra were obtained for samples of different thicknesses cleaved from the same original specimen. Trials of a base line location for a given band were made, and the resonance absorption coefficient was computed from each of the sample spectra. That orientation was chosen which yielded the least spread in the value of the coefficient for the particular band. This was repeated with a number of representative specimens. The base line for a multiple band region was so fixed that the coefficient for each of the included bands was so satisfied. The same procedure was extended to the shorter wavelengths of 0.3 to 1μ. Accuracy was usually obtained to within a few percent.

The α's so calculated are, of course, an approximate measure of absorption band intensity but the interest here is on relative behavior. Additional errors beyond that of the procedure itself, namely those from determination of t and T, can be considerable. Although the t of the thicker plates was determined within 1 percent, the value for the 5–12μ thick specimens could be in error by 20 percent because of variations due to cleavage faults. Values for faint absorption bands can be in error because of small differences between T_R and T_b. The consistency actually obtained can be seen in the data below.

Empirically consistent relationships between some of the intrinsic band intensities, as herein defined, and the color data have been found. It is felt that this correlation of itself justifies the chosen procedure.

685-226—63——3

4. Results

4.1. Absorption Spectra, 0.3 to 1μ, and Color

Absorption spectra obtained by other workers had indicated the 0.3 to 1μ wavelength region to be relatively featureless [32, 33], but closer examination of the range shows it to be populated by a number of weak bands of absorption. These lie along the base of a very deep absorption edge and vary from sample to sample. The activities of these bands are shown to be directly associated with color.

This region is represented in figures 2 and 3 for ruby micas. Representative samples were selected for each of the color subgroups from item 2 of table 1, a V–2 India mica. A representative spectrum for each subgroup is displayed in figure 2 except the tan-green which was omitted for clarity. Spectra for two specimens of pink-tan of different values of apparent optic angle are included.

Several features may be observed in these spectra. First is the wavelength shift with the color subgrouping of the deep band edge near 0.32μ. Popper [32] found this absorption to extend to wavelengths shorter than 0.25μ. Then, there is a characteristic weak spectral structure at 0.472 to 0.6μ which consists of a band at 0.472μ and a broad absorption at 0.51 to 0.6μ. The fine detail of this broad absorption region is better seen in figure 3 for two specimens taken from item 1, a V–1 India mica. Three overlapping bands of absorption are indicated at 0.505, 0.535, and approximately 0.57μ. There are, in addition, two faint bands of absorption at 0.417 and 0.442μ and a broad response between 0.77 and 0.97μ.

In general, the progression along the color series for ruby materials from pink toward green is accompanied, as shown, by an increase in transparency, a shift in the band edge and, particularly, a diminution of the 0.47 to 0.6μ spectral structure.

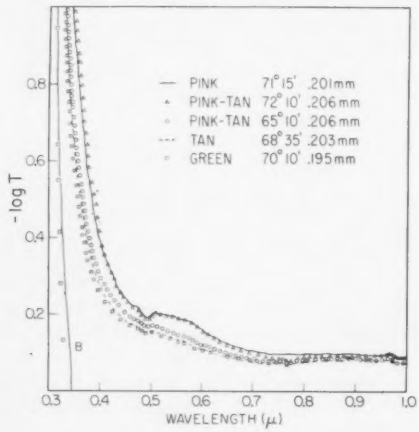

FIGURE 2. *The 0.3 to 1μ λ absorption spectra of specimens representative of the color subgroups of ruby mica.*

Color subgroup, apparent optic axial angle, and thickness are listed for each specimen. Curve B is—log T=1 to 2. Specimens from item 2, table 1 (V–2 ruby India).

The break in magnitude of the 0.47 to 0.6μ absorption between the two pink-tans of figure 2, otherwise distinguished by value of apparent optic angle, should be noted.

The 0.3 to 1μ wavelength absorption spectra for rum and green micas are summarized in figures 4 and 5 with spectra for representative specimens from a number of color subgroups. Colors included are amber, olive, dark green, white-green, light green, and lime in figure 4 along with several shades of the borderline rum-green (Canadian Clear Purdy) in figure 5. The spectrum of a pink ruby was inserted into figure 4 for comparison.

The spectral details characteristic of nonruby micas are the relatively sharp and "strong" absorp-

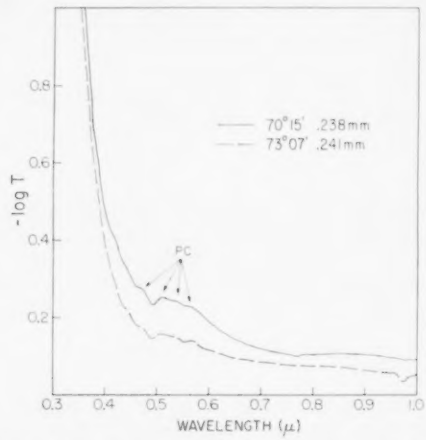

FIGURE 3. *Internal detail of the 0.47 to 0.6μ spectral structure for two representative ruby specimens.*

Maxima are indicated at 0.4725, 0.505, 0.535, and ~0.57μ. These are labeled as PC for pink correlation. Material—item 1, table 1(V–1 ruby India).

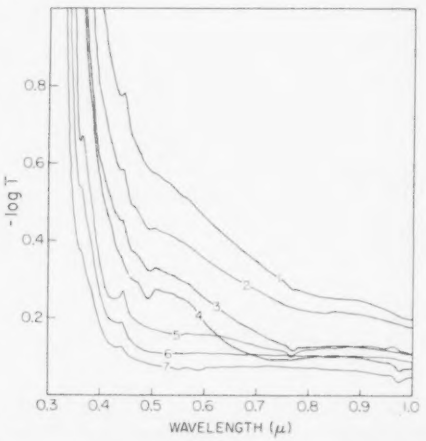

FIGURE 4. *The 0.3 to 1μ λ absorption spectra for specimens representative of the color subgroups of rum and green micas with a pink ruby spectrum included for comparison.*

Color subgroup, origin, quality, and specimen thickness corresponding to the numbered spectra are: (1)—*dark green*, Tanganyika, V–1, 0.262 mm, (2)—*olive*, U.S., V–4, 0.210 mm, (3)—*amber*, Brazil, V–1, 0.226 mm, (4)—*pink ruby*, Brazil, V–1, 0.325 mm, (5)—*green-white*, U.S., V–4, 0.315 mm, (6)—*lime*, India, V–1, 0.248 mm, (7)—*light green*, India, V–1, 0.246 mm.

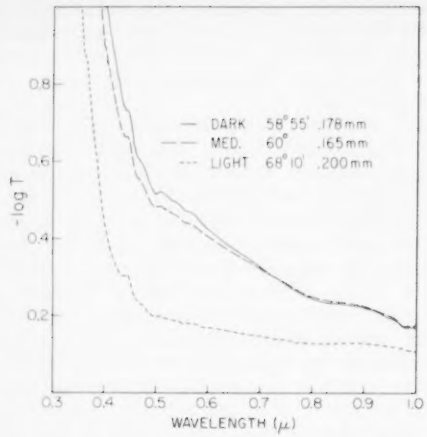

FIGURE 5. *The 0.3 to 1μ λ absorption spectra for specimens representative of the three shades of dark, medium, and light of a borderline rum-green mica (Canadian Clear Purdy, item 15—table 1).*

Apparent optic axial angle and specimen thicknesses are listed.

tions at 0.36μ and at 0.4425μ. The green micas have little of the 0.47 to 0.6μ absorption structure; whereas, the amber and olive associated spectra include moderate 0.47 to 0.6μ absorption. The difference between the dark green and light green spectra is the very much increased general absorption of the dark green with a long, almost straight rise from about 0.8 to 0.5μ.

Being an integrated response, the colors would not in themselves indicate details of the corresponding spectra, nor would the weak and sharp lines contribute much to the resultant color; thus, what is interesting in these results is that the color of muscovite is associated not with one spectral type but with spectra containing a number of distinctly different details. It is seen in the examples of figures 2 to 5 that all of these patterns may be described in terms of three basic spectral types and their combinations. One type is associated with ruby micas (curve 4, fig. 4). The main feature is the 0.47 to 0.6μ absorption structure which indicates the degree of pinkness. The other two are represented by the extreme curves of the greens, i.e., dark green (curve 1, fig. 4) and by light green (curve 7, fig. 4). The attenuation of the pink correlated region of 0.47 to 0.6μ transforms pink ruby to green ruby category, and its superposition upon the green spectral types is associated with olives, ambers, etc.

4.2. Absorption Spectra, 1 to 8μ, and Color

There are a number of prominent bands in this part of the spectrum as can be seen in figure 1. Some of these have not been reported before, some have appeared occasionally in previously reported spectra, and few have definite assignment. Most interesting from the present viewpoint is the absorption multiplet at 3 to 3.7μ. It appeared to be an anomaly to Sutherland et al. [37], since their muscovite spectra were normally devoid of the structure. On the other hand, it appears in some of the earliest spectra of ruby muscovites [34]. Matossi and Bronder [35] attempted assigning one of these bands, i.e., 3.05μ to an overtone of H—O—H deformation. In the present investigation, however, the component bands of this multiplet have always shown a common activity. Thus, any assignment of band origin must take this into consideration. Whereas, Sutherland et al., reported that they found no connection of this multiplet to color, the present group of samples show it to be associated with color in a most direct way. Examples of this 3 to 4μ absorption are shown in figures 6 and 7 for the specimens whose 0.3 to 1μ spectra appear in figures 2 and 4. This spectral structure has been found only in ruby specimens. It is particularly active in samples from the pink end of the color series but decreases to much smaller absorption values in those ruby specimens further along the color series, just as did the magnitude of the visible pink-correlated absorption region at 0.47 to 0.6μ. Other quantitative data obtained from many specimens are given in section 4.3.

Sutherland et al., also found the 7μ band to be companion to the 3.05μ band. This is verified in an appendix to the present paper. They further

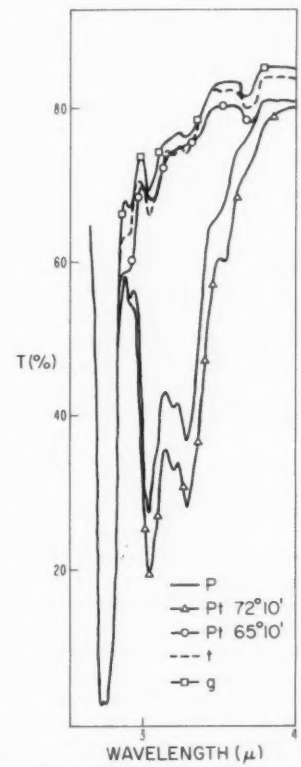

FIGURE 6. *The 2.5 to 4μ λ absorption spectra for specimens representative of the color subgroups of ruby mica.*

Specimens were the same as represented in figure 2.

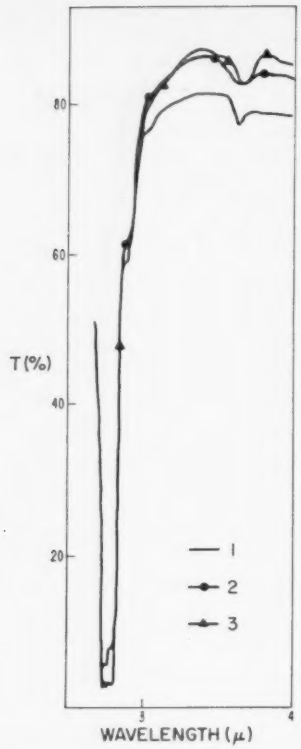

FIGURE 7. *Representative nonruby absorption spectra, 2.5 to 4μ λ.*

(1)—*dark green*, Tanganyika, 0.256 mm thick (see curve 1, fig. 4)
(2)—*amber*, Brazil, 0.266 mm (see curve 3, fig. 4)
(3)—*green white*, U.S., 0.304 mm (see curve 5, fig. 4)

found the 2.3 to 2.4μ spectral structure to have a polarization effect in the same direction as the 2.8μ OH band and in the opposite direction as the sharp 2.2μ band. It is shown in the appendix that this 2.3 to 2.4μ structure also has some behavior related to color but in less straightforward fashion.

4.3. Absorption Coefficient Representation, 0.3 to 8μ

In section 4.2 it was shown how colors are related to absorption spectra. These in turn are more directly indicative of crystal-chemical differences. The details of the spectra can be quantitatively analyzed in terms of absorption coefficients.

Of immediate interest are the two absorption regions associated with the pinkness of specimens, the 0.47 to 0.6μ visable absorption structure and the 3 to 3.7μ infrared absorption structure.

Of these two regions, the 3 to 3.7μ absorption is strongly associated with the redness of specimens, for it has only been found in ruby specimens and then with large absorption for pink rubies or with diminished values for the rest of the ruby subgroups. This situation is shown in figure 8 by data obtained for the two strong bands at 3.05 and at 3.3μ of λ. Data obtained from specimens from the pink end of the ruby color series, i.e., from pink and from pink-tan samples, usually appeared in the region for which values of absorption coefficient were greater than 1 mm^{-1} at both 3.05 and 3.3μ. In the case of pink-tans, this was usually true for those specimens with apparent optic angle $\geq 69°$. On the other hand, a few specimens from the visually selected pink color end of the series gave coefficients slightly less than 1 mm^{-1}. Points representative of all the other ruby subgroups are in the region of small values of α. Considering the complications inherent in the visual sorting of ruby muscovites into color subgroups because of ramifications of shade and other colorations than buff, this correlation is unusually strong. Re-examination of the specimens confirmed the strong inclination to red in those in the upper values of α at 3.05 and 3.3μ. It may be further noted that the density of points is relatively small in the vicinity of $\alpha = 1$ mm^{-1}.

Because of this strong correlation between the magnitudes of the absorption coefficients of the 3.05 and 3.3μ bands and the pinkness of ruby muscovite specimens, we hereafter designate rubies as being of two classes, i.e., either pink or green, as dependent upon the domain into which the values of $\alpha_{3.05}$ fall, with the division set at $\alpha = 1 mm^{-1}$. The data points are so coded in figure 8.

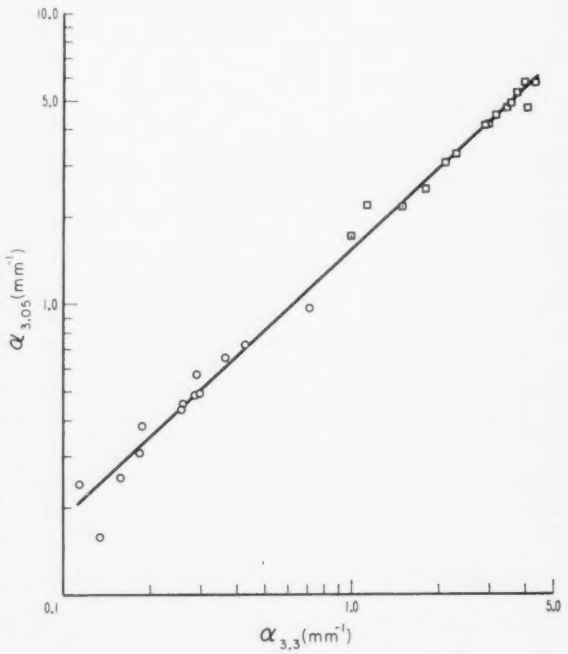

FIGURE 8. *The activities of the two strong absorption bands at 3.05 and 3.3μ λ found in ruby muscovite micas as measured by value of absorption coefficient, α.*

Data points with values >1mm^{-1} are defined as representative of pink ruby (□). Points with values <1mm^{-1} are defined as representative of green ruby (○).

It is noted that the absorption coefficient at 3.05μ ($\alpha_{3.05}$) is greater than that at 3.3μ ($\alpha_{3.3}$) in specimens for which the values are small. The intensities of the two became more nearly equal in specimens for which the values are large.

Of the individual absorption lines in the 0.47 to 0.6μ visible absorption region, the two most useful are those at 0.505μ and 0.58μ. It was observable in figures 2 to 4, e.g., curves 5 and 7 of figure 4, that when the amount of absorption in this region is small, the 0.58μ absorption can be present without that at 0.505μ. Many specimens, e.g., curve 6 of figure 4, had neither absorption. The intensities of these two lines and their relationship are shown in figure 9 with data drawn from many specimens representating the various color subgroups. Points for which both absorption coefficients were zero were excluded. Points are here coded according to color but, for facility, with some contraction in that several subgroups have been combined. The pale green colors of light green, lime, and white-green are now included in one category. The dark greens are considered separately. The ambers and olives are lumped together as rums. The rubies are considered only as pink or green according to value of $\alpha_{3.05}$. As can be seen, $\alpha_{0.505}$ and $\alpha_{0.58}$ are least for light greens and greatest for pink rubies. Rum and intermediate green colors, i.e., ambers, olives, etc., yield intermediate values of α. Again, it can be seen that the dependence of the 0.58μ line is a little different from that of the 0.505μ line. It is seen by comparision of figures 8 and 9 that the values of $\alpha_{3.05}$ and $\alpha_{3.3}$ are greater than those of $\alpha_{0.505}$ and $\alpha_{0.58}$.

Then, the relationship between the 0.47 to 0.6μ and 3 to 3.7μ regions is found in figure 10 where the visible wavelength region is represented by the 0.505μ line and the infrared region by the 3.05μ band. It is evident here that most points fall into one of two regions, i.e., low values of $\alpha_{3.05}$ representative of green ruby muscovite and large values of $\alpha_{3.05}$ representative of pink ruby. The region of the green ruby specimens is bounded by a value of $\alpha_{0.505}$ near 0.2 mm^{-1}. Two intermediate values of $\alpha_{3.05}$ were observed. The data for these two specimens have been additionally coded in this figure and in the others for distinction.

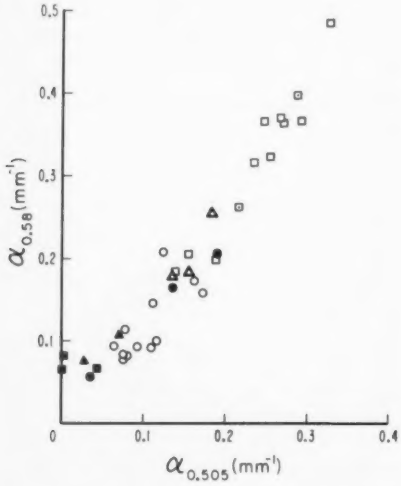

FIGURE 9. *The activities of the 0.505 and 0.58μ λ lines of the visible 0.47 to 0.6μ absorption structure as measured by values of absorption coefficient, α.*

□—pink ruby, ⊡—intermediate pink ruby, ○—green ruby, △—rum, ▲—dark green, ■—pale green, ●—rum-green (Canadian Clear Purdy).

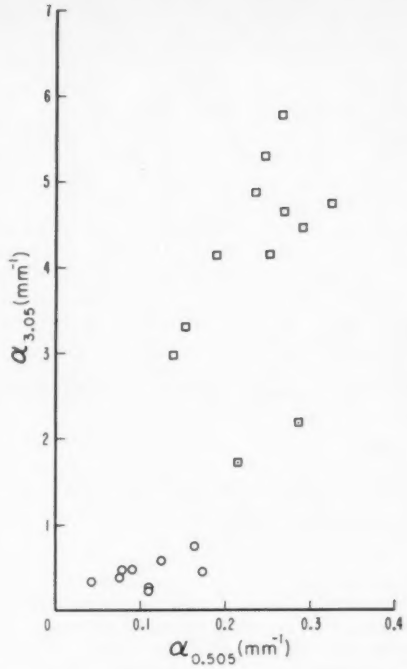

FIGURE 10. *The relationship of the visible pink associated region to the infrared pink associated region; $\alpha_{3.05}$ versus $\alpha_{0.505}$.*

□—pink ruby, ○—green ruby, ⊡—two specimens with intermediate values of $\alpha_{3.05}$.

There is one more pertinent relationship. This involves the 0.44μ line, the existence of which is an identifying feature of green micas. It is almost always vestigial in the pink ruby muscovites. The relationship between this line and the 3.05μ band is shown in figure 11. It is clear that these two absorptions are essentially mutually exclusive; that is, whenever $\alpha_{0.44}$ is relatively large, $\alpha_{3.05}$ has zero value; whenever $\alpha_{3.05}$ is relatively large, $\alpha_{0.44}$ has a near zero value. The progression from pink to green ruby muscovite is usually accompanied by an increase of $\alpha_{0.44}$. The nonruby muscovites observed have never had more than the barest value of $\alpha_{3.05}$.

It is now noted that the two pink ruby specimens represented in figure 10 by intermediate values of $\alpha_{3.05}$ are distinguished by values of $\alpha_{0.44}$ comparable to those of green ruby muscovite.

With these quantitative results it is possible to describe muscovite sheet mica in a reasonably

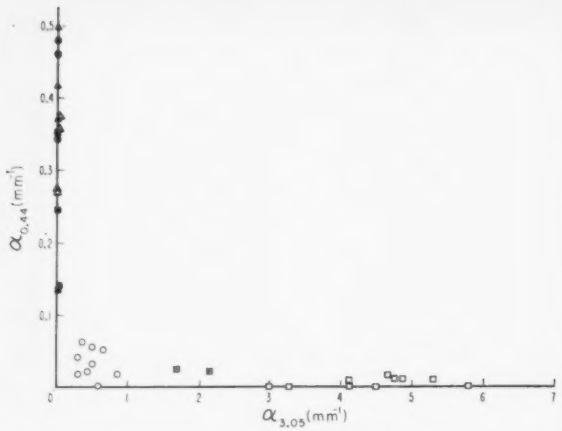

FIGURE 11. *The relationship of the green associated 0.44μ line to the pink associated infrared region; $\alpha_{0.44}$ versus $\alpha_{3.05}$.*

□—pink ruby, ⊡—intermediate $\alpha_{3.05}$, ○—green ruby, △—rum, ■—pale green, ▲—dark green, ●—rum-green.

definitive way by a 3-space of absorption coefficients, $\alpha_{0.44}$, $\alpha_{0.49}$, and $\alpha_{0.58}$. The $\alpha_{0.44}$ applies to the green correlated line at 0.44μ. The $\alpha_{0.508}$ is chosen instead of $\alpha_{0.505}$ to represent the visible pink correlated region because it allows a little more differentiation of specimens possessing small values, as indicated by figure 9. The $\alpha_{0.49}$ is the total absorption coefficient, i.e., $-\frac{1}{t}\ln T$, for the minimum point of the absorption window between the 0.4725 and 0.505μ lines (see the minimum in the $-\log T$ representation of figs. 2 to 4), uncorrected for reflection. This is chosen to represent the general level of the absorption curve and, hence, the position of the band edge. Such characterization is shown by the stereo representation in figure 12 of the 3 dimensional data space so generated. Projections of the data onto the coordinate planes are given by figures 13 and 14. Figure 13 is the projection downward onto the [$\alpha_{0.44}$, $\alpha_{0.58}$] plane and figure 14 represents the view into the 3-*d* data space from the left of the stereo presentation.

The data for all the ruby materials fall close to the [$\alpha_{0.49}$, $\alpha_{0.58}$] plane, as $\alpha_{0.44}$ is small, while $\alpha_{0.49}$ ranges from about 1 to 3.5 mm^{-1}. This is best seen in figure 14. As seen in figure 13, the pink rubies have large values of $\alpha_{0.58}$ but values for $\alpha_{0.44}$ near zero (except the two pink specimens with medium values of $\alpha_{3.05}$). The green ruby specimens are in the region of small values of $\alpha_{0.58}$ and $\alpha_{0.44}$. Data for the pale green specimens are located in figure 14 at small values of $\alpha_{0.49}$ of the order of 1 mm^{-1}, and so are relatively transparent, but the 0.44μ λ line is comparatively intense. Pale greens may also have small values of $\alpha_{0.58}$ (see fig. 13). As the series progresses from pale green to dark green, $\alpha_{0.44}$ and $\alpha_{0.49}$ increase (see fig. 14). The rum micas are represented by points intermediate in all coordinates. In fact for these data the ruby, pale green, dark green, and rum-green groups generate a rough parabola on the [$\alpha_{0.44}$, $\alpha_{0.58}$] plane with the rum colored specimens located in the hollow.

Thus, it appears that these three coordinates provide a detailed basis for discrimination of muscovite micas and can be used to classify samples on a numerical basis.

4.4. Apparent Optic Axial Angle

The apparent optic axial angle was determined for numerous specimens of each color subgroup in order to investigate the connection between angle and color. No significant correlation was found for the ruby micas, but a correlation did appear for the nonruby groups. In figure 15, results are shown for specimens of V–4 nonruby, item 12 of table 1, sorted according to color subgroup. The two color series

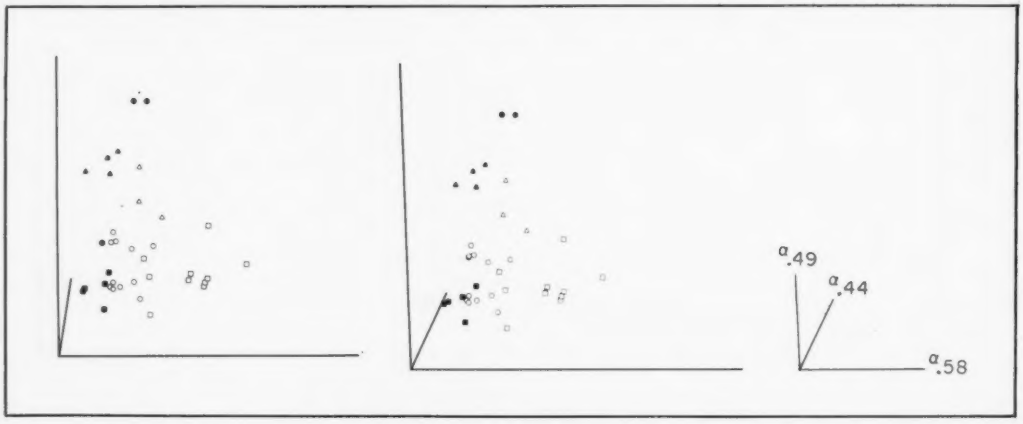

FIGURE 12. *Stereo representation of the 3-coordinate characterization of muscovite sheet with absorption coefficients at wavelengths of 0.44, 0.49, and 0.58μ.*

□—pink ruby, ○—green ruby, △—rum, ■—pale green, ▲—dark green, ●—rum-green.

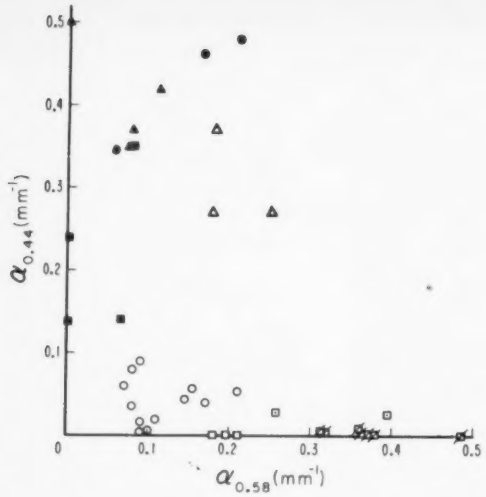

FIGURE 13. *Projection of the 3-coordinate data space of figure 12 onto the* $[\alpha_{0.44}, \alpha_{0.58}]$ *plane (view of the 3-coordinate space from above).*

□—pink ruby, ⊡—2 rubies of intermediate $\alpha_{3.05}$, ○—green ruby, △—rum, ■—pale green, ▲—dark green, ●—rum-green, ⊠—pink ruby specimens for which $\alpha_{0.58} > 0.2 mm^{-1}$.

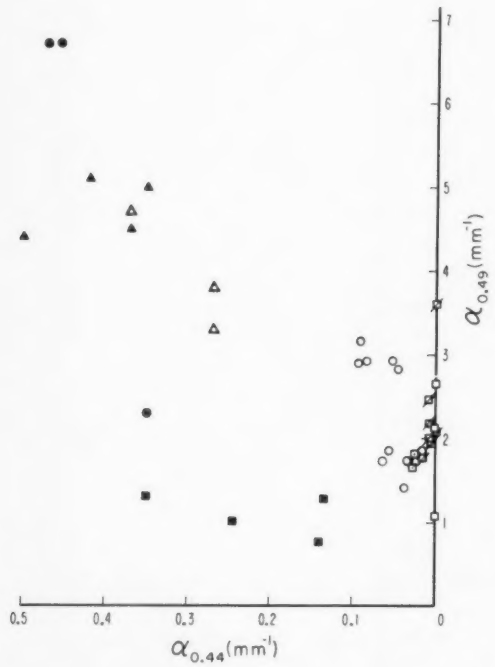

FIGURE 14. *Projection of the 3-coordinate data space of figure 12 onto the* $[\alpha_{0.49}, \alpha_{0.44}]$ *plane (view of the 3-d space from the left).*

See figure 13 for code.

branching off from olive are included, dark green being the end member of one branch and light green that of the other.

With reference to figure 4, the one factor which varies in common with the progression along the color series used in figure 15 is specular density, particularly in the region of the band edge. Therefore, being essentially of one hue but of variable shade (see fig. 5), the rum-green Canadian Clear Purdy (item 15 of table 1) was chosen for comparison of angle to specular density. Specimens were measured photometrically with a tungsten source and a deep violet filter which had the spectrophotometrically determined pass band of figure 16. This filter was chosen to give a measure of the height of the absorption curve in the vicinity of 0.4μ. The correlation obtained for angle to density is as shown in figure 17. Whereas the correlation shown in figure 17 is good, no similarly marked correlation was found for the ruby micas.

A comparison of representatives of all types of the micas, including rubies, showing the relation of apparent axial angle to $\alpha_{0.49}$, is seen in figure 18. This presentation tends to clarify the behavior of apparent axial angle. A certain grouping of values occurs for very pink ruby specimens; namely, those specimens for which $\alpha_{3.05}$ exceeds 1 mm^{-1} and $\alpha_{0.58}$ exceeds 0.2 mm^{-1} all fall within a given domain of moderately large axial angle and medium $\alpha_{0.49}$. The data for all other specimens including several representative of pink rubies, fall in a main sequence in which apparent angle decreases with increasing $\alpha_{0.49}$.

It is to be noted that pale green colored specimens, not the ruby, have apparent axial angles approaching that of muscovite proper which ought to be $\sim 78^\circ$ as obtained from quoted values of index of refraction and axial angle [22].

4.5. Absorption Spectra, 10 to 15μ of λ

The spectral region from 10 to 15μ is interesting from the present viewpoint inasmuch as the cationic molecular vibrations are involved and the relative band intensities show some relation to color.

Examples of spectral variations found in this λ region are indicated in figure 19 for specimens representative of the principal color groups, pink ruby, rum, dark green, and pale green. Generally, transmission increased as the color progressed toward dark green, except in the vicinity of 12μ where the opposite was true. The variations of particular band intensities, however, are more involved.

4.6. Absorption Coefficient Representation, 10 to 15μ of λ

The shape of the transmission maximum in the vicinity of 12μ is determined by the intensities of the four bands at 10.8, 11.4, 12, and 12.5μ. The 11.4μ band is too faint for evaluation. A representation which differentiates the absorption coefficient data for the other three bands on the basis of color is given in figure 20. In this the absorption coefficient of each band is normalized by the sum of the

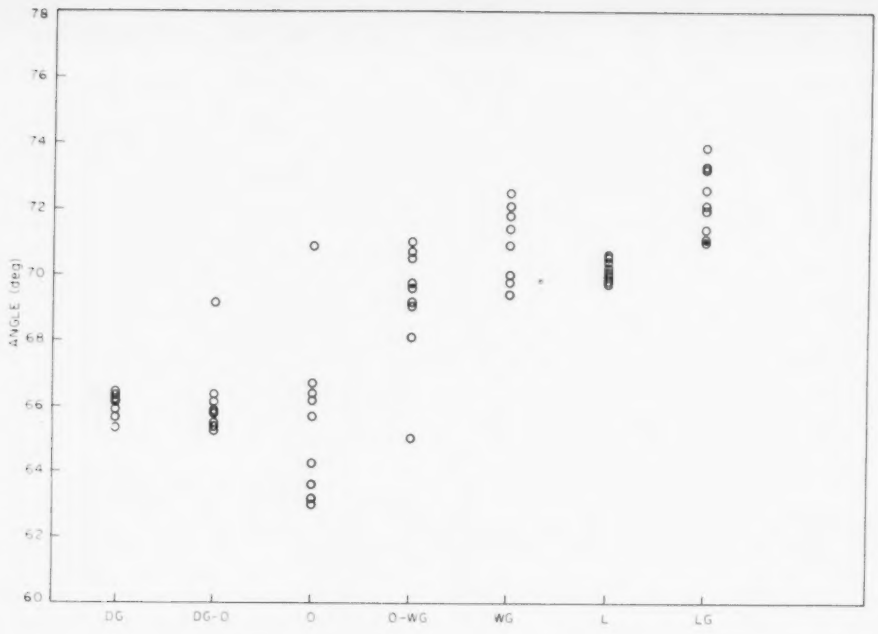

FIGURE 15. *The variation of apparent optic axial angle versus nonruby color subgroup.*

V–4 nonruby Domestic, item 12—Table 1. Both color series branching off olive are represented, i.e.—dark green to olive, and light green to olive.

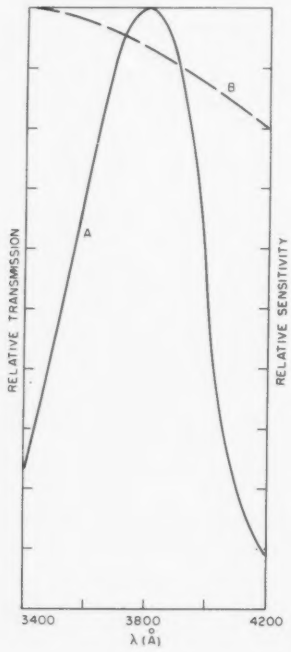

FIGURE 16. *Photometer spectral response for optical density measurements.*

A—relative transmission curve of filter. B—relative sensitivity of 1P28, hotomultiplier detector.

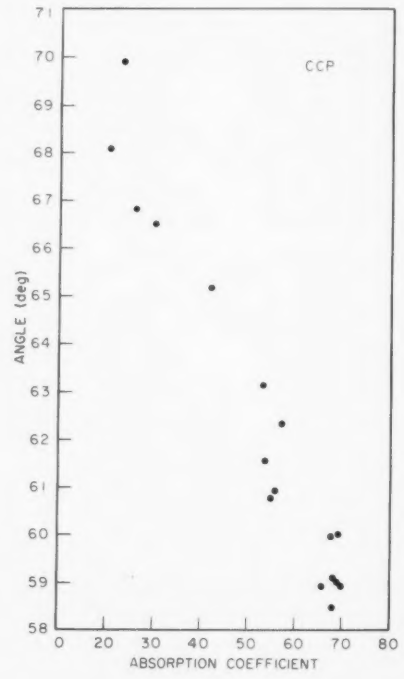

FIGURE 17. *The relationship of apparent optic axial angle to relative absorption coefficient for specimens of rum-green Canadian Clear Purdy (see fig. 5).*

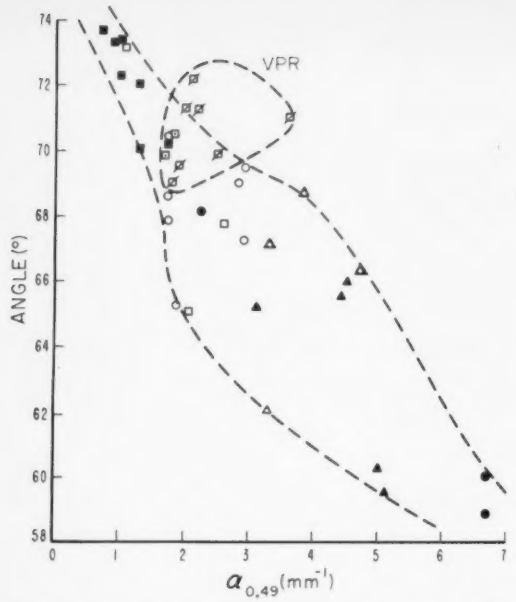

FIGURE 18. *The relationship of apparent optic axial angle to the height of the absorption edge as evaluated by* $\alpha_{0.49}$.

VPR represents the domain of very pink rubies, i.e., $\alpha_{3.05} > 1mm^{-1}$ and $\alpha_{0.54} > 0.2mm^{-1}$.

⊠—very pink ruby □—pink ruby ⊡—intermediate $\alpha_{3.05}$
○—green ruby △—rum ■—pale green
▲—dark green ●—rum-green

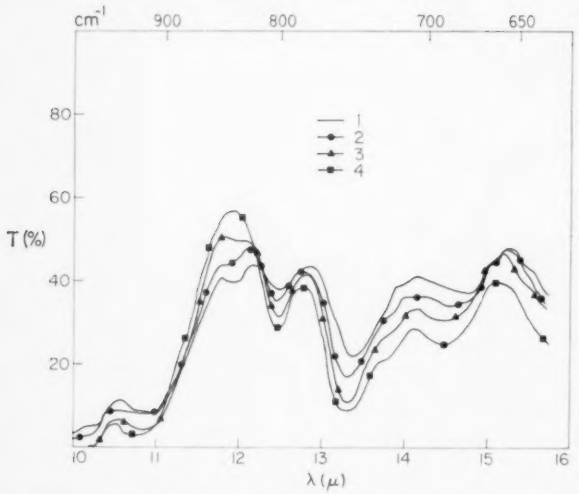

FIGURE 19. *The 10 to 15μ λ absorption spectrum and principal color group.*

1—*dark green* Tanganyika 6μ thick; 2—*amber (rum)* Brazil 8μ thick; 3—*green-white* domestic 7μ thick; 4—*pink ruby* India 8μ thick. Code and associated spectra are those of figures 6 and 7.

coefficients. It is evident that the points shift to the upper left as color progresses from pink ruby to dark green. In detail, pink rubies are characterized by a relatively intense 12.5μ band and by a missing or nearly missing 12μ band. Green ruby specimens have a faint 12μ band, usually a less intense 12.5μ band, but a more intense 10.8μ band than the pink ruby specimens. Dark green pieces usually show the greatest 12μ absorption and the least 12.5μ absorption. Rum and pale green specimens are associated with intermediate 12μ absorption.

A second, relatively weak band, at 13.8μ, is related to the 12μ band. This relationship, similar to that between the 0.44 and 3.05μ bands (see fig. 11), is shown in figure 21 in which $\alpha_{13.8}$ is plotted against α_{12}. Although comparatively weak for the 10 to 15μ region, these bands at 12 and 13.8μ have the same order of intensity as the pink ruby 3.05μ band. The pink ruby specimens possess the most intense 13.8μ band but little if any 12μ band. Dark green specimens are opposite and have least 13.8μ absorption but most 12μ absorption. Specimens of intermediate color groups show both bands. As lines connecting points to the origin are rotated from the $\alpha_{13.8}$ axis to the α_{12} axis, color progresses from pink ruby to dark green. Ruby specimens usually appear above a line of slope 1, while nonruby specimens usually appear below this line.

The strengths of the intense bands at 13.3 and at 14.5μ are associated with that of the 12.5μ band. The increase of the 14.5μ band with the 12.5μ band is shown in figure 22. As observable from the color code, both α_{12} and $\alpha_{14.5}$ increase as color types change from dark green, to rum, to green ruby to very pink ruby.

The strength of the 13.3μ band is not linearly related to that of the 12.5μ band, but the ratio of the absorption coefficients of the 12.5 and 13.3μ bands is somewhat linearly related to $\alpha_{12.5}$, as shown in figure 23. A separation of values by color is evident.

No direct correlation was found for any one band in the 10 to 15μ region to any one line or band in the shorter wavelength ranges of 0.3 to 1μ and 1 to 8μ.

5. Summary and Concluding Remarks

Muscovite sheet mica has traditionally been categorized primarily as ruby or nonruby, and although physical differences between these two categories have long been debated, no substantial evidence other than color has existed to warrant such differentiation. In the present paper, on the basis of color, apparent optic axial angle, and absorption spectra, we have shown that there are other measurable differences in muscovite mica which provide a more complex categorization than just ruby or nonruby.

The short wavelength absorption spectra (0.3 to 1μ λ) have a deep absorption edge at a wavelength near 0.32μ and a number of weak lines and absorption regions at the base of this edge. These spectra can be classified as of three types. All the colors observed in commercial muscovite sheet can be related to variations in these three spectral types. The position of the absorption edge and the activities of weak lines in the visible absorption region sensitively vary with color. These are further related to axial angle and longer wavelength absorption bands. This is interesting, since these lines would be related to energy differences an order of magnitude greater

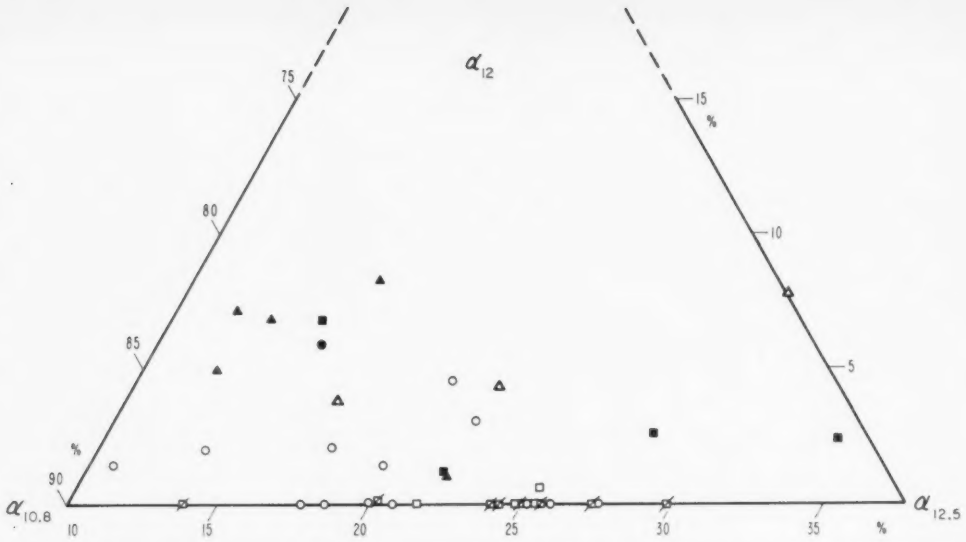

FIGURE 20. *A triangular plot of the relative intensities of the 10.8, 12, and 12.5μ bands:* $\alpha_{10.8}$, α_{12}, $\alpha_{12.5}$. See figure 18 for code.

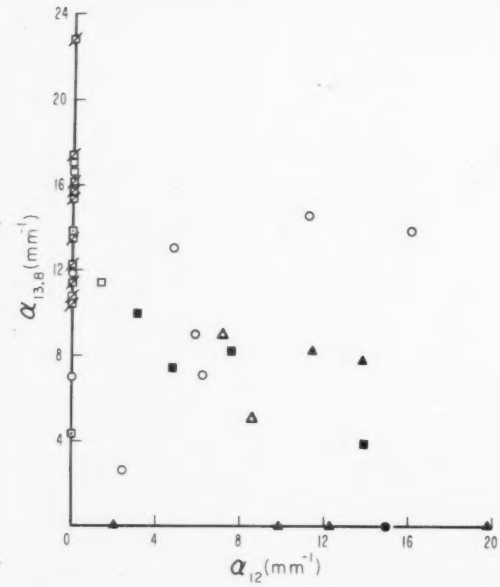

FIGURE 21. *A comparison of the activities of the two weak bands at 12 and 13.8μ for specimens of different color groups.* See figure 18 for code.

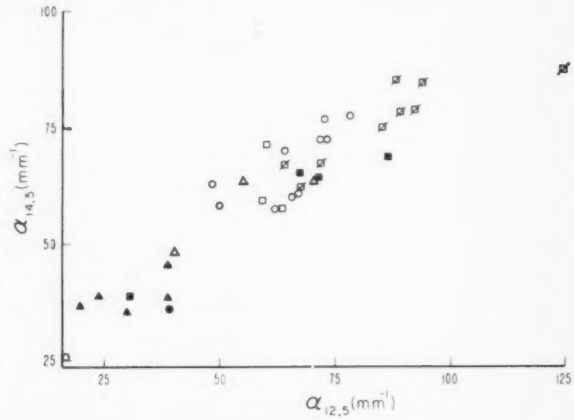

FIGURE 22. *A comparison of the activities of the two strong bands at 12.5 and 14.5μ for specimens of different color groups.*

than those directly related to the molecular vibrations. They are reminiscent of those found in a defect structure, e.g., color centers. The position of the absorption edge and the strengths of two weak lines at 0.44 and 0.58μ of λ are particularly useful for measuring the variations in these crystals.

The apparent optic axial angle is related to the position of the absorption edge, the angle diminishing as the edge shifts to longer wavelength and lower absorption energy. There are certain ruby specimens for which this relationship is not found. These are particularly absorbant in the blue to yellow region of the visible range and the near infrared at 3 to 3.7μ. The values of angle and position of the edge place these ruby materials outside of the main sequence of the other micas.

Ruby micas have an active multiplet in the near infrared between 3 and 3.7μ of λ. This multiplet does not appear in other muscovites. The amount of absorption further separates the ruby material into two subclasses.

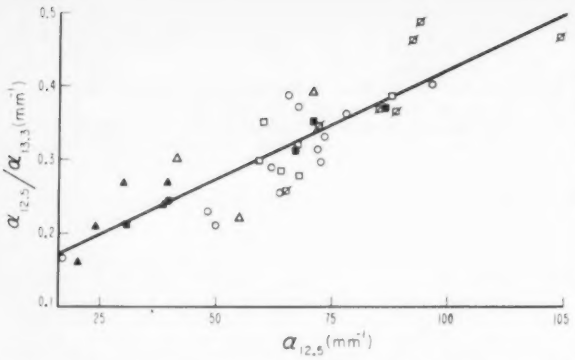

FIGURE 23. *A comparison of the activities of the two strong bands at 12.5 and 13.3μ for specimens of different color groups; $\alpha_{12.5}/\alpha_{13.3}$ versus $\alpha_{12.5}$.*

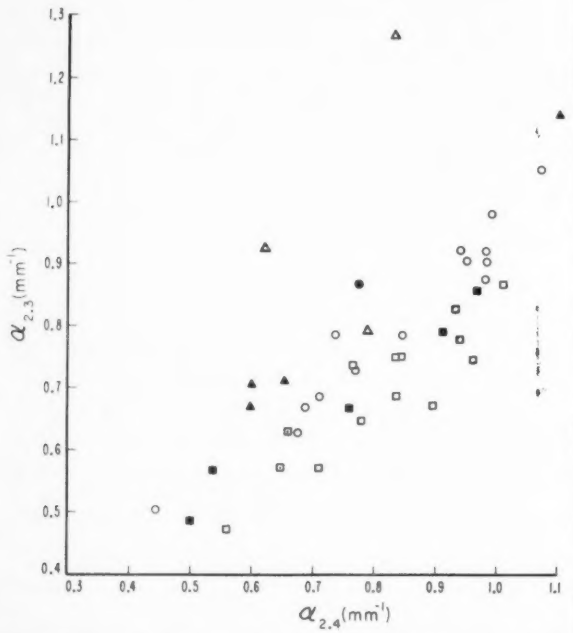

FIGURE 24. *Internal activity of the 2.3 to 2.4μ multiplet with color; $\alpha_{2.3}$ versus $\alpha_{2.4}$.*

The spectral bands in the middle infrared between 10 and 15μ λ are shown to be related to the color of the material. These bands are in a region which has been shown by others to indicate vibrations of such cationic-oxygen structures as Si—O—Al.

Thus, all in all, it is demonstrated that muscovite sheet micas have measureable differences which by their nature indicate basic chemical and structural variations.

We thank J. C. Schleter of the Metrology Division for determining the 0.3 to 1μ spectra, P. N. Moore and W. Lazear of the General Services Administration for the selected and classified samples.

6. Appendix

Several additional relationships are of interest.

The bands of the 2.2 to 2.5μ λ region consist of an absorption spike at 2.2μ and a multiplet at 2.3 to 2.4μ. These are said to be pleochroic [37]. The 2.3 and 2.4μ bands, however, are companions. There is a difference in their intensity ratio with color group (see fig. 24). The 2.4μ band is the more intense in pink ruby specimens, but as the color progresses to the other extreme, the 2.3μ band becomes stronger. Thus, a trace drawn through the values of the pink rubies in figure 24 is displaced upward on the $[\alpha_{2.3}, \alpha_{2.4}]$ plane as the color of specimens progresses to dark green and rum.

A faint band at 3.5μ which is part of the 3 to 3.7μ multiplet is comparable in intensity to the faint absorptions in the 0.3 to 1μ λ range. Because of its relative weakness, its α is not accurately determined, but figure 25 does indicate that the 3.5μ band is proportional to the 3.05μ band.

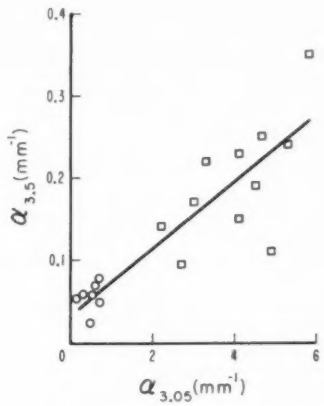

FIGURE 25. *Internal activity of the 3 to 3.5μ multiplet; association of the 3.5μ band to the 3.05μ band.*

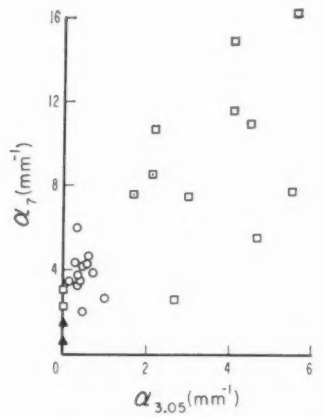

FIGURE 26. *Association of the 7μ band to the 3.05μ band*

The band at 7μ is even less accurately evaluated from our spectra (see fig. 1), but it too shows some relationsl ip to the 3.05μ band as Sutherland et al., reported [37], see figure 26.

7. References

[1] F. W. Horton, Mica, Bureau of Mines Inf. Circ. 6822 (1941).
[2] R. D. Thomson, Marketing sheet mica, Bureau of Mines Inf. Circ. 7729 (1955).
[3] H. H. Pool, Phil. Mag. **32,** 112 (1916).
[4] J. R. Weeks, Phys. Rev. **19,** 319 (1922).
[5] Dye and Hartshorn, Proc. Phys. Soc. Lond. **37,** 42 (1924).
[6] A. B. Lewis, E. L. Hall, and F. R. Caldwell, BS J. Research **7,** 403 (1931).
[7] S. Datta, J. Sen Gupta, and P. C. Mahanti, Ind. J. Phys. **17,** 79 (1943).
[8] E. L. Hall, Proc. IRE **32,** 393 (1944).
[9] P. C. Mahanti, M. K. Mukherjee, and P. B. Roy, Ind. J. Phys. **19,** 83 (1945).
[10] P. C. Mahanti and S. S. Mandal, Ind. J. Phys. **22,** 7 (1948).
[11] R. H. Jahns and F. W. Lancaster, Geological Survey Prof. Paper 225 (1950), Physical Characteristics of Commercial Sheet Muscovite in the Southeastern U.S.
[12] H. L. Curtis, Bul. BS, **11,** 359 (1915).
[13] S. S. Mandal and P. C. Mahanti, Ind. J. Phys. **27,** 294 (1953).
[14] W. Hackett and A. M. Thomas, J.I.E.E. **88,** 295 (1941).
[15] S. S. Mandal, Ind. J. Phys. **25,** 111 (1951).
[16] P. R. Pondy and G. E. Helmke, 2d Ann. Tech. Meet. on Elect. Devices of IRE paper II—c.4.
[17] R. W. Powell and E. Griffiths, Proc. Roy. Soc. **A163,** 189 (1937).
[18] P. Hidnert and G. Dickson, J. Research NBS **35,** 309 (1945).
[19] E. Wilson, Proc. Soc. London **96,** 429 (1920).
[20] J. T. Kendall and D. Yeo, Proc. Phys. Soc. Lond. **B64,** 135 (1931).
[21] F. D. Bloss, E. Shekarchi, and H. R. Shell, Am. Min. **44,** 33 (1959).
[22] A. N. Winchell and H. Winchell, Elements of Optical Minerology, Part II 4th ed. (John Wiley & Sons, New York, N.Y., 1951).
[23] H. R. Shell and R. L. Craig, Bur. of Mines Rept. of Invest., 5158 (1956), Synthetic mica investigations: VII, chemical analysis and calculation to unit formula of fluorsilicates.
[24] E. W. Heinrich and A. A. Levinson, Am. Min. **38,** 25 (1953).
[25] Margaret D. Foster, Geol. Survey Bull. 1036–D (1956), Correlation of dioctahedral potassium micas on the basis of their charge relations; see also Geol. Prof. Paper 354–B (1960), Interpretation of the composition of trioctahedral micas.
[26] A. J. Hall, Am. Min. **26,** 29 (1941).
[27] V. Stubican and R. Roy, Am. Min. **46,** 32 (1961) and Tech. Rept. 3 of Am. Petrol. Inst., Proj. 55, Annual Rept. 20 (7/1959).
[28] American Society for Testing Materials Specs. D351–53T.
[29] D. B. Judd, J. Research NBS, **35,** 245 (1945).
[30] A. Johannsen, Manual of Petrographic Methods, 2d Ed., (McGraw Hill) 1918, or E. E. Wahlstrom, Optical crystallography, 2d ed. (John Wiley & Sons, New York, N.Y., 1957).
[31] S. Ruthberg, J. Research NBS, **65C** (Eng. and Instr.) No. 2, 125 (1961).
[32] P. Popper, Nature **168,** 119 (1951).
[33] J. A. Dobrowolski, J. Opt. Soc. Am. **49,** 794 (1959).
[34] Rubens and Nichols, Ann. Physik 3, **60,** 418 (1897); Rosanthal, Ann. Physik 3, **68,** 791 (1899); Aschkinass, Ann. Physik 4, **1,** 42, (1900); W. W. Coblentz, Carnegie Inst. Of Wash. Pub. 65 (1906) and 97 (1908).
[35] Cl. Schaefer, F. Matossi, and K. Wirtz, Zeit. fur Phys. **89,** 210 (1934); F. Matossi and O. Bronder, Zeit. fur Phys. **111,** 1 (1938).
[36] V. C. Farmer, Min. Mag. **31,** 329 (1958).
[37] G. B. B. M. Sutherland, S. Krimm, R. T. Mara, and W. G. Simeral, unpublished reported (1st annual rept. of Infrared studies of crystals, U. of Mich., 8/1952, Proj. M957, Da 36–039 sc 5581, Armed Services Tech. Inf. Agency, TI 170, 180).
[38] H. H. Adler et al., Infrared spectra of reference clay minerals, Am. Petroleum Inst., Project 49, Reference Clay Minerals, Prelim. Rept. 8, Columbia Univ. (1950); J. M. Hunt, M. P. Wisherd, and L. C. Bonham An. Chem. **22,** 1478 (1950); and P. J. Launer, Am. Min. **37,** 764 (1952).
[39] J. J. Fox and A. E. Martin, Proc. Roy. Soc. **A174,** 234 (1940); A. M. Buswell and D. F. Dudenbostel, J. Am. Chem. Soc. **63,** 2554 (1941); W. D. Keller and E. E. Pickett, Am. J. Sci. **248,** 264 (1950); R. E. Rundle and M. Parasol, J. Chem. Phys. **20,** 1487 (1952); R. C. Lord and R. E. Merrifield, J. Chem. Phys. **21,** 166 (1953); Scholze and Dietzel, Naturwiss **42,** 242 and 575 (1955); R. T. Mara and G. B. B. B. Sutherland, J. Opt. Soc. Am. **43,** 1100 (1953); R. M. Hexter and D. A. Dows, J. Chem. Phys. **25,** 504 (1956); H. Beutelspacher, 6th Int's. Congress on Soil Sciences 1, 329, (1956), Repts. B; D. M. Roy and R. Roy Geochim, and Cosmochim. Acta **11,** 72 (1957); H. W. Van der Marel and J. H. L. Zwiers, Silicates Industrials July–Aug. 359 (1959).
[40] N. Wright, Ind. Eng. Chem. Anal. Ed. **13,** 1 (1941); J. J. Heig, M. F. Bell, and J. V. White, Ind. Eng. Chem. Anal. ed. **19,** 293 (1947); Brindley and Zussman, Amer. Min. **44,** 185 (1959).

(Paper 67A4–220)

JOURNAL OF RESEARCH of the National Bureau of Standards—A. Physics and Chemistry
Vol. 67A, No. 4, July–August 1963

Thermodynamic Properties of Magnesium Oxide and Beryllium Oxide from 298 to 1,200 °K [1]

Andrew C. Victor[2] and Thomas B. Douglas

(February 26, 1963)

As a step in developing new standards of high-temperature heat capacity and in determining accurate thermodynamic data for simple substances, the enthalpy (heat content) relative to 273 °K, of high purity fused magnesium oxide, MgO, and of sintered beryllium oxide, BeO, was measured up to 1,173 °K. A Bunsen ice calorimeter and the drop method were used. The two samples of BeO measured had surface-to-volume ratios differing by a factor of 15 or 20, yet agreed with each other closely enough to preclude appreciable error attributable to the considerable surface area. The enthalpies found for MgO are several percent higher than most previously reported values. The values are represented within their uncertainty (estimated to average ±0.25%) by the following empirical equations[3] (cal mole^{-1} at T °K)

$$\text{MgO: } H_T^\circ - H_{273.15}^\circ = 10.7409T + 1.2177(10^{-3})T^2 - 2.3183(10^{-7})T^3 + 2.26151(10^5)T^{-1} - 3847.94.$$

$$\text{BeO: } H_T^\circ - H_{273.15}^\circ = 11.1084T + 7.1245(10^{-4})T^2 + 8.40705(10^5)T^{-1} - 5.31245(10^7)T^{-2} - 5453.21.$$

Values of enthalpy, heat capacity, entropy, and Gibbs free-energy function are tabulated from 298.15 to 1,200 °K.

1. Introduction

A previous paper [1] [4] has described the need for heat-capacity standards at temperatures above the range of the present α-aluminum oxide (corundum) standard. Enthalpy measurements on thorium dioxide have been presented [1] as a first step in the investigation of new materials for this purpose.

The chemical stability and high melting points of MgO and BeO (3,000 and 2,800 °K, respectively [2]) recommend these materials for consideration as possible heat-capacity standards. Although both compounds have lower melting points than thorium dioxide (3,300 °K [2]), the lower sensitivity of their heat capacities to the influence of common impurities (because of smaller differences in atomic weights) is a decided advantage. The accurate knowledge of the thermodynamic properties of these substances over a large temperature range has added value because of the very frequent occurrence of these materials in high-temperature reactions and installations. The results of enthalpy measurements on fused MgO and on sintered BeO specimens of two different bulk densities are presented in this paper.

2. Samples and Containers

The magnesium oxide sample had been fused and was transparent, clear, and colorless; it was supplied by the Norton Company, of Niagara Falls, Ontario, Canada. Spectrochemical and spectrographic analyses at the National Bureau of Standards indicated that the sample contained 99.90 weight percent MgO if the detected metallic impurities are assumed to be present as their highest stable oxides (table 1).

TABLE 1. *Impurities in the samples*

Element [a]	BeO sample 1	MgO
	Weight %	*Weight %*
Ag	[c]	<0.001
Al	0.007	.004
Be	[b]	[c]
Ca	<.001	.025
Cr	[c]	<.001
Cs	.001	[c]
Cu	<.001	<.001
Fe	.001	.02
K	.002	[c]
Li	<.00005	[c]
Mg	<.00005	[b]
Mn	[c]	.008
Na	.002	<.002
Si	.01	.009

[a] The samples were also examined for the following elements which were not detected: Ag, Au, B, Ba, Bi, Cd, Ce, Co, Ga, Ge, Hf, In, Ir, La, Mo, Nb, Ni, Os, P, Pb, Pd, Pt, Rh, Ru, Sb, Sc, Sn, Sr, Ta, Te, Th, Ti, U, V, W, Y, Zn, Zr. In addition, the following elements were undetected in BeO: Dy, Er, Eu, Gd, Ho, Lu, Nd, Pr, Ra, Rb, Re, Sm, Tb, Tm, Yb.
[b] Major constituent.
[c] Not detected.

Two samples of beryllium oxide were used in the present study. BeO powder was pressed, fired, and sintered to obtain bulk densities of 2.3 g cm^{-3} and 1.6 g cm^{-3} (firing temperatures of 1,800 and 1,100 °C respectively). These two samples, whose densities were about 72 and 50 percent of the single-crystal (X-ray) value, will hereafter be referred to as BeO samples 1 and 2, respectively. Spectrochemical

[1] The measurements on MgO were supported by the Wright Air Development Division, Air Research and Development Command, United States Air Force, Wright-Patterson Air Force Base, Ohio.
[2] Present address: U.S. Naval Ordnance Test Station, China Lake, Calif.
[3] Using the defined thermochemical calorie = 4.1840 joules.
[4] Figures in brackets indicate the literature references at the end of this paper.

analyses of both samples at the Bureau indicated that they contained 99.96 percent BeO by weight (table 1). In a petrographic examination, sample 1 was found to consist of approximately isometric particles 25μ on an edge. BeO sample 2 was observed to be composed of needlelike particles estimated to average 10μ in length and 1μ^2 in cross section. The surface-to-volume ratio of such a particle is the same as that for a cube with an edge of 1.5μ. The sintered samples of BeO used in the enthalpy measurements each consisted of two cylinders 2 cm long and 1 cm in diameter.

The samples were sealed in containers of annealed pure silver preparatory to making enthalpy measurements [1]. BeO sample 2 lost weight during the first attempts at sealing it in its container. Further study of the weight following successive heat treatment and exposure to the room atmosphere showed that at least 0.3 percent of the original sample mass was lost on heating to about 1,100 °K, but was regained by the sample after cooling in a desiccator and then standing in room air for 30 min. Tests on six specimens of this lower-density sample of BeO all showed the same hygroscopic behavior. Similar tests made with BeO sample 1 showed no detectable mass change. When BeO sample 2 was finally sealed in its container its mass was the lowest attainable by the heat treatment mentioned above. It is possible, however, that the sample was still contaminated by a small amount of water.

3. Enthalpy Measurements

The "drop" method and calorimeter employed in the enthalpy measurements have been described in detail in a previous publication [3]. In brief, the method used was as follows. The sample, sealed in a silver container, was suspended in a silver-core furnace until it had time to come to a constant known temperature. It was then dropped (with almost free fall) into the Bunsen ice calorimeter, which measured the heat evolved by the sample plus container in cooling to 273.15 °K. In order to account for the enthalpy of the silver container and the heat lost during the drop, a similar experiment was made with an identical empty container at the same furnace temperature. The difference between the two values of heat is a measure of the enthalpy change of the sample between 273.15 °K and the furnace temperature.

The temperature of the central portion of the furnace was measured by a strain-free platinum resistance thermometer (ice-point resistance, about 24 ohms) up to and including 873 °K, and by an annealed Pt/Pt-10 percent Rh thermocouple at higher temperatures.[5] The thermometer and thermocouple were frequently intercompared during the heat measurements, were calibrated shortly afterwards, and were concordant with the good consistency of these two instruments over a period of more than 5 years.

[5] Temperatures are on the International Temperature Scale of 1948 as modified in 1954 [4].

TABLE 2. *Relative enthalpy of magnesium oxide* [a]

($H_T - H_{273.15}$°K)

Furnace temperature, T	Individual enthalpy measurements [b]	Mean observed enthalpy	Calc. eq (1)	Mean observed—calc.
°K	cal mole^{-1}	cal mole^{-1}	cal mole^{-1}	cal mole^{-1}
373.15	923.5 922.7	923.1	923.6	−0.5
473.15	1930.3 1961.1	1960.7	1960.1	+0.6
573.15	3060.4 3058.0	3059.2	3059.2	+0.0
673.15	4194.8 4203.6 4194.0	4197.5	4199.3	−1.8
773.15	5375.5 5371.0 5376.7	5374.4	5369.6	+4.8
873.15	6560.6 6558.2	6559.4	6563.5	−4.1
973.15	7777.6 7773.6	7775.6	7776.5	−0.9
1073.15	9007.5 9009.1	9008.3	9005.3	+3.0
1173.15	10245.4 10246.6	10246.0	10247.1	−1.1

[a] Mol wt = 40.311 g.
[b] Sample mass = 10.7578 g.

TABLE 3. *Relative enthalpy of beryllium oxide* [a]

($H_T - H_{273.15}$°K)

Furnace temperature, T	Individual enthalpy measurements		Mean observed enthalpy (sample 1)	Calc. eq (2)	Mean observed—calc.
	Sample 1 [b]	Sample 2 [c]			
°K	cal mole^{-1}	cal mole^{-1}	cal mole^{-1}	cal mole^{-1}	cal mole^{-1}
323.15	303.6 303.9	305.6 305.5	303.7	303.7	+0.0
373.15	660.9 663.6	665.5 665.8 666.6	662.2	662.6	−0.4
473.15	1503.1 1500.4	1499.3 1497.8	1501.8	1501.8	−0.0
573.15	2455.1 2452.3	2457.4 2452.6 2453.3	2453.7	2452.7	+1.0
673.15	3481.6 3477.0	3479.8 3481.0	3479.3	3478.9	+0.4
773.15	4558.0 4555.1 4560.3	4562.2 4562.9	4557.8	4559.6	−2.2
873.15	5679.8 5684.1	5684.0 5684.2	5682.0	5682.4	−0.4
973.15	6843.4 6838.1	6841.4 6843.3	6840.7	6839.5	+1.2
1073.15	8025.9 8026.8	8026.7 8022.2 8024.2	8026.3	8025.6	+0.7
1173.15	9242.4 9232.6 9237.6 9233.6	9228.5 9228.7	9236.5	9237.2	−0.7

[a] Mol wt = 25.012 g.
[b] Mass of sample 1 = 6.7171 g.
[c] Mass of sample 2 = 6.3747 g.

The measured heat values obtained in individual runs on an empty container that were used in the calculations of this paper are recorded in a previous publication [1]. The second column of table 2 gives the fully corrected measured enthalpy values, in defined thermochemical calories per mole, for the magnesium oxide. In table 3, the second and third columns contain the corresponding information for BeO samples 1 and 2. The individual enthalpy

values listed in these two tables were obtained by subtracting the empty container values (using the mean at each temperature) from the observed enthalpies for sample plus container and then converting to molar values. Corrections had been applied in the usual manner [1]. The enthalpy correction for the impurities in the MgO amounted to less than 0.02 percent of the enthalpy of the sample. For BeO an impurity correction of less than 0.01 percent of the sample enthalpy was used. These corrections were made assuming that the foreign chemical elements were present as the highest stable oxides and that their enthalpies contributed additively to the total observed enthalpy. The calculated values of enthalpy in tables 2 and 3 are smoothed values arrived at as described in section 4.

4. Smoothed Thermodynamic Functions

The mean enthalpy values for MgO and for BeO sample 1 were used to derive eqs (1) and (2) (in cal mole^{-1} at T °K) by the method of least squares. The results for BeO sample 2 were ignored, for the reasons discussed in section 5.

$$\text{MgO: } H_T^\circ - H_{273.15}^\circ = 10.7409T + 1.2177(10^{-3})\ T^2 - 2.3183(10^{-7})\ T^3 + 2.26151(10^5)\ T^{-1} - 3847.94. \quad (1)$$

$$\text{BeO: } H_T^\circ - H_{273.15}^\circ = 11.1084T + 7.1245(10^{-4})\ T^2 + 8.40705(10^5)\ T^{-1} - 5.31245(10^7)\ T^{-2} - 5453.21. \quad (2)$$

Enthalpy values calculated from eqs (1) and (2) are tabulated and compared with experimental values in the last two columns of tables 2 and 3. Tables 4 and 5, which give the common thermodynamic properties of magnesium oxide and beryllium oxide, were obtained by a four-point numerical integration, at 10-deg intervals, of heat-capacity values chosen as follows. The values of heat capacity for MgO at and above 340 °K were obtained from eq (1); below 340 °K, values from low-temperature measurements [5, 6] were smoothed so as to join the derivative of eq (1) at this temperature. Equation (2) was used to obtain heat-capacity values for BeO at and above 410 °K; below 410 °K the heat capacities obtained from recent low-temperature work [6] in the room-temperature region were used in the integration. The mathematical work was performed on an IBM 7090 computer.

The thermodynamic properties of MgO in table 4 (other than C_p°), which are based on values for 298.15 °K obtained by smoothing low-temperature data [5, 6], are given relative to 0 °K. Because no low-temperature thermodynamic data have been published for macrocrystalline BeO, the same thermodynamic properties of this substance are given relative to 298.15 °K.

On the basis of previous work with the Bunsen ice calorimeter, the authors believe that the uncertainty of the thermodynamic properties in tables 4 and 5 corresponds to 0.4 percent in the heat capacity. Changes in values of the thermodynamic properties introduced by smooth-joining to low-temperature data are within the experimental uncertainty.

TABLE 4. *Thermodynamic properties of magnesium oxide*

T	C_p°	$H_T^\circ - H_{0°K}^\circ$	$S_T^\circ - S_{0°K}^\circ$	$-\frac{F_T^\circ - H_{0°K}^\circ}{T}$
°K	*cal/mole-deg*	*cal/mole*	*cal/mole-deg*	*cal/mole-deg*
298.15	8.906	1234.6	6.439	2.298
300	8.939	1251.1	6.494	2.324
320	9.261	1433.2	7.082	2.603
340	9.532	1621.2	7.651	2.883
360	9.782	1814.4	8.204	3.164
380	10.000	2012.3	8.738	3.443
400	10.190	2214.2	9.256	3.721
420	10.359	2419.7	9.758	3.996
440	10.510	2628.4	10.243	4.269
460	10.645	2840.0	10.713	4.539
480	10.768	3054.2	11.169	4.806
500	10.880	3270.6	11.611	5.070
550	11.122	3820.9	12.660	5.712
600	11.324	4382.2	13.636	6.332
650	11.495	4952.8	14.549	6.930
700	11.643	5531.3	15,407	7.505
750	11.774	6116.8	16.215	8.059
800	11.891	6708.5	16.978	8.593
850	11.996	7305.7	17.702	9.108
900	12.090	7907.8	18.391	9.604
950	12.176	8514.6	19.047	10.084
1000	12.255	9125.4	19.673	10.548
1050	12.326	9739.9	20.273	10.997
1100	12.391	10358	20.848	11.432
1150	12.451	10979	21.400	11.853
1200	12.505	11603	21.931	12.262

TABLE 5. *Thermodynamic properties of beryllium oxide*

T	C_p°	$H_T^\circ - H_{298.15°K}^\circ$	$S_T^\circ - S_{298.15°K}^\circ$	$-\left(\frac{F_T^\circ - H_{298.15°K}^\circ}{T}\right) - S_{298.15°K}^\circ$
°K	*cal/mole-deg*	*cal/mole*	*cal/mole-deg*	*cal/mole-deg*
298.15	6.102	0	0	0
300	6.146	11.3	0.038	0.000
320	6.597	138.8	.449	.015
340	7.012	275.0	.862	.053
360	7.393	419.1	1.273	.109
380	7.746	570.5	1.683	.181
400	8.078	728.8	2.089	.267
420	8.375	893.4	2.490	.363
440	8.640	1063.6	2.886	.469
460	8.882	1238.8	3.275	.582
480	9.104	1418.7	3.658	.702
500	9.308	1602.9	4.034	.828
550	9.752	2079.7	4.943	1.161
600	10.120	2576.8	5.807	1.513
650	10.432	3090.8	6.630	1.875
700	10.700	3619.2	7.413	2.243
750	10.934	4160.2	8.160	2.613
800	11.142	4712.2	8.872	2.982
850	11.329	5274.0	9.553	3.348
900	11.499	5844.8	10.206	3.711
950	11.654	6423.7	10.831	4.070
1000	11.799	7010.1	11.433	4.423
1050	11.934	7603.4	12.012	4.771
1100	12.061	8203.3	12.570	5.112
1150	12.181	8809.4	13.109	5.449
1200	12.296	9421.4	13.630	5.779

5. Discussion

The statements made in an earlier paper [1] concerning the usual precision of enthalpy measurements made with the Bunsen ice calorimeter apply again in the present paper. The deviation of eq (1) from the mean observed enthalpies of MgO averages 0.04 percent or 1.9 cal/mole. The corresponding numbers for eq (2) and BeO sample 1 are 0.02 percent or 0.7 cal/mole. The maximum devia-

tion of eq (1) from the mean observed enthalpies is 0.09 percent, while that of eq (2) is 0.06 percent.

Beryllium oxide is at present difficult to obtain in the form of particles large enough to be sure that the total surface area is too small to affect the heat capacity appreciably. For this reason two samples of widely different surface-to-volume ratios were measured in this investigation in an effort to test this possible complication, which has been discussed by one of the authors in a recent publication [7]. Columns 2 and 3 of table 3 show that sample 2 consistently exhibited slightly higher relative-enthalpy values at 323 °K and 373 °K than did sample 1, though there is no consistent difference in sign at the higher temperatures. In contrast to sample 1, sample 2 had a surface-to-volume ratio 15 to 20 times as large, and also may have retained a very small amount of water (see sec. 2). Both factors would tend to increase the measured heat capacity somewhat, and may have contributed to the differences between the two samples noted up to 373 °K. However, since these differences do not exceed 1 percent, it appears unlikely that the relatively small surface area of sample 1 could in this temperature range have contributed more than a few hundredths of 1 percent to its heat capacity. All the smoothed results for beryllium oxide in this paper are based on sample 1.

Figure 1 affords a comparison of the present measurements on MgO with previously reported values [8, 9, 10] in the form of percentage deviation of individual unsmoothed measurements of $(H^\circ_T - H^\circ_{273.15\ °K})$ from eq (1). The deviations of other workers' values from the measurements reported in this paper are in general many times the estimated uncertainties of the authors' values, a fact which is in line with the belief that the latter are the most accurate available for this substance.

In figure 2 the present BeO measurements are compared with those of earlier workers [6, 11, 12, 13]. Of particular importance is the recent work by Rodigina and Gomel'skii on a sintered specimen, which shows a reproducibility comparable with that of the present measurements and agreement with eq (2) which is generally better than 0.5 percent of the enthalpy relative to 273.15 °K.

Magnesium oxide is probably the more favorable of the two materials as a high-temperature heat-capacity standard, since it is available in large crystals of reasonably high purity. The agreement between BeO samples 1 and 2 at and above 473 °K and the unusually good agreement with one other worker [12] on a specimen similar to sample 1 support the serious consideration of sintered beryllium oxide as a heat-capacity standard, subject to the conditions that the samples used do not have too small a particle size and are not contaminated by adsorbed water.

A phase change in BeO has reportedly been observed at approximately 2,220 °K [14]. Such a transition would adversely affect the use of beryllium oxide as a heat-capacity standard at higher temperatures. Measurements on this material up to 1,800 °K or higher are planned at the National Bureau of Standards to extend the temperature range of available accurate values. At the present time the heat-capacity discrepancy between reference [13] and the present work is greater than 2.5 percent at 1,200 °K.

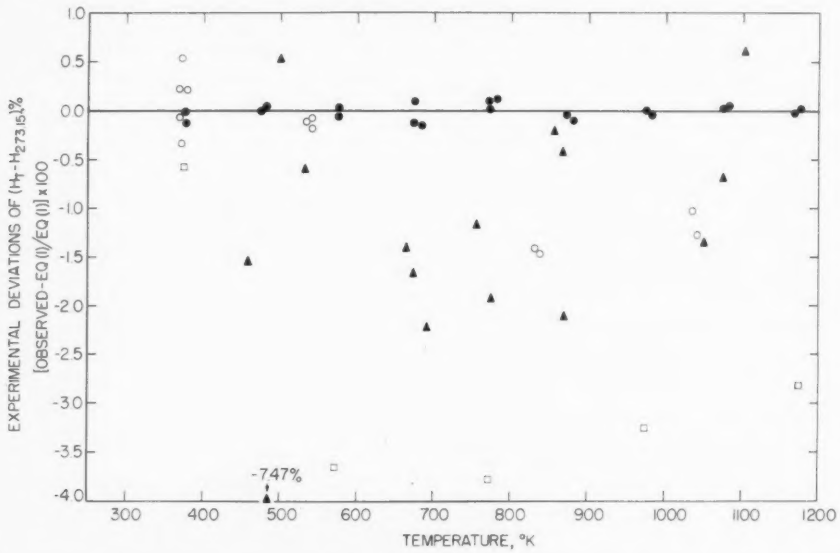

FIGURE 1. *Comparison of the enthalpy, relative to 273 °K, of magnesium oxide obtained from eq (1) with individual values obtained in various investigations.*

(Some of the observed points have been displaced horizontally by small amounts in order to avoid the confusion of overlapping.) ——, NBS smoothed, eq (1); ●, NBS observed (present paper); ▲, Arthur [8]; o, Magnus [9]; □, Wilkes [10].

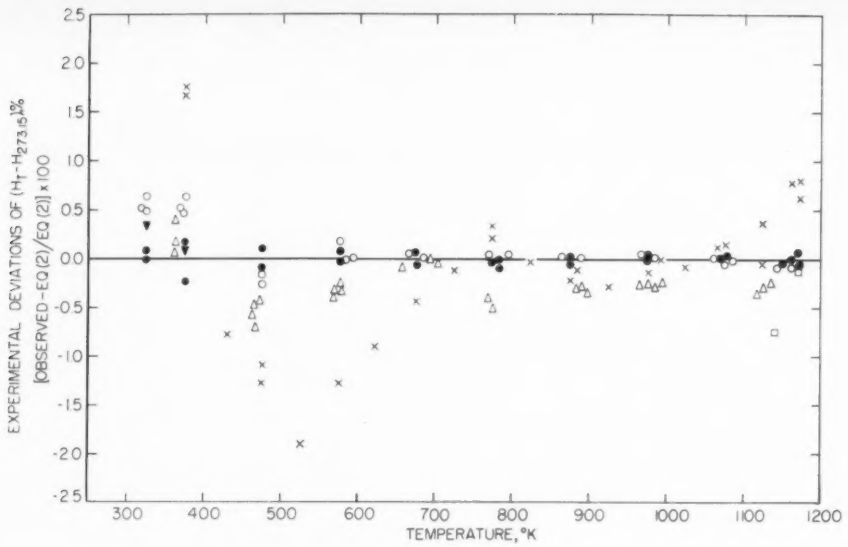

FIGURE 2. *Comparison of the enthalpy, relative to 273 °K, of beryllium oxide obtained from eq (2) with individual values observed in various investigations.*

(Some of the observed points have been displaced horizontally by small amounts in order to avoid the confusion of overlapping.) ——, NBS smoothed, eq (2); ●, NBS observed (present paper), sample 1 ("high density"); o, NBS observed (present paper), sample 2 ("low density"); x, Magnus and Danz [11]; △, Rodigina and Gomel'skii [12]; □, Kandyba et al. [13]; ▼, Furukawa and Reilly [6].

The authors acknowledge help from certain members of the Bureau: F. Knudsen prepared the samples of beryllium oxide, and B. F. Scribner and his associates analyzed all the samples spectrochemically.

6. References

[1] A. C. Victor and T. B. Douglas, J. Research NBS (Phys. and Chem.) No. 2, **65A,** 105 (1961).
[2] F. D. Rossini, D. D. Wagman, W. H. Evans, S. Levine, and I. Jaffe, Selected values of chemical thermodynamic properties, NBS Circ. 500 (U.S. Government Printing Office, Washington, D.C., 1952).
[3] G. T. Furukawa, T. B. Douglas, R. E. McCoskey, and D. C. Ginnings, J. Research NBS **57,** 67 (1956) RP2694.
[4] H. F. Stimson, Am. J. Phys. **23,** 614 (1955).
[5] T. H. K. Barron, W. T. Berg, and J. A. Morrison, Proc. Roy. Soc. (London) **250A,** 70 (1959).
[6] G. T. Furukawa and M. L. Reilly, private communication.
[7] A. C. Victor, J. Chem. Phys. **36,** 2812 (1962).
[8] J. S. Arthur, J. Appl. Phys. **21,** 732 (1950).
[9] A. Magnus, Phys. Ztschr. **14,** 5 (1914).
[10] G. B. Wilkes, J. Am. Ceram. Soc. **15,** 72 (1932).
[11] A. Magnus and H. Danz, Ann. Physik, [4] **81,** 407 (1926).
[12] E. N. Rodigina and K. Z. Gomel'skii, Zhur. Fiz. Khim. **35,** 1828 (1961).
[13] V. V. Kandyba, P. B. Kantor, R. M. Krasovitskaya, and E. N. Fomichev, Doklady Akad. Nauk S.S.S.R. **131,** 566 (1960).
[14] S. B. Austerman, High-temperature phase transition in beryllium oxide, paper presented before the American Physical Society, New York, N.Y. (Jan. 24, 1962).

(Paper 67A4–221)

JOURNAL OF RESEARCH of the National Bureau of Standards—A. Physics and Chemistry
Vol. 67A, No. 4, July–August 1963

Heat Exchange in Adiabatic Calorimeters

E. D. West

(April 3, 1963)

Heat flow in adiabatic calorimeters of various shapes and materials is described in terms of linear partial differential equations. From these equations it is deduced that in the intermittent heating method the heat exchange between the calorimeter and the adiabatic shield due to transients at the beginning and end of the heating period can be made to cancel. The remaining heat exchange is the same for intermittent or continuous heating methods and can be treated as the sum of effects due to gradients set up by heat flow (1) from the shield to the environment and (2) from the shield and calorimeter heaters to raise the temperatures of the shield and calorimeter, respectively. The first effect can be accounted for by measurements during fore and after periods in intermittent calorimetry and by varying the heating rate in continuous calorimetry. Under certain conditions the second effect can be accounted for by measurements with the empty calorimeter. Variation in heating rate fails as a test for the magnitude of the second effect.

1. Introduction

Standard materials for heat capacity measurements have now been used widely enough to show that different observers obtain data with systematic differences not ascribable to variations in samples. Well-established techniques for measuring electrical energy and temperature differences are accurate enough that the most likely source of the differences is in accounting for heat exchange between the calorimeter and its surroundings. A review of the ideas on which such calorimetry is commonly based therefore seems to be in order.

Heat flow in calorimeters is commonly analyzed using Newton's Cooling Law. The calorimeter and its surroundings are treated as isothermal bodies and the heat transfer between them as proportional to the differences in their temperatures. The constant of proportionality is the integral for all the radiation and conduction processes, which can properly be lumped together only if the same temperature difference applies to all of them. To satisfy this model, stress is laid on making the surfaces isothermal. The model is usually abandoned at this point to consider the temperature gradients. The attempt is often made to locate temperature sensing elements to average the temperature over the surface. The consideration of gradients also requires consideration of the variation in heat transfer coefficients over the surface, and some calorimeters use separate temperature measurements to account for surface radiation and for lead conduction. The accuracy of calorimeters designed using this model hinges on the intuition and experience of the designer in going beyond the model to allow for the effect of temperature gradients. A good example of how this method can lead to wrong conclusions is the use of the heating rate to demonstrate that the surface is adequately isothermal.

In principle, an adiabatic calorimeter is one in which heat is confined to the calorimeter usually by surrounding it with an adiabatic shield maintained at the temperature of the calorimeter. In practice, temperature gradients in the calorimeter and shield cause a net heat exchange during the experiment. The heat exchange during an experiment is commonly accounted for by the use of measurements at other times. In the intermittent heating method, for example, heat corrections to the energy input during the experiment depend on drift rates and heat transfer coefficients measured with no energy input and on the heat capacity of the empty calorimeter measured at a more remote time. The assumptions and approximations implied in such corrections and the experimental conditions necessary to insure their validity need to be reviewed for possible sources of the discrepancies in heat capacity data.

Variation of the heating rate is a time-honored test for adiabatic calorimeters [1–11, 22].[1] It recognizes that there are small temperature differences on the surface of the calorimeter and adiabatic shield during the heating period. A lower heating rate will decrease the temperature differences and the corresponding rate of heat exchange between the calorimeter and shield. If the same heat capacity is observed at very different heating rates, it is sometimes argued that the difference in heat exchange and hence the heat exchange itself must be negligible. This line of reasoning has been challenged [12] on the ground that it fails to consider the time required for an experiment. Since heat capacity is a function of temperature, comparisons must be made over the same temperature interval. Except for transient effects, the surface temperature differences and the

[1] Figures in brackets indicate the literature references at the end of this paper.

corresponding rate of heat exchange are approximately proportional to the heating rate, but the time required to heat through a given temperature interval is inversely proportional to the heating rate. Since the net heat exchange is the product of the rate of heat exchange and the time, it is practically the same for all heating rates. This unknown net heat exchange must be accounted for by making it the same in the experiments with the full and the empty calorimeter.

Starting with the partial differential equations describing the heat flow in a calorimetric apparatus, the mathematical analysis in the present paper will show that the transient effects, which weaken the qualitative argument [12], can be made to cancel for each experiment. The heating rate test for isothermal surfaces must then fail and the difference in the unknown heat exchange between measurements with the full and the empty calorimeter must be admitted as a cause of systematic deviations.

2. Statement of the Problem

2.1. Qualitative Description

The problem is to describe mathematically the heat flow in a calorimetric apparatus and to see what consequences can be deduced. The experiment will first be described qualitatively. A calorimeter is surrounded by an imperfect adiabatic shield. The temperature difference between the two is sensed at one or more points, usually with a thermopile. The temperature of the shield as observed at these points is controlled to be equal to that of the calorimeter. The treatment includes any supports, leads, and gas between the physical shield and the environment, which is taken to be at constant temperature.

The temperature of the calorimeter is observed during the initial equilibrium period until its rate of change becomes very small and constant within the limits of observation. The initial temperature of the experiment is then taken. Constant power is then supplied to the calorimeter for a measured time. The power is turned off and, after the rate of change of the calorimeter temperature again becomes constant, the final temperature is taken.

Usually the rate of change or "drift" of the calorimeter temperature in the equilibration periods is not zero, indicating that the temperature of the adiabatic shield is not perfectly matched to that of the calorimeter even when the controlled temperature difference is zero. The heat exchange indicated by this temperature change will be referred to subsequently as the "zero heat leak."

Whenever heat is supplied to the calorimeter or the adiabatic shield, it must flow from the heater to a surface where it is lost to other surfaces or to some volume where it raises the temperature. This heat sets up gradients throughout the body which have components along the surface. Since the temperature of the calorimeter and shield can be observed at only a relatively few points, it follows that the observed temperature differs from the average over the surface. Consequently, there is heat exchange between the calorimeter and the shield whenever power is supplied to *either* of them, even though the controlled temperature difference is zero. It is possible and often practicable to distribute heaters and thermocouples to make this heat exchange small. It does not appear possible to satisfy exactly the requirements that a shield heater, for example, should be distributed so as to generate at each point at equilibrium the heat lost from that point to the environment and that the same distribution should supply both heat lost and heat required to raise the shield temperature during the heating period without gradients along the surface. Such an exact distribution will be even more difficult if it must take into account the variation in heat capacity of the components when the apparatus is used over a considerable temperature range.

It is also apparent from working with these calorimeters that some time is required after turning on the heater before all parts begin to heat at the same rate and that some time is required after turning off the calorimeter for the temperature to come to equilibrium. The mathematical treatment must take these transients into account.

2.2. The Differential Equations

The method of treating the problem is (1) to set up the differential equations and boundary conditions for heat flow in the calorimeter and the adiabatic shield, making a minimum number of assumptions; (2) to use the principle of superposition, which states that the sum of solutions to a linear differential equation is also a solution, in order to show the causes of the temperature gradients; (3) to indicate the nature of the solutions and show from them how the heat loss depends on the heating rate and other factors.

Throughout the discussion it should be kept in mind that we are analyzing the apparatus for a heat leak correction which is a small part of the total heat added in an experiment. We can therefore use approximations which affect the heat leak by only a small percentage of itself. To obtain linear equations, the approximations are made that the heat capacities per unit volume, the heat transfer coefficients, and the thermal conductivities of all materials in the calorimetric apparatus are independent of temperature over the small temperature interval of the experiment. These approximations are implied in most calorimetry, in which the temperature rise during the reaction or heating period is corrected for heat leak on the basis of observations in fore and after periods. During phase transitions in the sample, where two phases are present in changing amounts, this approximation may not apply. A proposal for overcoming this difficulty is discussed in sec. 6.2. Heat transfer by convection is assumed negligible.

The differential equation for heat flow by conduction and its solution are treated by several authors [13, 14, 15]. The method followed here of substituting a sum of solutions is discussed in some detail by Boley and Weiner [14].

Temperature and Heating Rate Symbols:

T=the temperature distribution as a function of time and position. The scale is arbitrary, but it can be thought of as the Kelvin temperature.

T_0=the observed initial temperature of the thermometer in the calorimeter at the time the heater power is turned on.

T_f=final observed calorimeter temperature, corrected for zero heat leak.

T_{0e}=constant temperature of the environment, excluding supports, leads, and gas which are at different temperatures due to conduction from shield.

L=the temperature distribution due to heat exchange between the shield and its environment, which causes the "zero heat leak," sec. 2.1.

θ=the temperature distribution due to the quasi-steady state set up by constant power in the calorimeter heater.

τ and τ^*=the initial and final transient temperature distributions.

β_L=rate of change of temperature due to heat leak.

β_θ=rate of change of temperature due to constant power in the calorimeter heater.

Subscripts:

i, j, k differentiate the various regions of the calorimeter and shield under discussion.

w designates the heater wire regions in which heat is generated.

c, s, e refer to calorimeter, shield and environment, respectively.

con refers to the particular position at which a control temperature is taken.

Other Symbols:

P=power. P_c=constant for a given experiment; P_s contains transient terms.

Q=heat.

C=heat capacity per unit *volume*.

h=radiation heat transfer coefficient (in dimensions power÷ [area]^2).

K=thermal conductivity.

t=time. (The heater is turned on at $t=0$, off at $t=t_f$.)

A=area of a region of the calorimeter or shield.

A_s=sum of areas of shield regions which exchange heat with calorimeter and environment.

V=volume.

σ=Stefan-Boltzmann radiation constant.

α=absorptivity.

ϵ=emissivity.

δ_{iw}=1 when $i=w$, 0 when $i\neq w$. (Kronecker delta. Makes power term zero except in heater wire.)

$$\nabla^2 T=\frac{\partial^2 T}{\partial x^2}+\frac{\partial^2 T}{\partial y^2}+\frac{\partial^2 T}{\partial z^2}$$

$\frac{\partial}{\partial n_i}$=the partial derivative in the direction outward from and perpendicular to the surface of the ith region.

Because calorimeters are made up of a variety of materials, the analysis must treat them as composed of a number of homogeneous regions. The discussion will therefore treat a general ith region of the calorimeter or shield which is in thermal contact with one or more jth regions and may radiate to one or more kth regions if the jth region is transparent.

The experiment to be described is one with a constant-temperature environment (e.g., an ice bath) and with a zero heat leak which is observed to be the same before and after the heating period. This condition is likely to be observed when the heat leak is small and the fractional change in the temperature difference between the shield and the environment is small. The differential equations and the various boundary and initial conditions are shown in table 1. The overall temperature distribution T satisfies the equations in column II. The equation for heat conduction, II–A, is discussed by Carslaw and Jaeger [13] and by Boley and Weiner [14]. The equation in this form uses the approximation that the thermal conductivity is constant. The terms in P_c and P_s in equations II–A allow for power generation in the regions of the heater wires and are zero outside those regions. In the calorimeter heater, P_c is independent of time during the heating period and zero otherwise. It is assumed that the power is developed uniformly over the volume of the wire so that the power per unit volume is just the total power divided by the total volume of the wire. The shield power P_s is not constant because it is affected by the requirement that the controlled temperature difference between the shield and calorimeter be zero. The expression for the shield power is therefore derived from the requirement that energy is conserved and consists of the power used to raise the shield temperature plus the net power lost to the calorimeter and to the environment.

The general boundary condition, equation II–B, includes conduction from the ith region to the jth region. If the jth region is transparent, as in a space filled with a gas, the equation allows for radiation through that region to one or more kth regions. The radiation term is integrated over all kth regions, including the ith region. If the ith region is surrounded by opaque jth regions, the radiation heat transfer coefficient h_{ik} is zero; if the jth region is evacuated, the thermal conductivity K_j is zero and the continuity condition $T_i=T_j$ is not required. This equation applies to all regions of the calorimeter and shield and governs the heat transfer between them (cf., sec. 3.2). The equation takes into account the geometric variation of the temperature, the thermal conductivity and the radiation coefficients; i.e., Newton's law of cooling is not assumed to govern heat transfer between the calorimeter and the adiabatic shield. The radiation

TABLE 1. *Equations for heat flow in an adiabatic calorimeter*

I	II Temperature distribution (Sum of cols. III, IV, and V)	III Temperature distribution due to zero heat leak	IV Temperature distribution due to constant heating	V Transient temperature distribution
A. Heat conduction equations.	(1) $\frac{K_{ir}}{C_{ir}}\nabla^2 T_{ir}=\frac{\partial T_{ir}}{\partial t}-\frac{\delta_{ir}P_{ir}}{C_{ir}V_{ir}}$	$\frac{K_{ir}}{C_{ir}}\nabla^2 L_{ir}=\beta_L$	$\frac{K_{ir}}{C_{ir}}\nabla^2\theta_{ir}=\beta_\theta-\frac{\delta_{ir}P_{ir}}{C_{ir}V_{ir}}$	$\frac{K_{ir}}{C_{ir}}\nabla^2 \tau_{ir}=\frac{\partial \tau_{ir}}{\partial t}$
	(2) $\frac{K_{is}}{C_{is}}\nabla^2 T_{is}=\frac{\partial T_{is}}{\partial t}-\frac{\delta_{is}P_{is}}{C_{is}V_{is}}$	$\frac{K_{is}}{C_{is}}\nabla^2 L_{is}=\beta_L-\frac{\delta_{is}P_L}{C_{is}V_{is}}$	$\frac{K_{is}}{C_{is}}\nabla^2\theta_{is}=\beta_\theta-\frac{\delta_{is}P_\theta}{C_{is}V_{is}}$	$\frac{K_{is}}{C_{is}}\nabla^2 \tau_{is}=\frac{\partial(\tau_{is}+\tau_{conv})}{\partial t}-\frac{\delta_{is}P_\tau}{C_{is}V_{is}}$
	$P_\tau=\int_{V_r}C_{ir}\frac{\partial T_{ir}}{\partial t}dV+\int_{A_r}K_{ir}\frac{\partial T_{ir}}{\partial n_{ir}}dA$	$P_L=\beta_L\sum_i C_{is}V_{is}+\int_{A_s}K_{is}\frac{\partial L_{is}}{\partial n_{is}}dA$	$P_\theta=\beta_\theta\sum_i C_{is}V_{is}+\int_{A_s}K_{is}\frac{\partial\theta_{is}}{\partial n_{is}}dA$	$P_\tau=\int_{V_s}C_{is}\frac{\partial(\tau_{is}+\tau_{conv})}{\partial t}dV+\int_{A_s}K_{is}\frac{\partial\tau_{is}}{\partial n_{is}}dA$
B. General boundary conditions.	$K_i\frac{\partial T_i}{\partial n_i}=K_i\frac{\partial T_j}{\partial n_i}+\int_A h_{ik}(T_k-T_i)dA_k$	$K_i\frac{\partial L_i}{\partial n_i}=K_i\frac{\partial L_j}{\partial n_i}+\int_A h_{ik}(L_k-L_i)dA_k$	$K_i\frac{\partial\theta_i}{\partial n_i}=K_i\frac{\partial\theta_j}{\partial n_i}+\int_A h_{ik}(\theta_k-\theta_i)dA_k$	$K_i\frac{\partial\tau_i}{\partial n_i}=K_i\frac{\partial\tau_j}{\partial n_i}+\int_A h_{ik}(\tau_k-\tau_i)dA_k$
C. Temperature distribution, $t=0$.	$T_i=T_j$ $T_i=L_i+T_0$	$L_i=L_j$ (see note) L_i independent of time	$\theta_i=\theta_j$ (see note) $\theta_i=0, t<0$ and $t>t_f$ θ_i are functions of space variables only $0<t<t_f$	$\tau_i=\tau_j$ (see note) $\tau_{ir}=-\theta_{ir}$ $\tau_{is}=-\theta_{is}-\theta_{conv}$ } ON transient
D. Temperature distribution, $t=t_f$	$T_i=L_i+T_0+\theta_i+\beta_L t+\beta_\theta(t-t_f)+\tau_\infty$			$\tau_{ir}^*=\theta_{ir}$ $\tau_{is}^*=\theta_{is}+\theta_{conv}$ } OFF transient

NOTE: On boundaries between the calorimeter and the shield and between the shield and the environment the control temperature does not cancel in equations III–B, IV–B, and V–B and must be added to the shield temperature; e.g., $h_{sk}(\theta_{sk}+\theta_{conv}-\theta_e)$ and $L_{ir}=L_{is}+L_{conv}$. See for example eq (3). For heat leak by radiation from the shield to the environment, T_0 and T_{0e} do not cancel. See eq (5).

heat transfer coefficient h_{ik} is derived from the Stefan-Boltzmann equation [2] [15, Vol. I].

Where leads, supports, or gas are in thermal contact with the constant-temperature environment, the boundary condition at the surface of contact is simply

$$T_{ts}=T_{0e}. \tag{1}$$

The initial condition at $t=0$, II–C, allows for the temperature distributions due to the zero heat leak in the various regions of the calorimeter and shield just before the power is turned on in the calorimeter heater.

To facilitate the analysis, the experiment is considered in two parts—the heating period and the final equilibration period. A second "initial" condition, II–D, is therefore included for the time t_f when the calorimeter heater is turned off. This temperature distribution must include (1) the θ_i which are still present at time t_f due to power required to raise the temperature of the calorimeter and shield; (2) the general increase in temperature due to rates of change of the calorimeter temperature β_L and β_θ due respectively to heat exchange with the environment and to constant power during the heating period; (3) the net contribution of the initial transient which, at t_f, is merely a small constant τ_∞ added to the temperature at each point in the calorimeter and shield.

2.3. Temperature Distribution Due to Heat Leak, Constant Power, and a Transient

In order to assess the effects of different surface temperature distribution during the heating and equilibration periods, it is desirable to consider the overall temperature distribution T_i as a sum due partly to heat exchange with the environment and partly to power flowing in the calorimeter and the shield to raise their temperatures. With the approximation that the thermal conductivity, the heat capacity per unit volume and the heat transfer coefficients are independent of temperature over the small temperature rise of the experiment, the equations in column II, table 1, are linear in T and its

[2] The application of the radiation law to this particular case apparently has not been set down explicitly. We assume that absorptivities, emissivities, and the mean temperature do not change significantly during the experiment and that the regions in the apparatus where radiation is important are completely enclosed by surfaces of the calorimeter, the adiabatic shield, or the environment. A fraction f_{12} (proportional to dA_2) of the radiation emitted by a differential surface dA_1 strikes dA_2, some by a direct path and some by reflection from other surfaces enclosing the space. That which goes by an indirect path is reflected by the other surfaces dependent on their absorptivities but not on their temperatures. Similarly, a fraction f_{21} emitted by dA_2 strikes dA_1 and the net heat transfer by radiation P_{12} from dA_1 to dA_2 is given by the equation

$$P_{12}=\alpha_{21}\epsilon_1 f_{12}\sigma T_1^4\,dA_1-\alpha_{12}\epsilon_2 f_{21}\sigma T_2^4\,dA_2,$$

where ϵ is the emissivity and α_{21} is the absorptivity of surface dA_2 for radiation from surface dA_1, allowing for the fact that most of this radiation is reflected one or more times before striking dA_2 and arrives at various angles. The equation must hold at all temperatures, and, when $T_1=T_2$, P_{12} must be equal to zero from the second law of thermodynamics. The coefficients of the temperature must therefore be equal and the net radiation may be written

$$P_{12}=\sigma\alpha_{12}\epsilon_2 f_{21}(T_1^4-T_2^4)dA_2.$$

Using the approximation for small T_1-T_2 [14], one obtains

$$P_{12}=\sigma\alpha_{12}\epsilon_2 f_{12}T_m^3(T_1-T_2)dA_2\equiv h_{12}(T_1-T_2)dA_2.$$

This equation has the same form as Newton's law of cooling, but it applies to differential areas and radiation only.

derivatives. The T_i may therefore be written as a sum of solutions [14, pp. 201 and 231]. For the calorimeter during the heating period

$$T_{ic}=L_{ic}+\beta_L t+\theta_{ic}+\beta_\theta t+\tau_{ic}+T_0. \quad (2)$$

The temperature where the control thermocouple is attached to the shield is controlled to equal the temperature T_{conc} where the thermocouple is attached to the calorimeter. The temperatures in the shield are measured relative to this controlled temperature so that T_{is} is given for the heating period by the sum

$$T_{is}=L_{is}+L_{conc}+\beta_L t+\theta_{is}+\theta_{conc}+\beta_\theta t+\tau_{is}+\tau_{conc}+T_0. \quad (3)$$

The boundary and initial conditions III–B, IV–B, V–B, table 1 are not quite complete as shown. Where they involve T_i-T_k and derivatives with respect to the normal, the terms in t, T_0 and control temperatures do not appear when both the ith and kth regions are in the calorimeter, the shield, or the environment. But, for heat transfer between the calorimeter and shield or between the shield and environment, these terms must be retained, as in eqs (5) and (6). (See note, table 1.)

When the operations indicated in column II are performed on these sums the various terms can be separated as in columns III, IV, and V. The three sets of equations can be associated respectively with the observed zero heat leak which exists throughout the experiment, constant power in the calorimeter during the heating period, and transients allowing for the transitions between equilibration and heating periods.

The term θ_i is the temperature distribution for the quasi-steady state [14, p. 201] due to the constant power input in the calorimeter during the heating period. It satisfies the equations in column IV, table 1, and is a function of geometric variables only. Where the boundary conditions involve the temperature of the environment, θ_k is zero for radiation and θ_j is zero for conduction, since the environment temperature does not contain these terms (cf., eqs (1) and (6)). It can be verified by differentiation and substitution in the equations that, if θ_{ic} is the temperature distribution and β_θ the heating rate for a power P_c, $m\theta_{ic}$ is the temperature distribution and $m\beta_\theta$ the heating rate for mP_c; i.e., the quasi-steady state temperature gradient and the heating rate are directly proportional to the calorimeter power.

To allow for the transients in going from the equilibration conditions to heating conditions and the reverse, the transient terms τ_i and τ_i^* are included. These terms make the sums in eqs (2) and (3) satisfy the initial conditions II–C and II–D when the calorimeter heater power is turned on and off. Where the boundary conditions involve the temperature of the environment, τ_k is zero for radiation and τ_j is zero for conduction since the environment temperature does not contain these terms (cf., eqs (1) and (6)). The two transients, one, τ, when the power is turned on and one, τ^*, when it is turned off, satisfy identical sets of equations, except for their initial conditions, V–C and V–D, which are equal but of opposite sign. Considering the final transient τ^* a function of $(t-t_f)$, it is apparent from substituting in the equations of column V that, for equal magnitudes a of $(t-t_f)$ and t,

$$-\tau^*(a)=\tau(a). \quad (4)$$

The term β_L is the slow change of the calorimeter temperature due to the zero heat leak. It is equal to the net power transferred between the calorimeter and the shield during the equilibration periods divided by the heat capacity of the calorimeter. It may be either positive or negative depending largely on the relative locations of the heater and control thermocouple on the adiabatic shield. The term β_θ is the rate of rise of the calorimeter temperature due to constant power in the calorimeter heater. It is equal to the sum of this power and the small power flowing from the shield due to surface temperature distributions θ set up during the heating period divided by the heat capacity of the calorimeter.

The term L_i is the "zero heat leak" temperature distribution, due to gradients produced in the shield by heat transfer to the environment. As a consequence of eq (1), eq III–B, table 1 takes a slightly different form when the regions j or k are the environment. For radiation to the environment, the relation is

$$K_{is}\frac{\partial L_{is}}{\partial n_{is}}=K_{js}\frac{\partial L_{js}}{\partial n_{is}}+\int_{A_k}h_{ik}(L_{ks}-L_{is})dA+\int_{A_c}h_{ic}[T_{0c}-L_{is}-L_{conc}-T_0-(\beta_L+\beta_\theta)t]dA \quad (5)$$

where integration over the k regions does not include the environment. For conduction, where leads, supports, and gas are in thermal contact with the environment,[3] the boundary conditions reduce to the constant temperature on the surface:

$$L_{is}+L_{conc}+\beta_\theta t+\beta_L t+T_0=T_{0c}. \quad (6)$$

In eqs (5) and (6), the term $\beta_\theta t$, which has elsewhere been associated with constant power input to the calorimeter, is included because it increases the temperature difference for radiation between the shield and the environment and the value of L_{is} at conduction boundaries. These quantities cause the heat flow from the shield, which sets up the zero heat leak temperature distribution.

[3] The assignment of leads, supports, and gas to the shield is arbitrary, but convenient. Their inclusion with the environment would require discussion of environment temperature distributions as well as an environment surface at constant temperature. In a sense, we are evading the question of where the boundaries of the calorimeter and shield are located. For example, a lead wire between the shield and the calorimeter will usually conduct heat away from both of them during the heating period to some unknown part of the wire where the flow from both sides becomes zero. If the zero heat leak is negligible, heat flows out from the calorimeter to this surface, and the heat capacity out to this point is logically part of the calorimeter. If radiation could be neglected, the boundary might be taken as the mathematical surface where $\partial\theta_{ic}/\partial n_{ic}=0$. Then the unknown heat loss is zero and the problem in calibration is to measure the heat capacity within this "surface". The accuracy of the calorimetry then depends on having the same "surface" in measurements with the calorimeter full and empty. The problem is discussed by Dickenson for a different type of calorimeter [23, sec. III-7].

To satisfy the observed condition that the zero heat leak is the same in the initial and final equilibration periods, the effect of the increase in temperature on $\partial L_{is}/\partial n_{is}$ must be negligible. The effect of $(\beta_L+\beta_\theta)t$ must therefore be undetectably small and these terms are neglected in column III, table 1. To this approximation, the L_i are independent of time.

3. Interpretations of the Equations

3.1. The Thermal Transients

Good practice in adiabatic calorimetry is to make measurements with the calorimeter full and empty (or with large and small samples) reproducing the gradients on the surfaces of the calorimeter and shield in order to allow for the unknown heat transfer during the heating period. But placing a sample in the calorimeter alters the time required for heat to reach the surface, so that the transients for the full calorimeter differ from those for the empty. This effect is more easily visualized by reference to an example. Figure 1 is an idealized cross section through a calorimeter consisting of coaxial cylinders. For simplicity, it is assumed that heat transfer is by solid conduction only. Heat then flows from the heater along the vanes to the container wall, through the contact region to the calorimeter surface. If the temperature for control is measured at one point on the surface of the calorimeter, then, during the heating period, another point on the surface will be at a somewhat different temperature. During the equilibration period, the temperature difference between these two points will be very small. During the transient period, the temperature difference goes from one condition to the other, but the *time* required must depend on the thermal conductivity and heat capacity of the sample. During the initial transient, the curve for the empty calorimeter might resemble the empty-slow curve (fig. 2), for some heating rate β_θ. If the heating rate is $2\beta_\theta$, the time and geometric dependence are unchanged and the amplitude is doubled, as in the empty-fast curve.

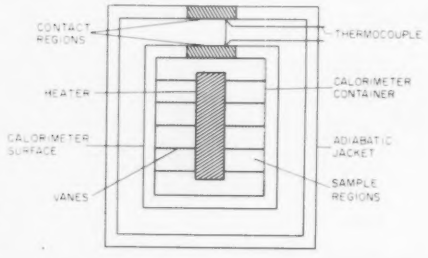

FIGURE 1. *Idealized cross section of a calorimeter.*

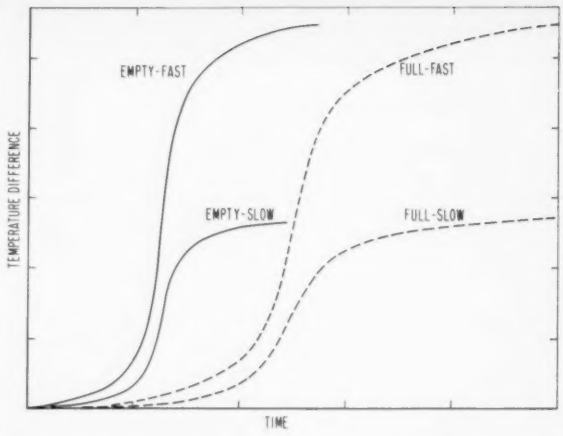

FIGURE 2. *Schematic of temperature difference between two points on the surface of the calorimeter as a function of time for different heating rates and loading conditions.*

If the calorimeter is now filled with a material of high heat capacity and low thermal conductivity, the time for heat to reach the surface will be greatly increased. With the assumption that all heat reaches the surfaces by way of the contact regions, the temperature difference between two points will ultimately come to the same values for the same heating rate. For a heating rate of β_θ in the full calorimeter, the full-slow curve might be obtained, and, for $2\beta_\theta$, the full-fast curve. Evidently the curves for the empty calorimeter do not compensate for the curves for the full calorimeter. That no error results from this difference is due to compensation of the final transient for the initial transient in each experiment. This compensation will be shown in the next section.

From eq V–B an explicit equation for τ_{is}, like that for L_{is} (eq (5)), can be written to show that the transients depend on conduction paths to the constant-temperature environment. If the calorimeter is to reach equilibrium quickly, these conduction paths must be short or of low heat capacity especially for poor thermal conductors.

3.2. The Unknown Heat Loss During the Heating Period

It is now possible to draw conclusions regarding the total heat exchange between the calorimeter and the shield during an experiment. Using the definition of thermal conductivity and integrating over the entire calorimeter surface and the time of the experiment, including the final equilibration period, the total heat loss Q from the calorimeter is

$$Q=\int_0^{t_r}\int_{A_c} K_{ic}\frac{\partial(\theta_{ic}+L_{ic}+\tau_{ic})}{\partial n_{ic}}\,dA\,dt + \int_{t_f}^{t_r}\int_{A_c} K_{ic}\frac{\partial \tau^*_{ic}}{\partial n_{ic}}\,dA\,dt. \quad (7)$$

Observations of the zero heat leak in the final equilibration period are continued until the time t_r at which the transients are no longer observable.

The experiment is arranged so that τ and τ^* become constant and equal to τ_∞ at a time $t_1 < t_r$. It was shown in sec. 2.3 that, for equal magnitudes a of t and $t-t_f$, $\tau(a) = -\tau^*(a)$. Their integrals up to t_1 are therefore equal and opposite and make no net contribution to Q.

The quantities remaining in eq (7) are independent of time, so that the time integration may be performed to obtain

$$Q = t_f \int_{A_c} K_{ic} \frac{\partial(\theta_{ic}+\tau_\infty)}{\partial n_{ic}} dA + t_r \int_{A_c} K_{ic} \frac{\partial L_{ic}}{\partial n_{ic}} dA. \tag{8}$$

The last integral is simply the zero heat leak multiplied by the time elapsed between the initial and the final temperature readings. This integral is evaluated from determinations of Q over a timed interval during the equilibration periods. The remaining unknown heat leak is that due to gradients set up during the heating period.

The heat exchange due to τ_∞ is included for generality, but its practical effect is negligible. It is the net effect of the initial transient on the calorimeter temperature, a small constant added to the temperature at all points in the calorimeter. Since the shield control will change the shield temperature to allow for τ_∞, the direct effect on the calorimeter is zero. The slight change of τ_∞ in the shield-to-environment temperature difference produces a much smaller effect than that due to the temperature rise during the experiment.

An estimate can be made of the maximum effect of τ_∞, assuming that all of the nearly 1 percent scatter in heat capacity data for Al_2O_3 obtained by various experimenters is caused by variation in heat exchange due to the θ_i during the heating period. This scatter corresponds to 1 percent of the temperature rise $\beta_\theta t_f$. The effect of τ_∞ is related to that of θ_i by the ratio of its "time constant" to t_f, the length of the heating period. The zero heat leak would have to be quite large for 1 percent of it to be important.

Since the first term contains t_f, the amount of heat exchange depends on the length of the heating period. It might appear to be possible to evaluate the integral by observing the apparent heat capacities as a function of t_f, corrected for the zero heat leak. The fallacy in this reasoning is easily demonstrated. The time t_f required to heat through the temperature range $T_f - T_0$ (corrected for zero heat leak) over which comparison is made is given by the equation

$$t_f = \frac{T_f - T_0}{\beta_\theta}. \tag{9}$$

Combining (8) with (9), the unknown part of the heat exchange is seen to be independent of the heating rate since increasing the power by a factor m increases β_θ, θ, and τ by the same factor. The unknown heat exchange is proportional to the temperature rise in an experiment, independent of the time of the heating period. It cannot be separated from the true heat capacity by changing the heating rate.

This conclusion contravenes the common practice of varying the heating rate to demonstrate that temperature differences on the surfaces of the calorimeter and shield are negligible, as has sometimes been asserted [7, 22]. The conclusion is borne out by measurements in this laboratory [12]. Observed heat capacities at one-half the usual heating rate agreed with the averages of the other data to 1 part in 25,000, although the temperature differences on both the calorimeter and shield surfaces were calculated and/or observed to be about one-tenth of a degree.

3.3. The Zero Heat Leak and Parasitic EMF's

The zero heat leak, which is due to temperature distributions set up by heat lost from the adiabatic shield, is present throughout the experiment. The present analysis is based on the observation that the rate of change of the calorimeter temperature is the same in the initial and final equilibration periods. It is conceivable that such an observation might be due to compensation of increased heat transfer and increased heat capacity of the calorimeter, but the experiment provides a direct check on the latter. For a small correction, as the zero heat leak should be, the ordinary variations in heat capacity with temperature can be ignored. The correction for the observed constant rate is simply the rate times the time elapsed between the initial and final temperature readings, and, for approximately constant heat capacity, the correction is equally well applied to the temperature rise or, after multiplication by the heat capacity, to the energy term.

There is nothing in the equations to indicate the sign of the zero heat leak, and, in most apparatus, heat probably flows from the calorimeter at some points and to it at others. The net effect depends on the relative locations of the shield heater and the control couple if there is no parasitic emf in the control circuit.

A constant parasitic emf in a lead of the control thermocouple can be taken into account by adding a corresponding constant temperature difference to L_{cone} (eqs (5) and (6), and III, table 1). Whatever changes the parasitic emf induces in the L_i persist throughout the experiment, and the proper correction is made based on observations during the equilibration periods.

The same reasoning applies to an intentional constant offset in the control apparatus. Accordingly, no error is introduced when the control point is deliberately shifted to make the observed temperature change during the equilibration period zero. This technique can be used to make temperature measurement easier (see sec. 6.1). One should not be deceived that gradients on the calorimeter are eliminated by this technique; it is merely a shift of the distribution on the shield relative to the distribution on the calorimeter to balance the small heat flow to the calorimeter against the heat flow from it.

4. Calorimeters With Temperature-Controlled Environment

When it is desirable to eliminate the effect of $\beta_\theta t$ on the zero heat leak or when β_L is large enough to cause difficulty with the temperature measurement, it is feasible to reduce them by providing a heated environment controlled about a degree below the temperature of the shield [5, 12, 16, 17]. This technique is especially useful at higher temperatures where the heat transfer coefficients are large.

Since the environment has a dynamic temperature variation in this case, the effect of the temperature gradients from the various sources must be considered and allowance made for various environment materials. The environment temperature will now be controlled relative to some point on the shields where the temperature is T_{cons}, and will have temperature distributions due to heating up and due to loss to the environment through the thermal insulation. The temperature of the ith region of the environment is given by the equation

$$T_{ie}=T_0-\Delta T+L_{ie}+L_{cons}+\theta_{ie}+\theta_{cons}+\tau_{ie}+\tau_{cons}+(\beta_L+\beta_\theta)t, \quad (10)$$

where ΔT is the controlled difference between the points on the shield and on the environment where the thermocouple junctions are located. This expression for T_{ie} combined with equations II–B, table 1, gives the heat flow to the environment from each point on the shield:

$$K_{is}\frac{\partial T_{is}}{\partial n_{is}}=K_{je}\frac{\partial(L_{je}+\theta_{je}+\tau_{je})}{\partial n_{is}}+\int_A h_{ik}(L_{ke}+L_{cons}+\theta_{ke}+\theta_{cons}+\tau_{ke}+\tau_{cons}-L_{is}-L_{conc}-\theta_{is}-\theta_{conc}-\tau_{is}-\tau_{conc}-\Delta T)dA_e \quad (11)$$

where gas regions are now arbitrarily part of the environment. On opaque conduction boundaries, $T_{is}=L_{je}+\theta_{je}+\tau_{je}$. This equation does not now contain explicitly the $\beta_\theta t$ term which caused the variation in the zero heat leak, but the corresponding expression for the heat loss from the controlled environment will contain $\beta_\theta t$. Consequently, the validity of the approximation that increasing the environment temperature by $\beta_\theta t$ has a negligible effect on the zero heat leak must still be verified by observation.

When eq (11) is separated into a sum it becomes apparent that all the transients depend on the transients of the environment. Whether these τ_{ie} have a negligible effect on the shield temperature distribution is subject to observation. A large environment insulated with a considerable mass of material may so extend the equilibrium time that observations of the apparent zero heat leak will contain contributions from the transients. It is not necessary to wait for the environment transients to die out if the zero heat leak is negligibly affected by the small variations in the environment temperature, an effect observed with an adiabatic calorimeter operated up to 400 °C in this laboratory [12]. In constant heating calorimeters (sec. 5) the temperature of the controlled environment can be made equal to that of the adiabatic shield, so that, except for stray thermoelectric emfs, the zero heat leak depends only on the small effect on the shield of the gradients in the environment. This effect has been observed to be negligible in a low-temperature calorimeter [11].

Two experimental checks on the environment are available. The obvious one is to look for the variation in a zero heat leak after the calorimeter power is turned off. If the leak is constant, either the τ_{ie} are short or have negligible effect on the shield. Another test is to increase the controlled temperature difference between the shield and environment by an amount larger than the most unfavorable estimate of the quasi-steady state temperature distribution in the environment, θ_{ie}. If the zero heat leak is not affected by this change, it should be independent of the transients in the environment because their maximum value is just θ_{ie}.

5. Continuous Heating Calorimeters

In the continuous heating method, data are taken without an equilibration period. Measurements are begun after the transient terms, column V, table 1, have become negligible. The observed heat capacity C_{obs} is related to the power input to the calorimeter by the equation

$$C_{obs}\frac{dT}{dt}=P_c+\int_{A_c}K_{ic}\left(\frac{\partial\theta_{ic}}{\partial n_{ic}}+\frac{\partial L_{ic}}{\partial n_{ic}}\right)dA. \quad (12)$$

Only two terms appear under the integral because the normal derivatives of the other terms (eq (2)) are zero. Integration is over the entire calorimeter surface A_c. This equation states that the power going to raise the temperature of the calorimeter is diminished by losses due to (1) gradients set up by power supplied from the shield to the environment and (2) gradients set up by power supplied to raise the calorimeter and shield temperatures. It was shown in sec. 3.2 that the power term and the θ_i integral in eq (12) are directly proportional to the heating rate. If measurements of C_{obs} are made at two heating rates and plotted against heating rate, the intercept for zero heating rate will give the heat capacity corrected for the zero heat leak. The intercept method of determining the zero heat leak assumes that the various parameters affecting the zero heat leak are constant between series of experiments. Thus, if there is a gradient across an inhomogeneity in a thermocouple lead wire producing an offset in the shield control, the assumption is that the same gradient is present in both series of measurements. The determination of the zero heat leak by initial and final equilibration experiments assumes the constancy of such effects over a shorter period.

Theoretically, then, there is no basis for choice between the two methods of constant heating rate

and alternating equilibration with heating. The choice of method depends on practical matters, such as control problems, the nature of the sample, and the length of time conditions can be expected to remain sufficiently constant to yield significant zero heat leak data.

6. Design and Testing of Adiabatic Calorimeters

Several conclusions can be drawn regarding testing and construction of calorimeters, some of which support practices in design and testing arrived at by less general methods.

6.1. Temperature Measurement Error

Because of temperature variations due to the zero heat leak, the thermometer for making absolute temperature measurements in the calorimeter will in general not be so located as to obtain the average temperature. The error may be appreciable where the absolute temperature is important, as in the determination of the temperature at which phase changes occur. Even if the observed calorimeter temperature is constant, the absolute temperature may still be in error due to heat flow into one part of the calorimeter and out from another (sec. 3.3). In heat capacity measurements, if the heat leak temperature distributions L_i are constant throughout the experiment, the region in which the temperature is measured will bear the same relationship to the average over the calorimeter before and after the heating period. The errors cancel for each individual experiment. It follows that the location of the sensing element in the calorimeter does not affect the heat capacity results, in agreement with Sturtevant [17], although the measured heat capacity will correspond to a temperature slightly different from the observed temperature. When the zero heat leak is observed to change between the initial and final equilibration periods the temperature measurement errors do not cancel exactly.

It appears possible to realize a net gain in the precision and perhaps in the accuracy of temperature measurement if the shield control is offset to make the observed temperature constant and the heat which enters the calorimeter at one part of the surface is by-passed around the sample and thermometer, as suggested in the next section, to that part of the surface where it leaves the calorimeter. Such construction might also reduce the possibility that a redistribution of the phases during protracted purity determinations might alter the temperature of the thermometer region relative to the temperature of the interface between the phases.

6.2. Correction for the Unknown Heat Exchange

In the usual good practice, the heat capacity of a sample is obtained as the difference between the observed heat capacities of the empty and the full calorimeter. This method allows not only for the heat capacities of the various regions of the calorimeter, but also for the unknown heat exchange, insofar as it is the same in the two experiments. The temperature distribution in the regions of the calorimeter heater and the sample and those regions between and adjacent to them will be especially altered, because the heater supplies much more heat for the same rate of temperature change in the experiments with the full calorimeter than it does in the experiment with the empty calorimeter. If any of these regions is part of the calorimeter surface, data for the empty calorimeter cannot provide an exact correction. In general, loading the sample directly against a thin outer calorimeter wall will alter the unknown heat exchange.

It has been shown above that the transients, which are different for the full and empty calorimeter, nevertheless do not contribute to the unknown heat exchange. The data on the empty calorimeter would therefore make an exact correction for the unknown heat exchange if only the θ_{ie} on the surface of the calorimeter could be made independent of the θ_{ie} for the sample and heater, assuming the θ_{is} are the same for experiments with the empty and full calorimeter.

It is apparent from condition IV–B, table 1, that for heat transfer by conduction only, the θ_i depend on the geometrical distribution of the θ_j and $\partial\theta_j/\partial n_i$. If there is interposed, between the surface of the calorimeter and the sample plus heater, a jth region in which the geometrical functions θ_j and $\partial\theta_j/\partial n_i$ are not affected by the sample and heater, then, other things being equal, the θ_i on the surface will be identical in the measurements on the full and empty calorimeter. A jth region made of a perfect conductor satisfies the requirements because all derivatives of θ_i are zero and θ_j is constant over the region. Another way to make the surface independent of the sample and heater is to interpose a jth region which has nearly a point contact with the ith region. The geometric temperature distribution is then exactly defined. Of course, the control temperature must be sensed in or outside this jth region or θ_{cone} will be affected by the heater and sample.

Since the error we seek to avoid is small, it may be possible to approximate closely enough one or both of these arrangements. Figure 1 is a sketch of such a design. The contact regions are small and of a good conductor. The sample region is connected to the calorimeter surface only through the contact region. If direct heat flow from the sample region to the surface (e.g., by radiation) is significant, another thin metallic surface may be interposed to carry this heat back to the contact region. The similar arrangement on the adiabatic shield serves to make the inner metal surface of the shield independent of variations in the environment.

The control temperature is shown measured at the calorimeter contact region. Compared to a thermometer or thermopile distributed over the surfaces, this arrangement would give a quicker response and perhaps make control easier or better. It is also subject to a larger error if the heat transfer coefficient changes between measurements with the empty and

full calorimeter. The integral effect of the heat transfer coefficient can be checked experimentally by offsetting the shield control at equilibrium.

Calorimeters have been reported [12, 18] which approximate such a design. The calorimeter surface is made of thin metal insulated by shielding or evacuation from the sample and heater regions except for a limited region of direct metallic contact. In one of these calorimeters, the observed heat of vaporization was not affected by the amount of fluid in the calorimeter; that is, the heat leak from the outer wall was independent of the liquid level and was properly accounted for in the heat leak correction based on data obtained at equilibrium.

To test the efficacy of such a design, the thermal characteristics of the sample region may be changed by changing the amount of sample, its distribution in the calorimeter, or its effective thermal conductivity. Agreement of the data for heat capacity would be a test of the independence of the temperature of the surface from that of the sample and heater. The value of the test would depend on how greatly one could exaggerate the effects of loading. Loading the calorimeter in such a way as to produce the maximum asymmetry should provide a rather severe test. Possibly comparing compact with loose samples or evacuated with helium-filled samples might provide a good test where gas adsorption is not a problem. Changing the effective thermal conductivity of the sample by substituting a fine powder for large crystals may not provide a good test. Small differences in observed heat capacity of fine and coarse samples have been ascribed to surface effects [19]. Reproducibility of the data is a necessary condition to show that the surface temperature distribution is reproduced, but it does not rule out the possibility of compensating effects.

6.3. Variation in Heating Rate as a Test

One of the variables which a calorimetrist has at his control is the heating rate of the calorimeter. It seems obvious from the experimental point of view to see if a different heating rate will give different results, and this test has been used by numerous experimentalists [1–11, 22]. For calorimeters which have the properties described in this paper, the observed heat capacity, corrected for the zero heat leak, is independent of the heating rate (sec. 3.2.).

The possibility remains of using the variation in heating rate to test the assumptions made regarding the environment temperature, the shield control, the zero heat leak, the thermal properties, and the decay of transients. Even if a relation can be shown between the heating rate and the first three of these, direct observation appears to be a more sensitive and useful method. It is the author's opinion that few cases will be found in which the effects of the temperature variation in thermal properties will be revealed by varying the heating rate. The amplitude of transients is proportional to the heating rate, so that variation of the rate should give information about transients. It may be questioned whether this technique will discover transients that are not observed in the equilibration periods.

In continuous heating calorimetry, varying the heating rate can be used to establish the time at which transient effects become negligible. The time response of the system is fixed, but the amplitude of the transients (τ and τ^*) is proportional to the heating rate. If two experiments are started from the same "rest" temperature but one at double the usual rate, the effect of the transients will be doubled. By observing the time at which the two rates give the same results, one can select a safe "warm-up" period. In intermittent calorimetry, of course, the transients are observed directly in the equilibration periods.

7. Conclusions

The treatment of adiabatic calorimeters in this paper assumes that the environment provides a constant-temperature surface, that heat capacities, thermal conductivities, and heat transfer coefficients are independent of temperature over the temperature rise of the experiment, that deviations of the shield control are negligible, that the calorimeter power is constant during the heating period, that the zero heat leak is constant and that transients have become negligible when the final temperature is observed. It is possible to check by observation or by calculation from observations all of these quantities. The approximation of temperature-independent thermal properties, which makes the partial differential equations linear, is implied in nearly all calorimetry, in which the heat observed is corrected for heat exchange during the heating period on the basis of observations during fore and after periods.

Under these conditions, the heat flow equations can be reduced to a sum of solutions satisfying the various boundary conditions and interpretable in terms of tangible physical quantities. In this way, it is possible to analyze the causes and effects of gradients set up by the calorimeter and shield heaters. The heat exchange between the calorimeter and the shield due to the transients at the beginning and end of the experiment cancel for each experiment.

The unknown heat transfer due to the temperature distribution set up during the heating period cannot be detected by varying the heating rate, but with proper precautions in the design, data for the empty calorimeter can be used to make a very good correction for it. The validity of the correction depends on the reproducibility of the gradients between experiments with the full and empty calorimeter. This reproducibility affects the accuracy of the measurements; variations produce a systematic error which cannot be determined experimentally, although experiments with varying sample size and distribution may be used to indicate that the error is small.

In intermittent heating, the time required for the transients to decay is best observed in an equilibration period following heating at the maximum rate

possible, which results in the maximum amplitude of the transients. For experiments in which the transient contribution to the temperature measurements is negligible it is valid to use data for the empty calorimeter taken at one rate to correct data for the full calorimeter taken at another rate. Within the limitations imposed by uncertainties in the zero heat leak, the rate of heating can therefore be selected to suit the observer's convenience in making the power and temperature measurements or maintaining temperature control. This flexibility is especially useful when the sample undergoes a change of state.

Since the zero heat leak depends on the locations of the control temperature sensing elements, an arbitrary offset of the controls to make this heat leak zero introduces no error in the calorimetry. This technique may be used to facilitate calculations, temperature measurement, or observations of protracted processes in the calorimeter.

To permit more thorough study by readers, reports on calorimeters intended for the most careful work might well include, in addition to measurements on Calorimetry Conference samples [20, 21], data taken over that part of the temperature range where the heat transfer coefficient is large on (1) the zero heat leaks and their variation with time, temperature, and the heating rate of the preceding heating period, (2) the overall coefficient for heat transfer between the calorimeter and the shield determined for both the full and empty calorimeter, and (3) the effect of changing the controlled temperature difference between the shield and the environment.

The author is indebted to Maxine Rockoff, H. W. Flieger, and M. L. Reilly for discussions of several points of mathematics and physics, and to D. L. Martin for comments on the manuscript.

8. References

[1] J. M. North, AERE M/R 1016 (1952).
[2] I. Backhurst, J. Iron and Steel Inst. (London) **189,** 124 (1958).
[3] H. E. O'Neal and N. W. Gregory, Rev. Sci. Instr. **30,** 434 (1959).
[4] E. E. Stansbury, D. L. McElroy, M. L. Picklesimer, G. E. Elder, and R. E. Pawel, Rev. Sci. Instr. **30,** 121 (1959).
[5] T. M. Dauphinee, D. K. C. MacDonald, and H. Preston-Thomas, Proc. Roy. Soc. (London) **A221,** 267 (1954).
[6] N. Bekkedahl and R. B. Scott, J. Research NBS **29,** 87 (1942).
[7] J. C. Southard and F. G. Brickwedde, J. Am. Chem. Soc. **55,** 4378 (1933).
[8] N. S. Osborne, H. F. Stimson, and D. C. Ginnings, J. Research NBS **23,** 197 (1939); **18,** 389 (1937).
[9] H. Moser, Physik. Z. **37,** 737 (1936).
[10] C. Sykes and F. W. Jones, J. Inst. Metals **59,** 257 (1936).
[11] D. L. Martin, Can. J. Phys. **38,** 17 (1960).
[12] E. D. West and D. C. Ginnings, J. Research NBS **60,** 309 (1958).
[13] H. S. Carslaw and J. C. Jaeger, Conduction of Heat in Solids, 2d Ed. (Oxford University Press, London, 1959).
[14] B. A. Boley and J. H. Weiner, Theory of Thermal Stresses (John Wiley & Sons, Inc., New York, 1960).
[15] M. Jakob, Heat Transfer, Vols. I and II (John Wiley & Sons, Inc., New York, 1949 and 1957).
[16] E. F. Westrum, Jr., J. B. Hatcher, and D. W. Osborne, J. Chem. Phys. **21,** 419 (1953).
[17] J. M. Sturtevant, Physics **7,** 232 (1936).
[18] N. S. Osborne and D. C. Ginnings, J. Research NBS **39,** 453 (1947).
[19] A. C. Victor, J. Chem. Phys. **36,** 2812 (1962).
[20] D. C. Ginnings and G. T. Furukawa, J. Am. Chem. Soc. **75,** 522 (1953).
[21] G. T. Furukawa, T. B. Douglas, R. E. McCoskey, and D. C. Ginnings, J. Research NBS **57,** 67 (1956).
[22] J. W. Edwards and G. L. Kington, Trans. Faraday Soc. **58,** 1313 (1962).
[23] H. C. Dickinson, Bul. BS **11,** 189 (1915).

(Paper 67A4–222)

JOURNAL OF RESEARCH of the National Bureau of Standards—A. Physics and Chemistry
Vol. 67A, No. 4, July–August 1963

Preparation of Anhydrous Single Crystals of Rare-Earth Halides

Norman H. Kiess

(February 26, 1963)

Anhydrous rare-earth halides are prepared by the conversion of the rare-earth oxide to the halide by means of its reaction with the appropriate ammonium halide. Without transfer from the reaction vessel, the halide is melted, then crystallized by slow cooling. The resulting solid usually contains single crystals large enough to permit spectroscopic studies of the compounds.

1. Introduction

In recent years much attention has been paid to the optical and magnetic properties of rare-earth compounds. The anhydrous halides have simpler crystal structures [1][1] than most of the other well-known rare-earth compounds, and yield experimental data that are easier to interpret. It is desirable to have an efficient method for the preparation of single crystals of the anhydrous halides, particularly if one wishes to study intensities of spectral lines as a function of concentration of absorbing ion.

Single crystals of anhydrous rare-earth halides are not difficult to grow from a pure melt. The production of the pure salts has, however, been time-consuming and difficult. Previous workers [2–8] have prepared them by dissolving the rare-earth oxide in the appropriate acid and subsequent evaporation to crystallize the hydrated halide, followed by dehydration of the hydrated halide in an atmosphere of dry hydrogen halide gas. It has sometimes been necessary, in order to crystallize salts prepared in this way, to purify them by distillation [5, 6]. A much simpler method for the preparation of anhydrous rare-earth halides, except fluorides, was first described by Reed [9] in 1934. None of the early workers [9–12] using this method reported attempts to crystallize their products. In this work it was found that, by using a modification of the basic procedure described by Reed, salts pure enough to crystallize could be produced.

2. Method and Apparatus

Anhydrous rare-earth halides can be prepared by the reaction, at high temperatures, of the rare-earth oxide with the appropriate ammonium halide, as represented by the following typical equation:

$$La_2O_3+6NH_4Cl \rightarrow 2LaCl_3+6NH_3+3H_2O.$$

A large excess of ammonium halide must be used. A fourfold stoichiometric excess is adequate for the chloride and the bromide, whereas a tenfold excess is necessary for the iodide. The reagents are ground together with a mortar and pestle until a powdery mixture is obtained, then poured into a vycor tube about 15 in. long and an inch or more in diameter. One end of this tube is drawn to a point and the other is the outer member of a standard taper joint. A stream of dry, inert gas (helium or nitrogen) is to be directed over the mixture. This is effected by the arrangement depicted in figure 1. A Pyrex inner tube extends several inches into the vycor tube. There is a distance of at least an inch between the reacting mixture and the end of the inner tube. A ring seal connects the Pyrex tube with the inner member of the tapered joint. The members of the joint are sealed by means of a silicone O-ring that fits into a groove in the inner member. A small flow of dry gas is started. The assembled reaction vessel is then inserted a sufficient distance into the tube of a horizontal furnace to allow the dry gas to enter the hot zone before passing out through the Pyrex tube. The temperature is raised to the point where the reaction becomes vigorous, which is between 200 and 400 °C, depending on which halide is being made, and is held there until the reaction is nearly complete. The flow of gas carries out the volatile products of the reaction, and the water vapor condenses on the cooler walls of tubing outside the furnace. The appearance and subsequent evaporation of this water is the best guide as to the course of the reaction. The water evaporates about an hour after it appears, indicating that the reaction is close to completion. The temperature is then raised about 100 °C, and is held at this point for several hours, in order to effect completion of the reaction. During this period most of the ammonium halide sublimes and is carried out of the furnace by the flow of gas. Condensation of ammonium halide on the cooler walls of tubing eventually obstructs the flow of gas, but the heating can be interrupted in order to clean and replace the tubing. The residual rare-earth halide is a powder and can react with traces of oxygen and water vapor.

[1] Figures in brackets indicate the literature references at the end of this paper.

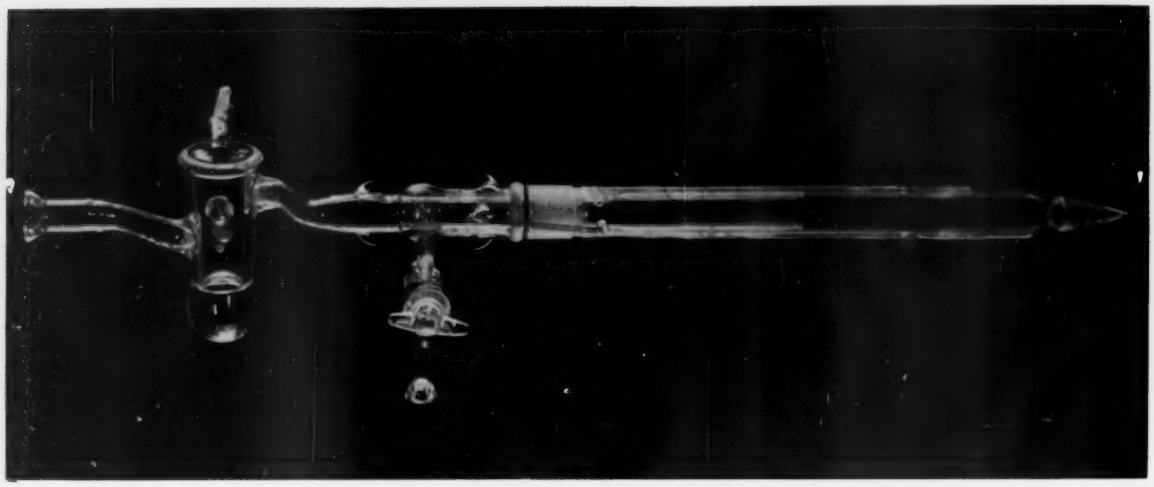

FIGURE 1. *Glassware for preparing crystals.*
Diameter of vycor tube: 30 mm.

The ammonium halide affords protection by reacting with possible decomposition products to regenerate anhydrous rare-earth halide; consequently the last traces of it are removed by evacuating the system. This must be done by careful, simultaneous adjustment of temperature and pumping speed, in order to prevent the rare-earth halide from being blown out of the furnace. When no more ammonium halide condenses on the cooler walls of tubing, the stopcocks are closed and the evacuated system is transferred to a vertical tube furnace.

The vertical furnace has a heating chamber 6 in. deep and 1½ in. in diameter. A chromel-alumel thermocouple is used to measure temperature in the furnace. There is a sharp temperature gradient at the bottom when power is applied. A saturable reactor in series with the resistance-winding is used to modulate the power. A model JSBG–2 programmer-controller, manufactured by the West Instrument Company, accepts the thermocouple signal and furnishes current for the control-winding of the reactor. By means of this device, control of the time-temperature cycle is achieved. The junction of the thermocouple is placed next to the heating element, about 3 in. from the bottom. The temperature at this point is adjusted to be about 100 °C above the melting-point of the salt. The vycor tube is placed in the furnace so that the tip of the point is below the thermocouple and at a temperature just above the melting-point of the salt. The temperature is then slowly lowered to room temperature over a period of about 18 hr, and the melt solidifies upwards along the axis of the tube.

3. Results and Discussion

The procedure described above produced solid masses usually containing regions of single crystal. They could be broken loose from the wall of the tube by tapping it lightly. Slabs of single crystal a centimeter square and a few millimeters thick could be cut, one of which is shown in figure 2. Most of the crystals prepared in this way were halides of lanthanum containing a small amount of optically active rare earth ion as an impurity. The case of samarium impurity in lanthanum halide is particularly interesting because of the two possible oxidation states of samarium in combination with halogens. The absorption spectra of samarium ion in lanthanum bromide prepared by this method proved to be those of triply ionized samarium.[2]

Although it sometimes happened, particularly when preparing iodides, that the resulting solid mass contained no single crystal, it was never found necessary to purify the salt by distilling the melt in order to obtain crystals large enough for spectroscopic work. Single crystals could usually be obtained from polycrystalline masses by grinding them up with a new batch of ammonium halide and repeating the above procedure. It is believed that the factor which is most important in limiting the size of the single crystals is the purity of the melt. The impurities may be due to incomplete reaction with the ammonium halide, reaction with the vycor, or foreign matter in the rare earth oxide. The use of quartz instead of vycor did not produce larger crystals, nor did lengthening the cooling period. As the crystals were large enough for spectroscopic work, these points were not investigated further.

The procedure given here for the synthesis of the anhydrous halides differs from that used by the earlier workers [9–12] in two respects. First, the excess of ammonium halide is greater than that

[2] These spectra were obtained at the Johns Hopkins University under the direction of Dr. G. H. Dieke.

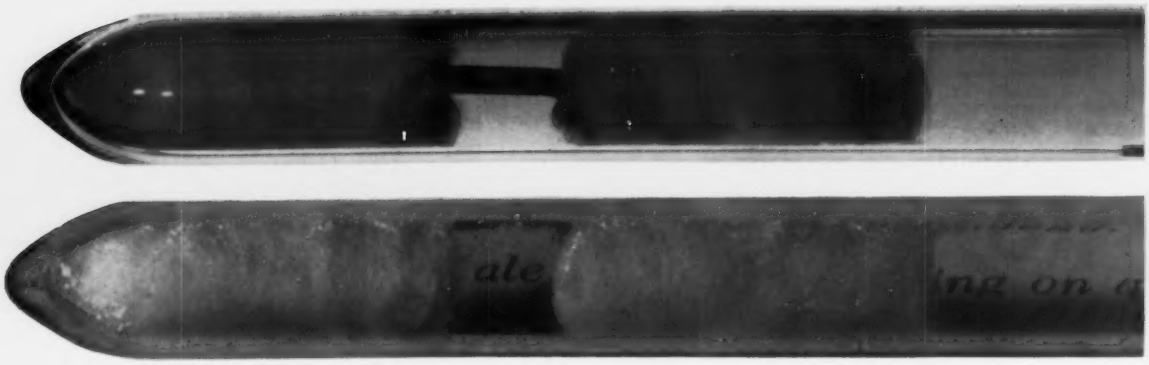

FIGURE 2. *Crystal, mounted in quartz tube, diameter 8 mm, with quartz wool packing.*
The crystal was cut and mounted by E. F. Williams of Johns Hopkins University.

used earlier. Second, the mixture is heated at atmospheric pressure for several hours longer. At the end of this time, most of the ammonium halide has evaporated. The earlier workers removed the ammonium halide by the application of a vacuum after heating at atmospheric pressure for from 1 to 4 hr. The early procedure suffices to produce salts pure enough to give clear solutions in water, but prolonged heating at atmospheric pressure is necessary to produce salts pure enough to crystallize readily. The immediate melting and subsequent crystallization of the salt follow the removal of the ammonium halide. In view of the extreme instability of these salts it is advisable not to retain them as powders.

The salts melted at temperatures near those commonly given as their melting points. No attempt was made to measure their melting points precisely. The colors exhibited by lanthanum iodide at various temperatures are interesting. The powder at low temperatures is almost white, but as the temperature is raised it turns yellow. The melt is brown and translucent. The crystal at room temperature is light yellowish-green. On the other hand, lanthanum chloride and bromide are almost completely colorless at all temperatures.

An important contribution to this work was the glassblowing and vycor-working of the Glassblowing Shop of the National Bureau of Standards, most of which was done by John Hydro, Jr.

4. References

[1] W. H. Zachariasen, Acta Cryst. **1,** 265 (1948).
[2] J. H. Kleinheksel and H. C. Kremers, J. Am. Chem. Soc. **50,** 959 (1928).
[3] J. H. Anderson and C. A. Hutchison, Jr., Phys. Rev. **97,** 76 (1955).
[4] E. V. Sayre, K. M. Sancier, and S. Freed, J. Chem. Phys. **23,** 2060 (1955).
[5] D. M. Gruen, J. G. Conway, and R. D. McLaughlin, J. Chem. Phys. **25,** 1102 (1956).
[6] E. Y. Wong (dissertation, University of Chicago, 1957).
[7] C. A. Hutchison, Jr., and E. Y. Wong, J. Chem. Phys. **29,** 754 (1958).
[8] E. Y. Wong and I. Richman, J. Chem. Phys. **36,** 1889 (1962).
[9] J. B. Reed, dissertation, University of Illinois, 1934.
[10] J. B. Reed, B. S. Hopkins, and L. F. Audrieth, J. Am. Chem. Soc **57,** 1159 (1935).
[11] R. C. Young and J. L. Hastings, J. Am. Chem. Soc. **59,** 765 (1937).
[12] W. A. Taebel and B. S. Hopkins, Z. Anorg. Allgem. Chem. **235,** 62 (1937).

(Paper 67A4–223)

685-226—63——5

JOURNAL OF RESEARCH of the National Bureau of Standards—A. Physics and Chemistry
Vol. 67A, No. 4, July–August 1963

A Phase Study of the System: Oxalic Acid/Acetic Acid/Water; Its Significance in Oxalic Acid Crystal Growth[1]

John Strassburger and John L. Torgesen

(April 3, 1963)

The presence of limited amounts of water appears to improve the quality of anhydrous oxalic acid single crystals grown from acetic acid solutions. Water concentrations in the saturated solutions which allow crystallization of the anhydrous acid have been determined from the phase study of this ternary system. Near 50 °C the anhydrous acid crystallizes from solutions containing up to 5.2 weight percent water, while the dihydrate appears when water is in excess of this amount.

The phase diagram shows a minimum content of oxalic acid in solution at a solvent composition near 83 percent acetic acid, 17 percent water. The solubility increases with increased acetic acid to the isothermal invariant point, found experimentally at a measured temperature of 50.21 °C to have the composition 20.94 percent oxalic acid, 73.89 percent acetic acid, 5.17 percent water. Decreasing solubility occurs at higher acetic acid concentrations. The maximum water content which allows crystallization of anhydrous acid increases with increasing crystallization temperature. The solubility of oxalic acid in acetic acid/water mixtures at 40° and 50 °C is reported.

1. Introduction

Attempts have been made to purify oxalic acid by growth of anhydrous single crystals from its solution in acetic acid. Even when using equipment [1][2] with precise control of solution temperture, good crystals only up to 1 cm in length could be grown from glacial acetic acid. Larger crystals became cloudy owing to the inclusion of mother liquor.

The production of anhydrous seed crystals by evaporation of acetic acid at 50 °C is rendered difficult, too, by an excessive nucleation rate resulting in the formation of polycrystalline clusters. However, it has been observed that a small quantity of water, about 5 percent by weight, suppresses the nucleation rate and also produces anhydrous seeds of high quality, more nearly free from inclusions. Water in excess of this amount leads to the formation of oxalic acid dihydrate crystals, which redissolve on further evaporation with the eventual crystallization of anhydrous oxalic acid.

Thus, the indications were that aqueous acetic acid may be the better solvent for the growth of large single crystals of anhydrous oxalic acid. Accurate phase rule data were needed to determine the permissible range of water concentration allowing crystallization and growth of the anhydrous acid. The ternary system oxalic acid/acetic acid/water has consequently been studied as described in this paper.

Hill, Goulden, and Hatton [2] have reported a phase study of the system oxalic acid/sulfuric acid/water at 60 °C. The solution composition at the invariant point is given as 20.5 percent oxalic acid, 44.6 percent sulfuric acid, and 34.9 percent water. This system does not lend itself to the growth of large single crystals of anhydrous oxalic acid because the required concentration of sulfuric acid induces decomposition of oxalic acid in solution. Knox and Richards [3] have measured the solubility of oxalic acid in water solutions of acetic acid. Their work did not extend to concentrations of acetic acid with which anhydrous oxalic acid is in equilibrium.

2. Reagents and Apparatus

Reagent-grade oxalic acid (both anhydrous and the dihydrate) and acetic acid were used to prepare all solutions. Assays of the hydrated oxalic acid determined its purity to be 99.97 percent. The acetic acid was assayed at 99.28 percent; the remainder was assumed to be water. No special steps were taken to remove this residual water because it was not essential for the study to include completely anhydrous conditions. The normal laboratory supply of distilled water was used.

The various mixtures of the three components were contained in 250-ml Florence flasks modified by attaching inner 24/40 standard-taper seals at the neck. Stopper caps constructed of the outer seal allowed the use of a sealing grease without danger of contamination. Stainless steel retainer springs insured a secure seal beteeen flask and stopper cap and the outer air space, indicated in figure 1, prevented influx of thermostat water.

The solution flasks were supported in a water thermostat of 13 gal capacity. A diagram of the assembled apparatus, shown in figure 1, indicates an upper support position used while sampling the equilibrium mixtures and a lower position used in attaining equilibrium. In the latter case the flasks were clamped around a center post about ¼ in. from the bottom of the bath. A maximum of five flasks

[1] Submitted by Mr. Strassburger in partia fulfillment of the requirements for the degree of Master of Science, Georgetown University, Washington, D.C.
[2] Figures in brackets indicate the literature references at the end of this paper.

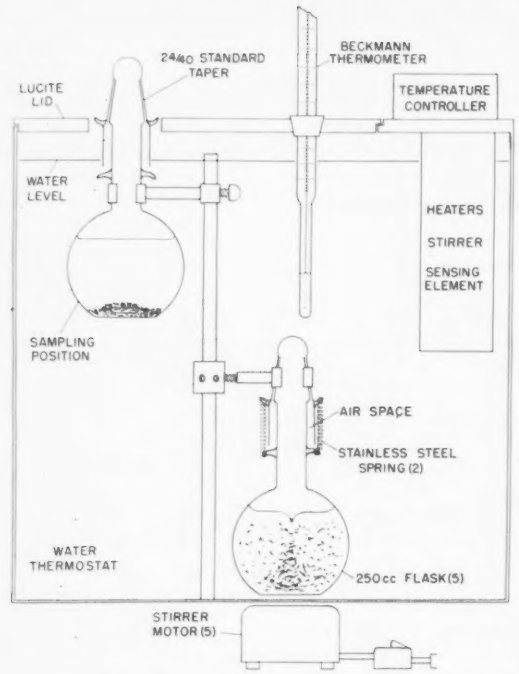

FIGURE 1. *Apparatus assembly for attaining equilibrium solutions.*

could be accommodated in equivalent positions. Each flask contained a Kel-F-coated magnetic stirring bar and continuous stirring was provided by individual magnetic stirring motors mounted under the thermostat below each flask.

The control of thermostat temperature was achieved with equipment of the type developed by Ransom [4], based on the principle of a time-modulated power supply in which the heat applied to the system is in direct relation to the departure of temperature from the desired point. The bulk of the heat was supplied to the bath by a large continuous heater, the sensitive control heat by two Nichrome-wound finger heaters. The bath temperature was observed with a Beckmann thermometer and was controlled to within ± 0.005 °C. The Beckmann thermometer was calibrated with a platinum resistance thermometer which had been previously calibrated at the National Bureau of Standards.

Electrometric titrations were performed with a *p*H meter, Beckman Model G, equipped with external leads.

3. Experimental Procedure

3.1. Sample Preparation

The saturated solutions were prepared by mixing the appropriate proportion of acetic acid, water, and the excess oxalic acid necessary to saturate the solutions and provide excess solid phase at the desired temperature. The mixtures were heated well above this temperature until complete dissolution of the excess oxalic acid was achieved and then were placed in the water thermostat and allowed to crystallize while being continuously stirred. Saturation equilibrium was achieved by allowing each flask to remain at least overnight in the constant temperature bath. The stirrer of that solution to be analyzed was turned off, and the crystalline material was allowed to settle for a period of approximately 2 hr. The flask was then raised from the bottom and clamped into position near the top of the bath so that only the neck protruded above the water level and through the hole provided in the lid (sampling position in fig. 1). This procedure allowed the solution flasks to be completely immersed in the thermostat until just before sampling.

A pipet was used to remove samples of clear solution which were placed in weighing bottles and stoppered quickly. The pipet was preheated to avoid crystallization while transferring the samples. The slurry was sampled by withdrawing a portion of solid-plus-liquid into a piece of preheated 6-mm glass tubing and transferring it quickly into a weighing bottle. Three samples of the liquid phase and one sample of the solid-plus-liquid mixture were removed. The solution was replaced at the bottom of the water bath, and the procedure was repeated in a day or two for each solution mixture.

Schreinemakers' "method of wet residues" [5], as described by Ricci [6], was the procedure followed for the determination of tie lines and the composition of the solid phase. The tie lines were determined by analyzing the saturated solution and also a sample of the solid phase mixed with the mother-liquor solution. These two analyses were then points fixing a line joining the liquid and solid phase compositions. Graphical extrapolation of the tie lines to their point of intersection determined the composition of the solid without the necessity of its separation from mother liquor and of its drying preparatory to chemical analysis.

3.2. Analysis

Since it was necessary to make a complete analysis on each sample, a procedure was devised to allow compatibility between titration for total acid with sodium hydroxide and titration for oxalate with potassium permanganate. Preliminary analyses showed that acid-base indicators (phenolphthalein or thymol blue) as well as the indicator solvent interfered with the permanganate titration for oxalic acid. For this reason, the samples were analyzed electrometrically for total acid present by titration with sodium hydroxide using a *p*H meter (endpoint= 9.0). The samples were reacidified with sulfuric acid and titrated hot with permanganate for percentage oxalic acid. Percentage water was calculated by difference.

The procedure used for the preparation, storage, and standardization of the sodium hydroxide and potassium permanganate solutions is described by Kolthoff and Sandell [7]. The sodium hydroxide

(approximately 0.2N) was standardized with NBS standard sample acid potassium phthalate. The permanganate was prepared to be approximately 0.1N and was standardized with NBS standard sample sodium oxalate. The analyses of the standard solutions were not considered acceptable until three consecutive determinations gave results which varied by no more than $\pm 0.0001N$.

4. Results and Discussion

Analytical data at 50.21 °C are given in table 1 and the phase diagram is shown in figure 2. All values are given in weight percent. The experimental values for the liquid-plus-solid analyses are plotted in figure 2 but are not given in table form. The solubility points were found to lie on a smooth curve and the isothermal invariant point was found experimentally to have the composition 20.94 percent $(CO_2H)_2$, 73.89 percent CH_3CO_2H, and 5.17 percent water. A minimum solubility of oxalic acid occurs in the region of composition 11.7 percent $(CO_2H)_2$, 73.3 percent CH_3CO_2H, and 15 percent water. On

TABLE 1. *Solubility of oxalic acid in acetic acid/water solutions; 50.21 ± 0.005 °C*

$(CO_2H)_2$	CH_3CO_2H	H_2O	Solid phase
wt %	*wt %*	*wt %*	
24.33	0.0	75.67	H[a]
23.71	6.84	69.45	H
23.14	11.47	65.39	H
21.52	21.90	56.58	H
19.39	33.09	47.52	H
16.62	45.74	37.64	H
15.53	50.62	33.85	H
14.42	55.61	29.97	H
12.42	66.05	21.53	H
12.10	68.37	19.53	H
11.92	69.85	18.23	H
11.66	74.09	14.25	H
11.89	76.21	11.90	H
11.98	76.56	11.46	H
13.05	78.02	8.93	H
16.12	77.34	6.54	H
19.84	74.62	5.54	H
20.94	73.89	5.17	H+A[b]
19.24	76.66	4.10	A
15.48	82.68	1.84	A
13.31	85.99	0.70	A

[a] $H = (CO_2H)_2 \cdot 2H_2O$.
[b] $A = (CO_2H)_2$.

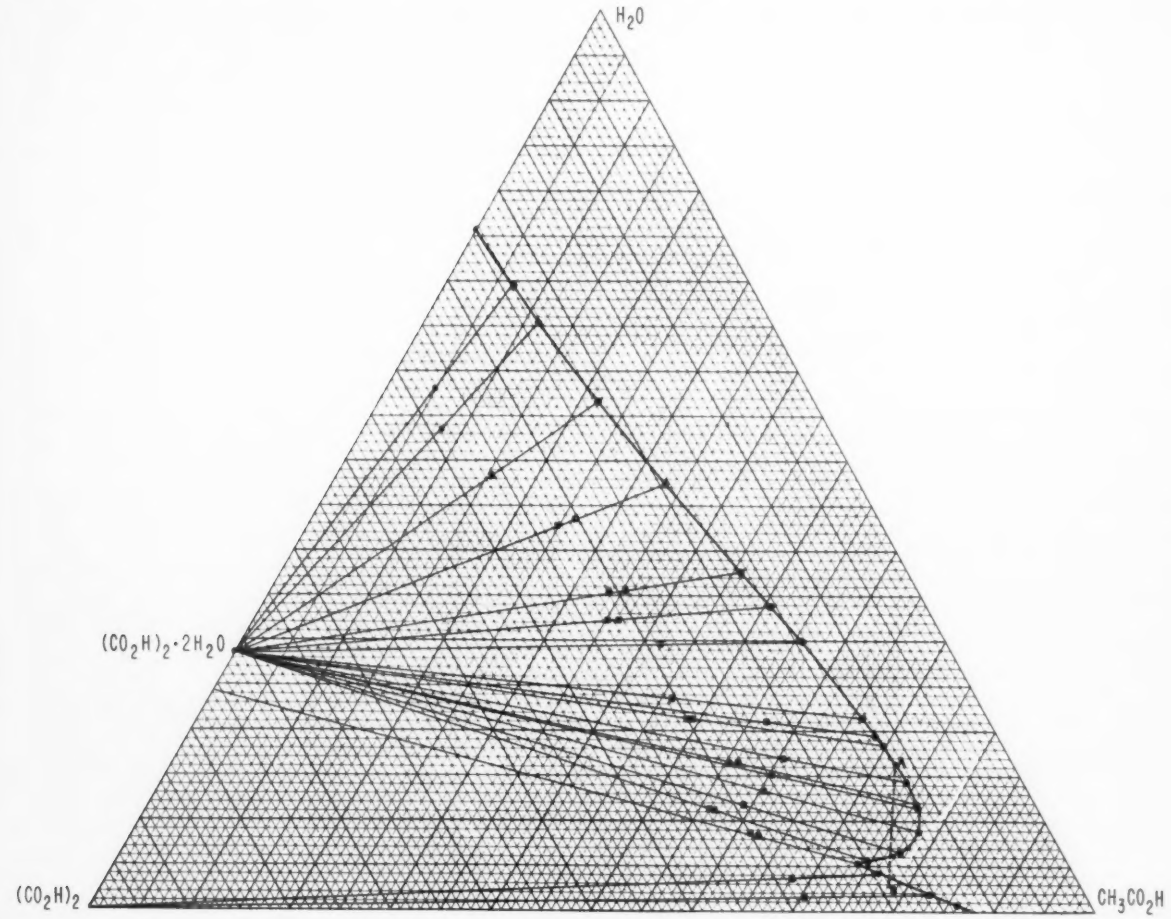

FIGURE 2. *The ternary system: oxalic acid/acetic acid/water; weight percent at 50.21 ± 0.005 °C.*

the aqueous side of this point, the solubility of oxalic acid increases continuously to a maximum in water alone. On the anhydrous side of the solubility minimum, a rapid increase in solubility occurs until the invarient point is reached, followed by a decrease until completely anhydrous conditions are reached. The tie lines all extrapolated to the theoretical dihydrate or anhydrous composition with good precision, although the large extrapolation from two (or sometimes three) points is not very accurate.

Limited data for the 40 °C isotherm are given in table 2. While the phase relationships at this temperature were not completely explored, the data show the influence of temperature on the crystallization of anhydrous oxalic acid in the presence of water. The maximum water content which allows crystallization of the anhydrous form decreases with decreasing crystallization temperature.

TABLE 2. *Solubility of oxalic acid in acetic acid/water solutions; 39.94 ± 0.005 °C*

$(CO_2H)_2$	CH_3CO_2H	H_2O	Solid phase
wt %	*wt %*	*wt %*	
17.83	0.0	82.17	H[a]
13.98	36.75	49.27	H
12.29	46.23	41.48	H
11.54	83.73	4.73	H
10.87	88.43	0.70	A[b]

[a] $H = (CO_2H)_2 \cdot 2H_2O$.
[b] $A = (CO_2H)_2$.

As expected, the solubility of oxalic acid in acetic acid is less than in water. When appropriate corrections are made for the small differences in temperature, the results for the solubility of oxalic acid in water compare with the literature values [8, 9] at least as well as the various literature values compare with each other.

The second set of analyses usually reproduced the first set quite well, showing that equilibrium was reached before the first sampling, and that day to day variability was negligible. If the difference between the mean values of the two individual sets exceeded the standard deviation of a single set, additional analyses were made. Each value in tables 1 and 2, therefore, represents the average of at least six independent determinations. The calculated standard deviations for a single determination, indicating the reliability of each mean value, have the following average values: $(CO_2H)_2$, 0.02; CH_3CO_2H, 0.03; water, 0.04.

The phase diagram can be utilized to explain the earlier observations of consecutive crystallization of the dihydrate and anhydrous forms of oxalic acid which occurred during seed growth by evaporation. Published vapor-liquid equilibrium data for the acetic acid/water system, at various temperatures down to 22 °C [10], show that over the entire concentration range the ratio of water to acetic acid is always greater in the vapor phase then in the liquid. We can reasonably assume that a similar relationship holds for the solvent in this ternary system, and that evaporation of the solvent will promote continuous enrichment of acetic acid in the liquid phase.

If a system of acetic acid and water saturated with oxalic acid contains more than 5.2 percent water, as represented by point A (fig. 2) for example, the total composition of the system may be expected to follow a line such as AB as the solvent is evaporated. Evaporation will, in this case, result in crystallization of the oxalic acid dihydrate and its eventual dissolution by the time the dihydrate saturation curve is again reached. Subsequent evaporation will undersaturate the solution with respect to both solid phases until the anhydrous saturation curve is reached, whereafter (upon further enrichment of solvent in acetic acid) anhydrous oxalic acid will crystallize.

5. Conclusions

Anhydrous oxalic acid will crystallize near 50 °C from its solution in acetic acid/water mixtures provided the water concentration of the solution does not exceed 5.2 percent. Crystallization of the anhydrous acid at higher temperatures may possibly be achieved over a still greater range of water concentration if necessary. The invariant point of the system at 50.21 °C was found at a solution composition of 20.94 percent $(CO_2H)_2$, 73.89 percent CH_3CO_2H, and 5.17 percent water.

6. References

[1] J. L. Torgesen, A. T. Horton, and C. P. Saylor, J. Research NBS **67C,** (Eng. and Instr.) No. 1, 25 (1963).
[2] L. M. Hill, T. P. Goulden, and E. Hatton, J. Chem. Soc. p. 78–81 (1946).
[3] J. Knox and M. B. Richards, J. Chem. Soc. **115,** 508–31 (1919).
[4] F. A. Ransom, Control Engineering **1,** 1 (McGraw-Hill Book Co., New York, N.Y., Jan. 1954).
[5] F. A. H. Schreinemakers, Z. Phys. Chem. **11,** 75 (1893).
[6] J. E. Ricci, The Phase Rule and Heterogeneous Equilibrium, p. 323 (D. Van Nostrand Co., Inc., New York, N.Y., 1951).
[7] I. M. Kolthoff and E. B. Sandell, Textbook of Quantitative Inorganic Analysis, pp. 550, 553, and 592–4. (The Macmillan Co., New York, N.Y., 1943).
[8] H. C. S. Snethlage, Rec. trav. chim. **69,** 5–13 (1950).
[9] A. Seidell, Solubilities of Organic Compounds, 3d ed., **II,** pp. 79–80 (D. Van Nostrand Co., Inc., New York, N.Y., 1941).
[10] D. F. Othmer, S. J. Silvis, and A. Spiel, Ind. Eng. Chem. **44,** 1864 (1952).

(Paper 67A4–224)

JOURNAL OF RESEARCH of the National Bureau of Standards—A. Physics and Chemistry
Vol. 67A, No. 4, July–August 1963

Wavelength Calibrations in the Far Infrared (30 to 1000 Microns)

K. Narahari Rao,* R. V. de Vore,* and Earle K. Plyler

(April 3, 1963)

A discussion is presented of certain calibration procedures employed in the region 30 to 1000 microns. Calculated positions for the pure rotational absorption lines of the CO, HCN, and N_2O molecules are given, and a map of the pure rotational absorption lines of the H_2O molecule as recorded with a Perkin-Elmer model 301 spectrophotometer is shown.

1. Introduction

During the recent meetings of the Triple Commission for Spectroscopy, there have been discussions about the need for systematizing the wavelength standards and the wavelength calibration techniques for the infrared region. To partially meet this need, a report [1][1] has been compiled consisting of maps and the spectral positions of several vibration rotation bands occurring in the region 2.5 to 15μ. Evidently, it is important to provide such data for use in the far infrared at wavelengths longer than 15μ and extending into the millimeter region of the electromagnetic spectrum. Furthermore, it is of interest to examine critically all the currently available wavelength calibration techniques because of the impossibility of devising one procedure that can be adopted for the entire spectral region between 30 to 1000μ.

2. Experimental Procedure

In the far infrared region we observe mostly the pure rotational spectra of molecules. It is possible to calculate the positions of the pure rotational lines of a diatomic molecule like CO and linear triatomic molecules like HCN and N_2O by employing the rotational constants derived from studies of the microwave and near infrared absorption spectra of these molecules. One may conceive of three different ways in which the pure rotational lines of simple molecules such as CO, N_2O, and HCN can be used for the calibration of far infrared grating spectrometers: (i) In the case of spectrometers facilitated to determine the angular rotation of the grating, it is possible to employ the grating equation

$$\nu = nK \operatorname{cosec} \theta,$$

n being the spectral order, K the grating constant (expressed in cm^{-1}), and θ the angle between the central image and the spectral line located at ν cm^{-1}. Observations on the pure rotational lines of CO, HCN, and N_2O can lead to a value for the grating constant K. This value for K can then be used in the subsequent measurements of the far infrared lines. Evidently, we should assume that the value for K does not change between the time the standards (viz, CO, HCN, and N_2O) are recorded and the time when the angular positions of the far infrared lines are measured. If several repetitive records are obtained, it is possible to minimize the errors arising from changes in the grating constant. The accuracy of the measurements made with this method depends on the accuracy with which the angular rotations of the grating can be determined. (ii) In commercial instruments, like the Perkin-Elmer model 301 far infrared spectrophotometer, the recorded data are considered to be linear in wave number units. This is accomplished by using [2]a "cosecant drive" for rotating the grating. "Pip" marks are recorded periodically on the chart. It has been our experience that, for a particular installation of the grating, the locations of these marks with respect to far infrared spectra are reproducible to accuracies of about ± 0.03 cm^{-1} at 100μ. With these limitations in mind, it should be possible to calibrate these "pip" marks by making observations on the pure rotational lines of the above simple molecules. (iii) A technique which has been extensively employed in the near infrared spectral regions consists in the simultaneous observation, by use of double-pen recorders, of two beams of radiation passing through the spectrometer at the

*The Ohio State University, Columbus, Ohio.

[1]Figures in brackets indicate the literature references at the end of this paper.

same time [3, 4]. One of two beams consists of the infrared spectra to be measured and the other provides a wave number scale to enable the determination of relative positions of the infrared spectral lines. If it becomes possible to impress a wave number scale on the far infrared spectra, the absolute positions of the scale can be determined by making use of the pure rotational lines of CO, N_2O, and HCN molecules. This technique of employing two beams of radiation may prove especially useful when investigations are made with grating spectrometers operating in a vacuum. The calibrating radiation may consist of higher orders of atomic lines or higher orders of vibration rotation bands of simple molecules. Some of the atomic lines of mercury, helium and neon have sufficient intensity so that they can be detected in orders above one hundred. Figure 1 shows a part of the higher orders of the 2μ line of helium $\nu_{air}=4858.874$ cm^{-1} and $\nu_{vac}=4857.525$ cm^{-1} from the 85th to 110th orders as observed with a 90 lines per inch grating and a lead sulfide cell as detector. The slits of the spectrometer should be sufficiently narrow to resolve the spectra of the various orders shown in figure 1. We are emphasizing this point because the physical slits used in a far infrared spectrometer are usually quite wide (of the order of a few mm) and therefore it may become necessary to use an independent set of slits for producing wave number markers like those shown in figure 1.

This method of calibration can be checked on an instrument by using the higher orders of a definite atomic line for calibration and then measuring the positions of the higher orders of other known atomic lines.

The feasibility of employing integral relation between wavelengths of overlapping orders for obtaining spectral positions in the near infrared when modern gratings are used has been discussed adequately in previous publications [5, 6]. Since the procedures employed for ruling far infrared gratings may differ from the precise techniques used for ruling near infrared gratings, it is important to ascertain the validity of the applicability of integral relation between overlapping orders when gratings ruled for use in far infrared are employed.

For the region from 200 to 400 cm^{-1} the pure rotational absorption spectrum of diatomic and simple polyatomic molecules are usually of low intensity. However, the pure rotational lines of water vapor are of sufficient intensity for this region. The higher orders of molecular bands can be obtained in this region and are useful. For instance, the ν_2 absorption band of HCN is well suited for this purpose since it has been precisely measured [7] and the band contains many rotational lines separated by about 3 cm^{-1}. Since a well resolved spectrum of this band has not been published, a trace of the observed band is included in figure 2.

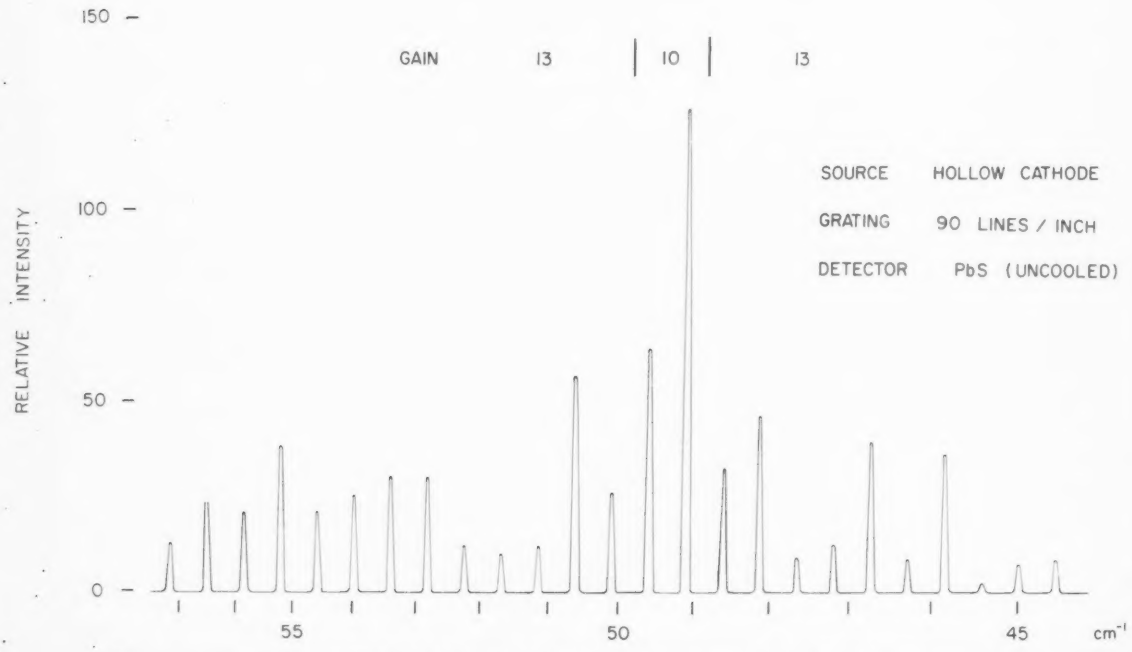

FIGURE 1. 2μ He *line recorded in higher orders (gain refers to the model 107 Perkin–Elmer amplifier).*

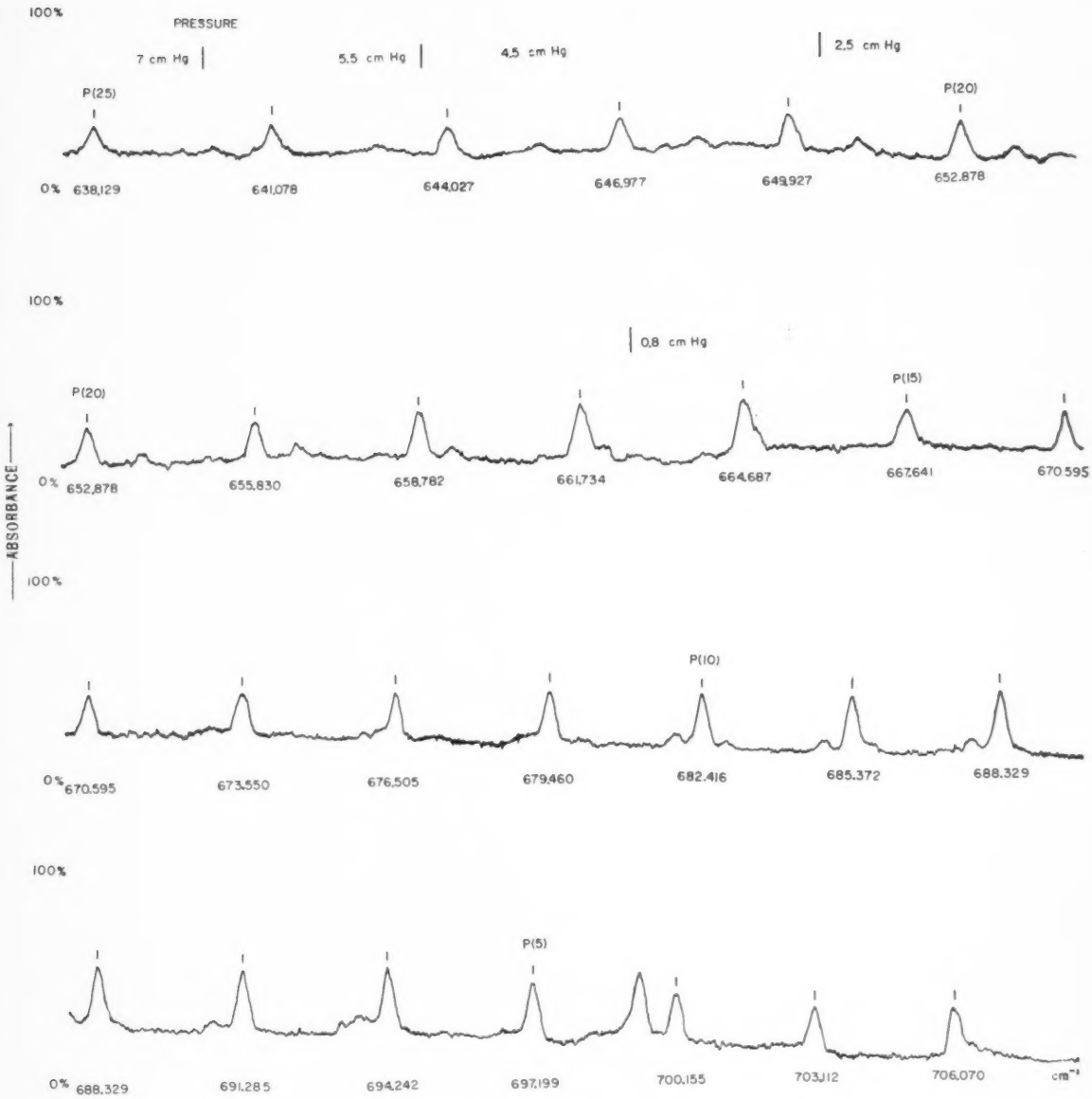

FIGURE 2. *ν_2 band of* HCN *at* 14μ.

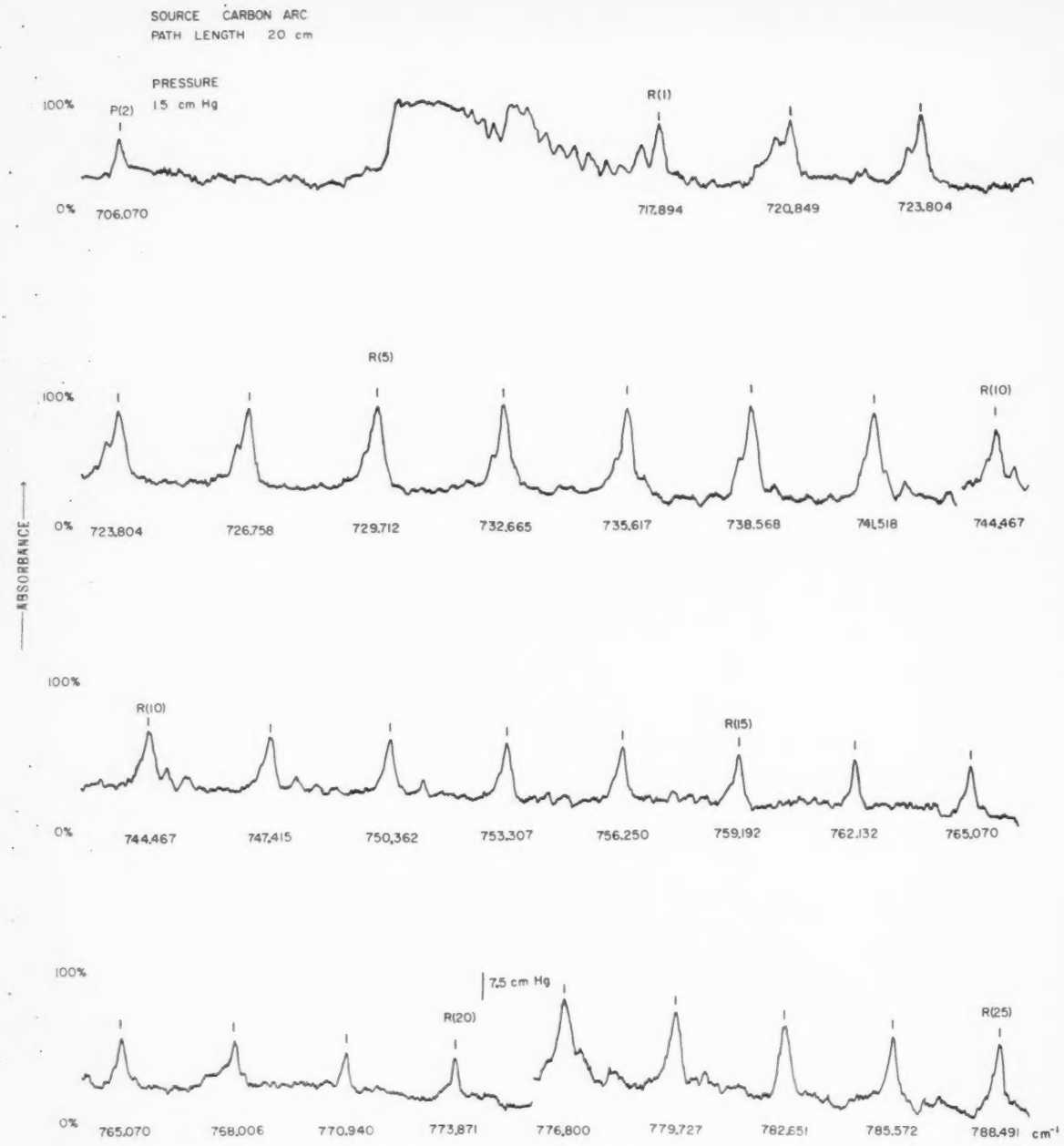

FIGURE 2. *band of* HCN *at* $14\mu\nu_2$.—Continued.

3. Wave Numbers of the Pure Rotational Spectrum of CO, HCN, and N_2O

Employing the rotational constants of the carbon monoxide [8, 9], hydrogen cyanide [10, 7], and the nitrous oxide [10, 11] molecules, the positions of their pure rotational spectra have been computed independently at The Ohio State University and the Bureau of Standards. The results are summarized in table 1. The path lengths and pressures necessary for the observation of these far infrared spectra are furnished as footnotes to the table.

TABLE 1. *Calculated positions of the pure rotational lines* of the* $C^{12}O^{16}$, $N_2{}^{14}O^{16}$, *and* $HC^{12}N^{14}$ *molecules (vacuum* cm^{-1})

J	$C^{12}O^{16}$	$N_2{}^{14}O^{16}$	$HC^{12}N^{14}$
0	3.84$_5$	0.83$_8$	2.95$_6$
1	7.69$_0$	1.67$_6$	5.91$_3$
2	11.53$_4$	2.51$_4$	8.86$_9$
3	15.37$_9$	3.35$_2$	11.82$_5$
4	19.22$_2$	4.19$_0$	14.78$_1$
5	23.06$_5$	5.02$_8$	17.73$_8$
6	26.90$_7$	5.86$_6$	20.69$_1$
7	30.74$_8$	6.70$_4$	23.64$_6$
8	34.58$_8$	7.54$_2$	26.59$_9$
9	38.42$_6$	8.38$_0$	29.55$_3$
10	42.26$_3$	9.21$_7$	32.50$_5$
11	46.09$_8$	10.05$_5$	35.45$_7$
12	49.93$_2$	10.89$_3$	38.40$_8$
13	53.76$_3$	11.73$_0$	41.35$_8$
14	57.59$_3$	12.56$_8$	44.30$_7$
15	61.42$_0$	13.40$_5$	47.25$_5$
16	65.24$_5$	14.24$_3$	50.20$_2$
17	69.06$_8$	15.08$_0$	53.14$_8$
18	72.88$_8$	15.91$_8$	56.09$_2$
19	76.70$_5$	16.75$_5$	59.03$_6$
20	80.51$_9$	17.59$_2$	61.97$_7$
21	84.33$_0$	18.42$_9$	64.91$_8$
22	88.13$_8$	19.26$_6$	67.85$_6$
23	91.94$_3$	20.10$_3$	70.79$_3$
24	95.74$_4$	20.94$_0$	73.72$_9$
25	99.54$_1$	21.77$_6$	76.66$_3$
26	103.33$_4$	22.61$_3$	79.59$_5$
27	107.12$_4$	23.44$_9$	82.52$_4$
28	110.90$_9$	24.28$_5$	85.45$_3$
29	114.69$_0$	25.12$_2$	88.37$_9$
30	118.46$_7$	25.95$_8$	91.30
31		26.79$_4$	94.22
32		27.62$_9$	97.14
33		28.46$_5$	100.06
34		29.30$_1$	102.98
35		30.13$_6$	105.89
36		30.97$_1$	108.80
37		31.80$_6$	111.71
38		32.64$_1$	114.61
39		33.47$_6$	117.51
40		34.31$_0$	120.41
41		35.14$_5$	
42		35.97$_9$	
43		36.81$_3$	
44		37.64$_7$	
45		38.48$_1$	
46		39.31$_4$	
47		40.14$_7$	
48		40.98$_0$	
49		41.81$_3$	
50		42.64$_6$	

*Path length 40 cm at pressures 2-3 cm of Hg for HCN and 40-60 cm of Hg for CO and N_2O.

4. Wave Numbers of the H_2O Lines in the Far Infrared

The pure rotational spectrum of water vapor extends from 10 to 5000μ, and many of the lines are intense from 25 to 400μ. By selecting lines which are not seriously overlapped, a number of calibrating points can be obtained. It was considered desirable to provide a map of the pure rotational lines of the H_2O molecule with the wave numbers marked on the spectrum. Figure 3 shows such a map of the water vapor lines as obtained with a Perkin-Elmer model 301 far infrared spectrophotometer under the conditions stated in the legend for the figure. The spectral position of each of the lines is indicated on the figure. These values have been derived by Benedict [12] after analyzing all the available data pertaining to the vibration rotation and pure rotational spectra of the H_2O molecule. The internal consistency of these data have been examined on the spectra shown in figure 3. Table 2 summarizes the findings. Tracings of the spectrum of atmospheric

TABLE 2. *Verification of the internal consistency pertaining to the data of the water vapor lines*

Lines used	Interpolated* less value in column 1	Lines used	Interpolated* less value in column 3
cm^{-1}	cm^{-1}	cm^{-1}	cm^{-1}
301.87		------	------
298.42	+0.08	166.71	
290.74	+0.09	161.79	−0.03
289.46	−0.13	160.17	−0.03
285.98	+0.01	------	------
------	------	152.50	
248.87		151.30	−0.24
247.94	−0.16	159.52	+0.08
245.34	+0.13	149.06	+0.15
------	------	144.96	+0.13
227.83		141.46	+0.03
226.27	+0.10	140.70	−0.01
223.72	−0.06	------	------
221.67	+0.06	139.02	
214.59	+0.06	135.89	−0.06
213.95	−0.03	135.06	+0.08
212.59	−0.01	133.43	−0.14
208.46	+0.02	------	------
------	------	127.02	
194.37		122.88	−0.06
193.45	+0.03	121.88	−0.07
188.21	−0.16	120.50	+0.08
183.46	+0.08	120.12	−0.10
181.40	−0.04	117.92	+0.07
116.64	−0.07	------	------
111.11	+0.01		
107.79	0.00		
107.15	−0.01		
106.12	−0.03		
105.67	+0.04	58.87	
		57.29	+0.06
------	------	55.69	−0.04
100.53			
99.07	−0.03		
96.05	+0.07		
92.54	−0.05		
89.53	+0.09		
88.87	−0.03		
88.06	−0.09		
85.60	+0.10		
82.11	−0.01		
80.98	+0.05		
79.77	0.00		
78.97	−0.08		
78.21	+0.08		
------	------		
74.09			
73.24	+0.04		
72.21	−0.05		
------	------		

*Interpolations are made between alternate lines, e.g., the value for line 298.42 cm^{-1} was obtained by linearlyi nterpolating between lines 301.87 and 290.74 cm^{-1}.

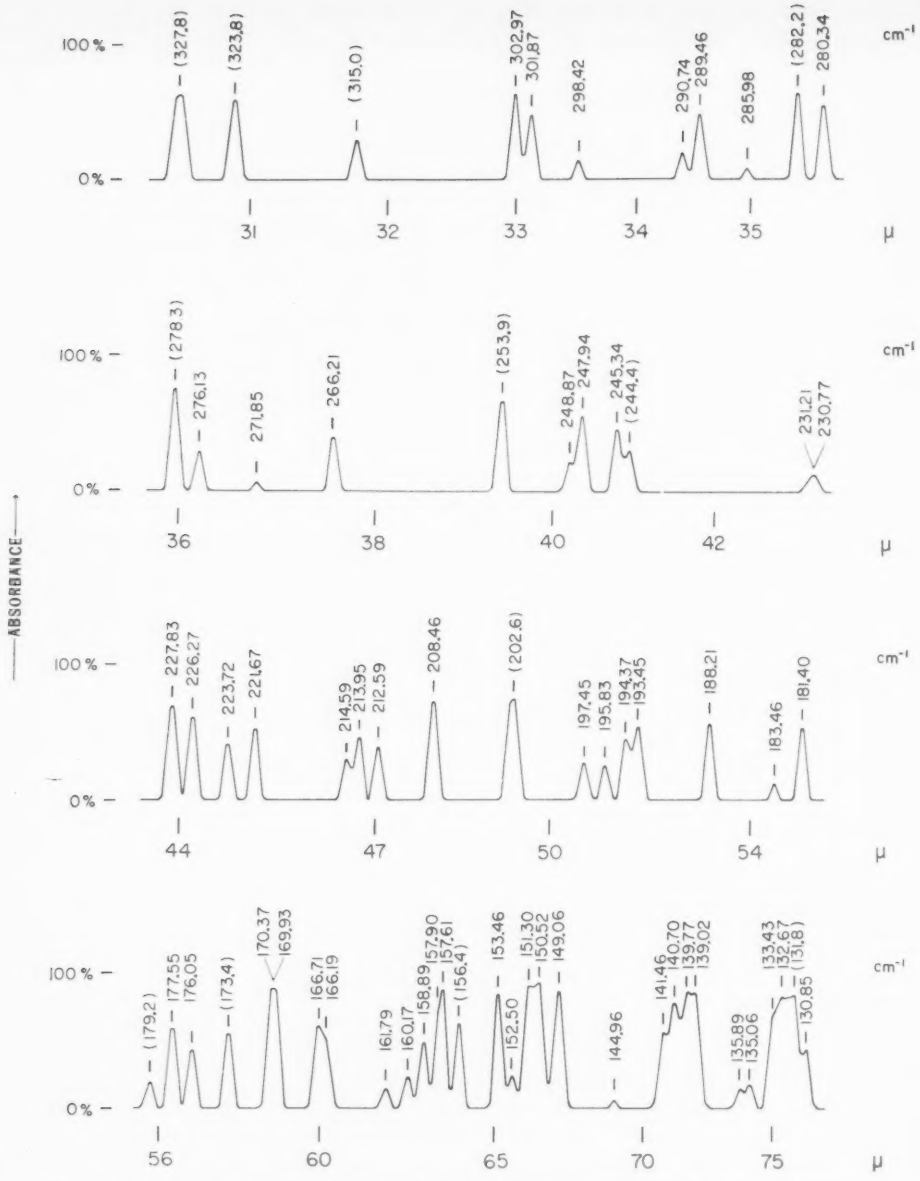

FIGURE 3. *Pure rotational lines of* H_2O *recorded with a Perkin–Elmer model 301 spectrophotometer.*

(A) Spectrometer flushed with dry nitrogen. (B) Spectrometer flushed with dry nitrogen and P_2O_5 trays were kept inside the spectrometer for 12 hours before observations were recorded. The wave number value given for each pure rotational line of the H_2O molecule refers to vacuum. The spectrum shown above has been recorded by keeping the grating in air. It is believed that these water vapor lines may serve to identify the spectral region and provide calibrations to an accuracy of ± 0.10 cm^{-1}.

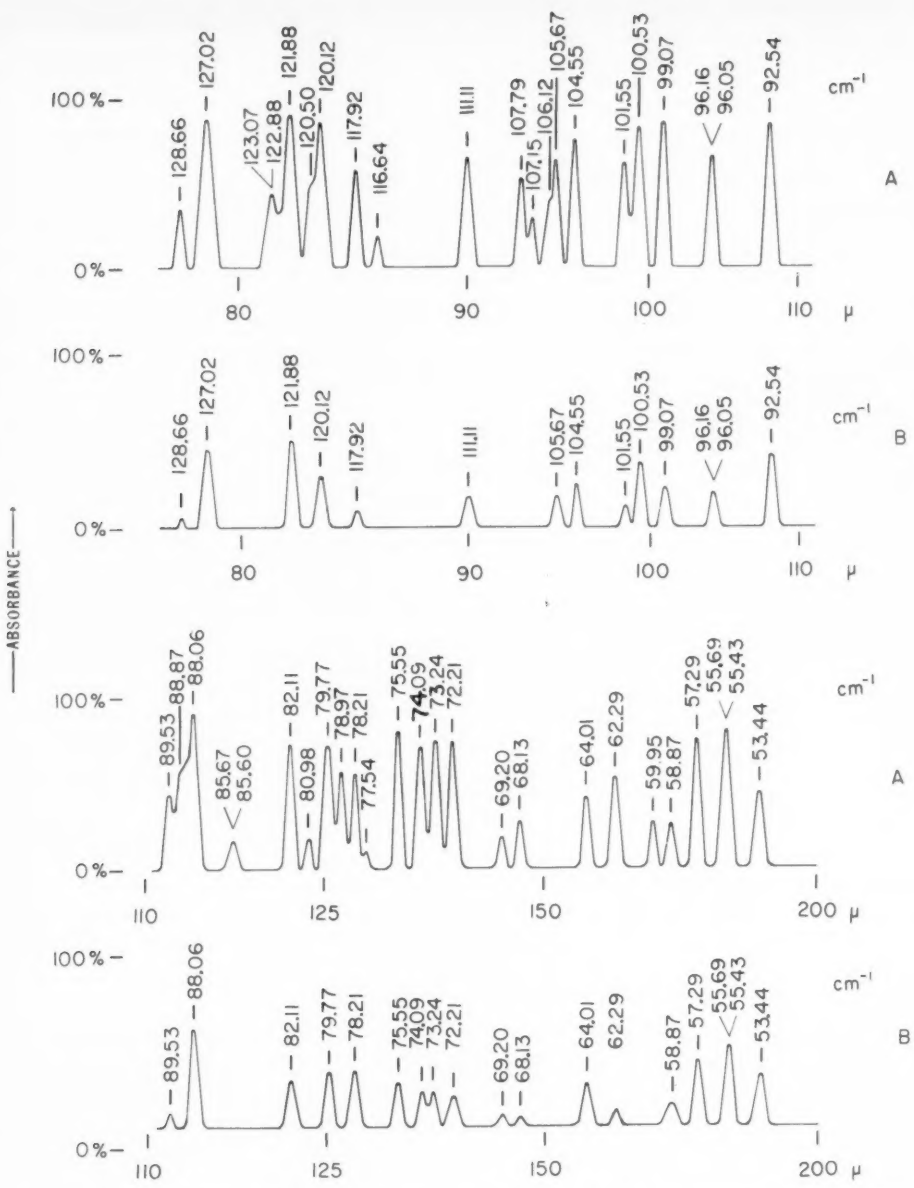

FIGURE 3. *Pure rotational lines of* H^2O *recorded with a Perkins–Elmer model 301 spectrophotometer.*—Continued.

water vapor obtained with a small grating spectrometer in the region 600 to 166 cm^{-1} have been published by Plyler et al. [13]. Also, the paper by Rao et al. [14] gives a map and measurements (to an accuracy of ± 0.02 cm^{-1}) of the pure rotational lines of the H_2O molecule, in the region 550 to 270 cm^{-1} as obtained with a 1000 lines per inch Bausch and Lomb plane replica grating installed in a Pfund-type vacuum spectrometer.

One of us (KNR) wishes to express his deep gratitude to the U.S. Army Research Office (Durham, N.C.) and to the National Science Foundation for their financial support through contracts with the Ohio State University Research Foundation. Our thanks are also due to Dr. W. S. Benedict for supplying us with his analysis of the presently available data pertaining to the infrared rotational lines of the H_2O molecule.

(Paper 67A4–225)

5. References

[1] Calibrating Wave Numbers for the Calibration of Infrared Spectrometers, published by the International Union of Pure and Applied Chemistry, Butterworths, London (1961).
[2] C. C. Helms and R. E. Anacreon, J. Opt. Soc. Am. **50,** 511 (1960).
[3] Earle K. Plyler, L. R. Blaine, and E. D. Tidwell, J. Research NBS **55,** 279 (1955).
[4] K. Narahari Rao, L. R. Ryan, and Harald H. Nielsen, J Opt. Soc. Am. **49,** 216 (1959).
[5] K. Narahari Rao, T. J. Coburn, J. S. Garing, K. Rossmann, and H. H. Nielsen, J. Opt. Soc. Am. **49,** 221 (1959).
[6] D. H. Rank, J. Opt. Soc. Am. **50,** 657 (1960).
[7] K. Narahari Rao, W. W. Brim, and J. M. Hoffman, J. Opt. Soc. Am. **50,** 228 (1960).
[8] D. H. Rank, A. H. Geunther, G. D. Saksena, J. N. Shearer, and T. A. Wiggins, J. Opt. Soc. Am. **47,** 686 (1957).
[9] Earle K. Plyler, L. R. Blaine, and W. S. Connor, J. Opt. Soc. Am. **45,** 102 (1955).
[10] D. H. Rank, D. P. Eastman, B. S. Rao, and T. A. Wiggins, J. Opt. Soc. Am. **51,** 929 (1961).
[11] E. D. Tidwell, E. K. Plyler, and W. S. Benedict, J. Opt. Soc. Am. **50,** 1243 (1960).
[12] W. S. Benedict (private communication).
[13] L. R. Blaine, E. K. Plyler, and W. S. Benedict, J. Research NBS **66A** (Phys. and Chem.) No. 3,223 (1962).
[14] K. Narahari Rao, W. W. Brim, V. L. Sinnett, and R. H. Wilson, J. Opt. Soc. Am. **52,** 862 (1962).

JOURNAL OF RESEARCH of the National Bureau of Standards—A. Physics and Chemistry
Vol. 67A, No. 4, July–August 1963

On the Fourth Order Hamiltonian of an Asymmetric Rotor Molecule of Orthorhombic Symmetry

Wm. B. Olson and H. C. Allen, Jr.

(March 2, 1963)

The fourth order Hamiltonian of an asymmetric rotor molecule of orthorhombic symmetry given recently has been considerably reduced in complexity through the use of equations derived from the basic relationship among the angular momentum operators. The reduced Hamiltonian obtained provides a most convenient starting point for the calculation of rotational energy levels from a solution of the complete secular equation, for a perturbation theory solution to the problem of centrifugal distortion, and for the deduction of sum rules among the energy levels.

1. Introduction

Recently Chung and Parker [1] [1] have examined the general molecular vibrational-rotational Hamiltonian in the Goldsmith-Amat-Nielsen [2] formulation. They deduced Hamiltonians for asymmetric rotor molecules of orthorhombic, monoclinic, and triclinic point group symmetries and have included in their work all terms in P^4 to the fourth order of approximation. No terms in P^6 were included in their work, nor will they be included subsequently in this.

For the case of the asymmetric rotor Hamiltonian for molecules of the orthorhombic point groups (C_{2v}, V, and V_h) it is possible to reduce the Hamiltonian considerably and, by a redefinition of coefficients, to make valid a considerable body of previous work. It is our purpose to carry out these reductions, relate the results to previous work, and to provide a first order perturbation theory solution to the problem of centrifugal distortion, which, while entirely equivalent to that of Kivelson and Wilson [3], is in somewhat simpler form.

2. The Hamiltonian

We start with eq (17) of Chung and Parker in the molecular axis system of coordinates defined by the standard spectroscopic convention $I_a^e<I_b^e<I_c^e$. The following relations among the angular momentum operators that are useful for reducing the Hamiltonian may be derived from the commutation rules for the angular momentum operators.

$$P_\alpha^2P_\beta^2+P_\beta^2P_\alpha^2=P^4+P_\gamma^4-P_\alpha^4-P_\beta^4-2P^2P_\gamma^2 \tag{1}$$

$$P_\alpha P_\beta P_\alpha P_\beta+P_\beta P_\alpha P_\beta P_\alpha=P^4+P_\gamma^4-P_\alpha^4-P_\beta^4-2P^2P_\gamma^2+\hbar^2(P_\gamma^2-P_\alpha^2-P_\beta^2) \tag{2}$$

$$P_\alpha P_\beta^2 P_\alpha=\tfrac{1}{2}[P^4+P_\gamma^4-P_\alpha^4-P_\beta^4-2P^2P_\gamma^2+2\hbar^2(P_\gamma^2-P_\beta^2)] \qquad \alpha\neq\beta\neq\gamma=a,\ b,\ \text{or}\ c\ (\text{or}\ x,\ y,\ \text{or}\ z). \tag{3}$$

With the help of these relations we obtain a reduced Hamiltonian for molecules belonging to the orthorhombic point groups,

$$H^r=h_v^{r*}+\sum_\alpha \alpha_v' P_\alpha^2-\tfrac{1}{2}P^2\sum_\alpha \tau_{\beta\beta\gamma\gamma}^v P_\alpha^2+\tfrac{1}{4}\sum_\alpha \tau_{\alpha\alpha\beta\beta}^v P^4+\tfrac{1}{4}\sum_\alpha(\tau_{\alpha\alpha\alpha\alpha}^v+\tau_{\beta\beta\gamma\gamma}^v-\tau_{\alpha\alpha\beta\beta}^v-\tau_{\alpha\alpha\gamma\gamma}^v)P_\alpha^4$$
$$\alpha\neq\beta\neq\gamma=a, b, \text{and } c \text{ in cyclic order.} \tag{4}$$

[1] Figures in brackets indicate the literature references at the end of this paper.

In (4) the following definitions have been used for the constants

$$\alpha_v' = \alpha_{v'} + \tfrac{1}{4}\hbar^2 \tau_a^v \tag{5}$$

in which the $\alpha_{v'}$ are the $\mathfrak{A}$, $\mathfrak{B}$, and $\mathfrak{C}$ of Chung and Parker and where the A, B, and C of Chung and Parker are the reciprocal of twice the respective moments of inertia. Also:

$$\tau_a^v = 3\tau_{\beta\gamma\beta\gamma} + \rho_{\beta\gamma\beta\gamma} + \rho_{\beta\gamma\gamma\beta} + \rho_{\gamma\beta\beta\gamma} - 2\tau_{\alpha\beta\alpha\beta} - \rho_{\alpha\beta\alpha\beta} - \rho_{\beta\alpha\alpha\beta} - 2\tau_{\alpha\gamma\alpha\gamma} - \rho_{\alpha\gamma\alpha\gamma} - \rho_{\gamma\alpha\alpha\gamma} \tag{6}$$

$$\tau_{aaaa}^v = \tau_{aaaa} + \rho_{aaaa} \tag{7}$$

$$\tau_{aa\beta\beta}^v = \tau_{aa\beta\beta}^{v'} + 2\tau_{a\beta a\beta}^{v'} \tag{8}$$

$$\tau_{aa\beta\beta}^{v'} = \tau_{aa\beta\beta} + \rho_{aa\beta\beta} \tag{9}$$

$$2\tau_{a\beta a\beta}^{v'} = 2\tau_{a\beta a\beta} + \rho_{a\beta a\beta} + \tfrac{1}{2}(\rho_{a\beta\beta a} + \rho_{\beta aa\beta}). \tag{10}$$

In the preceding $h_v^{\dagger *}$ and the $\tau_{\alpha\beta\gamma\delta}$ and $\rho_{\alpha\beta\gamma\delta}$ are those of Chung and Parker, the $\tau_{\alpha\beta\gamma\delta}$ of Chung and Parker being the reciprocal of $\hbar^4$ times those of Kivelson and Wilson.

This convenient form of the Hamiltonian reveals that a constant similar to D_J in the energy expression for linear, spherical and symmetric rotors may be defined, that is, a coefficient of $J^2(J+1)^2$ in the energy. Since this term is diagonal in J, K, M it may be factored out of the secular equation before its solution.

The cyclic nature of (4) indicates that this Hamiltonian may be solved using the systematic procedures introduced by King, Hainer, and Cross, [4] after extension of the latter to contain the matrix elements of the operators P_a^4, by the choice of the most convenient representation, $I^r \ldots . III^l$, defined by King, Hainer, and Cross (see table II, ref. 4).

Defining the effective rotational constants A_v, B_v, and C_v in energy units as:

$$\alpha_v = \alpha_v' \hbar^2, \tag{11}$$

remembering that $P^4 = P^2(P_x^2 + P_y^2 + P_z^2)$, and using the definition:

$$\tau_{aa}^v = \tau_{\beta\beta\gamma\gamma}^v - \tau_{\gamma\gamma aa}^v - \tau_{aa\beta\beta}^v, \tag{12}$$

where α, β and γ are taken as a, b, and c in cyclic order, we arrive at the following most convenient and explicit form for the vibrational-rotational part of the Hamiltonian:

$$\begin{aligned} H = H^t - h_v^{\dagger *} = {} & [A_v/\hbar^2 - J(J+1)(\hbar^2/4)\tau_{aa}^v]P_a^2 + [B_v/\hbar^2 - J(J+1)(\hbar^2/4)\tau_{bb}^v]\, P_b^2 \\ & + [C_v/\hbar^2 - J(J+1)(\hbar^2/4)\tau_{cc}^v]P_c^2 + \tfrac{1}{4}(\tau_{aaaa}^v + \tau_{aa}^v)P_a^4 \\ & + \tfrac{1}{4}(\tau_{bbbb}^v + \tau_{bb}^v)P_b^4 + \tfrac{1}{4}(\tau_{cccc}^v + \tau_{cc}^v)P_c^4 \end{aligned} \tag{13}$$

In (13) no cross terms between the components of the angular momentum appear explicitly and the secular equation is readily set up using only the matrix elements of P_a^2, P_b^2, P_c^2, P_a^4, P_b^4 and P_c^4.

In order to make use of the systematization introduced by King, Hainer, and Cross the elements of P_x^4 and P_y^4 must be used in the same phase as they chose for P_x and P_y. Nowhere in the literature are these elements given using this phase. They are, however, readily deduced from those given by Wilson [5] since the only change required from his matrix elements is a reversal in sign of the K, $K \pm 2$ elements of P_x^4 and P_y^4.

The coefficients of P_a^2, P_b^2, and P_c^2 can be regarded as effective inertial parameters with a J dependence in setting up the secular equation. Since the secular equation has no mixing between blocks of different J-factors, this observation can be used to reduce the work in solving the secular determinant. One merely uses a different set of effective inertial parameters for each J-factor.

Each J-factor can be further factored as in the case of the rigid asymmetric rotor into four factors that can be called $E^{\pm}$ and $O^{\pm}$ in complete analogy with the rigid case. These factors are conveniently written as:

$$E^{\pm}=\begin{vmatrix} E_{00} & \sqrt{2}E_{02} & \sqrt{2}E_{04} & 0 & . & . \\ \cdot & \cdot & \cdot & \cdot & \cdot & \cdot \\ \sqrt{2}E_{02} & (E_{22}\pm E_{2-2}) & E_{24} & E_{26} & 0 & . \\ \sqrt{2}E_{04} & E_{24} & E_{44} & E_{46} & E_{48} & 0 \\ 0 & E_{26} & E_{46} & E_{66} & E_{68} & E_{6,10} \\ 0 & 0 & . & . & . & \end{vmatrix}$$

and (14)

$$O^{\pm}=\begin{vmatrix} (E_{11}\pm E_{1-1}) & E_{13} & E_{15} & 0 & . & . \\ E_{13} & E_{33} & E_{35} & E_{37} & 0 & . \\ E_{15} & E_{35} & E_{55} & E_{57} & E_{59} & 0 \\ 0 & E_{37} & E_{57} & E_{77} & E_{79} & E_{7,11} \\ 0 & 0 & . & . & . & . \end{vmatrix}$$

where E^- is obtained from E^+ by removing the first row and column as indicated by the dots.

3. First Order Perturbation Theory

Equation (13) forms a convenient starting point for a perturbation treatment. In a first-order treatment the desired energies involve only the diagonal values of the perturbing operators. Consequently, eq (13) may be rewritten using only the average values of these operators in a representation in which the semirigid energy is diagonal,

$$E=E_0^J+\tfrac{1}{4}(\tau^r_{aaaa}+\tau^r_{aa})\langle P_a^4\rangle+\tfrac{1}{4}(\tau^r_{bbbb}+\tau^r_{bb})\langle P_b^4\rangle+\tfrac{1}{4}(\tau^r_{cccc}+\tau^r_{cc})\langle P_c^4\rangle. \tag{15}$$

The values of $\langle P_a^4\rangle$, $\langle P_b^4\rangle$, and $\langle P_c^4\rangle$ can be obtained from the work of Schwendeman [6].

For some purposes it may be convenient to use the symmetric rotor type centrifugal distortion constants given by Kivelson and Wilson rather than the $\tau^r_{\alpha\beta\gamma\delta}$. These centrifugal distortion constants of Kivelson and Wilson can be given accurate to the present order of approximation of the Hamiltonian by simply replacing the $\tau'_{\alpha\beta\gamma\delta}$ of Kivelson and Wilson by $\tau^r_{\alpha\beta\gamma\delta}$.

4. Sum Rules

Recently sum rules for the energy levels of an orthorhombic asymmetric rotor have been published [7]. By the substitution mentioned above in a I^r representation [4] these sum rules can be made valid to the present order of approximation. To obtain these sum rules substitute the right hand side of the following equations for the terms on the left hand side which appear in the sum rules.

$$A=A_v$$

$$B=B_v$$

$$C=C_v$$

$$R_6-\frac{1}{10}DK=\frac{1}{40}[(\tau^v_{aaaa}+\tau^v_{bbbb}+\tau^v_{cccc})+(\tau^v_{aa}+\tau^v_{bb}+\tau^v_{cc})]$$

$$-\frac{1}{30}(15D_J+5D_{JK}+3D_K)=\frac{1}{40}[(\tau^v_{aaaa}+\tau^v_{bbbb}+\tau^v_{cccc})-\tfrac{3}{5}(\tau^v_{aa}+\tau^v_{bb}+\tau^v_{cc})]$$

$$D_J-2\delta_J-\frac{1}{5}D_K=\frac{1}{20}[(\tau^v_{aaaa}+\tau^v_{bbbb}-4\tau^v_{cccc})+(\tau^v_{aa}+\tau^v_{bb}+\tau^v_{cc})]$$

$$D_J+2\delta_J-\frac{1}{5}D_K=\frac{1}{20}[(\tau^v_{aaaa}+\tau^v_{cccc}-4\tau^v_{bbbb})+(\tau^v_{aa}+\tau^v_{bb}+\tau^v_{cc})] \tag{16}$$

$$D_J-R_6-\frac{1}{10}D_K=\frac{1}{40}[(\tau^v_{aaaa}-4\tau^v_{bbbb}-4\tau^v_{cccc})+(\tau^v_{aa}+\tau^v_{bb}+\tau^v_{cc})]$$

$$6R_6+\frac{1}{5}D_K=\frac{1}{40}[(3\tau^v_{bbbb}+3\tau^v_{cccc}-2\tau^v_{aaaa})+(3\tau^v_{bb}+3\tau^v_{cc}-2\tau^v_{aa})]$$

$$2(R_5+R_6+\tfrac{1}{10}D_K)=\frac{1}{40}[(3\tau^v_{cccc}-2\tau^v_{bbbb}-2\tau^v_{aaaa})+(3\tau^v_{cc}-2\tau^v_{bb}-2\tau^v_{aa})]$$

$$2(R_5-R_6-\tfrac{1}{10}D_K)=\frac{1}{40}[(2\tau^v_{cccc}+2\tau^v_{aaaa}-3\tau^v_{bbbb})+(2\tau^v_{cc}+2\tau^v_{aa}-3\tau^v_{bb})].$$

5. Planar Orthorhombic Molecule

Dowling [8] and Oka and Morino [9] have given relations among the $\tau_{\alpha\beta\gamma\delta}$ of a planar orthorhombic molecule. Noting that the plane of the molecule must be the *ab* plane these become

$$\tau_{bcbc}=\tau_{caca}=0$$

$$\tau_{bbbb}=\left(\frac{B_e}{C_e}\right)^2\tau_{bbcc}-\left(\frac{B_e}{A_e}\right)^2\tau_{aabb}$$

$$\tau_{cccc}=\left(\frac{C_e}{B_e}\right)^2\tau_{bbcc}+\left(\frac{C_e}{A_e}\right)^2\tau_{ccaa}$$

$$\tau_{aaaa}=\left(\frac{A_e}{C_e}\right)^2\tau_{ccaa}-\left(\frac{A_e}{B_e}\right)^2\tau_{aabb}.$$

As corresponding relations among the $\rho_{\alpha\beta\gamma\delta}$ of the planar orthorhombic molecule have not yet been worked out, no special relations can yet be said to exist among the $\tau^v_{\alpha\beta\gamma\delta}$.

6. Conclusion

The Hamiltonian of an orthorhombic asymmetric rotor molecule, to the approximation considered in this work, has been set up in nine effective constants occurring as coefficients of six rotational operators.

This Hamiltonian appears to be in the simplest possible form, and to provide the most convenient starting point for any type of calculation concerning the rotation of this type of molecule.

7. References

[1] K. T. Chung and P. M. Parker, J. Chem. Phys. **38,** 8 (1963).
[2] M. Goldsmith, G. Amat, and H. H. Nielsen, J. Chem. Phys. **24,** 1178 (1956); **27,** 838 (1957). For further references to this series see ref. 1.
[3] D. Kivelson and E. B. Wilson, Jr., J. Chem. Phys. **20,** 1575 (1952).
[4] G. W. King, R. M. Hainer, and P. C. Cross, J. Chem. Phys. **11,** 27 (1943).
[5] E. B. Wilson, Jr., J. Chem. Phys. **5,** 617 (1937).
[6] R. H. Schwendeman, to be published.
[7] H. C. Allen, Jr., and W. B. Olson, J. Chem. Phys. **37,** 212 (1962).
[8] Jerome M. Dowling, J. Mol. Spectroscopy **6,** 550 (1961).
[9] T. Oka and Y. Morino, J. Phys. Soc. Japan **16,** 1235 (1961).

(Paper 67A4–226)

JOURNAL OF RESEARCH of the National Bureau of Standards—A. Physics and Chemistry
Vol. 67A, No. 4, July–August 1963

Measurement of the Thickness and Refractive Index of Very Thin Films and the Optical Properties of Surfaces by Ellipsometry[1]

Frank L. McCrackin, Elio Passaglia, Robert R. Stromberg, and Harold L. Steinberg

(April 11, 1963)

The use of the ellipsometer for the measurement of the thickness and refractive index of very thin films is reviewed. The Poincaré sphere representation of the state of polarization of light is developed and used to describe the reflection process. Details of the operation of the ellipsometer are examined critically. A computational method is presented by which the thickness of a film of known refractive index on a reflecting substrate of known optical constants may be calculated directly from the ellipsometer readings. A method for computing both the refractive index and thickness of an unknown film is also developed. These methods have been applied to the determination of the thickness of an adsorbed water layer on chromium ferrotype plates and on gold surfaces. In the former case the thickness was 23 to 27 Å, and in the latter was 2 to 5 Å. The measurement of the thickness and refractive index of barium fluoride films evaporated on chromium ferrotype surfaces is used as an illustration of the simultaneous determination of these two quantities.

1. Introduction

Ellipsometry is a convenient and accurate technique for the measurement of thicknesses and refractive indexes of very thin films on solid surfaces and for the measurement of optical constants of reflecting surfaces. The lower limit of film thicknesses that can be studied by ellipsometry is at least an order of magnitude smaller than can be studied by other means such as interferometry. Artifacts such as those caused by vacuum in the case of electron microscopy are not encountered. Neither interferometry nor electron microscopy are adaptable, as is ellipsometry, to the study of films under liquids, and only ellipsometry will give the index of refraction of films of unknown thickness.

The technique of ellipsometry is concerned with the measurement of changes in the state of polarization of light upon reflection from a surface. For a clean reflecting surface the optical constants of the surface and the reflection coefficients of the system may be calculated from these changes. A thin transparent film on the reflecting surface causes additional changes from which the thickness and refractive index of the film may be determined.

The principle of the ellipsometer has been described by several authors [e.g., 1–7][2] and a bibliography of the theoretical contributions of many authors, starting with the original equations of Drude [1] is given by Winterbottom [2]. This paper will describe certain measurement techniques and an application of the exact solution of the algebraic equations of Drude to the measurement of optical constants of surfaces and thickness and refractive index of thin films covering the surfaces. A generally applicable computational method is described. The complex and lengthy calculations required to solve the equations involved have been programmed for an electronic computer. Measurements carried out on chrome and gold surfaces with and without films will also be described.

In addition, the Poincaré sphere representation of the state of polarization of light will be developed since this is the most useful representation for the consideration of the effects occurring on reflection.

2. Representations of Elliptically Polarized Light

The state of polarization of elliptically polarized light may be described in many ways. For this purpose, consider a light wave traveling along the Z axis of a coordinate system. The electric vector of the wave is then given by:

$$\begin{aligned} E_X &= a_1 \cos(\tau+\delta_1) \\ E_Y &= a_2 \cos(\tau+\delta_2) \end{aligned} \qquad (1)$$

where $\tau=\omega\left(t-\frac{z}{v}\right)$, ω and v are the angular frequency and linear velocity of the light, respectively, and the total amplitude is the vector sum of a_1 and a_2. The polarization can be described by the amplitudes, a_1 and a_2, and the phase difference, $\delta=\delta_2-\delta_1$, of the components. As is well known, in a stationary plane whose normal is parallel to the Z axis the locus of the end of the electric vector is the ellipse shown in figure 1.

The ellipse, however, may also be described in relation to coordinates X' and Y' along the axes of the ellipse. Thus, the inclination φ of these coordinates and the semiaxes a and b of the ellipse also describe the polarization of the light.

[1] The work reported here was supported in part by the Army Research Office (Durham) and in part by the Bureau of Naval Weapons.
[2] Figures in brackets indicate the literature references at the end of this paper.

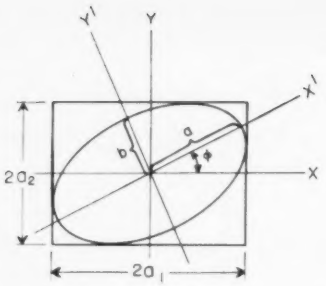

FIGURE 1. *The locus of the electric vector for elliptically polarized light in a plane normal to the direction of propagation.*

The coordinate axes XY and $X'Y'$ are both convenient for the description of the ellipse.

It will be convenient to introduce auxiliary angles α and χ defined by

$$\tan \alpha = \frac{a_2}{a_1} \tag{2}$$

$$\tan \chi = \pm \frac{b}{a}. \tag{3}$$

The numerical value of $\tan \chi$ represents the ratio of the minor to major axes of the ellipse and the sign of χ distinguishes the two senses in which the ellipse may be described. The angles χ and φ are called the ellipticity and azimuth of the light, respectively, and the representation may be made either in terms of a_1, a_2, and δ; α, δ, and the total amplitude; or φ, χ, and the total amplitude.

Another representation of the state of polarization, and one which leads quite naturally to the Poincaré sphere is by parameters which all have the same physical dimensions, called Stokes parameters [8]:

$$\begin{aligned} S_0 &= a_1^2 + a_2^2 \\ S_1 &= a_1^2 - a_2^2 \\ S_2 &= 2a_1 a_2 \cos \delta \\ S_3 &= 2a_1 a_2 \sin \delta. \end{aligned} \tag{4}$$

The parameter S_0 is proportional to the intensity of the wave and is related to the other parameters by the identity $S_0^2 = S_1^2 + S_2^2 + S_3^2$, so that the Stokes parameters are not all independent.

It has been shown [9, 10] that the Stokes parameters are also given by

$$\begin{aligned} S_1 &= S_0 \cos 2\chi \cos 2\varphi \\ S_2 &= S_0 \cos 2\chi \sin 2\varphi \\ S_3 &= S_0 \sin 2\chi. \end{aligned} \tag{5}$$

Therefore, the state of polarization may be represented by a point on a sphere of radius S_0 by the spherical coordinates S_0, 2φ, 2χ. This sphere is called the Poincaré sphere. Alternatively, the Stokes parameters S_1, S_2, and S_3 may be used as Cartesian coordinates to describe the polarization. This representation is illustrated in figure 2.

Since the intensity of the light is of secondary importance for use of the ellipsometer, the projection of the point on a sphere of unit radius is convenient. The coordinates are then given by

$$\begin{aligned} s_0 &= 1 \\ s_1 &= \frac{1 - \tan^2 \alpha}{1 + \tan^2 \alpha} = \cos 2\chi \cos 2\varphi \\ s_2 &= \frac{2 \tan \alpha \cos \delta}{1 + \tan^2 \alpha} = \cos 2\chi \sin 2\varphi \\ s_3 &= \frac{2 \tan \alpha \sin \delta}{1 + \tan^2 \alpha} = \sin 2\chi. \end{aligned} \tag{6}$$

Light of a given state of polarization is therefore represented by a point on the sphere, with the polar angles 2φ and 2χ representing, respectively, twice the azimuth and twice the ellipticity of the light. For example, for plane polarized light, the ellipticity χ is zero, and $s_3 = 0$. Therefore, plane polarized light is represented by points on the equator of the Poincaré sphere. Also, the ellipticity of circularly polarized light is 45°, whence $s_1 = s_2 = 0$, $2\chi = \pm\pi/2$; thus, circularly polarized light is represented by the poles of the sphere.

The Poincaré sphere may be used to represent elliptically polarized light with respect to any physical axes, say X'' and Y'' at an angle φ'' with the XY axis. The ellipticity χ is not dependent on the choice of axes and the azimuth of the light is changed by φ''. Thus the S_1 and S_2 axes must be rotated an angle $2\varphi''$ around the S_3 axis.

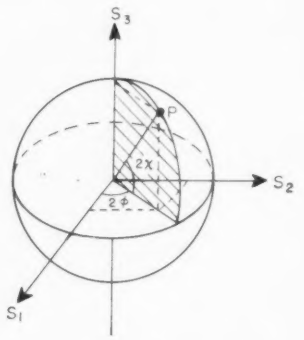

FIGURE 2. *Representation of polarized light on the Poincaré sphere.*

The point P represents light with ellipticity χ and azimuth ψ. The cartesian coordinates are Stokes parameters (after Born and Wolf [9]).

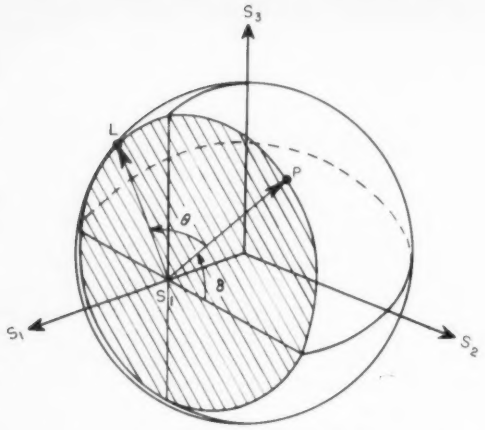

FIGURE 3. *The intersection of the Poincaré sphere and a plane normal to the S_1 axis at $s_1=(1-\tan^2\alpha)/(1+\tan^2\alpha)$ for the consideration of the effect of a doubly refracting plate with retardation θ on light with ellipticity represented by* P.

The plate rotates P to L. The fast axis of the plate is along S_1.

The Poincaré sphere is convenient for consideration of the effects of doubly refracting plates and reflection on the state of polarization of a light beam. For example, let the polarized wave represented in figure 1 pass through a doubly refracting plate of relative phase retardation θ. Choose the X and Y axes in figure 1 along the slow and fast axes of the plate. Since the azimuth of the fast axis of the plate is zero, it is represented by the positive S_1 axis. In this case there will be no change in the amplitudes a_1 and a_2 of the components of the light, and therefore no change in α or in s_1 as shown by eq (6), the only effect being to change the relative phase of the components by θ. Thus, upon passing through the plate the point representing the polarization will remain on the curve representing constant s_1, or on the intersection of the sphere and the plane $s_1=$ constant. The intersection of the Poincaré sphere by a plane perpendicular to the S_1 axis at s_1, shown in figure 3, is a circle of radius $\frac{2\tan\alpha}{1+\tan^2\alpha}$. The light incident on the plate is represented by the point P, and after passing through the plate is represented by the point L. The effect of the doubly refracting plate is seen to turn points on the sphere about the S_1 axis by an angle θ. If the plate had been oriented with its fast axis at an azimuth φ' with respect to the XY axes, the rotation by θ would have been about the line from the center of the sphere and the point $2\varphi'$ on the equator.

Reflection at a metal surface may be represented similarly. For reflection, the incident light wave is resolved into components in the plane of incidence and normal to the plane of incidence (the plane of the surface). The process of reflection introduces a phase difference Δ between these two components, and changes the ratio of their amplitudes by a factor $\tan\psi$; that is, $\tan\psi$ is a measure of the relative absorption of the two components. Thus, the ratio of the reflection coefficient for light polarized in the plane of incidence to that for light polarized in the plane of the surface is given (3) by

$$\rho=\frac{r_p}{r_s}=\tan\psi e^{j\Delta} \tag{7}$$

where ρ is the ratio of the reflection coefficients r_p and r_s, and ψ and Δ are functions of the optical constants of the surface, the wavelength of the light used, the angle of incidence, and, for a film covered surface, the thickness and refractive index of the film. (See also eqs 40 to 46.)

For consideration of the reflection process on the Poincaré sphere, represent the light with respect to Cartesian coordinates with the X and Y axes in and normal to the plane of incidence and the Z axis in the direction of propagation. Then $\tan\psi=a_s/a_p$. The Stokes parameters of the light before reflection are given by eq (6) and after reflection are

$$\begin{aligned} s_1'' &= \frac{1-\tan^2\alpha\cot^2\psi}{1+\tan^2\alpha\cot^2\psi} \\ s_2'' &= \frac{2\tan\alpha\cot\psi\cos(\delta+\Delta)}{1+\tan^2\alpha\cot^2\psi} \\ s_3'' &= \frac{2\tan\alpha\cot\psi\sin(\delta+\Delta)}{1+\tan^2\alpha\cot^2\psi} \end{aligned} \tag{8}$$

The reflection is represented on a Poincaré sphere in figure 4. The point I_p represents the intersection

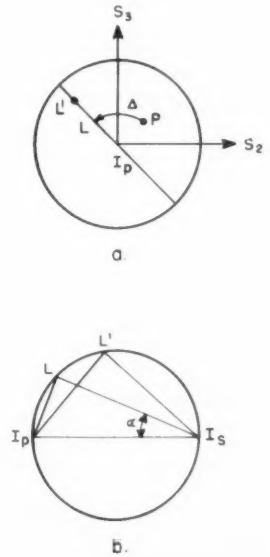

FIGURE 4. *Representation of metallic reflection on the Ponicaré sphere.*

The azimuth of the plane of incidence is represented by I_p and the plane of the surface by L. In part a the view is along the S_1 axis. The point P is rotated to L around the S_1 axis by the retardation Δ of the surface. Relative absorption of the components in and normal to the plane of incidence causes translation of L to L' along the great circle I_p-L. The view in b is normal to this great circle.

of the axis S_1 with the sphere and has the Cartesian coordinate $s_1=1$, $s_2=0$, $s_3=0$. By eq (6) this corresponds to zero ellipticity, χ, and azimuth, φ, so it represents the orientation of the X axis, or the plane of incidence. Likewise, the point I_s has Cartesian coordinates $(-1, 0, 0)$, so it corresponds to zero ellipticity and an azimuth $\pi/2$. Therefore, the point I_s represents the orientation of the Y axis or plane of the surface. The point P representing the polarization of the incident light is rotated around the S_1 axis through an angle Δ, the phase change produced by reflection, to the point L. The Stokes parameters of L are

$$s_1'=\frac{1-\tan^2\alpha}{1+\tan^2\alpha}$$

$$s_2'=\frac{2\tan\alpha\cos(\delta+\Delta)}{1+\tan^2\alpha} \tag{9}$$

$$s_3'=\frac{2\tan\alpha\sin(\delta+\Delta)}{1+\tan^2\alpha}$$

In addition, the relative absorption of the components translates the point L to the point L', the Stokes parameters for which are given by eqs (8).

From eqs (8) and (9) we have $s_3''/s_2''=s_3'/s_2'=\tan(\delta+\Delta)$. Points L and L' will, therefore, lie on the great circle given by the locus of points on the sphere with $s_3/s_2=\tan(\delta+\Delta)$. This locus is shown in figures 4a and 4b and is given by the intersection of the sphere with a plane passing through the point L and normal to the axis S_1. Thus the point L must be moved along the great circle defined above to point L' to represent the polarization of the reflected light. The position of L' on this great circle will now be derived. The Cartesian coordinates of I_p and of I_s are $(1, 0, 0)$ and $(-1, 0, 0)$, respectively, and the coordinates of L are given by eqs (9). Therefore, the length of the chords I_pL and I_sL are

$$I_pL=\frac{2\tan\alpha}{(1+\tan^2\alpha)^{1/2}}$$

$$I_sL=\frac{2}{(1+\tan^2\alpha)^{1/2}} \tag{10}$$

so

$$\frac{I_pL}{I_sL}=\tan\alpha. \tag{11}$$

The angle I_pLI_s is a right angle since it is inscribed in a semicircle. Therefore, the angle I_pI_sL is equal to α, and it is clear by eq (2) that the tangent of this angle is equal to the ratio of the amplitudes of the components of the incident light.

The position of L' is determined by the angle I_pI_sL'. The tangent of this angle again gives the ratio of the amplitudes of the components of the reflected light, which is now equal to $\tan\alpha/\tan\psi$. Therefore,

$$\frac{I_pL'}{I_sL'}=\tan(I_pI_sL')=\tan\alpha/\tan\psi \tag{12}$$

and the chord I_pL' may be calculated as

$$I_pL'=\frac{2}{(1+\cot^2\alpha\tan^2\psi)^{1/2}}. \tag{13}$$

Moreover, by eqs (11) and (12), we have

$$\tan\psi=\frac{I_pL/I_sL}{I_pL'/I_sL'} \tag{14}$$

and, in general, the ratio of the chords between a point representing the state of polarization of a given light wave and any two diametrically opposed points on the sphere is equal to the ratio of the amplitudes of the components when the electric vector of the light is resolved along axes represented by these two opposed points.

The Poincaré sphere representation of the reflection of light from a surface with known complex reflection coefficient $\tan\psi e^{j\Delta}$ may now be summarized. The point P, representing the state of polarization of the incident light is moved by the reflection process through an angle Δ on the sphere in a plane normal to the S_1 axis to the point L. The chords I_pL and I_sL are measured and $\tan\alpha$ calculated by eq (11). Finally the angle I_pI_sL' is calculated from eq (12), or the chord I_pL' is calculated from eq (13), thus determining the state of polarization of the reflected light. We shall show later how this representation may be used conveniently for the calculation of the effects occurring on reflection. First, however, we give a brief description of the instrument.

2.1. Instrument

Figure 5 shows the various components of an ellipsometer. Collimated monochromatic light, usually the mercury green line (5460.73Å), is used. The polarizer, a Glan-Thompson or a Nicol prism mounted in a graduated circle, serves to polarize the light emitted by the source. The compensator, also mounted in a graduated circle, is a birefringent plate usually of quarter-wave thickness; it is used to con-

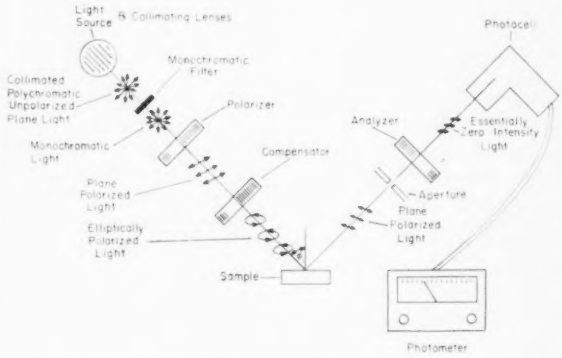

FIGURE 5. *The component parts of an ellipsometer.*

vert the linearly polarized light into elliptically polarized light. The light incident upon the sample has an azimuthal angle and an ellipticity predictable from the settings of the polarizer and compensator. In general, the light will have its ellipticity and azimuth changed by reflection from the sample.

The "aperature" is an adjustable opening allowing a variation in the area of surface examined and the amount of light reaching the phototube. The analyzer, a second prism in a graduated circle, can be rotated until a minimum intensity is achieved, as indicated by the photometer. If some ellipticity exists in the light reaching the analyzer, extinction of the light cannot be obtained by rotation of only the analyzer. The polarizer and analyzer are then adjusted alternately to remove this ellipticity and obtain extinction. When this occurs, the light reflected from the sample is plane polarized and can be thereby extinguished by the analyzer. The phototube and photometer permit determination of the null point with a high degree of sensitivity. For more accurate null point determinations graphical plots of the intensity of the transmitted beam versus angle of polarizer and analyzer may be used [11].

2.2. Alinement

Alinement of the ellipsometer is not too critical for the measurement of thickness and refractive index of thin films. Here the important quantity is the change in readings of the polarizer and analyzer as compared to the values for the bare substrate. However, for obtaining accurate values of the optical constants of surfaces, alinement *is* critical. Moreover, during alinement certain confusing phenomena may occur, and it is worthwhile here to develop the theory of the alinement process.

The procedure for alining the ellipsometer is typical of that generally used in optical spectrometers except for the adjustment of the analyzer (A) and polarizer (P) scales. When alined, the scales for the polarizer and analyzer read zero when the planes of transmission of the prisms are parallel to the plane of incidence. This is accomplished by first adjusting the polarizer and analyzer prisms in their scales so that these scales differ in setting by 90° when the prisms are crossed. These scales, imagined as a unit, must then be rotated so that when the P and A scale read 0 and 90° respectively, the planes of transmission of the two prisms are respectively in the plane of incidence and normal to the plane of incidence. That is, the coordinate system defined by the 0 and 90° settings of both P and A must be made to correspond to the coordinate system defined by the plane of incidence and the plane of the surface.

In principle, the adjustment is relatively simple. With the compensator removed and the polarizer and analyzer arms in the 'straight-through' position, the polarizer and analyzer prisms are adjusted in their respective scales until extinction is achieved with the scale readings differing by 90°. The arms are then set for reflection from a metal surface. A minimum in the photometer reading is sought at which the scale readings differ by 90°. The planes of transmission of the two prisms should then be in the plane of incidence and normal to it. The prisms may now be rotated in their holders until the scale readings are $0 \pm 180°$, and $90 \pm 180°$, and the alinement is complete.

In practice, however, certain subtle effects occur. After having first crossed the prisms when reflecting from the surface, a minimum may be achieved either by fixing P and adjusting A, or vice versa. If the light issuing from the polarizer is accurately plane polarized, then the minimum achieved by either of these two means, and with the P and A scales crossed, occurs at a single value of P and A independent of the procedure followed. However, if the light issuing from the polarizer has some slight ellipticity due to some imperfection in the polarizer, then there are *two* positions at which the prisms are crossed and minimum photometer readings are obtained, depending upon whether the minimum is achieved by fixing P and adjusting A or vice versa. Moreover, the deepest minimum or most complete extinction of the reflected light now occurs at a third point, at which the scales are not crossed. Fortunately, with certain assumptions, even in this case alinement may be achieved quite accurately. We shall first give a theoretical explanation of the phenomena observed, and then give a procedure for alining the ellipsometer.

We shall assume that the polarizer produces light of a constant ellipticity χ whose azimuth changes as the polarizer is rotated. The analyzer is taken to be perfect. It is assumed that the P and A prisms have been adjusted without reflection so that when minimum transmission is achieved the scale readings differ by 90°. The compensator is removed from the system. The process will be depicted on the Poincaré sphere. We consider only ellipticity and azimuth much smaller than unity. In this case the Stokes parameters given by eq (6) are approximated by

$$\begin{aligned} s_1 &= 1 \\ s_2 &= 2\alpha \cos\delta = 2\varphi \\ s_3 &= 2\alpha \sin\delta = 2\chi. \end{aligned} \tag{15}$$

Hence the state of polarization may now be represented by the plane polar coordinates 2α and δ, and this corresponds to representing as a plane surface the portion of the sphere on the equator around the azimuth representing the plane of incidence, i.e., around I_p.

Under the above assumptions, the states of polarization of the light issuing from the polarizer all lie on the line

$$2\alpha \sin\delta = 2\chi \tag{16}$$

$$P = \frac{\chi}{\tan\delta}. \tag{17}$$

Any point P_1^0 with the polar coordinates 2α, δ, on this line is rotated and translated by the process of re-

flection to the point P' with coordinates $2\alpha'$, δ', with the relations

$$2\alpha'=\frac{2\alpha}{\tan\psi} \qquad (18)$$
$$\delta'=\delta+\Delta.$$

This process is illustrated in figure 6, where $I-I'$ represents the locus of points representing the incident light and $R-R'$ the reflected light.

The state of polarization of the light after reflection, represented by the point P', may be resolved into components along the plane of transmission of the analyzer and normal to it. The latter direction is represented in the figure by the point $2L$. Under these conditions of very small azimuth and ellipticity, and by eqs (11) and (2), the amplitude of the light transmitted by the analyzer is proportional to the distance D between P' and $2L$.

By the triangle P', $2L$, I_p, the intensity of the transmitted light is proportional to

$$D^2=4L^2+\frac{4\chi^2}{\tan^2\psi\sin^2\delta}-\frac{8L\chi}{\tan\psi}\left(\frac{\cos\Delta}{\tan\delta}-\sin\Delta\right) \qquad (19)$$

where $2L$ is to be considered an algebraic quantity, negative in figure 6.

The process of taking readings may be accomplished in two ways. First, the azimuth of P may be set and A adjusted for minimum transmission. This is equivalent to fixing δ and adjusting L, i.e.,

$$\frac{\partial(D^2)}{\partial L}=0,$$

whence

$$L\tan\psi=\chi(\cos\Delta\cos\delta-\sin\Delta)$$

or

$$\left(A+\frac{\pi}{2}\right)\tan\psi=P\cos\Delta-\chi\sin\Delta \qquad (20)$$

which is the equation of the locus of points obtained in this manner.

Equation (20) is plotted in figure 7. The polarizer and analyzer will be crossed for only one point on this curve. For this point, $P=A+\frac{\pi}{2}$, and

$$P=\frac{\chi\sin\Delta}{\cos\Delta-\tan\psi} \qquad (21)$$

and this crossed position is in general not at zero azimuth $\left(\delta=\frac{\pi}{2}\right)$, but is determined by the constants Δ and ψ of the surface.

However, the scales may also be adjusted by first setting A and moving P. In this case, the condition for a minimum in transmitted light is

$$\frac{\partial(D^2)}{\partial\delta}=0, \qquad L\tan\psi\tan\delta\cos\Delta=\chi$$

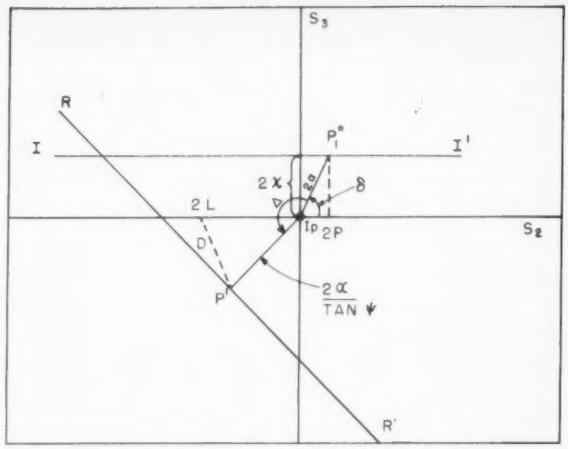

FIGURE 6. *The Poincaré representation of metallic reflection for light of very small azimuth and ellipticity caused by an imperfect polarizer.*

The point along $I-I'$ such as P_1^0 is translated to a point on $R-R'$ such as P' by the process of reflection. This is passed through as analyzer with plane of transmission at an azimuth $L+\pi/2$. The amplitude of the light issuing from the analyzer is proportional to D.

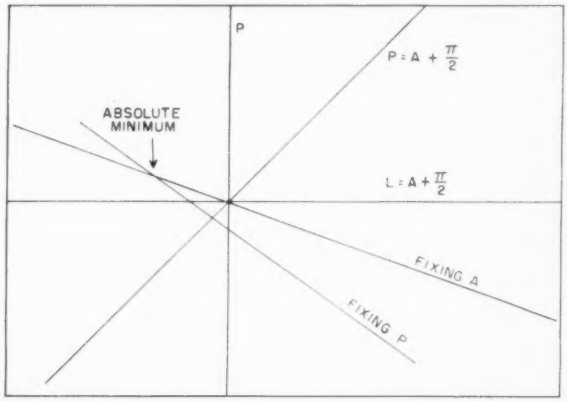

FIGURE 7. *The locus of points* P *and* A *representing extinction of reflected light for an imperfect polarizer and perfect analyzer.*

The upper line is achieved by fixing A and adjusting P for each setting, and the lower by fixing P and adjusting A for each setting. Note that the upper line passes through zero azimuth.

and

$$\left(A+\frac{\pi}{2}\right)\tan\psi\cos\Delta=P \qquad (22)$$

which is different from eq (20). The point for which P and A are crossed is given by

$$P(1-\tan\psi\cos\Delta)=0. \qquad (23)$$

Since the quantity in parentheses is not in general zero,

$$P=0. \qquad (24)$$

Thus it seems clear that the crossed position of the prisms achieved by setting A and adjusting P for a minimum will always be the true azimuth under these circumstances, i.e., an imperfect polarizer, but perfect analyzer. This is represented in figure 7, where we show both the line achieved by fixing P and adjusting A and the line achieved by fixing A and adjusting P. These curves were calculated from eqs (4) and (6) for $\Delta=135$ deg and $\tan\psi=\frac{1}{2}$, and P and A are in the units of χ. It will be noticed that the curve obtained by first fixing A passes through the zero azimuth.

For comparison, a curve obtained experimentally is shown in figure 8, where the numbers indicate meter readings and hence are proportional to the transmission. Since the axes of figure 8 are inverted with respect to figure 7, the ellipticity of the polarizer must be negative. However, the similarity is striking. The value of χ computed from this figure and eq (21) is -0.18 deg.

It will be clear from a consideration of eqs (20), (22), and (12), that it is best to use a polarization azimuth near the plane of incidence rather than near the plane of the surface, since $\tan\psi$ is generally less than unity, and this has the effect of magnifying the angular difference between P and $A\pm\pi/2$ by an amount $1/\tan\psi$. If the polarizer were set near the plane of the surface the angular spread between P and $A+\pi/2$ would be decreased by an amount $\tan\psi$, thus decreasing experimental precision.

The condition for the deepest minimum or best extinction is

$$\frac{\partial(I^2)}{\partial L}=\frac{\partial(I^2)}{\partial\delta}=0$$

and is thus given by the simultaneous solution of eqs (20) and (22). This gives

$$A+\frac{\pi}{2}=\frac{-\chi}{\tan\psi\sin\Delta} \tag{25}$$

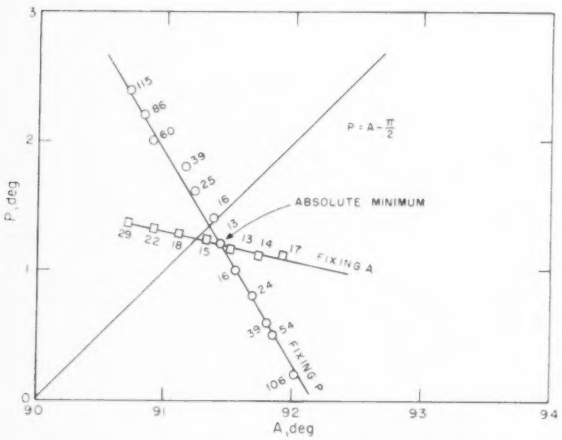

FIGURE 8. *The experimental counterpart of figure 7.*

The P and A coordinates of the intersection of the line $P=A-\pi/2$ and the "fixing A" line represent the azimuth of the plane of incidence and the plane of the surface, respectively.

$$P=\frac{-\chi}{\tan\Delta} \tag{26}$$

By eqs (17) and (26)

$$\tan\Delta=-\tan\delta$$

or

$$\delta+\Delta=\pi \tag{27}$$

so that the deepest minimum occurs when the reflected light is linearly polarized, as would be expected. This minimum is shown in figures 7 and 8 by the intersection of the two lines. The absolute minimum determined by alternate adjustment of P and A is the same as this point of intersection within experimental error. It will be noticed that this point is *not* on the line $P=A+\frac{\pi}{2}$. However, if $\chi=0$, then the deepest minimum occurs at zero azimuth for both P and L, and thus either method of alinement may be used if the light is perfectly plane polarized. Thus, there appears to be only one unambiguous way of alining the ellipsometer when the light from the polarizer has ellipticity, namely, to seek that point at which both $P=A\pm\frac{\pi}{2}$ and minimum transmission is obtained when A is set and P adjusted.

2.3. Alinement Procedure

A step-by-step procedure for alinement of the ellipsometer is as follows:

First, remove the quarter-wave plate. Lower the arms to the "straight through" position. Set the P scale to read zero or any convenient value. Adjust A until minimum transmission is achieved. The A scale will now in general read $(P\pm90)+\epsilon$. Rotate the A prism in its holder until ϵ is zero. The P and A scales are now crossed when the prisms are crossed. The scales should track within ±0.02 deg throughout one revolution.

With a metal surface set for reflection, raise the arms to an angle near the principal angle. Set A so that the plane of transmission of the analyzer is approximately in the plane of the surface. Adjust P until minimum transmission is achieved, and note the readings of the P and A scales. Move A by 0.1 deg and again adjust P and note the values. If the meter reading is higher than for the previous set of values, adjust A by 0.1 deg in the other direction. If it is lower, continue in the same direction. Take a series of readings in this manner, changing A by 0.1 deg and adjusting P for minimum transmission at each setting of A, making sure that the settings encompass the lowest meter reading.

Plot the values of P and A and determine the readings of the P and A scales at which $P=A\pm90°$. At this point the plane of transmission of the P prism is in the plane of incidence and the plane of transmission of the A prism is in the plane of the surface. However, the scale readings will in general not be some multiple of 90°. Let the values of P and A at this point be, for example, $0°+\epsilon'$ and $90°+\epsilon'$ respectively. The quantity ϵ' is now the amount by

which both scales are displaced from the true zero azimuth. Set A at the value obtained from the graph. Adjust the P prism in its holder until ϵ' is zero by turning the prism a small amount in its holder and again adjusting the P scale for minimum transmission. This will require a series of adjustments. (It is imperative that the A scale and prism not be moved at this stage and that the adjustment be done in this way. If, for example, the P scale were held and A adjusted, the ellipsometer would be alined to the value of $P=A\pm\frac{\pi}{2}$ obtained by fixing P and adjusting A, which has been demonstrated to be incorrect.) Having adjusted ϵ' to be zero, remove the reflecting surface and lower the arms to the "straight through" position. Set the P scale at zero and adjust the A scale for minimum. The A scale will now read $90+\epsilon'$. Turn the A prism in its holder until ϵ' is zero. The ellipsometer P and A scales are now alined.

This procedure eliminates alinement errors due to ellipticity produced by the polarizer. The effect of ellipticity in the analyzer on alinement has not been determined but is expected to be small since the analyzer is used for extinction of the light. Thus, any ellipticity by the analyzer after extinction of the light will have no effect on the photometer reading.

2.4. Determination of Δ and ψ From Ellipsometer Scale Readings

By eq (7) the reflection of light from a surface is characterized by the complex reflection coefficient $\tan\psi e^{i\Delta}$, and hence by the two quantities ψ and Δ. It will later be shown how the refractive index of a surface and the thickness and index of films on a surface are calculated from values of Δ and ψ. However, the determination of Δ and ψ from P and A readings merits some discussion, for this is not always a perfectly direct matter.

For any given surface there is a multiplicity of polarizer, analyzer, and compensator scale settings that produce extinction by the analyzer of the reflected light from the surface, and it becomes somewhat of a problem to determine the values of Δ and ψ from these various readings. In order to explain how these numerous readings arise and how Δ and ψ may be computed from them it is well to keep two facts in mind: (a) all azimuthal angles are measured positive counter-clockwise from the plane of incidence when looking into the light beam, and (b) the compensator, which may be set at any azimuth, is generally set so that its fast axis is in an azimuth of $\pm\pi/4$. The present discussion is for an instrument such as that shown in figure 5 with the compensator before reflection. If the compensator is placed after reflection, suitable corrections will have to be made.

The various readings fall into four sets called zones, two with the fast axis of the compensator set at $\pi/4$, numbered 2 and 4, and two with it set at $-\pi/4$, numbered 1 and 3. In each zone there is one independent set of polarizer and analyzer readings, making four independent sets of P and A readings in all. However, since both analyzer and polarizer may be rotated by π without affecting the results, there are 16 polarizer and analyzer settings falling into four independent zones. Since the compensator may also be rotated by π without affecting the results, there are 32 possible sets of readings on the ellipsometer.

Rather than calculating Δ and ψ directly from the P and A values, it is useful to calculate three other quantities, p, a_p, and a_s from the P and A values, p being related to the P readings, a_p related to the A readings in zones 1 and 4, and a_s related to the A readings in zones 2 and 3. For a perfect quarter-wave plate these are related to Δ and ψ by the eq (2)

$$\Delta=\frac{1}{2}\pi+2p \tag{28}$$

$$\psi=a_p=a_s. \tag{29}$$

If the compensator is not a perfect quarter-wave plate, the relationships are

$$-\tan\Delta=\sin\delta\cot 2p \tag{30}$$

$$\tan^2\psi=\tan a_p\tan a_s \tag{31}$$

where δ is the relative retardation of the compensator. If the retardation δ is near $\pi/2$, then, to first order, eqs (28) and (30) are the same. However, it is now necessary to distinguish between a_p and a_s. The relationship of p and a_p and a_s to the P and A readings observed on the ellipsometer is best derived by a consideration of the process as represented on the Poincaré sphere, and since this has been adequately treated by Winterbottom [2], we shall merely list the results. The meanings of p, a_p, and a_s in the four zones are as follows:

Zone 1. The fast axis of compensator is at $-\pi/4$. The polarizer plane of transmission makes an angle of $+p$ with the plane of incidence. The analyzer plane of transmission makes an angle of $+a_p$ with the plane of incidence.

Zone 2. The fast axis of the compensator set at $+\pi/4$. The polarizer plane of transmission makes an angle of $-p$ with the surface (an angle of $\pi/2-p$ with the plane of incidence). The analyzer plane of transmission makes an angle of $+a_s$ with the plane of incidence.

Zone 3. The fast axis of compensator is at $-\pi/4$. The polarizer plane of transmission makes an angle of $+p$ with the surface (an angle of $p+\pi/2$ with the plane of incidence). The analyzer plane of transmission makes an angle of $-a_s$ with the plane of incidence.

Zone 4. The fast axis of compensator is at $+\pi/4$. The polarizer plane of transmission makes an angle of $-p$ with the plane of incidence. The analyzer plane of transmission makes an angle of $-a_p$ with the plane of incidence.

The meanings of p, a_p, and a_s are now clear. The first is the angle between the polarizer plane of transmission and either the plane of incidence or the plane of the surface, while a_p and a_s represent the angle between the analyzer plane of transmission

and the plane of incidence, being labeled either a_p or a_s according to whether p is the angle between the polarizer plane of transmission and the plane of incidence or the plane of the surface, respectively. With these relationships, it is a simple matter to compute the relationship of P and A to p and a_p or a_s, and hence to Δ and ψ, by means of eqs (28) and (29), or (30) and (31). These relationships are summarized in table 1.

TABLE 1. *Relation of* P *and* A *readings to* p, a_p, *and* a_s

Zone	Compensator	P	A
1	$-\pi/4$	p	a_p
		$p+\pi$	a_p
		p	$a_p+\pi$
		$p+\pi$	$a_p+\pi$
3	$-\pi/4$	$p+\pi/2$	$\pi-a_s$
		$p+3\pi/2$	$\pi-a_s$
		$p+\pi/2$	$2\pi-a_s$
		$p+3\pi/2$	$2\pi-a_s$
2	$+\pi/4$	$\pi/2-p$	a_s
		$3\pi/2-p$	a_s
		$\pi/2-p$	$a_s+\pi$
		$3\pi/2-p$	$a_s+\pi$
4	$+\pi/4$	$\pi-p$	$\pi-a_p$
		$2\pi-p$	$\pi-a_p$
		$\pi-p$	$2\pi-a_p$
		$2\pi-p$	$2\pi-a_p$

For the purposes of this table, it has been assumed that the P, A, and compensator scales have been adjusted to read angles with respect to the plane of incidence as previously defined. If the instrument is not arranged in this manner, it is necessary to adjust the readings before using table 1.

The table gives the 16 possible readings for the two settings of the compensator. When working with a completely unknown surface it is still not a simple matter to identify the P and A readings with one of the entries on this table and hence to compute p, a_p, or a_s. As a first step in this identification it is worthwhile to consider the ranges for Δ and ψ and hence for p, a_p, or a_s. For all surfaces, including multiple reflections,

$$0<\psi<\frac{\pi}{2}. \tag{32}$$

In fact, in the large majority of cases

$$0<\psi\leq\frac{\pi}{4} \tag{33}$$

and from eq (29) the range of a_p and a_s is the same. For the special case of reflection from a dielectric surface at an angle of incidence smaller than the Brewster angle, $\Delta=-\pi$. For all other cases

$$0\leq\Delta\leq 2\pi \tag{34}$$

which gives as a range for p,

$$-\frac{\pi}{4}\leq p\leq\frac{3\pi}{4}. \tag{35}$$

When working with a completely unknown surface, and particularly if multiple reflections are used, it is best to take a complete set of 16 readings for the two settings of the compensator. Then, with the relations (33) and (35), and the further condition that the values of p, a_p, and a_s calculated from these readings must be approximately the same, it is a simple matter to identify each of the scale readings with one of the possibilities outlined in the table. To continue to do this when the surface is known would be redundant and one reading in each zone is sufficient. We have found that the average of one reading in each of two zones with the same compensator setting gives approximately the same result as the average of one reading in each of all four zones.

2.5. Differences Among the Zones

In practice, the values of p, a_p, and a_s found from the P and A readings in the various zones are not identical. A typical set of values is shown in table 2. Differences of as much as 3 deg occur in the values of p and somewhat less in the values of a_p and a_s. On the other hand, it will be noticed that the average of the observed values of p in zones 1 and 3 is the same as the average of the value obtained in zones 2 and 4. This strongly implies the following equations

$$\begin{aligned} p_1&=p+\delta & p_4&=p+\delta' \\ p_3&=p-\delta & p_2&=p-\delta' \end{aligned} \tag{36}$$

where δ and δ' are error terms. These error terms are not constant from run to run, but are usually 1 to 1.5 deg as in table 2. (In this particular set, δ and δ' are approximately the same. This is not true in general). They are not caused by misalinement or any other readily detectable cause, and their source remains obscure. However, among very many experiments, not a single one has been found where the averages from zones 1 and 3 did not check the average from zones 2 and 4 within experimental error.

TABLE 2. *Values of* P *and* A *for a typical chrome slide in air in all four zones*

Zone	P	A	p	a_p	a_s
1	19.71	31.04	19.71	31.04	
2	167.17	31.73	22.83		31.73
3	113.00	147.75	23.00		32.25
4	169.20	148.52	19.80	31.48	
Average of four zones			21.34	31.63	
Average of zones 1 & 3			21.36	31.65	
Average of zones 2 & 4			21.32	31.61	

The situation for a_p and a_s is not quite so clear-cut. If the compensator is not a perfect quarter-wave plate, then differences in a_p and a_s are to be expected. In fact, it may be shown that for a compensator with retardation θ near $\pi/2$,

$$a_p-a_s=(\theta-\pi/2)\cos 2p \sin 2\psi \tag{37}$$

where, for the purposes of this calculation, we have used $\psi=a$. Again, an inspection of the table indi-

cates that the average of a_p and a_s from zones 1 and 3 is equal to the average of a_p and a_s from zones 2 and 4 which again strongly implies

$$\begin{aligned} a_1 &= a_p + \delta & a_4 &= a_p + \delta' \\ a_3 &= a_s - \delta & a_2 &= a_s - \delta' \end{aligned} \tag{38}$$

where the a's with the numerical subscript are observed values in the various zones. Many experiments indicate that these equations seem to be followed quite faithfully. The values of δ and δ' in eqs (38) are, in general, different from those in eqs (36).

It will be observed that the equations are not independent, and they cannot be solved for a_p and a_s directly from the observed values of a. Fortunately, for a small value of $a_p - a_s$, and for ψ not too close to zero it may be shown that

$$(\tan a_p \tan a_s)^{1/2} = \tan \frac{(a_p + a_s)}{2} \tag{39}$$

to first order in $a_p - a_s$. Thus rather than using eq (31) for computing ψ, the above equation is used. This requires a compensator not too different from quarter-wave, and independent measurements indicate that the compensator used in this work has a retardation which differs from $\pi/2$ by about 1 deg.

Because the averages from zones 1 and 3 check so closely the averages from zones 2 and 4 for both p and a, measurements are usually taken in zones 1 and 3 only and averaged.

2.6. Surfaces

The substrates most easy to work with are those with high reflectance, such as metals. Both smoothness and flatness are factors that must be considered in the selection of a substrate. Irregularities that are small compared to the dimensions of the light beam, which is commonly of the order of 1 mm^2, are averaged and do not affect the results [4]. Long range regularity (flatness) is desirable if more than one location on a specimen is to be studied. An indication of the regularity is obtained by determination of p and a at several points on the specimen. Measurements on 1-in. long steel gage blocks of 0.09 μ in. tolerance varied only about 0.1° in the polarizer readings from top to bottom, and less in analyzer readings. Acceptable slides prepared by shearing small rectangles from a large ferrotype plate varied about 0.2° for similar lengths and these make convenient and readily available surfaces for study.

Various techniques have been used for the preparation and cleaning of the substrate surface. The chrome ferrotype plate slides used in these investigations were washed in warm distilled organic solvents to remove organic contamination. Since the resulting surface was hydrophobic, the slides were further cleaned with warm chromic acid cleaning solution followed by several washings in warm distilled water. This treatment should not appreciably affect the character of the chromium-chromium oxide surface, but it did remove organic contamination, the surface now being hydrophilic. However, in less than 1 hr the surface became sufficiently contaminated to become hydrophobic, even when enclosed in a covered container. These precleaned slides were passed through a flame immediately before use to remove this contamination; this flaming of the slides restored the hydrophilic character to the surface. For studies under liquids, the slides were placed under the liquid while still warm from the flame. The cleaning of surfaces by flaming has been described by Patrick [12] and Bartell and Betts [13].

2.7. Cells

Cells have been used for ellipsometer measurements in vacuum or gaseous environments [2, 14, 15] and under liquids [2]. The cell shown in figure 9 has been used in our studies for measurements under liquids. The specimen is situated on the base of the cell which is filled with liquid of known refractive index. The light beam enters and leaves the cell through optically flat windows. These windows are inclined at the angle of incidence ϕ with respect to the base of the cell so that the light passes through them at normal incidence. Therefore, reflection of light at the surface of the cell windows will be independent of its direction of polarization and the polarization of the light will not be changed. There should be no stresses in the glass sufficient to cause detectable birefringence; moreover, the inner and outer sides of each window should be parallel. They may be sealed to the cell body either by fusion or by epoxy resin; the epoxy seal has been used more successfully for our cells. The differences in polarizer and analyzer readings in air for a metallic reflecting surface outside and inside the cell were no larger than 0.1° for our cells.

Difficulties with photometer fluctuations have occurred as a result of convection currents caused by evaporation of liquid. A small area of liquid in contact with the air, a tightly fitting cover, and solutions filtered through fritted glass disks minimize this effect.

The angle of incidence should generally be chosen to give the maximum sensitivity for the measurement of film thickness. For this purpose, sensitivity may be defined as the change of P reading or A reading with film thickness, t, i.e., dP/dt and dA/dt. One is then faced with the problem of selecting an angle of incidence such that these two quantities are a maximum. No general rules can be laid out for this selection, and the choice of angle of incidence will depend upon the particular substrate, film and surrounding medium. However, for the common case of an organic film on a chromium surface in an organic medium, the sensitivity for both P and A has been calculated for various angles of incidence and film thicknesses up to 1000 Å. The results are shown in figures 10 and 11.

The maximum sensitivity for A occurs at angles of incidence between 75 and 80 deg, and decreases with film thickness. For P, the maximum sensitivity (the absolute value of dP/dt) occurs at an angle

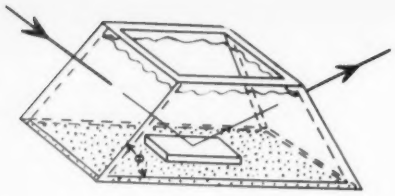

FIGURE 9. *A cell used for studies of surfaces under liquids.*

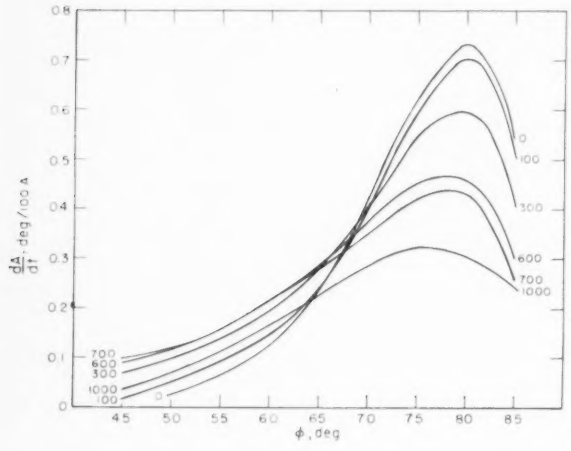

FIGURE 10. *The sensitivity,* dA/dt, *of* A *for measuring thickness* t, *plotted as a function of angle of incidence.*

The parameters are those for a typical organic film on chrome: $n_1=1.4268$, $n_2=1.4700$,* $n_3=3.14800-4.14279j$.

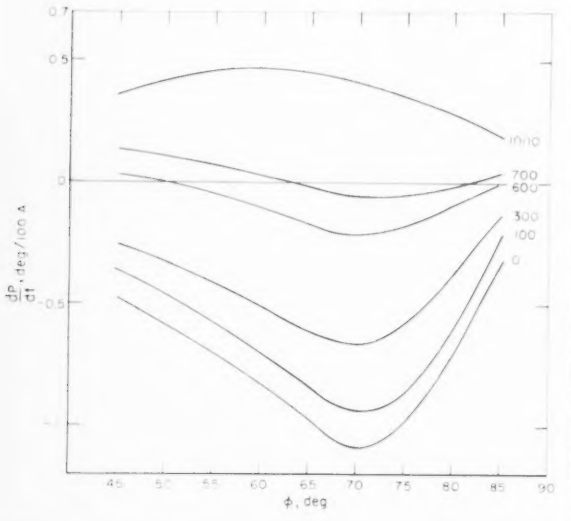

FIGURE 11. *The sensitivity,* dP/dt *of* P *for measuring thickness* t, *for the same conditions as figure 10.*

Note the very low sensitivity at a film thickness of 700 Å.

of incidence of 70°, and decreases with increasing film thickness up to a thickness of about 700 Å. At this thickness, the sensitivity in P is very small, making the thickness determination entirely dependent on A, which is relatively insensitive in this region. Thus, under these conditions, the accurate determination of film thickness is difficult for films 600 to 800 Å thick. For films thicker than 800 Å, the sensitivity in P again becomes usable, but the maximum occurs at angles less than 70 deg.

For any film thickness, therefore, the best angle of incidence is always a compromise between the most sensitive angle for P and that for A. The selection will, in part, depend on the relative importance of P or A to the determination of the thickness.

These sensitivities apply only to the given specific conditions but the sensitivities for other conditions with a nonabsorbing film are expected to have similar behavior although specific values will be different.

2.8. Methods of Computation

A typical system for study by the ellipsometer consists of a film of index n_2 and thickness d on a reflecting substrate of index n_3 immersed in a medium of index n_1, as shown in figure 12. Let all media be isotropic and n_1 represent a real index of refraction, while n_2 and n_3 may be complex.

Consider light incident at the boundary between the immersion medium and film. The cosine of the refraction angle is

$$\cos \varphi_2 = \left[1 - \left(\frac{n_1}{n_2} \sin \varphi_1\right)^2\right]^{1/2}. \tag{40}$$

The parallel and normal reflection coefficients for light incident at this boundary are:

$$r_{12}^p = \frac{n_2 \cos \varphi_1 - n_1 \cos \varphi_2}{n_2 \cos \varphi_1 + n_1 \cos \varphi_2} \tag{41}$$

and

$$r_{12}^s = \frac{n_1 \cos \varphi_1 - n_2 \cos \varphi_2}{n_1 \cos \varphi_1 + n_2 \cos \varphi_2} \tag{42}$$

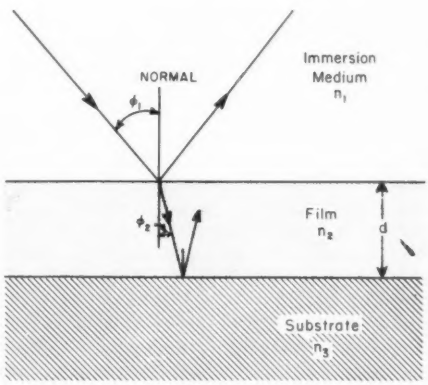

FIGURE 12. *Reflection from a film-covered surface.*

The substrate is a reflecting metal surface.

respectively. The reflection coefficients, r_{23}^p and r_{23}^s at the boundary between the film and substrate are given by similar expressions.

The total reflection coefficients, R^p and R^s that include the contributions of reflections from lower boundaries are given [2] by:

$$R^p=\frac{r_{12}^p+r_{23}^p \exp D}{1+r_{12}^p r_{23}^p \exp D} \tag{43}$$

and

$$R^s=\frac{r_{12}^s+r_{23}^s \exp D}{1+r_{12}^s r_{23}^s \exp D} \tag{44}$$

where cos φ_3 values needed for these reflection coefficients are given by an expression similar to eq (40) and D represents the quantity

$$D=-4\pi j n_2 \cos \varphi_2 d_2/\lambda \tag{45}$$

where λ is the wavelength of the light used, in vacuum, and $j=\sqrt{-1}$. The ratio of the parallel and normal total reflection coefficients is defined as ρ:

$$\rho=R^p/R^s. \tag{46}$$

This may be expressed in terms of the relative attenuation and phase shift of the parallel component with respect to the perpendicular component that occurs, represented by the azimuthal angle Δ, and relative phase shift ψ by:

$$\rho=\tan \psi \exp (j\Delta) \tag{47}$$

as in eq (8). Thus ρ is determined from ellipsometer readings.

The value of the complex index of a reflecting surface can be calculated from the equation

$$n_3=n_1 \tan \varphi_1 \left[1-\frac{4\rho \sin^2 \varphi_1}{(\rho+1)^2}\right]^{1/2} \tag{48}$$

where φ_1 is the angle of incidence and ρ is determined from ellipsometry measurements on the base substrate.

Several methods of determining the thicknesses of films on reflecting substrates from ellipsometry measurements are available [2–5]. When the indexes of the substrate and film are known, tables or graphs of Δ and ψ may be computed from given values of d. This is accomplished by calculating values of ρ from eqs (40) to (46) and values of Δ and ψ from eq (47). Figure 13 shows curves computed for three different values of film index n_2. The numbers along each curve are thickness values of the film, d_2. Experimental values of Δ and ψ are then interpolated in such tables or related graphs to determine unknown thicknesses.

However, it is usually more efficient to solve the equations directly from the thickness of a film. Substituting eqs (43), (44), and (46) in eq (47) and rearranging gives a quadratic of the form:

$$C_1(\exp D)^2+C_2(\exp D)+C_3=0 \tag{49}$$

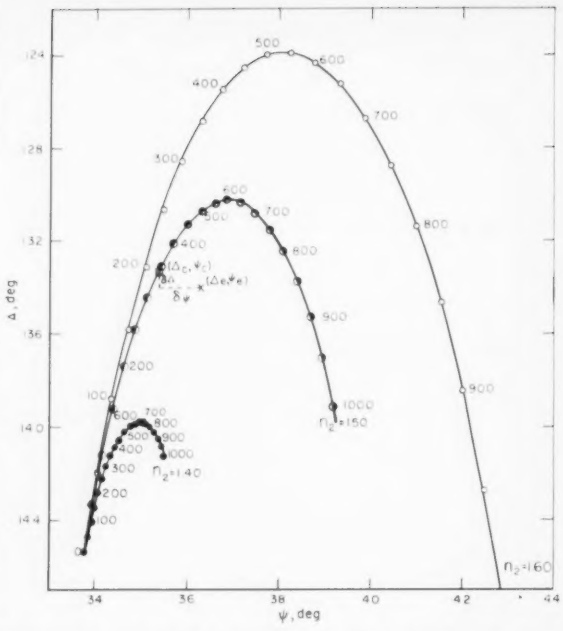

FIGURE 13. *A plot of Δ against ψ for films of refractive index as shown, in a medium with a refractive index of 1.359.*

The numbers along the curves are film thicknesses in Angstrom units. From such a figure and an experimental point ψ_e, Δ_e, both the refractive index and thickness of the film may be obtained (see text).

where C_1, C_2, and C_3 are complex functions of the refractive indexes, angles of incidence, Δ and ψ. For a given value of the coefficients eq (49) gives two solutions for exp D and a value of d may be calculated from each. Since the coefficients are complex, the film thicknesses calculated from this equation would also be expected to be complex. However, the correct film thickness, d, must be a real number as it represents a real quantity. Therefore, the solution of the quadratic that yields a real film thickness is the correct solution. In practice, various experimental errors will result in both solutions yielding complex values for d. The thickness with the smallest imaginary component is selected as the correct solution; the real portion is taken as d and the imaginary part, d_j, is taken as a relative measure of error.

The real portion of d is then used to compute Δ and ψ by eqs (43) to (47). As the imaginary component of d has been dropped, these values will differ from the experimental angles by amounts $\delta\Delta$ and $\delta\psi$, and d_j, $\delta\Delta$, and $\delta\psi$ are all measures of the experimental error. However, $\delta\Delta$ and $\delta\psi$ must be within the limits of experimental error of ψ and Δ for the results to be valid. This is a more direct determination of the validity of an experiment than the magnitude of d_j.

If both the thickness and index of refraction of the film, n_2, are not known, the equations cannot be solved for d and n_2 in closed form. For this case, a series of refractive indexes are assumed and a thickness is calculated from the experimental measurements. These calculations will result in error terms, described above, of different magnitudes. The

range of refractive indexes and related thicknesses within the experimental errors $\delta\Delta$ and $\delta\psi$ are then chosen. The magnitude of the possible ranges of refractive indexes and thicknesses will depend upon the magnitude of the error and on several parameters such as n_1, n_2, n_3, etc.

Some of the principles described above are illustrated in figure 13, which shows theoretical Δ and ψ values for a range of given film indexes and thicknesses. An experimentally determined point (Δ_e, ψ_e) for a film of unknown n_2 falls near one of these curves. For an assumed film index of 1.5, a thickness will be calculated corresponding to the point (Δ_e, ψ_e). The error terms, $\delta\Delta$ and $\delta\psi$ are also illustrated. The error terms are usually much smaller than indicated on this figure.

The calculations discussed above can be computed manually, but the equations are complicated and the computation of any appreciable amount of data would be impractical. Several "Fortran" programs have been written in this laboratory for IBM 704 and 7090 computers to enable the computation of data from ellipsometer measurements. The programs are general enough to permit their use in most situations encountered. The following is a brief description of problems that can be solved with these programs.

The refractive index of the substrate, n_3, may be computed directly from experimental readings on the bare substrate. Immersion media of different refractive indexes may be used for this determination.

When a_p and a_s are known, the correct retardation of the compensator can be calculated. This retardation may then be used in subsequent calculations. Thus, the ellipsometer data may be used even if the compensator is not a quarter-wave plate.

Curves and tables of Δ ψ, and reflection coefficients can be computed for a series of given film thicknesses and refractive indexes, n_2, as shown in figure 13.

For experimental values of Δ and ψ, a thickness, d, and error terms, $\delta\psi$ and $\delta\Delta$, are computed for a given n_2. If n_2 is unknown, a series of n_2 can be assumed and corresponding film thichness and error terms computed. The selection of the correct n_2 and thickness has been discussed and is illustrated in the next section. All the above calculations have been extended for multiple films and for multiple reflections.

3. Applications

Inasmuch as surfaces in air will usually have an adsorbed film of water or other contaminants, in order to determine the index of a substrate it is necessary either to measure the surface in a vacuum or in a medium with a refractive index identical to that of the adsorbed film ($n_1=n_2$).

In the work reported here chrome slides with and without a vacuum deposit of gold were flamed to remove adsorbed gases and immediately immersed in a liquid. Table 3 gives the refractive indexes of slides measured in air and measured under water. The differences in the refractive index of the metals calculated from measurements made in air and under water are probably caused by the presence of an adsorbed film of water on the slides when measured in air. Such a film would not be observed, of course, when the measurements were made under water, assuming the refractive index of the film to be the same as that of water. It is presumed, therefore, that the measurements made under water yielded the correct indexes for these slides.

TABLE 3. *Measured refractive index,* $n=N-jK$, *of chrome and gold*[a] *in air and in water*

Immersion medium	Chrome		Gold	
	N	K	N	K
Air	2.954	4.224	0.446	2.134
Water	3.231	4.354	.528	2.165
Air	3.005	4.274	.427	2.119
Water	3.218	4.302	.546	2.100
Air	2.950	4.258		
Water	3.285	4.426		

[a] Slides had been flamed prior to examination.

The measurements described above were also repeated for immersion media of different refractive indexes. The optical constants of the metal calculated under these conditions are given in table 4.

TABLE 4. *Refractive indexes,* $N-jK$, *calculated for chrome slides immersed in various liquids immediately after flaming*

φ	Immersion medium	n	Refractive index[a]	
			N	K
Degree				
60	methanol	1.329	3.212	4.335
60	water	1.337	3.416	4.358
70	water	1.337	3.278	4.371
60	acetone	1.360	3.275	4.363
70	acetone	1.360	3.296	4.398
70	cyclohexane	1.426	3.254	4.396
70	toluene	1.498	3.344	4.437
60	air[b]	1.00	2.899	4.170
70	air[b]	1.00	2.918	4.198

[a] All refractive indexes are averages of two or more sets of measurements, except for methanol.
[b] Slides measured in air had been exposed to air from 1 to 24 hr.

The slides measured under liquids were flamed and immediately immersed in the liquid before a film could form on them from the air. These slides are therefore not expected to have any adsorbed film on them, so that their true refractive indexes are measured. If some film did remain on them, its refractive index would probably be near that of the immersion liquid, causing only a small error in the measured refractive index of the slide. Hence the rerfactive indexes of the slides under the various liquids are all approximately the same, and independent of the liquid and the angle of incidence. The variation is due mainly to variations among the individual slides used for the different measurements.

The refractive index measured in air shows a difference due to neglect of the films that is larger than the variations among the individual slides.

This film is expected to be adsorbed water and, perhaps, other gases and is expected to have an index near that of water. By first measuring slides in air and then measuring them under water, it is therefore possible to calculate a thickness of the adsorbed layer in air, assuming the refractive index of the adsorbed film to be the same as that of liquid water. Such results are shown in table 5, where $\delta\Delta$ and $\delta\psi$ are the differences obtained as described above. The reproducibility of the results is seen to be quite good, although the actual value of the thickness may be somewhat in error due to the assumption of the refractive index value.

TABLE 5. *Thickness of adsorbed layer* [a] *on slides in air*

	Slide number	φ	Δ	$\delta\Delta$	ψ	$\delta\psi$	d
		Degree	*Degree*	*Degree*	*Degree*	*Degree*	Å
Chrome	76	50	163.44	0.00	39.51	0.04	23
	76	60	152.56	.02	36.33	.11	24
	76	70	132.52	.06	31.85	.13	26
	75	70	132.72	.08	31.57	.16	27
	74	70	131.78	.04	31.83	.08	24
	79	70	132.04	.06	31.76	.12	23
	76	80	85.04	.06	28.15	.18	26
Average							25
Gold	72	70	90.36	0.06	40.53	0.15	2
	73	70	91.96	.09	40.98	.02	3
	74	70	88.38	.12	39.89	.26	5
	77	70	88.36	.06	40.39	.16	4
Average							4

[a] Calculated as water
T=22° C,
RH=50 percent.

The determination of both the thickness and refractive index of a barium fluoride film vacuum evaporated onto a chrome surface is given as an example of the measurements and calculations described earlier. The index, n_3, of the substrate was first determined from the reading taken on the bare chrome surface, then the film was vacuum deposited on the surface and the angles Δ and ψ were measured for the film-covered surface. A series of refractive indexes are assumed for the film, and thickness and the corresponding error terms, $\delta\Delta$ and $\delta\psi$, are calculated for each index by the methods given earlier. The results are given in table 6. The reproducibility of the readings is $\pm 0.1°$ for Δ and $\pm 0.05°$ for ψ and the maximum experimental error is expected to be about $\pm 0.2°$ for Δ and $\pm 0.1°$ for ψ. It will be observed from table 6 that the index 1.456 gives zero error terms $\delta\Delta$ and $\delta\psi$, and is, therefore, the best fit with the experimental reading. However, n_2 values from 1.454 to 1.458 also give error terms within the limits of experimental error, and are the range of possible indexes of the film. The corresponding thicknesses are 654 and 665 Å.

The actual range of possible thicknesses is greater than this range as is illustrated in figure 14. This figure is an enlargement of the center portion of figure 13. Curves for additional refractive indexes have been added. The dashed lines represent the limits of experimental error for the point (Δ_e, ψ_e). The true values of n_2 and d must fall within these limits. A range of possible thicknesses for each refractive index rather than only a single selected value of thickness for each possible refractive index is obtained. The range of possible thicknesses is thus approximately 630 to 680 Å.

TABLE 6. *Thickness of evaporated barium fluoride film on chrome slide* [a, b]

Δ	$\delta\Delta$	ψ	$\delta\psi$	n_2	d
Degree	*Degree*	*Degree*	*Degree*		Å
133.96	3.64	36.30	0.60	1.420	753
	2.64		.40	1.430	726
	1.58		.22	1.440	701
	1.08		.14	1.445	688
	0.58		.07	1.450	676
	.28		.03	1.453	668
	.18		.02	1.454	665
	.10		.01	1.455	662
	.00		.00	1.456	660
	.10		.01	1.457	657
	.20		.02	1.458	654
	.28		.03	1.459	651
	.38		.04	1.460	647
	.70		.38	1.475	453

[a] Immersed in acetone, n_1=1.359, at an angle of incidence of 60°. The refractive index of the slide was n_3=3.316−4.383j.
[b] Film prepared by Frank E. Jones, National Bureau of Standards.

These methods do not determine the index of the film as accurately when the film is very thin. This can be observed in figure 13 by the close proximity of the curves for small thicknesses. Since the experimental error is independent of film thickness, the range of refractive indexes and thicknesses that would be included in the rectangle of experimental error described above is increased. When the refractive index is known, the thickness can be accurately determined even for very thin films, except that as the film index approaches that of the medium, the sensitivity in determining the film thickness decreases. This can be seen in figure 13 by the decreasing sensitivity to thickness of Δ and ψ as the refractive index of the film, n_2, approaches the index of the medium, 1.359.

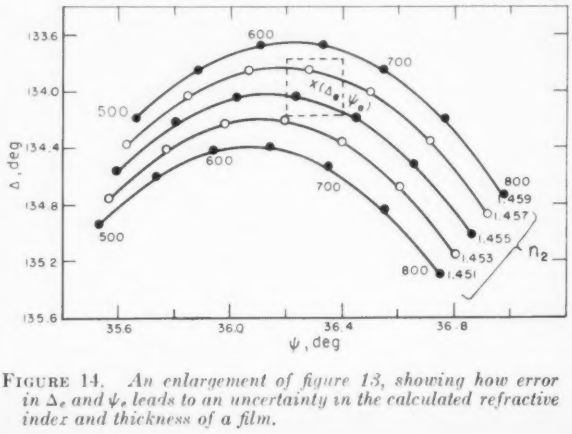

FIGURE 14. *An enlargement of figure 13, showing how error in Δ_e and ψ_e leads to an uncertainty in the calculated refractive index and thickness of a film.*

4. Summary

The use of the ellipsometer for the measurement of the thickness and index of refraction of very thin films is described and illustrated by examples. The representation of elliptically polarized light by means of the Poincaré sphere is developed in detail since it is necessary for a complete understanding of the changes in the polarization of light in the ellipsometer.

Some unusual effects in alinement have been observed and explained as due to the light from the polarizer having a slight ellipticity. A method of alinement that is not affected by the ellipticity is given.

Chrome ferrotype plates have been found to be a convenient substrate for study of thin films. Means of preparing and cleaning the plates are discussed. Also, cells used to study films under liquids are described.

In order to study a film by ellipsometry, the reflection coefficient of a bare substrate is first measured and the complex refractive index of the substrate computed from the reflection coefficient. A film is then deposited on the substrate and the reflection coefficient of the combination is measured. If the index of the film is known, the thickness of the film may be computed. In one method, the reflection coefficient of the substrate with a film is computed for many thicknesses of the film. Then the measured reflection coefficient is interpolated in the calculated results to determine the thickness of the film. However, in this paper the required equations are solved to give the thickness of the film directly in terms of the measured reflection coefficients so that interpolation is not required. These measurements and calculations are applied to determining the thickness of an adsorbed film on ferrotype plates. The index of refraction of this film was assumed to be that of water.

Both the index of refraction and thickness of a film may be calculated from the complex reflection coefficient of the film-substrate combination. The procedure is to assume a series of refractive indexes and compute a corresponding thickness for each index. If the refractive index chosen is not the exact index of the film, and if the measurements are not sufficiently precise, the calculated thickness of the film is complex. The imaginary part of the computed complex thickness is taken as a relative measure of error either of the assumed refractive index or of the original measurement. The film refractive index with its corresponding thickness that yields the smallest error terms is taken as the best fit. This calculation is illustrated for a barium fluoride film.

5. References

[1] P. Drude, Ann. Physik **272,** 532 (1889); ibid. **272,** 865 (1889); ibid. **275,** 481 (1890).
[2] A. B. Winterbottom, Optical Studies of Metal Surfaces, The Royal Norwegian Scientific Society Report No. 1, 1955, published by F. Bruns, Trondheim, Norway; Trans. Faraday Soc. **42,** 487 (1946).
[3] L. Tronstad, Z. Physik. Chem. **A142,** 241 (1929); Trans. Faraday Soc. **31,** 1151 (1935); The Royal Norwegian Scientific Society Report No. 1 (1931).
[4] F. A. Lucy, J. Chem. Phys. **16,** 167 (1948).
[5] A. Rothen, Annals New York Academy Sci. **53,** Art. 5, 1054 (1951); Rev. Sci. Instr. **16,** 26 (1945); and M. Hanson, ibid. **19,** 839 (1948), **20,** 66 (1949); ibid. **28,** 283 (1957).
[6] J. B. Bateman and M. W. Harris, Annals New York Academy Sci. **53,** Art. 5, 1064 (1951).
[7] J. A. Faucher, G. M. McManus, and H. J. Trurnit, J. Opt. Soc. America **48,** 51 (1958).
[8] G. G. Stokes, Trans. Cambr. Phil. Soc. **9,** 399 (1852).
[9] M. Born and E. Wolf, Principles of Optics (Pergamon Press, 1959).
[10] W. A. Shurcliff, Polarized Light (Harvard University Press, (1962).
[11] R. L. Patrick, Alpha R and D Inc., Blue Island, Ill. (private communication).
[12] R. L. Patrick and G. O. Payne, Jr., J. Colloid Sci., **16,** 93 (1961).
[13] L. S. Bartell and J. F. Betts, J. Phys. Chem. **64,** 1075 (1960).
[14] F. B. Bowden and W. R. Throssell, Proc. Royal Soc. **A209,** 297 (1951).
[15] J. Kruger and W. J. Ambs, J. Optical Soc. America **49,** 1195 (1959).

(Paper 67A4–227)

JOURNAL OF RESEARCH of the National Bureau of Standards—A. Physics and Chemistry
Vol. 67A, No. 4, July–August 1963

Color Phenomena Associated With Energy Transfer in Afterglows and Atomic Flames

Arnold M. Bass and H. P. Broida

(April 10, 1963)

Reactions involving reactive species produced in electric discharges are frequently characterized by the emission of visible light of many different colors. Some typical afterglows and atomic flames have been photographed, and the observed colors (or spectral distributions) are discussed with regard to the reactions from which they arise. Laboratory studies of this sort are helpful for the understanding of the energy transfer processes which occur in flames, in electrical discharges, and in the upper atmosphere.

1. Introduction

Brightly colored afterglows from electric discharges have provided a source of laboratory demonstrations and wonder for nearly 80 years. In 1884 Warburg [1] [1] noticed that, in a tube of nitrogen at low pressure which was subjected to an electric discharge, glows persisted for a long time after the exciting voltage was removed. Since the beginning of this century, afterglows in nitrogen [2] and oxygen [3] have been investigated extensively. Most of the phenomena associated with these afterglows are caused by reactions of atomic species [4]. It also has been found that under some conditions, in products of electric discharges condensed as solids at very low temperatures, there is an "afterglow" from the solid [5, 6].

When dissociation products from an electric discharge through gases at low pressure (0.01 to 100 mm Hg) are mixed with suitably reacting gases or vapors, bright regions known as atomic flames are observed [7]. In addition to the visible light which is observed and discussed below, there is also ultraviolet and infrared emission. Spectra of flames obtained on mixing hydrocarbons with atomic oxygen [8, 9] have been used as a method to help in the understanding of reaction zones in combustion processes. Emission spectra of brilliant glows obtained at the point of mixing of certain organic compounds with atomic nitrogen have been studied [10, 11] and used to obtain information about the reactions [12, 13] taking place. There is little emission from reactions taking place with hydrogen atoms [7, 8] but weak flames are observed from mixing ozone with hydrogen atoms, and much brighter flames from ozone mixed with both hydrogen and nitrogen atoms [14].

Very few studies have been made of glows which occur in short times after the discharge. However some observations have been made as part of wind tunnel visualization efforts [15].

Previous attempts to obtain color photographs of these phenomena have met with only partial success. However, recent developments in photographic techniques and color film, as well as improved control of the afterglow and flame systems have made possible the satisfactory photographic recording of these glows. A group of photographs of characteristic glows and flames has been assembled in figures 2 through 9, and 11 through 24; figures 1 and 10 show the apparatus used for the excitation of the glows.

2. Experimental Procedure

Afterglows and atomic flames were photographed in the apparatus shown in figure 1. High purity gases from cylinders were admitted to the discharge region by means of control valves visible near the top of the picture. An electrodeless discharge was maintained in a quartz tube of 10 mm i.d. by means of a microwave cavity operated at 2450 Mc/s with a maximum input power of 125 w. With this arrangement, glows could be observed at pressures between 0.1 and 100 mm Hg. The brightest glows occurred at pressures between 1 and 10 mm Hg. Two different gases could be separately admitted and mixed before the discharge. A side tube in the cylindrical chamber (9.5 cm diameter) allowed the mixing of another gas downstream from the discharge. Another inlet tube allowed pressure measurements to be made with an aneroid type, direct reading manometer. A pumping line (2.5 cm diameter) was connected to a high speed, mechanical vacuum pump.

[1] Figures in brackets indicate the literature references at the end of this paper.

In order to observe very short time phenomena the apparatus shown in figure 10 was used. In this apparatus, which was made of Pyrex glass, the electric discharge (2450 Mc/s) occurred in a converging-diverging (de Laval) nozzle with a throat of about 2 mm diam and an exit of 6 mm. The gases were emptied into a 9 cm diam chamber, 100 cm long. A vacuum pump with a capacity of 500 liters/sec was used. Cleanliness of the apparatus and of the gases were essential for many of the phenomena which are pictured in this paper.

The critical factor for the reproducible photography of these phenomena is the correct control of exposure time. This was achieved through the use of a Honeywell Pentax 3°/21° exposure meter which has very high sensitivity for an acceptance angle of 3°. The narrow acceptance angle permits exposure readings from restricted regions of the flames and thus adjustments may readily be made for small changes in brightness. These photographs were made on Kodachrome II film (daylight type) rated at an exposure index of 32. Exposure times were varied from 1/25 sec to 30 sec. Changes of exposure time by as little as a factor of 2 made the difference between good and poor color reproduction. For the longer exposures attempts were made to take account of the reciprocity-law failure by the use of color correction filters as recommended by the film manufacturer. However, it was found that the best color reproduction was obtained without the use of filters.

3. Discussion

Two general methods have been used in the study of afterglows. In a static gas system after pulsing an electrical discharge, changes of color can be observed as function of time. Alternatively, the same phenomena can be observed in a flowing gas system as a function of distance downstream from the discharge. The observed phenomena are caused by various reactions of energetic species. Different color regions indicate different concentrations of atoms, molecules, and ions and the collision processes occurring between these species.

There are many known species in discharges in pure atomic and diatomic gases: atoms and diatomic molecules each in several electronic states, ions of atoms and molecules, electrons, and photons. Conditions in the discharge affect the relative concentrations of these species. Concentrations change as a function of time after the discharge with most of the more energetic species decreasing monotonically with time. However in some cases, the collision processes cause increases of certain species. In nitrogen at times a few milliseconds after the discharge, the number of ions [16] and of electronically excited molecules is increased [17], (see fig. 6). A very energetic N_4 molecule has been postulated as the energy carrier in this case [18]. At times of tens of microseconds after a discharge in very pure helium, there is a large increase in the concentration of electronically excited helium atoms and diatomic helium molecules [19], (see fig. 13). The details of the energy exchange mechanisms involved in these short-time afterglows are not yet understood.

Some collision processes occurring in afterglows have been carefully studied. For example, the long-time nitrogen afterglow is understood in terms of reactions of nitrogen atoms to form molecular nitrogen [20]:

$$N(^4S)+N(^4S)+M\rightarrow N_2(^5\Sigma_g^+)+M \qquad (1)$$

M is any third body in the three body collision process. The electronically excited molecule of nitrogen, $N_2(^5\Sigma_g^+)$ can undergo a collision to change its electronic state to the upper state of the first positive system of nitrogen, $N_2(B\,^3\Pi_g)$:

$$N_2(^5\Sigma_g^+)+M\rightarrow N_2(B\,^3\Pi_g)+M. \qquad (2)$$

This is followed by radiation of a photon, $h\nu$:

$$N_2(B\,^3\Pi_g)\rightarrow N_2(A\,^3\Sigma_u^+)+h\nu. \qquad (3)$$

Because the energy available in reaction (1) is equal to the dissociation energy of nitrogen, 9.76 ev (plus a small addition of kinetic energy of the colliding particles), the total energy of the $B\,^3\Pi_g$ molecular nitrogen is limited to this amount. As a consequence, the twelfth vibrational level of the $B\,^3\Pi_g$ state is the highest one that can be populated. The emission from reaction (3) is the First Positive system of N_2 with a non-Boltzmann distribution of vibrational populations, characterized in the visible region by a maximum near $v'=10$.

It is this particular emission of the First Positive system of N_2 which gives the "straw-yellow" color of figures 2 and 11 to the Lewis-Rayleigh nitrogen afterglow. If the nitrogen is diluted with large amounts of a rare gas such as helium, the population distribution in the $N_2(B\,^3\Pi_g)$ state is changed [21] moving to maximum populations near $v'=8$. This corresponds to a shift toward the red end of the spectrum and is observed visually as a change in color of the afterglow. The change in color can be seen by comparing figures 2 and 3, and figures 11 and 12.

Impurities in the discharge cause large changes in concentrations and in the kinds of species. Additions of small amounts of oxygen cause large changes in the colors of the afterglow because of reactions with oxygen atoms formed in the discharge. Oxygen atoms can react with nitrogen producing NO molecules in the upper state of the β bands of NO, $B\,^2\Pi$:

$$N(^4S)+O(^3P)+M\rightarrow NO(B\,^2\Pi)+M \qquad (4)$$

followed by

$$NO(B\,^2\Pi)\rightarrow NO(X\,^2\Pi)+h\nu \qquad (5)$$

where $h\nu$ represents radiation which is brightest in

the blue region of the spectrum [3, 22], (fig 4). Nitrogen atoms react rapidly with the NO to make N_2 and oxygen atoms:

$$N(^4S) + NO \rightarrow N_2 + O(^3P) \quad (6)$$

When sufficient oxygen is added all the nitrogen atoms are consumed in the reactions. In the absence of nitrogen atoms, NO reacts with oxygen atoms to give NO_2 in an electronically excited state [23] and this is followed by the emission of a photon.

$$NO + O(^3P) + M \rightarrow NO_2^* + M \quad (7)$$

$$NO_2^* \rightarrow NO_2 + h\nu. \quad (8)$$

Reaction (8) causes the yellow green "air afterglow" shown in figure 5.

Bright "atomic flames" often can be seen when gases or vapors are added to the atoms produced in the discharge. For example the glow produced by reaction (8) is formed by adding NO in excess of the amount of nitrogen atoms to the afterglow of pure nitrogen. Thus the color, and the spectral emission, of figures 5 and 7 are the same. If hydrocarbon vapors are added to nitrogen, as in figures 8 and 22, bright visible emission caused predominatly by CN is observed [10, 11, 13]. Atomic oxygen mixed with hydrocarbons shows a completely different appearance (figs. 9 and 21) because the emission is due to CH and C_2 [8, 9].

To observe steady-state afterglows at very short times after a discharge, it has been necessary to use supersonic flows from a discharge in a de Laval nozzle [15, 19]. At such high gas velocities, or rather in such short times, there is very little mixing of gases as illustrated in figure 14. However it is possible to observe some very efficient collision processes with metastable helium triplet state atoms. Energy exchange collisions with neon cause excitation of many electronic states of neon (figs. 15 and 16). Oxygen and nitrogen are ionized as well as electronically excited by collisions with metastable helium atoms, by what is known as the Penning process [24]:

$$He\ (2\,^3S) + N_2 \rightarrow N_2^+ + He\ (1\,^1S) + e \quad (9)$$

$$He\ (2\,^3S) + O_2 \rightarrow O_2^+ + He\ (1\,^1S) + e \quad (10)$$

Some dissociation of molecules also occurs since emission of atomic oxygen has been observed [19]. In figures 17, 18, and 19 the zones in the flames in which the various species are excited are clearly distinguishable from the colors: atomic and molecular helium is pink; N_2^+ is blue; O_2^+ and O are green. The diamond-shaped regions in which the different species appear are characteristic of shock fronts in the supersonic flow regime.

4. References

[1] E. Warburg, Arch. de Gen. (3) **12**, 504 (1884).
[2] R. E. Jennings, and J. W. Linnett, Quart. Rev. **12**, 116 (1958).
[3] F. Kaufman, in Progress in Reaction Kinetics **1**, pp 1 (Pergamon Press, N.Y. 1961).
[4] K. R. Jennings, Quart. Rev. **15**, 237 (1961).
[5] C. M. Herzfeld and A. M. Bass, Sci. Amer. **90** (Mar., 1957).
[6] H. P. Broida, Endeavour **17**, 208 (1958).
[7] A. G. Gaydon, The Spectroscopy of Flames, pp 39–42, 158, 252 (Chapman and Hall, 1957).
[8] A. G. Gaydon and H. G. Wolfhard, Proc. Roy. Soc. **A213**, 366 (1952).
[9] R. E. Ferguson and H. P. Broida, 5th Symposium on Combustion p. 754 (Reinhold Publ. Co., N.Y. 1955).
[10] N. H. Kiess and H. P. Broida, 7th Symposium on Combustion p. 207, (Butterworths Scientific Publications, London 1959).
[11] K. R. Jennings and J. W. Linnett, Trans. Faraday Soc. **56**, 1737 (1960).
[12] H. G. V. Evans and C. A. Winkler, Can. J. Chem. **34**, 1271 (1956).
[13] H. E. Radford and H. P. Broida, J. Chem. Phys. **38**, 644 (1963).
[14] D. Garvin and H. P. Broida, 9th Symposium on Combustion (Academic Press, N.Y. 1963).
[15] W. B. Kunkel and F. C. Hurlbut, J. App. Phys. **28**, 827 (1957).
[16] I. Tanaka and H. P. Broida, J. Chem. Phys. **36**, 236 (1962).
[17] G. E. Beale and H. P. Broida, J. Chem. Phys. **31**, 1030 (1959).
[18] A. B. Prag and K. C. Clark, J. Chem. Phys. (to be published).
[19] A. L. Schmeltekopf, Jr. and H. P. Broida, J. Chem. Phys. (to be published).
[20] P. K. Carroll, J. Chem. Phys. **37**, 805 (1962).
[21] U. H. Kurzweg and H. P. Broida, J. Molecular Spect. **3**, 388 (1959).
[22] U. H. Kurzweg, A. M. Bass, and H. P. Broida, J. Molecular Spect. **1**, 184 (1957).
[23] H. P. Broida, H. I. Schiff, and T. M. Sugden, Trans. Faraday Soc. **57**, 259 (1961).
[24] E. E. Benton, E. E. Ferguson, F. A. Matsen, and W. W. Robertson, Phys. Rev. **128**, 206 (1962).

(Paper 67A4–228)

(See figures 1 to 24 on the following pages.)

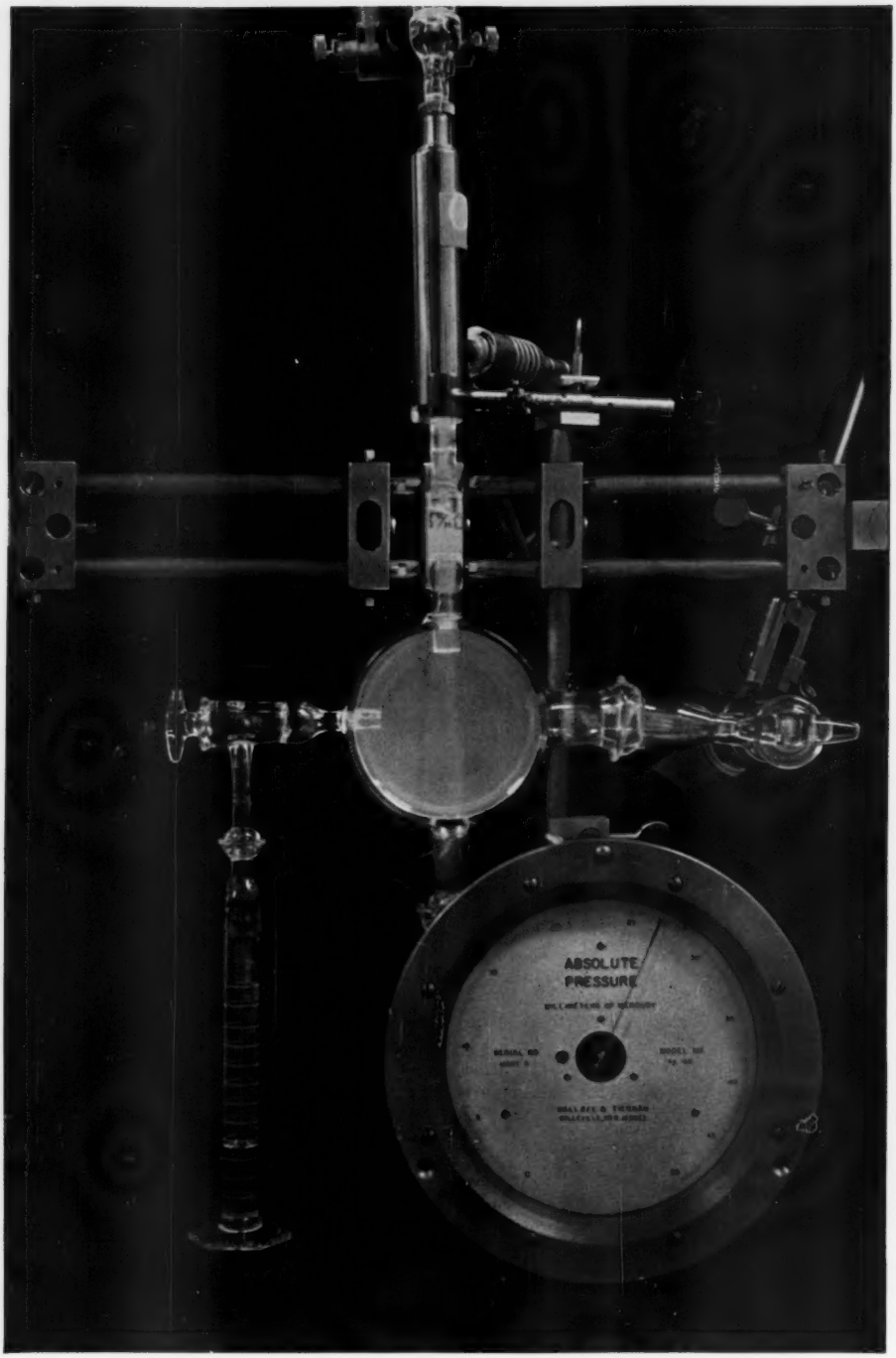

FIGURE 1. Apparatus for producing afterglows and atomic flames. The pink glow in the cylindrical vessel is a nitrogen afterglow in an excess of helium at a pressure of 27 mm Hg.

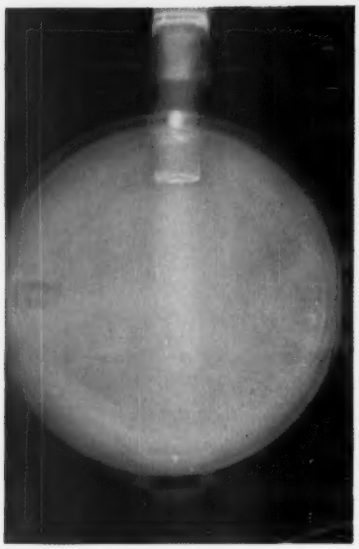

2

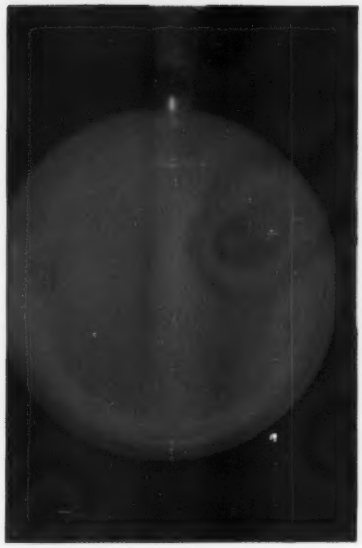

3

4

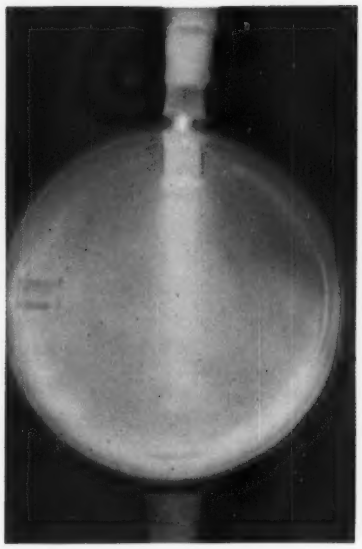

5

Afterglows from Discharges Through Nitrogen

FIGURE 2. Pure nitrogen at 4 mm Hg, pressure showing the typical Lewis-Rayleigh afterglow.
FIGURE 3. Same amount of nitrogen in large excess of helium at 50 mm Hg.
FIGURE 4. Approximately 1 percent O_2 added to the nitrogen of figure 2.
FIGURE 5. Approximately 3 percent O_2 added to the nitrogen, showing the "air-afterglow."

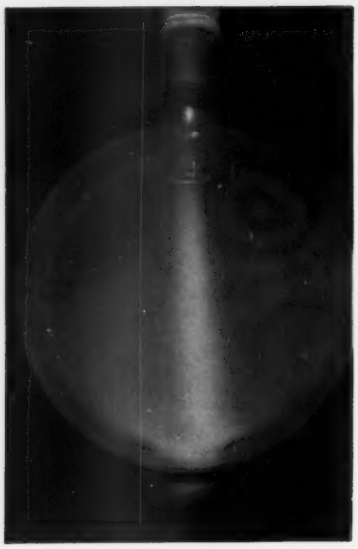

6

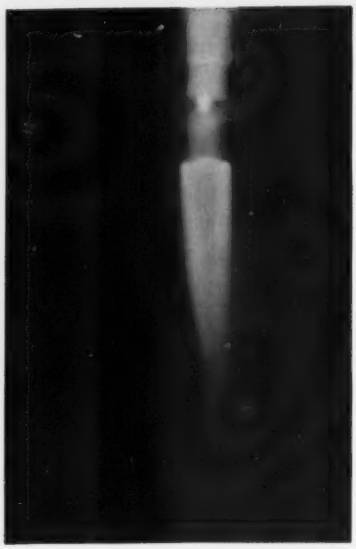

7

8

9

Afterglows from Discharges Through Nitrogen—Continued

FIGURE 6. Short-duration, pink "auroral" afterglow surrounded by the Lewis-Rayleigh afterglow at 4 mm Hg.

Atomic Flames

FIGURE 7. Nitrogen atoms with added nitric oxide (NO).
FIGURE 8. Nitrogen atoms with added methylene chloride (CH_2Cl_2).
FIGURE 9. Oxygen atoms with added acetylene (C_2H_2).

10

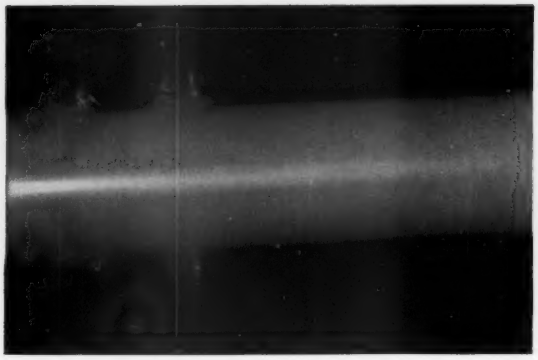

11

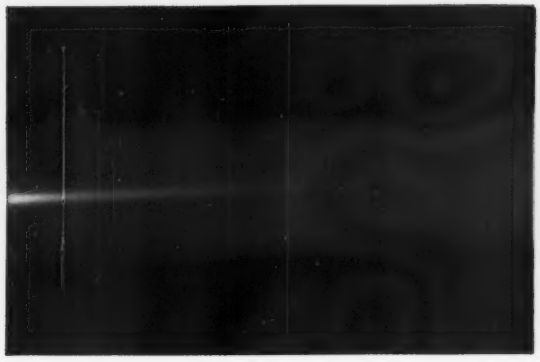

12

Atomic Flames—Continued

FIGURE 10. Astrojet apparatus for producing helium afterglows and flames.

Afterglows from Discharges Through Nitrogen in the Astrojet

FIGURE 11. Pure nitrogen.

FIGURE 12. Nitrogen with large excess of helium.

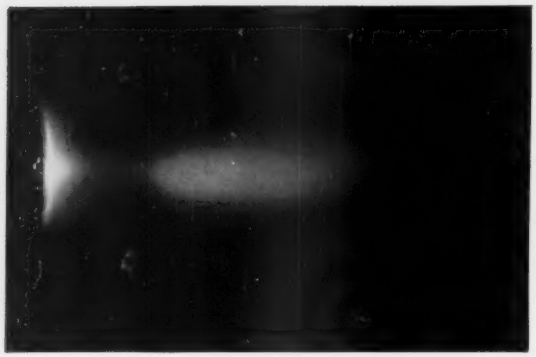

13

14

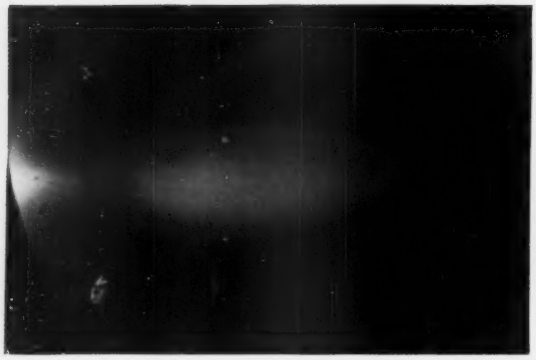

15

16

Short-Duration Glows from Discharges Through Helium in a deLaval Nozzle

FIGURE 13. Pure helium afterglow at 1.4 mm Hg.

FIGURE 14. Intersection of two high-velocity gas streams each showing the pure helium afterglow.

FIGURE 15. Same conditions as 13 (1.4 mm Hg) with the addition of less than 0.01 percent neon downstream from the discharge.

FIGURE 16. Same mixture as 15 at 10 mm Hg.

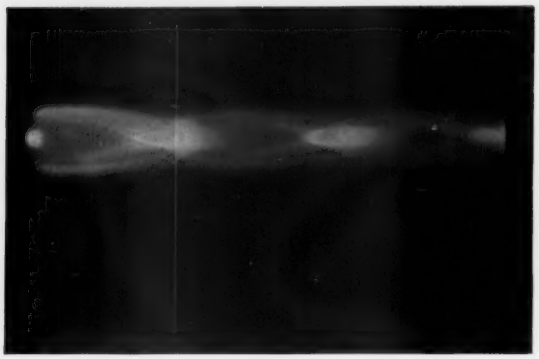

17

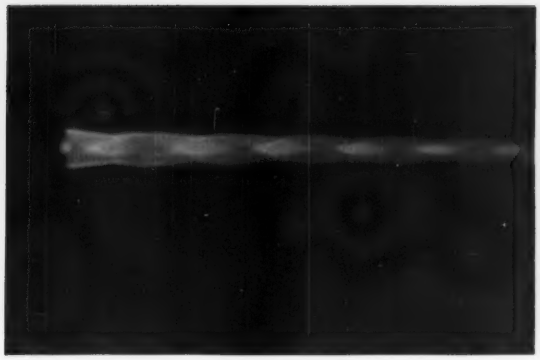

18

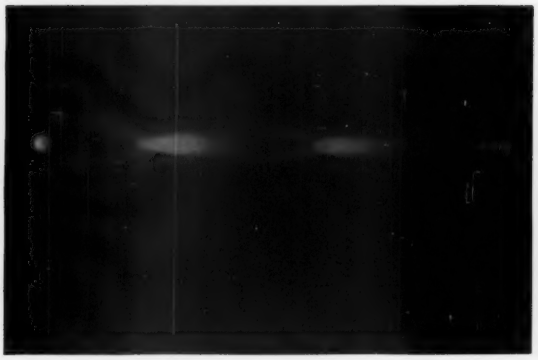

19

20

Helium Flames at Supersonic Velocities

FIGURE 17. Metastable helium at 2 mm Hg with oxygen added downstream from the discharge.
FIGURE 18. Same mixture as 17, at 4 mm Hg.
FIGURE 19. Metastable helium at 2 mm Hg with oxygen added downstream from the discharge.
FIGURE 20. Same mixture as 19, at 20 mm Hg.

21

22

23

24

Flames

FIGURE 21. Atomic oxygen with added acetylene (C_2H_2).
FIGURE 22. Atomic nitrogen with added methylene chlorine (CH_2Cl_2).
FIGURE 23. Metastable helium with added oxygen.
FIGURE 24. Metastable helium with added nitrogen.

JOURNAL OF RESEARCH of the National Bureau of Standards—A. Physics and Chemistry
Vol. 67A, No. 4, July–August 1963

Publications of the National Bureau of Standards*

Selected Abstracts

Effect of molecular weight on viscoelastic properties of polymers as predicted by a molecular theory, H. Oser and R. S. Marvin, *J. Research NBS* **67B** (*Math. & Math. Phys.*), *No. 2, 87 (Apr.–June 1963).*

Calculations have been made covering the predictions of a model representing the viscoelastic behavior of rubberlike polymers for molecular weights greater than M_c, M_c being the lower limit of the range in which the viscosity is proportional to $M^{3.4}$. A pronounced difference in the character of G'' is predicted for polymers with molecular weights between five and ten times M_c as compared with those whose molecular weights are outside this range.

The specific heat of saturated liquid para-hydrogen from 15 to 32°K, B. A. Younglove and D. E. Diller, *Cryogenics* **2,** *No. 5, 1–5 (Sept. 1962).*

The specific heat of saturated liquid *para*-hydrogen C_σ has been measured as part of a programme for determining the thermodynamic properties of *para*-hydrogen at high densities and low temperatures. Thermodynamic properties of the compressed liquid have been computed using C_σ as the baseline. The specific heat of argon has been measured for comparison with that of Flubacher, Leadbetter, and Morrison. Also the C_σ of *para*-hydrogen has been measured by others, which provides an additional comparison. The results obtained in this work serve to evaluate the accuracy that may be expected in future measurements of compressed fluids with this apparatus.

Thermal reactions of isobutyl radicals, W. M. Jackson, J. R. McNesby and B. deB. Darwent, *J. Chem. Phys.* **37,** *No. 10, 2256–2260 (Nov. 1962).*

Deuterium labeled isobutane $(CH_3)_3CD$ was pyrolyzed to generate $(CH_3)_3C$ and $CH_2CD(CH_3)_2$ radicals. The competition between reactions (5) and (6) was studied by isotopic analysis of the hydrogen, methane and isobutene fractions.

$$CH_2CD(CH_3)_2 \rightarrow CH_2{=}C(CH_3)_2 + D \qquad (5)$$

$$CH_2CD(CH_3)_2 \rightarrow CH_2{=}CDCH_3 + CH_3 \qquad (6)$$

Reaction (5) was found to be of negligible importance relative to reaction (6) up to 540°C and it is concluded that previous estimates of $k5/k6$ (in the non-deuterated species) are too high by at least an order of magnitude. The expulsion of molecular hydrogen by isobutyl or *t*-butyl does not occur in competition with other unimolecular reactions of these radicals.

Intramolecular rearrangements. V. Formation of ethylene in the photolysis of ethyl acetate from 4 to 500°K, P. Ausloos and R. E. Rebbert, *J. Phys. Chem.* **67,** *No. 1, 163–167 (Jan. 1963).*

The formation of ethylene in the gas, liquid and solid phase photolysis of $CH_3COOC_2H_5$, $CH_3COOCD_2CD_2H$ and $CH_3COOC_2D_5$ has been investigated at various wavelengths and temperatures. The intramolecular isotope effect increases with a decrease in temperature in both the gas and liquid phase photolysis. In the liquid phase an activation energy difference of 1 kcal/mole was obtained for D and H-atom transfer in the photolysis of $CH_3COOCD_2CD_2H$. A variation in wavelength influences the formation of ethylene in the gas and solid phases but does not affect the intra and inter molecular isotope effects in the liquid phase. A comparison of the product yields in the mercury sensitized decomposition with those obtained in the direct photolysis, as well as a study of the effect of biacetyl on the ethylene yield, indicates that the formation of ethylene by an intramolecular rearrangement of the ester molecule excited to an upper triplet state cannot be ruled out.

Microwave studies of butadiene derivatives. I. Spectrum of fluoroprene, D. R. Lide, Jr., *J. Chem. Phys.* **37,** *No. 9, 2074–2079 (Nov. 1962).*

The microwave spectrum of fluoroprene ($CH_2{=}CHCF{=}CH_2$) has been studied in the 8–35 kMc region. The molecule is shown to have a planar *trans* configuration with ground-state rotational constants $a = 10000.26$, $b = 4264.35$, $c = 2989.21$ Mc. The spectra of five excited vibrational states, including the first three excited torsional states, have been analyzed in detail. Relative intensity measurements give a torsional frequency of 156 ± 9 cm^{-1} with no detectable anharmonicity. Negative inertial defects are observed in the excited torsional states; this is explained by a simple model of the torsional oscillation. The dipole moment in the ground state has a magnitude of 1.417 ± 0.010 D and makes an angle of 10°–15° with the C–F bond. Possible forms of the torsional potential function which are consistent with the experimental results are discussed. It is suggested that a function which allows for a non-planar isomer in butadiene-type molecules (so far unobserved) gives a reasonable explanation of all the present data.

Critical opalescence of polystyrene solutions, D. McIntyre, A. Wims, and M. S. Green, *J. Chem. Phys.* **37,** *No. 12, 3019–3020 (Dec. 1962).*

An experimental study of the critical opalescence of polystyrene solutions was made. The angular variation of intensity and the temperature dependence of intensity indicates some differences from the Debye and Ornsteim-Zernicke theory.

Refraction and dispersion of synthetic sapphire, I. H. Maltison *J. Opt. Soc. Am.* **52,** *No. 12, 1377–1379 (Dec. 1962).*

The refractive indices of synthetic sapphire were measured at selected wavelengths and the values of index range from 1.834 at 0.265μ in the ultraviolet to 1.586 at 5.58μ in the infrared. A three-term Sellmeier dispersion equation of the form

$$n^2 - 1 = \sum_i \frac{A_i \lambda^2}{\lambda^2 - \lambda_i^2}$$

was fitted to the experimental data. Dispersive quantities were computed which estimate the optical performance to be expected from sapphire.

Thermophysical properties of zirconium hydrides, R. L. Beck and T. B. Douglas, *Trans. Am. Soc. Metals* **55,** *1075–1076 (1962).*

Attention is called to the emphasis by metallurgists and physical chemists of different sets of properties of metal hydrides, but it is pointed out that almost all properties indicate and are influenced by the phase-field boundaries. The author (of the paper discussed) shows commendable caution in interpreting data in terms of these boundaries. More two-way approach to immobile equilibria is recommended, and the writer cites some of his own experience. One heat capacity reported, while not precise, agrees with a recent correlation by the writer of the Zr-H system. The writer criticizes the implication that two coexistent phases have the same heat capacity. He points out that an ideal heat-capacity curve has a discontinuity on entering a two-phase field and that for a given simple composition the heat capacity in the latter field is always greater than in an adjacent one-phase field.

Nuclear magnetic resonance of Ni^{61} in dilute alloys of nickel in cobalt, R. L. Streever, L. H. Bennett, R. C. LaForce, and G. F. Day, *Phys. Rev.* **128,** *No. 4, 1632–1633 (Nov. 1962).*

The nuclear magnetic resonance of Ni^{61} has been observed in 1% Ni^{61} —99% Co and 2% Ni^{61} —98% Co alloys. The

685-226—63——9

esonance frequency is 70.4 Mc/sec at room temperature and 71.7 Mc/sec at 77° K. The hyperfine field at nickel in cobalt is about two and a half times its value in pure nickel, implying a nearly proportional increase in the local magnetic moment.

The bound-free absorption coefficient of the hydrogen negative ion, S. Geltman, *Astrophys. J.* **136,** *No. 3, 935–945 (Nov. 1962).*
The bound-free absorption coefficient of H^- is evaluated using a set of successively improved bound and free state wave functions. Better agreement with experiment and greater theoretical consistency are shown to result. The best theoretical result is tabulated for use in astrophysical applications.

Heats of formation of two isomers of difluorodiazine, G. T. Armstrong and S. Marantz, *J. Chem. Phys.* **38,** *No. 1, 169–172 (Jan. 1963).*
The heats associated with the reaction

$$N_2F_2(g)+\frac{8}{3}NH_3(g)-2NH_4F(c)+\frac{4}{3}N_2(g)$$

were observed for two mixtures containing the trans and the "active" isomeric forms of difluorodiazine (N_2F_2) in different proportions. From the observed heats of reaction of the two samples the heat of isomerization, $\triangle H^\circ_{298}$, of "active" to trans-N_2F_2 was found to be 3.0 kcal mole^{-1} with calculated standard error of 0.3 kcal mole^{-1} based on four degrees of freedom. With the use of auxiliary data for NH_3 and NH_4F, the heats of formation $\triangle Hf^\circ_{298}$ were determined to be +19.4 and +16.4 kcal mole^{-1} for the trans and the "active" isomers respectively. The bond energies in the two substances are discussed in terms of the possible molecular configurations.

Method for finding the density expansion of transport coefficients of gases, R. Zwanzig, *Phys. Rev.* **129,** *No. 1, 486–494 (Jan. 1, 1963).*
This article presents a new method for finding the density expansion of certain transport coefficients of gases. These are the self-diffusion coefficient, and the momentum contributions to viscosity, thermal conductivity, etc. The method is to calculate the time-correlation function associated with the transport process. To lowest order in density, the results are identical with those found by Enskog's first order perturbation solution of the Boltzmann equation. The first density correction requires the solution of a certain three body problem. This problem is stated precisely, but is not solved.

γ-Irradiation of small molecules at 4 and 77° K, R. E. Florin, D. W. Brown, and L. A. Wall, *J. Phys. Chem.* **66,** *2672–2676 (Dec. 1962).*
The gamma irradiation of CH_4, CF_4 and SiF_4 was investigated by electron spin resonance both at 4° K and 77° K. The influence of inert matrices of Xe was also studied and found to be useful in trapping radical species, particularly at 77° K. The electron spin resonance spectra for the radicals CH_3, CF_3 were profoundly altered by both temperature and presence of the matrix, whereas that for SiF_3 was not. Spectra from several irradiated fluorocarbons are also reported.

Measuring plasma density of the magnetosphere, K. L. Bowles, *Science* **139,** *No. 3553, 389–391 (Feb. 1, 1963).*
This note reports a brief review of the incoherent scatter technique for measuring electron density and temperate profiles in the magnetosphere. Examples of early data are given.

Complex formation between manganese (II), nickel (II), and zinc (II) ions and some symmetrically substituted ethylenediamines: The use of E_r and δH values in assessing inductive and steric effects, D. L. Leussing, *Inorganic Chem.* **2,** *No. 77, 77–82 (1963).*
Using the procedures of George and McClure, E_r and δH_{Ni} values have been calculated from the formation constants of manganese (II), nickel (II), and zinc (II) complexes with some symmetrically substituted ethylenediamines. It is shown that *C*-substitution by alkyl groups appreciably increases the E_r values in the direction expected for an increase in the ligand nucleophilicity. *N*-substitution brings about an effect in the same direction but of smaller magnitude. The δH_{Ni} values are lower for the substituted ethylenediamines than for the unsubstituted ligand. It is possible to correlate the δH_{Ni} values with both the spectral band positions of the respective complexes and their activation energies for dissociation. The data indicate that the stabilities of nickel (ii) complexes are highly sensitive to steric influences. A comparison of the properties of the amine complexes of nickel (II) with those of mercaptide indicates that d_π–p_π bonding between nickel (II) and sulfur is the cause for the unusually low stabilities of these latter complexes.

Calorimetric determination of half-cell entropy changes, J. M. Sherfey, *J. Electrochem. Soc.* **110,** *No. 3, 213–221 (Mar. 1963).*
The reversible heat effects ($T\triangle S$) of half-cell processes have been measured in a twin calorimeter consisting of a Dewar flask divided into two halves by means of a vertical partition. Both compartments contain the same electrolyte and each has an electrode. A hole in the partition, covered by filter paper, permits the passage of electrolytic current between the compartments.
The total heat effect and the heat due to irreversible phenomena are measured separately for each compartment. The difference between these two gives the desired reversible heat. The half-cells studied include copper in acid copper sulfate, silver in acid silver perchlorate, and silver-silver chloride in various chloride solutions. The effect of "transport entropies" on these measurements is outlined. Presently accepted theories of the "irreversible" or "steady state" thermodynamics of electrolytic cells predict the equivalence of half-cell entropy data obtained by the present calorimetric method and data obtained from thermocell studies. This predicted agreement was not obtained in the case of the half-cell silver-silver perchlorate.

Hartree-Fock approximation of CH_4 and NH_4^+, M. Krauss, *J. Chem. Phys.* **38,** *No. 2, 564–565 (Jan. 15, 1963).*
Molecular energies, which approach the Hartree-Fock limit, have been computed for the CH_4 and NH_4^+ molecules at their equilibrium distances. These results verify the suitability of exponential quadratic functions as basis functions in molecular calculations.

Formation of decay of atoms and small free radicals at low temperatures, D. W. Brown, R. E. Florin and L. A. Wall, *J. Phys. Chem.* **66,** *2602–2612 (Dec. 1962).*
The maximum numbers of atoms that can be produced by exposing solid H_2, D_2, N_2, and CH_4 to gamma radiation at 4.2° K were investigated using the electron spin resonance method. The limiting values expressed in mole percent were estimated to be 0.1% N atoms in N_2; 0.2% each of H atoms and CH_3 radicals in CH_4; less than 0.008% D atoms in D_2; and 0.0001% H atoms in H_2. The lifetimes of the atoms were found to be highly dependent on the nature of their surrounding media. The decay behavior suggests complex mechanisms involving several types of processes including autoignition types. Certain spectral changes were observed upon decay or annealing of the irradiated materials. Besides obtaining sharper and more resolved spectra, additional lines, usually of weak intensity, were seen. The possible interactions or species responsible for these lines are discussed.

Gas-phase radiolysis of isobutane, R. P. Borkowski and P. J. Ausloos, *J. Chem. Phys.* **38,** *No. 1, 36–44 (Jan. 1, 1963).*
The radiolysis of $(CH_3)_3CD$-I_2 and $(CH_3)_3CH$-$(CD_3)_3CD$-I_2 mixtures have been investigated as a function of pressure from 30° to 225° C. Propane, which is the major product, is mostly formed by a hydride transfer reaction such as sec-$C_3H_7^+ + (CH_3)_3CH \rightarrow C_3H_8 + (CH_3)_3C^+$. From the distribution of the isotopic propanes produced in the radiolysis of $(CH_3)_3CD$ it can be concluded that hydrogen atoms in the sec-propyl ion are randomized in various degrees depending on the pressure of isobutane. Ethane is mainly formed by a hydride transfer reaction

$$C_2H_5^+ + (CH_3)_3CH \rightarrow C_2H_6 + C_4H_9^+$$

Two distinct processes lead to the formation of ethylene, (a) molecular elimination from isobutane and (b) reaction of vinyl ions with isobutane. The effect of zenon krypton and argon on the product distribution and the randomization of the sec-propyl ion is discussed in some detail.

Comparative measurements on polystyrene with three different equilibrium ultracentrifuges, D. McIntyre, L. C. Williams, P. E. Haxner, H. G. Kim, F. N. Weber, R. F. Bunting, and D. W. Kurke, *J. Polymer Sci.* **62,** *No. 174, S136–S140 (Dec. 1962).*

A magnetically suspended equilibrium centrifuge of new design was compared with two other equilibrium ultracentrifuges in the determination of the molecular weight of a synthetic polymer. The speed control and optics of the magnetically suspended centrifuge allow a very precise determination of weight-average molecular weight although the *z*-average molecular weight is not in agreement with fractionation results.

Some stochastic processes in polymer systems, J. Mazur, *J. Chem. Phys.* **38,** *No. 1, 193–201 (Jan. 1, 1963).*

Certain distributional problems involving polymer configurations can be treated as special classes of stochastic processes known as regenerative processes. These processes have the property that the interval (of time or of length) between two consecutive events is a random variable. The method of regeneration point is applied to the problem of random crystallization of polymers and to the problem of force-length relationships in a one-dimensional simulation of a polymer network. By assuming that the events of randomly placing crystalline units on a polymer chain are statistically independent, and that the probability of the first event occurring in a given interval is a simple step function, the direct application of the method of regeneration point leads to a well-known equation from the theory of molecular distribution in one-dimensional hard-core fluids. In the second problem it is assumed that a single polymer chain consists of mesh points connected by flexible chains. A restriction is imposed that these mesh points cannot pass through each other. The molecular distribution functions for these mesh points are derived with the help of the regeneration-point process. By applying this method, the relationships of the network extension to the fixed force are derived. It is also found that the affine transformation rule for the force-biased distribution of chain lengths holds strictly only if the array represents a Poisson distribution of mesh points.

On the three-particle scattering operator in classical gases, J. Weinstock, *Physics Letters* **3,** *No. 6, 260–262 (Feb. 1, 1963).*

The three-particle scattering operator is the central quantity which must be calculated in order to determine the density dependence of transport coefficients in gases. A perturbation method is presented, for such a calculation, which is based upon the "binary collision expansion" of the "Greens function" form of the three-particle scattering operator. In addition, it is pointed out that the *n*-particle scattering operators of non-equilibrium statistical mechanics are actually the asymptotic forms of more general time dependent *n*-particle operators, and that a complete description of non-equilibrium phenomena may be obtained from a knowledge of the time dependence of these more general operators.

Rotational, vibrational, and electronic energy transfer in the fluorescence of nitric oxide, H. P. Broida and T. Carrington, *J. Chem. Phys.* **38,** *No. 1, 136–147 (Jan. 1, 1963).*

A sharp emission line of ionized cadmium from an electric discharge excites NO molecules to the $K'=13$ rotational level of the $v'=1$ vibrational level of the $A^2\Sigma^+$ electronic state. Steady-state fluorescence has been observed from this level and from neighboring levels populated by collisional interaction between the excited and added inert molecules. Cross sections have been measured in He, Ar, H_2, N_2, NO, and CO_2 for electronic deactivation to the ground $X^2\Pi$ state, for vibrational deactivation to the $v'=0$ level of the $A^2\Sigma^+$ state, and for rotational exchange in the $A^2\Sigma^+$ state. It has been established that rotational transitions having changes in rotational quantum number greater than unity take place with high probability, contrary to the optical selection rule.

Observations of synchrotron radio noise at the magnetic equator following the high altitude nuclear explosion of July 9, 1962, G. R. Ochs, D. T. Farley, Jr., K. L. Bowles, and P. Bandyopadhay, *J. Geophys. Res.* **68,** *701–711 (Feb. 1963).*

This paper describes the results of radio measurements made in Peru of synchrotron radiation at 30 Mc/s and 50 Mc/s. This radiation was produced by relativistic electrons injected into trapped orbits in the earth's magnetic field during the high altitude nuclear explosion of July 9, 1962. A preliminary interpretation of these results is also given.

At 50 Mc/s there was a brief transient increase in the antenna temperature of 4.5×10^6 °K shortly after the explosion. This can be compared to the normal antenna temperature at that time of 5.5×10^2 °K. The excess temperature soon decreased to about 1×10^4 °K and has since decayed only very slowly from this value, with a time constant of about two months. From the early transient changes in the antenna temperature, a fairly accurate description of the energy distribution of the electrons is obtained. This spectrum is found to vary almost exactly as the fission spectrum, $\exp(-0.575\ E-0.055\ E^2)$, in the range $1 \leq E \leq 5$, where E is the kinetic energy in Mev. Above 5 Mev the spectrum falls off somewhat faster than this expression, but the measurements are rather poor in this range. The value 2×10^{24} is obtained as a rough estimate of the total number of electrons with energies of the order of 1 Mev or greater that were trapped after the explosion.

The measurement of voltage by the use of the Stark effect, Y. Beers and G. L. Strine (*Intern. Conf. Precision Electromagnetic Measurements, Boulder, Colo., 1962*), *IRE Trans. Instr.* **I–II,** *171 (Dec. 1962).*

The theory of the Stark effect is reviewed with regard to its possible application of measuring voltages. It is pointed out that the effect can be used only to measure relative voltage and that the accuracy is likely to be limited by the accuracy with which the electrode separation can be determined. Therefore, the most sophisticated types of molecular frequency standards may not be required. The Stark method appears to hold a particular advantage for the measurement of high voltage since no voltage divider is required. Also, two possible methods of comparing ac voltages to dc voltages are discussed. Finally, an experimental Stark voltmeter employing a millimeter wave Fabry-Perot absorption cell is discussed. Calculations concerning $J=2\rightarrow3$ transition of methyl cyanide at 55 Gc indicate that in principle the precision obtainable with a field strength of 10^4 volts/cm should be in the neighborhood of one part in a million, if field inhomogeneities can be neglected.

The sequence selection problem in the crystallization of polymers. I. Homopolymers, F. Gornick and J. L. Jackson, *J. Chem. Phys.* **38,** *No. 5, 1150–1154 (Mar. 1963).*

The crystallization of linear polymer chains is considered as a process involving the selection of crystallizable sequences from the melt. If, owing to the requirements of thermodynamic stability, such sequences must exceed in length some critical value less than the chain length, and if the selection process is random, then the melt will be increasingly subdivided into uncrystallized sequences of varying length. Some of these may be expected to be less than the critical length so that the segments comprising them are "wasted" insofar as participation in further crystallization is concerned. An approximate sequence length distribution function for the uncrystallized sequences in the system is derived and utilized in connection with the problem of retardation in crystallization kinetics.

Detection of high altitude nuclear detonations using the VLF phase shift technique, A. G. Jean and D. D. Crombie, *IEE Trans. Nucl. Sci.* **NS–10,** *242–253 (Jan. 1963).*

It is well known that nuclear detonations at heights of about 30 km or more can create large increases in the electron density of the upper atmosphere not only in the general area of the blast but also in areas remote from it. In this paper, the effects of such nuclear explosions on the lower ionosphere are considered. The influence of these ionospheric changes on the propagation of VLF signals is then discussed from the point of view of the detection of such nuclear explosions.

Infrared spectrum of difluoramine, J. J. Comefore, D. E. Mann, L. J. Schoen, and D. R. Lide, Jr., *J. Chem. Phys.* **38,** *No. 2, 461–463 (Jan. 1963).*

The infrared spectrum of gaseous difluoramine, NF_2H has been investigated over the range 250–4000 cm^{-1}. Four bands of NF_2D have also been observed. The fundamental frequencies (in cm^{-1}) and their species are as follows:

NF_2H: $\nu_1(a')$:3193; $\nu_2(a')$:1307; $\nu_3(a')$:972; $\nu_4(a')$:500; $\nu_5(a'')$: 1424; $\nu_6(a'')$:888

NF_2D: $\nu_1(a')$:[2333]; $\nu_2(a')$:1008; $\nu_3(a')$:972; $\nu_4(a')$:[500]; $\nu_5(a'')$:1042; $\nu_6(a'')$:888

where the bracketed values were not observed directly. The fine structure resolved in several of the bands led to a value for $A-(B+C)/2$ in agreement with the microwave result. No inversion splitting was detected.

Homogeneous anionic polymerization. I. Molecular weights of polystyrene initiated by sodium napthalene, M. Morton, R. Milkovich, D. McIntyre, and J. L. Bradley, *J. Polymer Sci.* **1,** *Pt. A, 443–459 (Jan. 1963).*

Studies of the anionic polymerization of styrene by sodium napthalene have shown the type of molecular weight distributions that can be obtained under suitable experimental conditions. Detailed descriptions and techniques are given for all experimental work because of their importance in the preparation of polymers having narrow molecular weight distributions. It has been found, however, that the presence of even trace quantities of impurities are sufficient to prevent the preparation of a "monodisperse" sample, and that it cannot be arbitrarily assumed that even in the same laboratory a successful reaction can always be completed.

Other NBS Publications

J. Research NBS 67B (Math. & Math. Phys.), No. 2 (Apr.–June 1963). 75 cents.

Maximum cellular Boolean functions and perfect Gray codes. A. J. Goldman and B. K. Bender.

The meaning of Betti's reciprocal theorem. C. Truesdell.

Effect of molecular weight on viscoelastic properties of polymers as predicted by a molecular theory. H. Oser and R. S. Marvin. (See above abstract).

Selected bibliography of statistical literature: supplement, 1958–1960. L. S. Deming.

J. Research NBS 67D (Radio Prop.), No. 4 (July–Aug. 1963). 70 cents.

Influence of the lower ionosphere on propagation of VLF waves to great distances. J. R. Wait.

Comments on a paper "Auroral Sporadic-*E* Ionization" by Robert D. Hunsucker and Leif Owren. J. M. Bullen and G. A. M. King.

Reply to J. M. Bullen and G. A. M. King's "Comments on a paper 'Auroral Sporadic-*E* Ionization' by Robert D. Hunsucker and Leif Owren." R. D. Hunsucker and L. Owren.

Optimum reception pattern of the Beverage wave antenna at very low frequencies. E. W. Seeley.

Effect of a dissipative medium of finite size on antenna measurement. K. Iizuka and R. W. P. King.

Some implications of aircraft interference patterns in tropo-scatter reception. J. A. Bradshaw.

Asymptotic behavior of the current on an infinite cylindrical antenna. K. S. Kunz.

A dipole approximation of the backscattering from a conductor in a semi-infinite dissipative medium. M. B. Kraichman.

Small electric and magnetic antennas with cores of a lossy dielectric. J. Galejs.

Profiles of electron density over the magnetic equator obtained using the incoherent scatter technique, K. L. Bowles et al., NBS Tech. Note 169 (Mar. 16, 1963), 25 cents.

Lectures on ion-atom collisions, M. R. C. McDowell, NBS Tech. Note 185 (Mar. 15, 1963), 40 cents.

Transmission and reflection of electrons by aluminum foils, M. J. Berger, NBS Tech. Note 187 (April 1, 1963), 15 cents.

Lasers, T. R. Lawrence, J. Wash. Acad. Sci. **53,** 25–34 (Feb. 1963).

Gas evolution from metal surfaces during fatigue stressing, W. L. Holshouser and J. A. Bennett, Am. Soc. Testing Mater. Preprint 62 (June 1962).

The evolution of a conference, J. M. Richardson (Intern. Conf. Precision Electromagnetic Measurements, Boulder, Colo., 1962), Trans. IRE Instr. **I–II,** 82 (Dec. 1962).

Infrared absorption spectra of B_2O_3, B_2O_2, and BO_2 in solid argon matrices, A. Sommer, D. White, M. J. Linevsky, and D. E. Mann, J. Chem. Phys. **38,** No. 1, 87–98 (Jan. 1963).

The collaborative test, W. J. Youden, J. Assoc. Offic. Agric. Chem. **46,** 55–62 (Feb. 1963).

Conductive floors, F. L. Hermach, Intern. Assoc. Elec. Inspectors News Bull., p. 40–44 (July 1962).

Ionic interactions with sugar colorant during char filtration, F. G. Carpenter, D. Larry, and V. R. Dietz, Proc. 7th Tech. Session on Bone Char 1961, p. 259 (Bone Char Research Project Inc., Charlestown, Mass. 1962).

Note on the Kubelka method of measuring water absorption of leather, R. L. Hebert and A. E. McDonell, J. Am. Leather Chemists' Assoc. **LVII,** No. 9, 461–469 (Sept. 1962).

Intercomparisons of laboratory test results, J. Mandel, Proc. Instr. Soc. Am., Paper 44–3, 5 pages (1962).

Heat transfer between a cryo-surface and a controlled atmosphere. Part I. Experimental investigation, R. J. Richards, K. Edmonds, and R. B. Jacobs, Intern. Inst. Refrigeration, Suppl. Bull. Inst. Intern. Froid, p. 1–22 (1962).

Coatings formed on steel by cathodic protection and their evaluation by polarization measurements, W. J. Schwerdtfeger and R. J. Manuele, Corrosion **19,** No. 2, 59t–68t (Feb. 1963).

Microscopy of color phenomena in polymer fracture, S. B. Newman and I. Wolock, Proc. Symp. Adhesion and Cohesion, p. 218–239 (Elsevier Publ. Co., Amsterdam, The Netherlands, 1963).

Sum rules for vibrational-rotational energy levels including centrifugal distortion, H. C. Allen, Jr., and W. B. Olson, J. Chem. Phys. **37,** No. 2, 212–214 (July 15, 1962).

Studies of within-the-horizon propagation at 9300 Mc, A. P. Barsis, A. F. Barghausen, and R. S. Kirby, IEEE Trans. Ant. Prop. **AP–11,** 24–38 (Jan. 1963).

Dosimetry. Chemical and film media, M. Ehrlich, Book, Technology Needs for Reduction of Patient Dosage from Diagnostic Radiology, Ed. M. L. Janower, p. 81–100 (C. Thomas, Publ. Co., Springfield, Ill., 1962).

Variance of radiofrequency caused by atmospheric turbulence in line-of-sight transmissions, K. A. Norton, E. C. Barrows, M. C. Thompson, Jr., and H. B. Janes (Intern. Conf. Precision Electromagnetic Measurements, Boulder, Colo., 1962), IRE Trans. Instr. **I–II,** 153 (Dec. 1962).

Instrument for the continuous measurement of the density of flowing cryogenic fluids, C. E. Miller, R. B. Jacobs, and J. Macinko, Rev. Sci. Instr. **34,** 24–27 (Jan. 1963).

Some problems in temperature measurements from line spectra, J. T. Jefferies, Book, Temperatures Its Measurement and Control in Science and Industry **3,** Pt. 1, 703–711 (Reinhold Publ. Corp., New York, N.Y., 1962).

Direct observation of charge storage in the surface states of silicon, G. G. Harman, R. L. Raybold, and O. I. Meyer, J. Appl. Phys. **34,** No. 2, 380–382 (Feb. 1963).

Confidence limits for the reliability of complex systems, J. R. Rosenblatt, Book, Statistical Theory of Reliability, Ed., M. Zelen, p. 115–148 (Univ. of Wisconsin Press, Madison, Wisc., 1963).

Third international conference on precision electromagnetic measurements, W. D. George, Nature **139,** No. 4858, 921–929 (Dec. 8, 1962).

Improved zinc oxide-eugenol type cements, G. M. Brauer, L. Simon, and L. Sangermano, J. Dental Res. **41,** No. 5, 1096–1102 (1962).

Some early results from the ionospheric topside sounder satellite, R. W. Knecht and T. E. VanZandt, Nature **197,** 641–644 (Feb. 16, 1963).

Decibels return loss to magnitude of voltage reflection coefficient, R. W. Beatty, Microwave Eng. Handb. and Buyer's Guide, p. TD188–TD192 (1961–62).

Dielectric constant of Cr_2O_3 crystals, P. H. Fang and W. S. Brower, Phys. Rev. **129,** No. 4, 1561 (1963).

Curves for ground wave propagation over mixed land and sea paths, J. R. Wait and L. C. Walters, IEEE Trans. Ant. Prop. **AP-11,** 38–45 (Jan. 1963).

Alteration of the muscovite absorption spectrum by KBr pellet preparation, S. Ruthberg, M. W. Barnes, and R. H. Noyce, Appl. Opt. **2,** No. 2, 177 (Feb. 1963).

A survey of some mathematical models in the theory of reliability, G. H. Weiss, Book, Statistical Theory of Reliability, Ed. M. Zelen, p. 3–54 (University of Wisconsin Press, Madison, Wisc., 1963).

Thickness determination, V. A. Lamb, Electroplaters Process Control Handb. Ed. D. G. Foulke and F. E. Crane, Jr., Chapt. 12, p. 327–346 (Reinhold Publ. Corp., New York, N.Y., 1963).

Measurement of RF peak pulse power by a sampling-comparison method, P. A. Hudson, W. L. Hudson, W. L. Ecklund, and A. R. Ondrejka (Intern. Conf. Precision Electromagnetic Measurements, Boulder, Colo., 1962), IRE Trans. Instr. **I–II,** 280 (Dec. 1962).

Radiation of sound by ocean waves, R. K. Cook., Proc. 4th Intern. Congress Acoustics, Preprint 043 (Organization Committee, Copenhagen, Denmark, 1962).

Radiation effects on man, L. S. Taylor, Nucleonics **21,** No. 3, 58–60 (Mar. 1963).

Identification of Ga II lines in stellar spectra, W. P. Bidelman and C. H. Corliss, Astrophys. J. **135,** No. 3, 968–969 (1962).

Current trends and prospects, R. B. Stewart, R. V. Smith, and T. R. Strobridge, Cryogenics **2,** No. 6, 321–324 (Dec. 1962).

Hyperfine structure in the spectrum of mercury hydride, T. L. Porter and S. P. Davis, J. Opt. Soc. Am. **53,** No. 3, 338 (Mar. 1963).

Measurement and standardization of dielectric samples, H. E. Bussey and J. E. Gray (Intern. Conf. Precision Electromagnetic Measurements, Boulder, Colo., 1962), IRE Trans. Instr. **I–II,** 162 (Dec. 1962).

Primary processes in the photochemical decomposition of nitroalkanes, R. E. Rebbert and N. Slagg, Bull. Soc. Chim. Belges **71,** 709–721 (1962).

Polysulfide sealants, pt. II. Service properties, D. A. George, F. Roth, and P. Stone, Adhesives Age **6,** 35ff (Mar. 1963).

Plating specifications, F. Ogburn, Electroplaters Process Control Handb. Ed. D. G. Foulke and F. E. Crane, Jr., chapt 17, p. 406–407 (Reinhold Publ. Corp., New York, N.Y., 1963).

Spectrum analysis of extremely low frequency variations of quartz oscillators, W. R. Atkinson, L. Fey, and J. Newman, IEEE Trans. Ant. Proc. **51,** 379 (Feb. 1963).

A note on *E*-field and *H*-field losses for gound-based antennas, J.R.Wait, IEEE Trans. Ant. Proc. **51,** 366 (Feb. 1963).

Improved sample holder for X-ray diffractometer furnace, E. M. Levin and F. A. Mauer, J. Am. Ceram. Soc. **46,** No. 1, 59–60 (Jan. 1963).

Fluorescence of teeth, A. F. Forziati and M. P. Kumpula, Frontiers of Dental Sci., p. 106–112 (Natl. Sci. Teachers Assoc., Washington, D.C., Dec. 1962).

A note on diurnal phase changes of very-low-frequency waves for long paths, J. R. Wait, J. Geophys. Res. **68,** No. 1, 338–340 (Jan. 1, 1963).

Helium, V. Arp and R. H. Kropschot, Book, Applied Cryogenic Engineering, Ed. R. W. Vance, chapt. 12, 321–343 (John Wiley & Sons, Inc., New York, N.Y., 1962).

Pitfalls in determinations of the compressive strength of concrete, J. R. Dise, Mod. Concrete **26,** No. 3, 48–51 (July 1962).

Determination of lead in leaded steels by X-ray spectroscopy, B. A. Kilday and R. E. Michaelis, Appl. Spectry. **16,** No. 4, 136–138 (1962).

Infrasonics, R. K. Cook, McGraw-Hill Yearbook of Science & Technology, p. 275–276 (1962).

The aurora and trapped electrons, F. E. Roach, J. Geophys. Res. **68,** 1015–1021 (Feb. 15, 1963).

Behavior of revivified char in storage, J. Redd and F. G. Carpenter, Proc. 7th Tech. Session on Bone Char 1961, p. 223 (Bone Char Research Project, Inc., Charlestown, Mass., 1962).

A method for determining the height and geographical position of an auroral arc from one observing station, M. H. Rees, J. Geophys. Res. **68,** No. 1, 175–183 (Jan. 1, 1963).

A high-latitude investigation of the natural very-low-frequency electromagnetic radiation known as chorus, J. H. Pope, J. Geophys. Res. **68,** No. 1, 83–99 (Jan. 1, 1963).

The reactions of methyl radicals with aromatic compounds. I. Toluene, ethylbenzene, and cumene, I. B. Burkley and R. E. Rebbert, J. Phys. Chem. **67,** No. 1, 168–169 (Jan. 1963).

A comparison of direct and servo methods for utilizing cesium beam resonators as frequency standards, R. E. Beehler, W. R. Atkinson, L. E. Heim, and C. S. Snider (Intern. Conf. Precision Electromagnetic Measurements, Boulder, Colo., 1962), IRE Trans. Instr. **I–II,** 231 (Dec. 1962).

Image-gloss test; Apparatus and procedure, W. N. Harrison, Proc. Porcelain Enamel Inst. Forum **23,** 154–163 (1962).

Safety levels in military inventory management, F. L. Alt, Operations Res. **10,** No. 6, 786–794 (Dec. 1962).

Size-dependent spin lattice relaxation time, P. H. Fang, Phys. Rev. **129,** No. 4, 1548–1549 (1963).

Mathematical services for standards laboratories, A. T. McPherson, Rev. Math Fisica Teorica, **XIV,** Series A, Publ. 861, Nos. 1 & 2, 277–285 (Univ. Nacional de Tucuman, Argentina, 1962).

Artificial heating of the electrons in the *F* region of the ionosphere, D. T. Farley, Jr., J. Geophys. Res. **68,** No. 2 401–413 (Jan. 15, 1963).

Cryogenic impurity adsorption from hydrogen, M. J. Hiza, Chem. Eng. Progr. **56,** 68–71 (Oct. 1960).

Shear strength of beams without web reinforcement containing deformed bars of different yield strengths, R. G. Mathey and D. Watstein, J. Am. Concrete Inst. **60,** No. 2, 183–207 (Feb. 1963).

Corrosion resistance, G. A. Ellinger, Welding Handbook, 5th Ed. p. 6.1–6.72 (American Welding Society, New York, N.Y., 1963).

Cryogenic testing of structural solids, R. M. McClintock, Eng. Quart. **2,** No. 1, 28–35 (Feb. 1962).

Thermometric cells for calibration of liquid-in-glass thermometers, D. P. Enagonio, Book, Temperature, Its Measurement and Control in Science and Industry **3,** Pt. 2, 219–230 (Reinhold Pub. Corp., New York, N.Y., 1962).

Roger Joseph Boscovich and the combination of observations, C. Eisenhart, Actes Symp. Intern. R. J. Boskovic 1961, p. 19–25 (1962).

Tentative U.S. standard for colors of signal lights, F. C. Brechenridge, Illum. Eng. **57,** 575–576 (Sept. 1962).

Comment of empirical inference of Doppler widths, R. N. Thomas, Astrophys. J. **137,** No. 1, 38–40 (Jan. 1963).

Uncertainties in calibrations, W. J. Youden, IRE Trans. Instr. **I–II,** Nos. 3 & 4, 133–138 (Dec. 1962).

Reaction of oxygen with unkilned bone char at low temperatures ($<300°$ C), F. G. Carpenter and V. R. Dietz, Proc. 7th Tech. Session on Bone Char 1961, p. 237 (Bone Char Research Project Inc., Charlestown, Mass., 1962).

Horizons in dentistry, G. C. Paffenbarger, Frontiers of Dental Sci., p. 122–128 (Natl. Sci. Teachers Assoc., Washington, D.C., Dec. 1962).

Experimental determination of the frequency ratio of optical harmonics, H. S. Boyne and W. C. Martin, J. Opt. Soc. Am. **52,** No. 8, 880–884 (Aug. 1962).

The reactions of methyl radicals with aromatic compounds. II. The xylenes, W. A. Saunders and R. E. Rebbert, J. Phys. Chem. **67,** No. 1, 170–171 (Jan. 1963).

Desorption of calcium and sulfate ions from revivified bone char, H. M. Rootare, V. R. Dietz, and F. G. Carpenter, Proc. 7th Tech. Session on Bone Char, 1961, p. 293 (Bone Char Research Project Inc., Charlestown, Mass., 1962).

Energy use and power demands in all-electric houses equipped with air-to-air heat pumps, J. C. Davis and P. R. Achenbach, ASHRAE J. **4,** No. 9, 87–95 (Sept. 1962).

Ferroelectric switching and the Sievert integral, P. H. Fang and I. R. Stegun, J. Appl. Phys. **34,** No. 2, 284–286 (1963).

The conjugacy of magnetic disturbance variations, G. M. Boyd, J. Geophys. Res. **68,** No. 4, 1011–1013 (Feb. 13, 1963).

The giant resonance of the nuclear photoeffect, E. G. Fuller and E. Hayward, Book, Nuclear Reactions II, pp. 113–194 (North-Holland Publ. Co., Amsterdam, The Netherlands, 1962).

Comparison of the rubidium-87 and proton Zeeman transition frequencies in the earth's magnetic field, P. L. Bender, Phys. Rev. **128,** No. 5, 2218–2221 (Dec. 1962).

Precision millimeter wave interferometry at the U.S. National Bureau of Standards, W. Culshaw, J. M. Richardson, and D. M. Kerns, Interferometry Symp., June 9–11, 1959, paper 4–3, p. 331 (National Physical Laboratory, Teddington, Middlesex, England, 1960).

Mechanical properties of materials, R. H. Kropschot, Book, Applied Cryogenic Engineering, Ed. R. W. Vance and W. M. Duke, 44–59 (John Wiley & Sons, Inc., New York, N.Y., 1962).

A sing-around velocimeter for measuring the speed of sound in the sea, M. Greenspan and C. E. Tschiegg, Book, Underwater Acoustics, Lecture **5,** p. 87–101, (Plenum Press, Inc., New York, N.Y., 1962).

Relative signs of proton spin-spin coupling constants, E. Lustig, J. Chem. Phys. **37,** No. 11, 2725–2726 (Dec. 1962).

Quantitative metallographic evaluations of graphitic microstructures, L. L. Wyman and G. A. Moore, Mod. Castings **43,** No. 1, 7–16 (Jan. 1963).

A possible effect of lower atmospheric divergence on the local electron density in the ionosphere, N.J. Macdonald and R. W. Knecht, Inst. Solar Terrestrial Res. Tech. Report **8** (High Altitude Observatory, University of Colorado, Boulder, Colo,, 1960).

On the realistic measurement of precision and accuracy, C. Eisenhart, ISA Proc. Eighth Natl. Aero-Space Instrumentation Symp., Washington, D.C., p. 75–83 (May 1962).

Interpolation of platinum resistance thermometers, 10° to 273.15° K, R. J. Corruccini, Book, Temperature, Its Measurement and Control in Science and Industry **3,** Pt. 1, 329–338 (Reinhold Publ. Corp., New York, N.Y., 1962).

Polysulfide sealants: Part I. Formulation and application properties, D. A. George, L. Dunlap, and P. Stone, Adhesives Age **6,** No. 2, 32–36 (Feb. 1963).

Studies of errors in economic statistics, D. Rosenblatt, 1962 Proc. Business and Economic Statistics Section, Am. Stat. Assoc., p. 217 (1962).

Low temperature insultation, R. H. Kropschot, Book, Applied Cryogenic Engineering, Ed. R. W. Vance and W. M. Duke, p. 152–169 (John Wiley & Sons, Inc., New York, N.Y., 1962).

Communications in electronics, J. Stern, Signal **16,** No. 10, 78–79 (June 1962).

Theory of the deep penetration of electrons and charged particles, L. V. Spencer and J. Coyne, Phys. Rev. **128,** No. 5, 2230–2237 (Dec. 1962).

Quantities and units for dosimetry in diagnostic radiology, H. O. Wyckoff (Symp. under the auspices of the Division of Radiological Health, U.S. Public Health Service, Wash., D.C., March 5–6, 1962), Book, Technological Needs for Reduction of Patient Dosage from Diagnostic Radiology, Ed. M. L. Janower, p. 5–9 (Charles C. Thomas, Publ., Springfield, Ill., 1963).

Precision of methods for measuring tensile strength, stretch, and tensile energy absorption of paper, T. W. Lashof, Tappi **46,** No. 1, 52–59 (Jan. 1963).

Dimensional changes in dentures, G. C. Paffenbarger, J. B. Woelfel, and W. T. Sweeney, Dental Practitioner **13,** No. 2, 64–69 (Oct. 1962).

Current trends and prospects in cryogenics, R. W. Stewart, R. V. Smith and T. R. Strobridge, Cryogenics **2,** No. 6, 321–324 (Dec. 1962).

Tunneling between a normal metal and a superconductor, J. Harden and R. S. Collier, Cryogenics **2,** No. 6, 369–370 (Dec. 1962).

Comments on the Rosen interaction potential of two helium atoms, B. M. Axilrod, J. Chem. Phys. **38,** No. 1, 275–277 (Jan. 1963).

Effective impedance of a wire grid parallel to the earth's surface, J. R. Wait, IRE Trans. Ant. Prop. **AP–10,** No. 5, 538–542 (Sept. 1962).

Dislocations and chemical etch pits in copper, A. W. Ruff, Jr., J. Appl. Phys. **33,** No. 12, 3392–3400 (Dec. 1962).

The intensity and spectral distribution of scattered radiation from Co^{60} sources, B. Petree and J. C. Humphreys, Radiology **80,** No. 1, 120 (Jan. 1963).

Performance characteristics of turbine flowmeters, M. R. Shafer, J. Basic Eng. **84,** Series D, No. 4, 471–485 (Dec. 1962).

Experimental *gf*-values for seventy elements, C. H. Corliss, Astrophys. J. **136,** No. 3, 916–934 (Nov. 1962).

Scientific information activities at the National Bureau of Standards, W. R. Tilley (53rd Special Libraries Assoc. Conv., Metals Division, May 29, 1962, Washington, D.C.) Spec. Lib. p. 29–34 (Jan. 1963).

Properties of a silica-reinforced polymer for dental restorations, R. L. Bowen, J. Am. Dental Assoc. **66,** No. 1, 57–64 (Jan. 1963).

Mechanical basis of diffusion, C. Truesdell, J. Chem. Phys. **37,** No. 10, 2336–2344 (Nov. 1962).

Current status of the statistical theory of mass spectra, H. M. Rosenstock and M. Krauss, Book, Advances in Mass Spectrometry **2,** 251–284 (Pergamon Press, London, England, 1962).

Available heat sinks for protected underground installations, B. A. Peavy, Proc. Natl. Acad. Sci.-Natl. Res. Council Meeting on Environmental Engineering in Protective Shelters, p. 237–248 (Feb. 1960).

The sudden ionospheric disturbance, C. S. Warwick, Book, Radio Astronomical and Satellite Studies of the Atmosphere, p. 457–475 (North-Holland Publ. Co., Amsterdam, The Netherlands, 1963).

Realistic estimates of error, W. J. Youden, J. Instr. Soc. Am. **8,** No. 10, 57–58 (Oct. 1962).

**Publications for which a price is indicated are available from the Superintendent of Documents, U.S. Government Printing Office, Washington, D.C., 20402 (foreign postage one-fourth additional). Reprints from outside journals and the NBS Journal of Research may often be obtained directly from the authors.*

U.S. GOVERNMENT PRINTING OFFICE:1963

UNIVERSITY MICROFILMS
313 NORTH FIRST STREET
ANN ARBOR, MICHIGAN
SJR-A-OCT

UNITED STATES
GOVERNMENT PRINTING
DIVISION OF PUBLIC DOCUM
WASHINGTON, D.C. 20402

OFFICIAL BUSINESS

ALTY FOR PRIVATE USE TO AVOID
PAYMENT OF POSTAGE, $300
(GPO)

JOURNAL OF RESEARCH of the National Bureau of Standards Vol. 67A, No. 4 July–August 1963
A Physics and Chemistry

Contents

	Page
Symmetry splitting of equivalent sites in oxide crystals and related mechanical effects. J. B. Wachtman, Jr., H. S. Peiser, and E. P. Levine.	281
Relaxation modes for trapped crystal point defects. A. D. Franklin.	291
A note on the galvanomagnetic and thermoelectric coefficients of tetragonal crystalline materials. W. C. Hernandez, Jr., and A. H. Kahn.	293
Photolytic behavior of silver iodide. G. Burley.	301
Correlation of muscovite sheet mica on the basis of color, apparent optic angle, and absorption spectrum. Stanley Ruthberg, Mary W. Barnes, and Ralph H. Noyce.	309
Thermodynamic properties of magnesium oxide and beryllium oxide from 298 to 1,200 °K. Andrew C. Victor and Thomas B. Douglas.	325
Heat exchange in adiabatic calorimeters. E. D. West.	331
Preparation of anhydrous single crystals of rare-earth halides. Norman H. Kiess.	343
A phase study of the system: oxalic acid/acetic acid/water; its significance in oxalic acid crystal growth. John Strassburger and John L. Torgesen.	347
Wavelength calibrations in the far infrared (30 to 1000 microns). K. Narahari Rao, R. V. de Vore, and Earle K. Plyler.	351
On the fourth order Hamiltonian of an asymmetric rotor molecule of orthorhombic symmetry. Wm. B. Olson and H. C. Allen, Jr.	359
Measurement of the thickness and refractive index of very thin films and the optical properties of surfaces by ellipsometry. Frank L. McCrackin, Elio Passaglia, Robert R. Stromberg, and Harold L. Steinberg.	363
Color phenomena associated with energy transfer in afterglows and atomic flames. Arnold M. Bass and H. P. Broida.	379
Publications of the National Bureau of Standards.	389

For sale by the Superintendent of Documents, U.S. Government Printing Office, Washington D.C. 20402. Price 70 cents (single copy). Subscription price: $4 a year; 75 cents additional for foreign mailing.
UNITED STATES GOVERNMENT PRINTING OFFICE, WASHINGTON : 1963